

Measurement of Parity Violating Asymmetry in Elastic Electron Scattering off ^{48}Ca

A Dissertation Presented

by

Cameron Clarke

to

The Graduate School

in Partial Fulfillment of the

Requirements

for the Degree of

Doctor of Philosophy

in

Physics

Stony Brook University

December 2021

Stony Brook University

The Graduate School

Cameron Clarke

We, the dissertation committee for the above candidate for the

Doctor of Philosophy degree, hereby recommend

acceptance of this dissertation.

Krishna Kumar – Dissertation Advisor

Affiliated Professor, Department of Physics and Astronomy

Derek Teaney – Chairperson of Defense

Professor, Department of Physics and Astronomy

Rouven Essig

Professor, Yang Institute of Theoretical Physics

David Armstrong

Chancellor Professor of Physics

College of William and Mary

This dissertation is accepted by the Graduate School.

Eric Wertheimer

Dean of the Graduate School

Abstract of the Dissertation

**Measurement of Parity Violating Asymmetry in
Elastic Electron Scattering off ^{48}Ca**

by

Cameron Clarke

Doctor of Philosophy

in

Physics

Stony Brook University

2021

Atomic nuclei are composed of nucleons governed by the strong nuclear force. Although the proton distributions in nuclei are well measured with electromagnetic probes, the neutron distributions are relatively unconstrained. The nuclear symmetry energy governs the distribution of the excess neutrons in asymmetric nuclei, as well as the dynamics of neutron-rich nuclear matter up to the scale of neutron stars. Parity-violating electron scattering (PVES) is a mature experimental method by which the parity-violating weak interaction provides access to the neutron distributions. We report the result of the CREX experiment which is sensitive to bulk and surface isospin asymmetry effects through the measurement of the parity-violating scattering asymmetry, A_{PV} , with 2.18 GeV highly polarized

electron beam scattering elastically from an unpolarized ^{48}Ca target at 5° forward angle. CREX ran in Hall A at Jefferson Lab in the Spring and Fall of 2020 and measured $A_{PV} = 2659 \pm 106$ (stat) ± 40 (syst) ppb. This corresponds to a measurement of the weak form factor of $F_W(Q^2 = 0.0297(2)\text{GeV}^2) = 0.1297(55)$ with an implied experimental precision on the weak charge skin of $\delta R_{skin}^W \simeq \pm 0.025$ fm. After describing the apparatus, the experimental techniques employed to analyze helicity correlated beam asymmetries, their systematic uncertainties, and the data-set's statistical properties are discussed in detail. The ongoing theoretical interpretation of the CREX F_W measurement will provide significant constraints to the isovector parametrizations of theoretical nuclear structure models and the density dependence of the nuclear equation of state (EOS) relevant to the physics of heavy ions, radioactive isotopes, and neutron stars.

Contents

List of Figures	x
List of Tables	xxix
Acknowledgements	xxxiii
1 Theory and Motivation	1
1.1 Semi Empirical Mass Formula	5
1.2 Nuclear Equation of State	7
1.3 Electron Nucleus Scattering	10
1.3.1 Electroweak Theory	11
1.3.2 Parity Violation	13
1.3.3 Form Factor	15
1.3.4 Figure of Merit	18
1.4 Physics Impact	21
1.4.1 Density Functional Theory	23
1.4.2 Dispersive Optical Model	24
1.4.3 Ab Initio models	25
1.4.4 Model Predictions and Hadronic Measurements	28

1.5	Calcium Radius EXperiment	31
2	Experimental Overview	32
2.1	Injector at Jefferson Lab	35
2.1.1	The Polarized Electron Source	38
2.1.2	Slow Helicity Reversals	41
2.1.3	Helicity Signal Electronics	43
2.1.4	Helicity Correlated Beam Asymmetries	45
2.1.5	Charge Asymmetry and Feedback	47
2.1.6	Position Differences	49
2.2	The Accelerator, CEBAF	50
2.3	Hall A	55
2.4	Target Ladder	58
2.4.1	Beam Rastering	63
2.5	Pivot Area	69
2.5.1	Collimation	71
2.5.2	Shielding	75
2.5.3	Septum Magnet	76
2.6	High Resolution Spectrometers	77
2.7	Detector Package	80
2.7.1	Vertical Drift Chambers (VDCs)	81
2.7.2	Trigger Scintillators	84
2.7.3	Integrating Cherenkov Detectors	85
2.8	Data Acquisition	91
2.8.1	Counting DAQ	91

2.8.2	Integrating DAQ	92
2.8.3	Integration Triggering	95
2.8.4	Integration Sampling	98
2.9	Beam Monitors	102
2.9.1	Position	105
2.9.2	Beam Intensity	107
2.9.3	Energy	110
2.9.4	Beam Modulation	112
2.10	Small Angle Monitors	114
2.11	Polarimetry	116
2.11.1	Injector Mott Polarimeter	117
2.11.2	Compton Polarimeter	119
2.11.3	Møller Polarimeter	121
2.12	Experimental Summary	123
3	Data Analysis	124
3.1	Pedestal Calibration	126
3.1.1	Unser	127
3.1.2	BCMs and BPMs	129
3.1.3	PMT-Based Detectors	132
3.2	Normalized Asymmetry	133
3.3	Cuts	136
3.3.1	Current Monitor Cuts	137
3.3.2	Position Monitor Cuts	140
3.3.3	Data Stream Cuts	141

3.3.4	Additional Cuts	142
3.3.5	Data After Cuts	143
3.4	Raw Asymmetry	144
3.5	Beam Corrections	148
3.5.1	Regression	151
3.5.2	Dithering	152
3.5.3	Eigenvector Beam Monitor Basis	157
3.5.4	Lagrange Multiplier Analysis	162
3.6	Uncertainty on the Beam Corrections	166
3.6.1	Residual Sensitivities	166
3.6.2	Weighted Average	170
3.6.3	Differences Between Correction Methods	173
3.6.4	Systematic Error Estimate	176
3.6.5	Statistical Quality	178
3.7	Including BMOD Data	190
3.8	Beam Corrections Confidence	192
4	Conclusion	194
4.1	Parity-Violating Asymmetry	194
4.2	Model Extraction	197
4.3	Neutron Skin	201
4.4	Physics Implications	203
4.5	Future Prospects and Concluding Remarks	205
A	Run-ranged Segmentation Definitions	209
A.1	Dithering Segmentation	209

A.2	Eigenvector Monitor Parts	212
A.3	Slugs, Slow Controls, and Pitts	212
B	Non-Technical Overview	217
B.1	Quantum Mechanics	217
B.2	Quantum Field Theory	218
B.3	Nuclear Physics	219
B.4	Effective Field Theory	220
B.5	Electroweak Theory	220
B.6	Calcium Radius EXperiment	221
B.7	Outline	222
	Bibliography	223

List of Figures

1.1	The chart of nuclides versus neutron and proton number with overlay depicting the range of modern theoretical modeling techniques. Large nuclei are described by nuclear DFT while small and medium mass nuclei are described by <i>ab initio</i> methods using NN and 3N nucleon potentials. The PREX II and CREX points are indicated with stars, and CREX will provide a point of reference between the various approaches. Reproduced from [1].	3
1.2	Predictions of the ^{48}Ca neutron skin thickness, R_{skin}^{48} , compared to the ^{208}Pb theoretical R_{skin}^{208} predictions and recent extraction from PREX II (vertical band) [2]. The yellow horizontal band is from a Dispersive Optical Model (DOM) calculation from [3], the blue band is from <i>ab initio</i> couple cluster chiral effective field theory (χEFT) calculations from [4], and the points are from relativistic (blue squares) and non-relativistic density functional theory (DFT) models from [5] and [6]. Figure adapted from [1, 7] by Bob Michaels.	4
1.3	Droplet model (DM, squares) parametrized R_{skin} calculations and antiprotonic scattering measurements (circles) versus the neutron-proton asymmetry. Reproduced from [8].	5

1.4	Measured nuclear root mean square (RMS) electromagnetic charge radius for all nuclei versus mass, with the simple spherical drop $R \sim A^{1/3}$ model fit (left). Binding energy per nucleon, $B(N, Z)/A$, with inset showing the percent difference between measured data and the predictions from the simple drop model (right). Reproduced from [8].	6
1.5	Constraints on the symmetry energy, J (or S_v), and its density-dependent slope, L , from experimental results on neutron skins, heavy ion collisions, and more, including two independent global studies denoted by G and H [8–10]. The recent PREX II result, presented in [2, 11], adds the additional constraints of $J = 38.1 \pm 4.7$ MeV and $L = 106 \pm 37$ MeV, not shown in the figure, which are in tension with those shown here. Reproduced from [10].	8
1.6	Form factor versus momentum transfer (left) and correlation between form factor and the weak skin thickness (right) for PREX and CREX using the FSUGold relativistic mean field model. Reproduced from [1].	16
1.7	Predicted A_{PV} sensitivity $\epsilon_{R_n} = d \ln A_{PV} / d \ln R_n$ to a 1% change in R_n^{48} versus scattered angle (left) and sensitivity to skin thickness, $\epsilon_{a_n} = \epsilon_{a_n} = d \ln A_{PV} / d \ln a_n$, (right) for two possible CREX energies. The SLY4 neutron density was used. The red arrows indicate the approximate average scattering angle for CREX running. Figures adapted from [12].	18
1.8	Calculations from 48 DFT models of R_{skin}^{208} versus R_{skin}^{48} , including constraints from PREX I and II [2]. Adapted from [13].	22

1.9	(a) Fit of neutron- ^{48}Ca elastic-scattering data to the DOM best-fit (solid curves) and also constrained to match the the <i>ab initio</i> $R_{skin}^{48} = 0.132\text{fm}$ results (dashed curves). (b) Similar comparison of the total neutron cross section data, with similar best fit (solid) and <i>ab initio</i> result constrained (dashed) lines. (c) The data-fit χ^2 space, indicating the constribution from the elastic scattering data (short dashed) and total neutron cross section data (long dashed) separately, and displaying the <i>ab initio</i> value and best-fit values on the plot. Reproduced from [3].	23
1.10	Two-nucleon (NN) and three-nucleon (NNN, 3N) chiral effective field theory (χEFT) interactions at various orders in perturbation theory used to construct potentials in <i>ab initio</i> nuclear structure models. Reproduced from [4].	26
1.11	Plots showing the χEFT NN and 3N potential derived NNLO_{sat} (red circle) and N3LO (squares, fit line and error band) model predictions of the proton and neutron radii, neutron skin, and dipole polarizability α_D . The green band is the experimental value of R_p and its intersection with the blue error band from the less constrained N3LO models generates the (orange) theoretical systematic uncertainty band for the predicted isovector sensitive quantities on the horizontal axis. The blue diamond points come from DFT models, including the SLY4 model, and display trends independent from the <i>ab initio</i> models, particularly for the R_{skin}^{48} predictions. Reproduced from [4].	27

1.12	(a) Plots showing the χ EFT NN and 3N potential derived NNLO _{sat} (red circle) and N3LO (squares, fit line and error band) model predictions of the neutron radii, taken from Fig. 1.11b, versus and the predicted $F_W(Q^2)$, whose error band is calculated in a similar way. (b) The $F_W(Q^2)$ from DFT and <i>ab initio</i> model calculations for the full range of Q^2 , with the proposed CREX kinematic $q_c = 0.778 fm^{-1}$ point indicated [4](supplementary) (c). The weak and electric charge densities from the <i>ab initio</i> model discussed in the text, indicating a non-trivial neutron skin. Reproduced from [4].	27
1.13	Plot showing the experimental result for the electric dipole polarizability of ^{48}Ca from [14] (blue band) alongside model predictions from χ EFT (green triangles) and DFT models (red squares). The green bar indicates the χ EFT models whose α_D results match the experimental measurement and which are used to predict R_{skin}^{48} , and the black bar is the same for the DFT models. Reproduced from [15].	29
1.14	The difference in charge and weak form factors of ^{48}Ca vs. q , along with the predictions from relativistic DFT models and the DOM and NNLO _{sat} <i>ab initio</i> model discussed in the text. A point is shown for the predicted CREX precision at an arbitrary location. Reproduced from [16].	30
2.1	CEBAF cartoon, adapted from [17].	33
2.2	Aerial view of the Continuous Electron Beam Accelerator Facility (CEBAF), where CREX takes place.	34
2.3	Schematic drawing of the injector laser and polarized electron source. Adapted from [18].	36

2.4	Schematic drawing of the CEBAF injector’s polarized source. The double Wien system, not shown, is located along the beamline after the photocathode. Reproduced from [19].	37
2.5	Diagram of the strained GaAs crystal’s electron band structure and dynamics for one helicity handedness. As a result of breaking the spin-dependent degeneracy it is possible to preferentially promote and eject electrons from the conduction band of a specific helicity, producing a polarized beam. Reproduced from [20].	39
2.6	Polarization ellipses for the electric field vector of nearly-perfectly circularly-polarized light in the two opposite helicity states. The asymmetric phase shift Δ represents residual linear polarization and is responsible for the PITA effect in devices with linear polarization analyzing power. Reproduced from [18]. .	40
2.7	Helicity logical signals timing diagram for CREX. This figure shows the four helicity-control signals for CREX 120 Hz “free clock” running, alongside the reference freely floating “beam sync” signal that indicates the starting phase of each 60 Hz power supply oscillation.	42
2.8	Schematic of the helicity-control electronics. The helicity-state logical signal is transmitted via fiber optic cables and determines the high voltage on the Pockels cell. The Pockels Cell and helicity-signal generator are both electrically isolated from the beamline and data acquisition components elsewhere in the laboratory (dashed box). Adapted from [21].	43

2.9	Maximal PITA effect sensitivity from the cathode's analyzing power (A_p) due to residual linear polarization asymmetry between two imperfectly circularly-polarized laser helicity states (left handed, dashed, and right handed, solid, lines) is shown on the left, and the case with minimal PITA effect sensitivity by rotating the axes of the two states' residual linear polarization to 45° with respect to the cathode's A_p optical axis is shown on the right. Reproduced from [22].	47
2.10	CEBAF 12 GeV upgrade design schematic. Reproduced from conference proceedings slide 5 of [23].	50
2.11	Cartoon depiction of the horizontal separator RF-cavity acting on phase and time separated electron beams generated in the injector. Shown on the right are cases of separating or maintaining beams, based on the relative timing of the copper cavities. Reproduced from [24].	53
2.12	Schematic of the double Wien filter in the CEBAF injector, used for optimizing polarization launch angle and for performing slow-control helicity reversals. Reproduced from [19].	54
2.13	Schematic of the crossed electric and magnetic fields in a Wien filter used to rotate the spin but not perturb the trajectory of passing electrons. Reproduced from [25].	55
2.14	Cartoon depicting the beam delivery and monitoring systems of Hall A. Adapted from [21].	56
2.15	Simplified CAD depicting the target scattering chamber on the left, acceptance-defining collimator and septum magnets in the middle, and HRS acceptance on the right.	56

2.16	15 K gaseous helium cooled “production” target ladder, viewed from downstream. The calcium targets are on the far left in the 1 <i>cm</i> diameter top-hat shaped insert plugs. Reproduced from [26].	58
2.17	Water cooled “optics” target ladder, viewed from upstream. Reproduced from [26].	59
2.18	Annotated CAD view of the PREX II and CREX target system. Reproduced from [27].	59
2.19	The ^{40}Ca (left) and damaged original ^{48}Ca target (middle). A miss-steering event on January 18th 2020 caused the beam to strike the copper frame and dissipate the generated heat by melting the ^{48}Ca target. Reproduced from [28].	61
2.20	PREX I data, showing the left- and right-arm regression-corrected asymmetry distributions. Reproduced from [20]. With the unsynchronized raster there is still some residual correlation between the two detectors’ measurements, even after correcting for beam position and energy correlations using linear regression, which go away in the synchronized case.	66
2.21	Target face area covered by the raster within the same amount of time for a frequency difference of 120 Hz (left) and 960 Hz (right). Reproduced from [26].	66
2.22	CFD simulation results showing the time dependence of the maximum temperature (red) and average temperature (blue) within the PREX II lead targets under various raster frequency and beam spot size conditions. Reproduced from [26].	68

2.23	Simulated raster pattern showing the improvement in target face coverage by going from raster frequencies which are divisible (a) by the difference between them to frequencies which are not (b). In red is a fraction of the pattern to display the trajectories, and in black is one full helicity flip period's pattern to display the change in target face coverage.	70
2.24	Schematic of the raster frequency controls. The 10 MHz signal is used in the injector to give a consistent clock while the measured MPS signal sent from the injector to Hall A over fiber optic cables marks the beginning of new helicity windows and is used to tune the raster frequencies in two independent channels of the Agilent 33522A function generator. Updated and adapted from [19, 24].	70
2.25	CAD snapshot and picture, both taken by Ciprian Gal, of the PREX II and CREX collimation, shielding, and septum magnet systems, along with the target and beamline components.	71
2.26	CAD cross-section of the central beamline collimator, showing the spiraling water cooling channel and recirculation system.	72
2.27	Photograph taken during installation of the Q_1 magnet entrances, with the acceptance-defining collimators, painted blue, installed. Reproduced from [28].	73
2.28	Schematic diagram of the septum magnet bending $\sim 5^\circ$ scattered electrons into the acceptance-defining collimators at the HRSs minimum 12.5° angle. Reproduced from [29].	76
2.29	Cartoon of the layout of the HRS magnetic transport and momentum spectrometry in Hall A, also showing the detector systems used for optics and asymmetry measurements. Reproduced from [28].	78
2.30	Drawing of the HRS along with the rest of Hall A and the beam dump, to scale. Reproduced from [30].	78

2.31	Cartoon of the HRS optics system, from Kent Paschke, showing the focusing feature of the QQD _n Q HRS magnet setup and the separation of inelastic states from the primary detector.	79
2.32	CAD drawing of the HRS detector systems on the movable support structure. The relative positioning of the various detectors is shown, although the S3 detector depicted represents only one third of the scintillators actually used at that location during CREX and the “A _T ” background detectors are not shown. The beam enters the detectors from the bottom left. Reproduced from [28].	82
2.33	Schematic views of the Hall A HRSs’ VDC chambers (not to scale). Reproduced from [28] and [30].	83
2.34	Schematic of the Cherenkov cone produced by relativistic charged particles ($\beta \sim 1$) in fused silica quartz, with a Cherenkov emission angle of 46.6°. Reproduced from [28].	86
2.35	Cartoon, drawn by Tyler Kutz, of the detection of total internal reflected Cherenkov light (DIRC) in the CREX detector design.	86
2.36	Example single electron photoelectron (PE) spectrum for the upstream (red) and downstream (black) CREX detectors using 5mm thick fused silica (quartz) Cherenkov radiator tiles. The downstream detector’s spectrum has a more significant tail due to charged particle showering (delta rays) generated in the upstream quartz.	88
2.37	Pulse height spectrum from single electron tracks in the upstream integrating detector taken during CREX, analyzed by Devi Adhikari. The left figure shows the raw signal, including the pedestal peak which is fit with a Gaussian and subtracted in the figure on the right.	89

2.38	Photograph, taken by Dustin McNulty, of the tandem mounted “main” integrating fused silica (quartz) Cherenkov detectors. The plastic and Kapton covering is not shown. The black paper around the quartz is only for light tightness and is in loose contact to avoid affecting the optical properties of the quartz.	90
2.39	Schematic of the integrating quartz detector signal chain, from PMT to pre-amplifier to ADC integrator. Adapted from [31].	93
2.40	Schematic diagram of the integrating DAQ. The helicity information (red) is transported by fiber optic cables from the helicity control board to the injector and CH integrating DAQs. The CH DAQ generates copies of the helicity information, integration gate and latch signals, and the MPS based trigger for itself and the HRSs and TS (green). The TS initiates the DAQ readout with a global shared trigger (black arrows). The data (light blue) is extracted by each ROC and sent via gigabit ethernet to the Hall A Counting House Linux workstation where it is processed by CODA to be used in online and offline analyses.	93
2.41	Schematic representation of the $\Delta t = 2\mu s$ sampling of analog signals, digitized by 18 bit QWeak ADCs. The samples are summed in four sub-blocks and a full sum for each helicity state. The input signal fluctuations are exaggerated to show the significance of the sampling process. Reproduced from [32]. . . .	97
2.42	Schematic representation of the ADC and scaler integration timing for CREX. The $10\mu s$ VQWK internal delay and integration gate with $\sim 50\mu s$ integration holdoff at the end are shown. The signal fluctuations are exaggerated to show the significance of integration. Adapted from [31].	100

2.43	Battery asymmetry distribution from run 5408 at the beginning of CREX, showing the RMS (“Std Dev” in the statistics box) stability of the QWeak ADC channels at the few <i>ppm</i> level.	100
2.44	Diagram showing the delayed helicity state read latch signal timing, delayed after the beginning of the integration. This is done so the CODA DAQ process can read the the prior helicity state information and store it in memory, before the latching scaler (FLEXIO or STR7200) reads the current state. The delay is $\sim 150\mu s$, to allow sufficient time for the CODA read out list (ROL) to safely finish reading all prior helicity state data.	101
2.45	Schematic of the Hall A beamline monitoring and beam modulation hardware, along with approximate locations of the current monitors and beam optics tuning quadrupole magnets. The modulation coils are indicated by their “trim” control systems, with trim 7 dithering energy in the final cavities of the south linear accelerator, measured in BPMs 11 and 12, trims 1, 3, and 5 dithering the X position, and trims 2, 4, and 6 dithering the Y position of the beam, measured in the hall BPMs 1, 4A, and 4E. Reproduced from [28].	104
2.46	Schematic diagram of the upstream (US) and downstream (DS) analog (AN) beam current monitors’ (BCM) signal chain and cabling.	108
2.47	Schematic diagram of the Hall A arc magnets and super harps used in the arc energy measurement. Reproduced from [24].	110
2.48	Images of the SAMs implemented in CREX. On the left is an engineering drawing of the SAM placements in the beamline, showing the PMTs protruding from the vacuum insert tubes. In the middle is a beam line view of the vacuum inserts protruding into the beamline. On the right are CAD views of the SAM PMT, quartz, and light guide design. Reproduced from [28].	115

2.49	CAD drawing of the Mott polarimeter in the 5 MeV region of the injector. Reproduced from [25].	118
2.50	Schematic drawing of the Compton polarimeter in the Hall A beamline. Re- produced from [28, 33].	119
2.51	CAD schematic of the Møller polarimeter in Hall A. Reproduced from [21]. .	121
3.1	Example Unser-relative calibration data showing the beam-off pedestal values for the Unser on the left, with their cleaned source distributions on the right. The cleaned data is shown in blue and the red data is cut to provide a stable pedestal with no beam-on data included. The RMS of the data in the blue distribution is used as the uncertainty for the Unser pedestal, on the left, and its uncertainty is propagated to the points used in the Unser-relative pedestal calibration fit shown in the next figure.	128
3.2	Example Unser-relative calibration fit for the BCM AN US pedestal on the left, and residuals of the fit on the right. The Unser-relative calibrations use the RMS of the beam-on and beam-off data as the uncertainty in the mean values and Unser's subtracted pedestal, shown in the previous figure.	128
3.3	Global average of the Unser-relative pedestals for the normalizing BCM AN US.	130
3.4	Example Normalizing BCM AN US-relative calibration fit for the USL main detector pedestal on the left, and residuals of the fit on the right. The Nor- malizing BCM AN US-relative calibrations use the RMS/\sqrt{N} of the beam-on data as the uncertainty in the mean values.	131
3.5	Global average over the first run period of CREX of the Normalizing BCM AN US-relative pedestals for BCM DG DS.	132

3.6	Beam-off pedestals measured for each run in CREX (left), their stable-segment averages (middle), and the percent deviation from the full beam-on signal size of the difference between the stable-segment averaged and run-wise beam-off pedestals (right). The effect on precision of averaging is seen to be minimal, well below the 0.1% level.	133
3.7	Plots showing the response of the normalizing BCM AN US versus injected RF signal on the left, and the percent deviation from the linear fit across that range on the right. RF injection tests were performed before CREX to optimize the signal input into the analog BCMs' 10 MHz down-converter box to maximize the linearity in the CREX current range around $150\mu A$. The non-linearity measured in these RF injection scans is approximately at the 0.3% level.	134

3.8	Plots showing the cumulative bias in the beam intensity asymmetry following beam trip recoveries, separated into the four states of the IHWP and Wien across the experiment. The beam trip recovery cut used in the online charge feedback analyzer is an additional 1000 events (250 multiplets) too long compared to what is used in the offline analysis, and these 250 multiplets are not included in the online charge feedback correction calculations and do not have corrections applied to them. The following 250 multiplets, starting at multiplet 250, are included in the correction calculations and begin to receive corrections based on the running feedback analyzer's event loop calculation including data from before the beam trip began. The third set of 250 multiplets, starting at 500, are fully corrected by the calculation made on the second set of 250 multiplets, and show a trend closer towards average null charge asymmetry. The effect changes sign under the Wien flip, indicating that it comes from a systematic effect in the Pockels Cell related to the beam ramping back to full current.	138
3.9	Correlations between the USR main detector asymmetry and the energy sensitive BPM 12X, left, and between the USL and USR main detectors, right. .	145
3.10	Display of the spread in the raw asymmetry RMS (left) compared with the stable and smaller corrected asymmetry RMS (right). The spread in the raw asymmetry RMS does not correspond to counting statistics, but rather comes from changing amounts of beam position noise and changes in measured rate's position sensitivity over the course of the experiment.	145

3.11	Display, for one representative run, of the spread in the raw asymmetry RMS (red) compared with the stable and smaller corrected asymmetry RMS (blue) corresponding approximately to the counting statistics distribution width, displaying the power of and necessity for performing beam corrections.	149
3.12	An example of beam modulation data accumulated over many cycles of modulation for the horizontally dithering coil 1. The USL main detector and one of the X sensitive BPMs responses as a function of modulation phase are shown on the left, and the correlation sensitivity response versus the modulation amplitude are shown on the right.	153
3.13	BPM 4eY sensitivity to coil6 throughout the CREX run, as an example of the changing dithering sensitivities. Red data points are removed due to insufficient data for slope calculations or are removed by hand.	153
3.14	Plots showing the dithering-segment averaged slopes for each BPM from the 5 BPM regression and dithering analyses. The slopes do not match between the two analysis methods due to differences in their correlations and systematics.	158
3.15	Two example eigenvector composition calculations for each minirun (left) and averaged across the three “part” optics tune segmentations of CREX (right).	159
3.16	Plots showing the dithering-segment averaged slopes for each BPM from the 5 eigenvector monitor regression and dithering analyses. The slopes are in better agreement than the plain BPM basis set correction slopes, but still do not totally match.	160

3.17	Plots showing the USL and USR main detector dithering-segment averaged slopes for each BPM from the 12 eigenvector monitor regression and Lagrange analyses. The segment averaging of the slopes is done to simplify the visual display, though both regression and Lagrange analyses both calculate slopes for each minirun.	162
3.18	The same as Fig. 3.17 but for the six eigenvectors with smaller RMS jitter. .	163
3.19	Grand-averaged 12 evMon Lagrange corrected main detector A_{det} versus slug number.	165
3.20	Example of dithering sensitivities and residuals showing the raw (top two) and residual (bottom two) US Avg sensitivities to the dithering energy modulation, with the mean and standard deviation shown for each slug. The fits give the experiment-averaged sensitivity mean and standard deviations, used to evaluate the systematic uncertainty in the corrections.	167
3.21	Pull plot of the minirunwise grand-averaged 12 evMon Lagrange multipliers analysis corrected A_{det}	179
3.22	Pull plot of the slugwise grand-averaged 12 evMon Lagrange multipliers analysis corrected A_{det}	179
3.23	Multiplwise asymmetry distribution, “mul plot,” of the 12 evMon Lagrange multipliers analysis corrected A_{det} . The distribution is Gaussian for ~ 5 orders of magnitude, and the tails are primarily due to occasional noise in beam delivery that evades cuts and have no effect on the Gaussian fit σ compared to the distribution standard deviation. A cut is applied for this mul plot to only include data with both HRSs active and with beam current close to the optimal $150\mu A$ level, which removes 4×10^6 events, corresponding to only 5% of the data.	182

3.24	Differences between 12 evMon Lagrange multipliers analysis vs. regression corrected A_{det} averaged over miniruns, where the difference distribution is obtained from the multipletwise distribution. The uncertainty used in the weighted average weights comes from the multipletwise difference distribution's RMS/\sqrt{N} widths. The pull distribution is very close to the statistical ideal.	183
3.25	Weighted mean.	184
3.26	12 evMon Lagrange multipliers analysis corrected A_{det} vs. slow-control flip timescale minirun averages. Numbers 1, 3, and 5 are IHWP In, 2, 4, and 6 are IHWP Out. 3 and 4 are both Wien Left and the others are Wien Right.	184
3.27	12 evMon Lagrange multipliers analysis corrected $A_{null\ Pitt}$ vs. Pitts. Each null Pitt average equally weights the IHWP In and Out state data and looks at the disagreement between them to illuminate IHWP dependent HC A_{beam} . The null Pitt average without a sign multiplication between the Wien states also cancels any HC A_{beam} which are not affected by the Wien, to the degree that there are similar amounts of Wien Right and Left data across the experiment.	187
3.28	Slugwise charge asymmetry A_Q across CREX. The non-trivial Wien-dependence in A_Q due to the improperly set charge feedback engine cuts during production running is visible to the eye. The χ^2 and fit probability are non-statistical because of the Wien-dependent trip-recovery A_Q and also because the charge asymmetry distribution is intentionally driven, non-statistically, to zero with the feedback system during production running.	190

3.29	Pull plot of the difference in corrected A_{det} between the BMOD active and inactive cut data-sets within each minirun containing BMOD calibration data. This shows the well behaved statistical behavior and independence of the BMOD active vs. inactive data within each minirun.	191
3.30	Minirunwise (left) and histogram (right) showing the ratio of the corrected A_{det} RMSs of the BMOD active vs. inactive data, indicating their consistent and statistical behavior within each minirun.	191
4.1	Plot of the weak form factor calculated with various relativistic and non-relativistic DFT models at the average $\langle Q^2 \rangle = 0.0297 \text{GeV}^2$ for CREX. The red band shows the experiment $A_{PV}^{meas} = 2658.6 \pm 113.2$ ppb intersecting a linear fit line to the F_W points, extracting $F_W(\langle Q^2 \rangle) = 0.1297(55)$	198
4.2	The electromagnetic charge form factor minus the weak charge form factor for the ^{48}Ca nucleus as a function of $q = \sqrt{Q^2}$. The curves show the calculated difference in form factors for a family of nuclear structure models corresponding to different weak charge RMS radii over a range of relevant skin thicknesses, which are labelled next to each curve. The CREX result is shown as a point with the experimental error bar [34].	204
4.3	The difference in electromagnetic charge form factor minus the calculated weak charge form factor result from a family of relativistic and non-relativistic DFT models for CREX versus that of PREX. The model calculation for both experiments' results are plotted, and the values consistent with the experimental results are shown in the red (PREX) and blue (CREX) bands. The yellow ellipses show the 1σ and 90% confidence levels of the overlap region for the two experiment results [34].	206

4.4	The extracted weak radius (left) and neutron skin (right) for the ^{208}Pb nucleus with the experimental electromagnetic charge radius and the PREX II asymmetry result shown. The theoretical uncertainty in the skin extraction is determined by the spread in the correlation of the models' predictions versus A_{PV} and the central value and experimental uncertainty are obtained by projecting the experimental asymmetry result to the fit line. Reproduced from [2].	207
A.1	Relative statistical weights of the Pitts (in arbitrary units, approximately normalized to the average weight for all Pitts) versus Pitt number. Orange is Wien right and purple is Wien left.	214
A.2	Relative statistical weights of the slugs used to assign Pitt definitions (in arbitrary units, approximately normalized to the average weight for all slugs) versus slug number. The sign corresponds to the IHWP state, indicating the similar amounts of data taken in each slow control setting. See table A.7 for the slug to Pitt correspondence. Orange is Wien right and purple is Wien left.	216
A.3	12 eigenvector monitor Lagrange multipliers analysis corrected A_{det} vs. Pitt.	216

List of Tables

1.1	Table of fermion electromagnetic and weak charges, t_L^3 weak isospin, and vector and axial-vector weak couplings.	10
1.2	Approximate kinematic parameters for CREX [12].	21
1.3	Theoretical calculation and experimental constraint results for R_{skin}^{48} discussed in the text.	28
2.1	Table of parameters used in CREX running.	33
2.2	“Warm” optics target ladder positions and thicknesses. Reproduced from [27].	62
2.3	“Cold” production target ladder positions and thicknesses. Index 1 indicates the initial configuration and thicknesses before the ^{48}Ca target melting incident, and 2 indicates the configurations afterwards. Reproduced from [27], where the precise carbon-lead-carbon sandwich targets’ descriptions may also be found.	62
2.4	Second ^{48}Ca target’s three puck components’ thicknesses and isotopic purities. Reproduced from [27].	63
3.1	CREX data quantities after cuts.	144
3.2	Table of miniruns cut after the final analysis respin due to missed beam position and hardware problems [35].	144

3.3	Table of fractional residual dithering sensitivity RMSs, given in percent, from the 12 evMon Lagrange corrections for USL, USR, and US Avg main detectors. Coils 1, 3 and 5 are horizontal (X) modulation directions, coils 2, 4 and 6 are vertical (Y) modulation directions, and coil 7 is the energy (E) vernier. Coils 2 and 5 are not included in the Lagrange multiplier constraints, and are used to cross check the sufficiency of correction slopes, and are shown in red. The X coils have small raw sensitivities in the US Avg, due to cancellation of sensitivity between the HRS arms, yielding large fractional residuals.	168
3.4	Main detector statistically-weighted averages of the 12 eigenvector monitors HC differences vs. CREX parts. The mean and error are in units of nm while the RMS is in units of μm . The eigenvectors are ranked by their eigenvalue magnitudes, corresponding to the monitor RMS size.	174
3.5	Main detector statistically-weighted averages of the 12 evMon Lagrange multipliers analysis slopes for the US Avg main detector vs. CREX parts, in units of $ppm/\mu m$. The average slopes are shown along with the average difference between Lagrange and regression slopes ΔC , and the RMS of that difference.	174
3.6	Main detector evMon corrections vs. CREX part, main detector statistics weighted. The correction standard error is calculated by using the slope \times evMon multipletwise difference mean error, propagated through the average calculation, with main detector statistical uncertainties as weights. The mean and error are in units of ppb, while the RMS is in units of ppm.	175

3.7	A_{det} grand weighted averages, using the 12 evMon Lagrange analysis σ_A as weights, from the 5 evMon regression and dithering and 12 evMon regression and Lagrange analysis techniques. The uncertainty on the correction amount is obtained through $\delta A_{beam} = \text{adding } 5\% \times \text{the grand-averaged corrections per monitor in quadrature separately over the three eigenvector definition parts of CREX.}$	176
3.8	Main detector evMon corrections vs. CREX part, main detector statistics weighted, as in table 3.6, while also showing the sum and uncertainty in the sum of corrections per evMon averaging part and statistically-weighted grand average. All units are ppb.	177
3.9	Blinded main detector asymmetry and net correction per evMon averaging part of CREX and the statistically-weighted grand average A_{det} and A_{beam} correction final results. All units are ppb.	177
3.10	Main detector grand-averaged 12 evMon Lagrange multiplier analysis corrected A_{det} and correction, as well as χ^2 results from performing the average over different timescales, each of which are the result of weighted averages with their constituent miniruns' $A_{det\ i}$ and $\sigma_{det\ i}$. The asymmetry and uncertainties are given in units of ppb, and the RMS is in ppm. The reduced χ^2 are close to 1 for all averaging time scales.	180
3.11	Slow-control flip timescale A_{det} averaged over miniruns.	184
3.12	Table of weighted average helicity-correlated target and energy beam parameters across the CREX Wien flips.	187
3.13	Table of weighted average raw and corrected detector asymmetry and A_Q across the CREX Wien flips.	189

4.1	Table of error contributions for the CREX A_{PV} measurement.	195
A.1	Runranges for the CREX dithering segmentation. Segments 25-32 are the transverse polarization running period. There is no segment 1, due to a lack of beam modulation measurements for the first run-range.	210
A.2	List of run numbers and beam modulation cycle numbers that are removed from the calibration data-set for calculating slopes and sensitivities.	211
A.3	Table of eigenvector monitor “part” segmentations for CREX.	212
A.4	CREX part averaged 12 BPM eigenvector monitor combinations, for the first part, averaged across runs 5000-6327.	213
A.5	CREX part averaged 12 BPM eigenvector monitor combinations, for the sec- ond part, averaged across runs 6328-7500.	213
A.6	CREX part averaged 12 BPM eigenvector monitor combinations, for the third part, averaged across runs 7501-8558.	214
A.7	Table of Pitt slug range definitions, indicating the Wien and IHWP states included.	215

Acknowledgements

I would like to thank my advisor, Dr. Krishna Kumar, for his continuous support and care for myself, as well as the other students and post doc researchers at UMass, Stony Brook, and at UMass again. Dr. Kumar's wide ranging network and reliable support paved the way for my success at Stony Brook, Jefferson Lab, and UMass Amherst, for which I am grateful. Each of the researchers I have met and worked with as a graduate student welcomed me as a result of Dr. Kumar's trust, without which I would have struggled to find my footing.

I would like to thank each of Dr. Kumar's other students. Tao Ye developed the analysis tools and online data monitoring scripts that everyone, especially myself, relied on for daily data collection and offline analysis, and most importantly the newest tools, the eigenvector BPM tools and Lagrange analysis for optimizing and characterizing the systematic control of the beam corrections. Ryan Richards took leadership on setting up the spectrometers and detector placements and helped illuminate and eliminate serious backgrounds, without which the experiments would be much less precise.

Special thanks is due to Bob Michaels for hosting me at Jefferson Lab, teaching me all about the technical operation of the data acquisition system, and introducing me to every expert available at the lab.

I also would like to thank Devi Adhikari and the Idaho State University group led by

Dustin McNulty, as well as Paul King and the Ohio University group for their expertise and help in all of the technical aspects of setting up and running the experiment.

Similarly I would like to thank Victoria Owen and Ye Tian, as well as Kent Paschke, Ciprian Gal and Caryn Palatchi for their invaluable assistance in the design, maintenance, and analysis of the experiment.

Chandan Ghosh has proved to be a valuable friend throughout my years at Stony Brook, Jefferson Lab, and UMass Amherst, who made the long road trips much more fun and taught me to approach technical subjects with a directness and courage I had not known before.

I must also thank all of the rest of the graduate students, postdocs, professors, staff scientists and engineers at Stony Brook and at Jefferson Lab who have befriended, helped out, or collaborated with me in any way.

Thanks to my parents for supporting my journey through the Ph.D. process and for visiting me, very far away from my home state of Mississippi, in New York, Virginia, and Massachusetts where I have lived during the coursework, experiment running, and analysis phases of my Ph.D.

Finally, I must thank Hanjie for her unwavering support and wisdom. Her confidence, expertise, and companionship has guided me through unclear times and cleared the way for my success.

Chapter 1

Theory and Motivation

Nuclear matter is composed of nucleons, protons and neutrons, which are governed by the strong nuclear force but are difficult to describe via perturbative Quantum Chromo-Dynamics (QCD) involving the fundamental quark and gluon degrees of freedom. Several theoretical techniques have developed effective field theories of hadrons and bulk nuclear matter [1]. Lattice QCD describes the nucleons from the fundamental QCD first principles, but it uses discretized and truncated space-time which, with modern computational power, only allows modeling simple nuclear systems. Chiral effective field theory (χ EFT) and nuclear density functional theory (DFT) describe nuclear matter with effective field theories built on the approximate chiral symmetry in nuclear matter and the nuclear mean field respectively.

These effective field theory (EFT) approaches are very good at describing features in symmetric nuclear matter, corresponding to isoscalar observables. Nuclear isospin is the approximate SU(2) symmetry of the up and down isospin doublet of quarks, and consequently also of the proton and neutron isospin doublet of nucleons they comprise. Nuclear EFT isovector parametrizations however are generally poorly constrained due to insufficient experimental data on isovector observables, especially the χ EFT three-nucleon (3N) interac-

tions and the DFT difference between proton and neutron densities. Because the difference between proton and neutron distributions in nuclei is sensitive to nuclear isovector sector physics, the neutron skin thickness, which is defined as the difference in RMS radii of the neutron and proton distributions,

$$R_{skin} = \langle R_n^2 \rangle^{1/2} - \langle R_p^2 \rangle^{1/2}, \quad (1.1)$$

is a convenient isovector observable [7].

The neutron distribution is accessible through hadronic scattering, though model uncertainty in the strong nuclear interactions make extractions of nuclear structure physics difficult. Because of the large weak charge of neutrons compared to protons, the neutron distribution is accessible via scattering mediated by the weak nuclear force. Polarized electron scattering allows model-independent access to the weak charge distribution via the interference between the dominant electromagnetic interaction and the parity-violating weak neutral-current interaction. The neutral weak interaction is not purely left-handed, but the parity-violating electron scattering (PVES) contribution gives rise to a helicity-dependent scattering rate asymmetry. This allows measurements with polarized beams to illuminate the weak charge distribution, which is sensitive to neutrons due to their large weak charge, $|Q_W^n| \simeq 1 \gg |Q_W^p|$. Such measurements are possible at Jefferson Lab, which allows the extraction of isovector observables, such as the neutron skin.

Recent advances in computational methods have allowed for the development of *ab initio* microscopic calculations in theoretical models incorporating nucleon-nucleon (NN) and three-nucleon (3N) forces from coupled-cluster χ EFT theory, which are able to calculate properties of nuclei as large as ^{48}Ca [4]. Additionally, the recent PREX II measurement of PVES in ^{208}Pb [2] provides a strong constraint to macroscopic calculations in DFT models

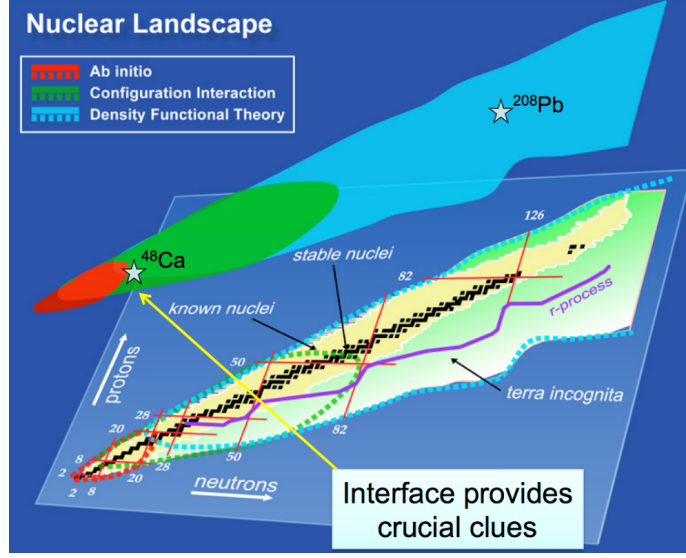


Figure 1.1: The chart of nuclides versus neutron and proton number with overlay depicting the range of modern theoretical modeling techniques. Large nuclei are described by nuclear DFT while small and medium mass nuclei are described by *ab initio* methods using NN and 3N nucleon potentials. The PREX II and CREX points are indicated with stars, and CREX will provide a point of reference between the various approaches. Reproduced from [1].

near the nuclear saturation density, but leaves them relatively unconstrained for low and medium mass nuclei where surface terms become more important [7, 8, 36]. The landscape of nuclear structure models positions a measurement of the weak charge distribution in ^{48}Ca as uniquely valuable for constraining and testing their isovector parametrizations and bridging microscopic and macroscopic theoretical approaches in the overlap region of medium mass nuclei where both are applicable, shown schematically in Fig. 1.1 [1]. Such a strong interaction model-independent measurement sensitive to isovector observables constitutes a major contribution to nuclear structure theory, as there is as yet no fundamental theory for the neutron equation of state or microscopic calculation of macroscopic model parameters [37].

We therefore perform the Calcium Radius Experiment (CREX) using PVES with a highly polarized electron beam in Hall A at Jefferson Lab (JLab) in Newport News, Virginia to

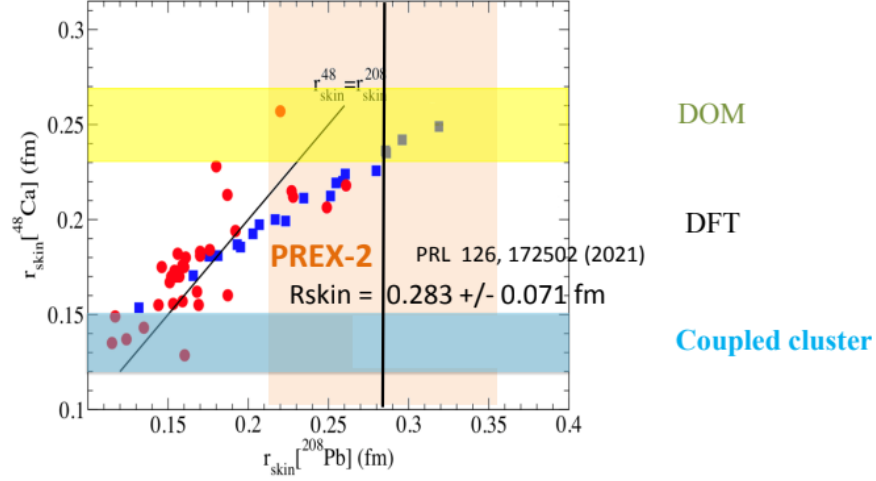


Figure 1.2: Predictions of the ^{48}Ca neutron skin thickness, R_{skin}^{48} , compared to the ^{208}Pb theoretical R_{skin}^{208} predictions and recent extraction from PREX II (vertical band) [2]. The yellow horizontal band is from a Dispersive Optical Model (DOM) calculation from [3], the blue band is from *ab initio* couple cluster chiral effective field theory (χEFT) calculations from [4], and the points are from relativistic (blue squares) and non-relativistic density functional theory (DFT) models from [5] and [6]. Figure adapted from [1, 7] by Bob Michaels.

measure the weak form factor in ^{48}Ca . The CREX kinematics are tuned to be sensitive to the isovector neutron skin thickness, R_{skin}^{48} , theoretical predictions of which are shown explicitly in Fig. 1.2 alongside the recent PREX II result for ^{208}Pb [2]. In either the case of the agreement or disagreement with theoretical models this constitutes a major advance for nuclear structure physics that is especially relevant to other neutron-rich systems such as neutron stars. The remainder of this chapter gives an overview of nuclear theory, shows the utility of measuring a parity-violating elastic electron-nuclear scattering asymmetry to access isovector observables, and gives a preview of the CREX measurement's impact on nuclear structure theory.

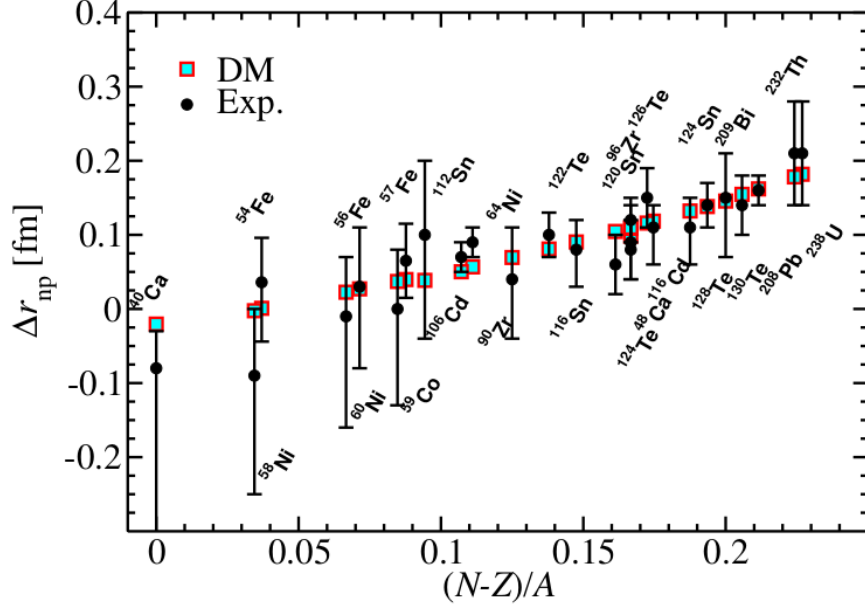


Figure 1.3: Droplet model (DM, squares) parametrized R_{skin} calculations and antiprotonic scattering measurements (circles) versus the neutron-proton asymmetry. Reproduced from [8].

1.1 Semi Empirical Mass Formula

The structure of nuclei is determined by the interactions of the protons and neutrons, which are difficult to calculate from first principles. However, because the nuclear medium is so dense and the nuclear force is short range, only on the scale of fm , the first successful models parametrized nuclei as approximate liquid spheres, in what is called the liquid drop model, where the dominant contributions come from the competing pressures of the interior volume and the surface area [38]. This simple model assumes a hard edge sphere of constant density with volume $V \sim A$ and therefore radius $R \sim A^{1/3}$, and parametrizes the binding energy, yielding the Bethe-Weisäcker formula, part of the Semi-Empirical Mass Formula,

$$B(Z, N) = a_V A - a_S A^{2/3} - a_C \frac{Z(Z-1)}{A^{1/3}} - a_P \frac{\delta}{A^{1/2}} - (a_{AV} A - a_{AS} A^{2/3}) \left(\frac{N-Z}{A} \right)^2. \quad (1.2)$$

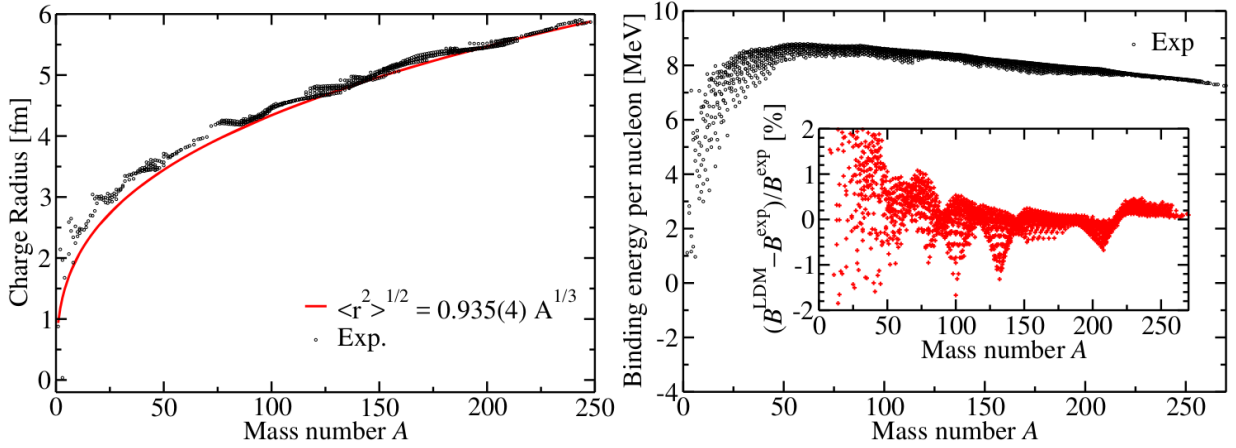


Figure 1.4: Measured nuclear root mean square (RMS) electromagnetic charge radius for all nuclei versus mass, with the simple spherical drop $R \sim A^{1/3}$ model fit (left). Binding energy per nucleon, $B(N, Z)/A$, with inset showing the percent difference between measured data and the predictions from the simple drop model (right). Reproduced from [8].

In this equation Z and N are the proton and neutron numbers, respectively, and A is their sum. The a_V and a_S terms correspond to the volume energy and counteracting surface tension energy, which rely on the relationship of $A \sim R^3$. The Coulomb repulsion term, a_C , grows with radial size, $R \sim A^{1/3}$, and the number of charged protons, but constitutes a small correction for small nuclear systems due to the relative weakness of the electromagnetic force compared to strong interactions. The pairing term a_P captures the cost of having unpaired fermions in the quantum system, and the asymmetry terms $a_{AV}A - a_{AS}A^{2/3}$ capture the high cost of asymmetry, $\frac{N-Z}{A}$, in the volume, but which is reduced at the surface. The a_{AV} asymmetry volume term is constrained by measurements of the nuclear masses, while a_{AS} is a relatively unconstrained isovector observable which relies on measurements of neutron skins, shown with data in Fig. 1.3 obtained from systematically limited antiprotonic scattering experiments. The asymmetry terms enter at the quadratic level due to the approximate nuclear isospin symmetry.

This simple model in terms of the numbers of protons and neutrons with coefficients

fit to observed values is sufficient to capture the behavior of the electric charge radius and binding energy per nucleon at the percent level, as seen in Fig. 1.4, even without explicitly considering the quantum statistics, interaction terms, or quantum shell structure of the protons and neutrons. Extensions to the liquid drop model allow for diffuse surfaces and are able to model isovector quantities such as the neutron skin thickness [8]. Although these kinds of empirical models are capable of fitting the existing data and are somewhat instructive, they lack inclusion of important quantum effects, do not describe the fundamental degrees of freedom, are not well constrained due to insufficient measurements, and are not generally applicable to all nuclear matter due to their narrow descriptive perspective. As a result, it is customary to define general parameters that characterize the Equation of State of nuclear matter (EOS), allowing the development of more advanced theoretical descriptions while facilitating comparison amongst different kinds of models and observables.

1.2 Nuclear Equation of State

The nuclear EOS is a means of parametrizing the intrinsic properties of nuclear physics in a generalized way. The EOS describes the state of a nuclear system under ideal zero temperature, and uniform and infinite size conditions in terms of the neutron and proton densities, ρ_n and ρ_p , interacting only under the effective nucleon-nucleon force. These conditions are approximately realized inside nuclei, due to the $\sim fm$ scale short range nature of the nuclear force compared to their $R \sim 0.9A^{1/3}fm$ size. This allows nuclear models to apply constraints from observations of finite nuclear properties and extrapolate their predicted behavior to the ideal EOS conditions through applying Coulomb corrections and separating model-dependent surface properties from EOS-relevant bulk properties. The EOS provides a common description of the underlying physics which is comparable between all models,

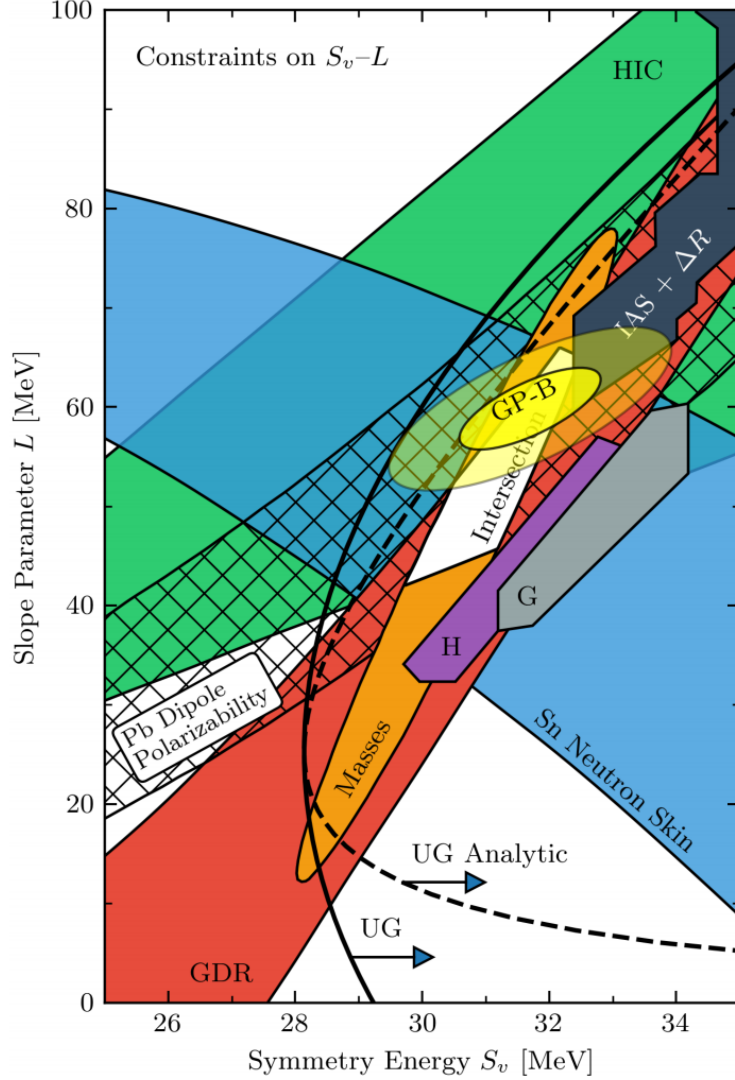


Figure 1.5: Constraints on the symmetry energy, J (or S_v), and its density-dependent slope, L , from experimental results on neutron skins, heavy ion collisions, and more, including two independent global studies denoted by G and H [8–10]. The recent PREX II result, presented in [2, 11], adds the additional constraints of $J = 38.1 \pm 4.7$ MeV and $L = 106 \pm 37$ MeV, not shown in the figure, which are in tension with those shown here. Reproduced from [10].

regardless of the parametrization of their quantitative descriptions of finite nuclei or other specific systems.

Customarily, and to simplify comparisons between models, the EOS is parametrized with respect to ideal conditions through a double Taylor series expansion, both in terms of density, ρ , around the nuclear saturation density, $\rho_0 = 0.16 fm^{-3}$, and in terms of the $\delta = \frac{\rho_n - \rho_p}{\rho_n + \rho_p}$ asymmetry around symmetric nuclear matter, $\delta_0 = 0$,

$$e(\rho, \delta) = e(\rho, 0) + S(\rho)\delta^2 + \mathcal{O}[\delta^4], \quad (1.3)$$

where $e(\rho, 0)$ is the EOS of symmetric nuclear matter and $S(\rho) = \left. \frac{\partial e(\rho, \delta)}{\partial \delta} \right|_{\delta=0}$ is the symmetry energy expansion,

$$S(\rho) = J + L \frac{\rho - \rho_0}{3\rho_0} + \frac{1}{2} K_{sym} \left(\frac{\rho - \rho_0}{3\rho_0} \right)^2 + \mathcal{O}[(\rho - \rho_0)^3], \quad (1.4)$$

where J is the symmetry energy at nuclear saturation density, $L = 3\rho_0 \left. \frac{\partial S(\rho)}{\partial \rho} \right|_{\rho=\rho_0}$ is the slope of the symmetry energy at saturation, and $K_{sym} = 9\rho_0^2 \left. \frac{\partial^2 S(\rho)}{\partial \rho^2} \right|_{\rho=\rho_0}$ is the incompressibility of the symmetry energy at saturation [8]. The EOS only contains even powers of δ because of the approximate isospin symmetry between protons and neutrons. Notably, the EOS expanded in terms of the symmetry energy is accurate even for the $\delta = 1$ pure neutron matter extreme case, and so $S(\rho) \simeq e(\rho, 1) - e(\rho, 0)$.

Constraints of the nuclear symmetry energy in the EOS are accessible with measurements of heavy nuclei where $S(\rho) \simeq S(\rho_0)$, as is the case for ^{208}Pb at around 2/3 the saturation density, and with the parametrization of surface symmetry energy effects accessible from medium mass nuclei such as ^{48}Ca . Global studies pin the symmetry energy at saturation density, $J \simeq 31$ MeV, and constrain the slope near saturation density, $30 \lesssim L \lesssim 90$ MeV

Table 1.1: Table of fermion electromagnetic and weak charges, t_L^3 weak isospin, and vector and axial-vector weak couplings.

f	$q_f = Q_{EM}$	$g_A^f = t_{fL}^3$	$g_V^f = t_{fL}^3 - 2 \sin^2 \theta_W = \frac{1}{2} Q_W$
e^-	-1	$-\frac{1}{2}$	$-\frac{1}{2} + 2 \sin^2 \theta_W \simeq 0$
ν	0	$+\frac{1}{2}$	+1
u, c, t	$+\frac{2}{3}$	$+\frac{1}{2}$	$+\frac{1}{2} - \frac{4}{3} \sin^2 \theta_W$
d, s, b	$-\frac{1}{3}$	$-\frac{1}{2}$	$-\frac{1}{2} + \frac{2}{3} \sin^2 \theta_W$
$p^+ = uud$	+1	$\sim +\frac{1}{2}$	$\sim \frac{1}{2} - 2 \sin^2 \theta_W \simeq 0$
$n^0 = udd$	0	$\sim -\frac{1}{2}$	$\sim -\frac{1}{2}$

[8]. Experimental constraints of J and L are shown in Fig. 1.5, with which the recent PREX II results are in some tension, the latter yielding $J = 38.1 \pm 4.7$ MeV and $L = 106 \pm 37$ MeV [2, 11]. The parametrization of macroscopic DFT models predicts a strong correlation between R_{skin}^{208} and R_{skin}^{48} , shown in Fig. 1.2, which provides a handle for evaluating their accuracy in conjunction with the recent PREX II result. Additionally, microscopic calculations with χ EFT models are also capable of describing medium mass nuclei as large as ^{48}Ca , which is sensitive to the surface symmetry energy EOS terms [7]. These opportunities for illuminating the poorly constrained nuclear symmetry energy and relating microscopic and macroscopic models to each other motivate the CREX measurement.

1.3 Electron Nucleus Scattering

To measure the neutron distribution in ^{48}Ca from the dominantly-electromagnetic charged electron scattering we rely on the parity-violating weak neutral-current interaction.

1.3.1 Electroweak Theory

In the Standard Model (SM), before the spontaneous symmetry breaking (SSB) caused by the Higgs mechanism, the $SU_L(2)$ weak bosons only couple to the left-handed components of SM fermion fields. This maximally violates parity in the charged current weak interactions, and shows up in the neutral-current (NC) portion of the SM Lagrangian, \mathcal{L}_{SM} , after SSB as

$$\mathcal{L}_{NC} = g \sin \theta_W J_\mu^Q A^\mu - \frac{g}{2 \cos \theta_W} J_\mu^Z Z^\mu, \quad (1.5)$$

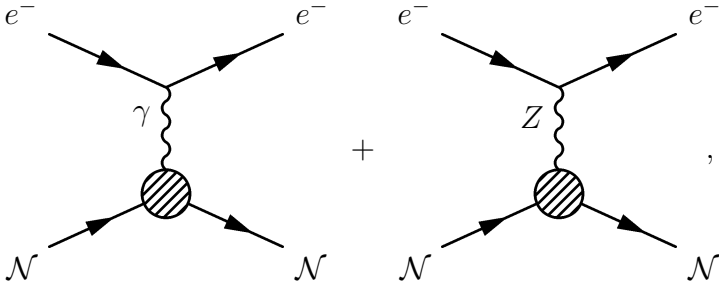
where $\sin \theta_W = \frac{e}{g} = \frac{g'}{\sqrt{g^2 + g'^2}}$ is the weak mixing angle coupling, A^μ is the familiar massless $U_Q(1)$ electromagnetic force mediating photon and, Z^μ is the neutral weak boson, which gains a mass of $m_Z = 91.2$ GeV after SSB [39]. The J_μ^Q and J_μ^Z terms are the electromagnetic and weak neutral-currents respectively, which sum over the SM fermions as,

$$J_\mu^Q = \sum_f \bar{\psi}_f q_f \gamma_\mu \psi_f \quad \text{and} \quad J_\mu^Z = \sum_f \bar{\psi}_f [t_{fL}^3 \gamma_\mu (1 - \gamma^5) - 2q_f \sin^2 \theta_W \gamma_\mu] \psi_f. \quad (1.6)$$

The γ_μ terms are vector interactions while the $\gamma_\mu \gamma^5$ terms are axial-vector. The q_f coupling is the electromagnetic charge, $q_f = Q_{EM} = t_l^3 + \frac{1}{2} Y_W$, where Y_W is the weak hypercharge and t_{fL}^3 is the weak isospin eigenvalue from the purely left chiral $SU_L(2)$ weak interactions. These couplings amount to perfectly left chiral interactions for neutrinos and primarily vector interactions for charged fermions in the SM. It is convenient to rewrite J_μ^Z in terms of the vector and axial-vector couplings, $g_V^f = t_{fL}^3 - 2 \sin^2 \theta_W q_f = \frac{1}{2} Q_W$, which is identified as the weak charge, and $g_A^f = t_{fL}^3$, respectively

$$J_\mu^Z = \sum_f \bar{\psi}_f \gamma_\mu [g_V^f - g_A^f \gamma^5] \psi_f. \quad (1.7)$$

From this expression we can see that for scattering from a nucleus with similar numbers of protons and neutrons, whose charges and couplings in the Standard Model are given in table 1.1, the axial current will approximately cancel between the neutrons and protons, and the electron and proton vector currents are negligible because $1 - 4\sin^2\theta_W \simeq 0$, leaving the vector neutron and axial-vector electron currents as the dominant contributions. This makes neutral-current weak scattering in nuclei primarily a probe of the neutron distribution. The Feynman diagrams for elastic electron scattering from the nucleus, \mathcal{N} , are

$$\mathcal{M} = \mathcal{M}_\gamma + \mathcal{M}_Z =$$

(1.8)

which is equal to the sum of the photon and Z mediated matrix elements,

$$\mathcal{M}_\gamma = g^2 \sin^2 \theta_W J_{\mu\mathcal{N}}^Q \frac{-ig^{\mu\nu}}{q^2} J_{\nu e}^Q \quad \text{and} \quad \mathcal{M}_Z = \frac{g^2}{4 \cos^2 \theta_W} J_{\mu\mathcal{N}}^Z \frac{-ig^{\mu\nu}}{m_Z^2 + q^2} J_{\nu e}^Z. \quad (1.9)$$

We identify the $q^2 = -Q^2$ as the four momentum transfer, and for low-energy scattering, $q \ll m_Z$, and $G_F = \frac{\sqrt{2}}{8} \frac{g^2}{\cos^2 \theta_W m_Z^2}$ and $g^2 \sin^2 \theta_W = e^2 = 2\alpha$, we can simplify

$$\mathcal{M}_\gamma = \frac{2\alpha}{Q^2} J_{\mathcal{N}}^Q J_e^Q \quad \text{and} \quad \mathcal{M}_Z = \sqrt{2} G_F J_{\mathcal{N}}^Z J_e^Z. \quad (1.10)$$

The differential cross section for electrons scattering off of a nucleus is

$$\frac{d\sigma}{d\Omega} = \frac{dQ}{Flux} \left| \mathcal{M}_\gamma + \mathcal{M}_Z \right|^2, \quad (1.11)$$

which is dominated by the electromagnetic interaction at low Q^2 , due to the weak interac-

tion's suppression by a factor of G_F due to the large mass of the Z boson.

1.3.2 Parity Violation

A handle that provides sensitivity to the G_F -suppressed weak interaction comes from the fact that the vector and axial-vector components of the currents behave differently under parity transformations of the fermion fields. The parity transformation changes the spatial components of the fermion fields,

$$\mathcal{P}\{\psi(t, x_1, x_2, x_3)\} = \psi' = \psi(t, -x_1, -x_2, -x_3), \quad (1.12)$$

and is related to the γ^0 matrix as

$$\mathcal{P}\psi = \psi' = \gamma^0\psi, \quad (1.13)$$

$$\mathcal{P}\bar{\psi} = \bar{\psi}' = (\psi')^\dagger\gamma^0 = (\gamma^0\psi)^\dagger\gamma^0 = \psi^\dagger\gamma^0\gamma^0 = \psi^\dagger = \bar{\psi}\gamma^0, \quad (1.14)$$

where we have used the conjugate fermion field $\bar{\psi} = \psi^\dagger\gamma^0$, and $\gamma^{0\dagger} = \gamma^0$, $\gamma^0\gamma^0 = 1$ identities. The resulting transformations of the vector and axial-vector currents cause the space components of vector currents to change sign and the time component of axial-vector currents to change sign,

$$\mathcal{P}\{\bar{\psi}\gamma^\mu\psi\} = \bar{\psi}'\gamma^\mu\psi' = \bar{\psi}\gamma^0\gamma^\mu\gamma^0\psi = +\bar{\psi}\gamma^\mu\psi(\mu = 0) - \bar{\psi}\gamma^\mu\psi(\mu > 0) \quad (1.15)$$

$$\mathcal{P}\{\bar{\psi}\gamma^\mu\gamma^5\psi\} = \bar{\psi}'\gamma^\mu\gamma^5\psi' = \bar{\psi}\gamma^0\gamma^\mu\gamma^5\gamma^0\psi = -\bar{\psi}\gamma^\mu\gamma^5\psi(\mu = 0) + \bar{\psi}\gamma^\mu\gamma^5\psi(\mu > 0). \quad (1.16)$$

It is clear that under parity transformation the product of vector and axial-vector currents, AV or VA, changes sign on all four components, violating parity, while the products of

AA or VV combinations of currents do not change sign and conserve parity. From this observation, coupled with the observation of negligible electron and proton vector couplings, we see that a parity-violating asymmetry is produced in the AV mixing part of the axial-vector electron and vector nuclear weak neutral-currents' interactions,

$$\mathcal{P}\{\mathcal{M}_Z^{AV}\} = \mathcal{P}\{\sqrt{2}G_F J_N^{ZV} J_e^{ZA}\} = -\sqrt{2}G_F J_N^{ZV} J_e^{ZA}. \quad (1.17)$$

Rather than changing the parity of the entire experimental setup, we opt for changing the helicity,

$$A_{hel} = \frac{\frac{d\sigma^+}{d\Omega} - \frac{d\sigma^-}{d\Omega}}{\frac{d\sigma^+}{d\Omega} + \frac{d\sigma^-}{d\Omega}}, \quad (1.18)$$

and therefore, in the ultrarelativistic limit $E \gg m$ and $E \simeq |p|$, approximately changing the handedness of the electrons involved in the axial weak current,

$$\psi^\pm = P_R \psi^\pm + P_L \psi^\pm = \frac{1}{2}(1 \pm \frac{|p|}{E + m_e})\psi_R + \frac{1}{2}(1 \mp \frac{|p|}{E + m_e})\psi_L \simeq \psi_{R,L} \quad (1.19)$$

which accomplishes the same effect as a parity transformation, as the difference in right versus left-handed cross section is proportional to the electron axial-vector current

$$\overline{\psi}\gamma^\mu\gamma^5\psi = \overline{\psi}_R\gamma^\mu\psi_R - \overline{\psi}_L\gamma^\mu\psi_L, \quad (1.20)$$

such that

$$\mathcal{M}_Z^R \simeq -\mathcal{M}_Z^L \equiv \mathcal{M}_Z^{AV} \quad (1.21)$$

from equation 1.17. This leaves us with the chirality-dependent difference in cross sections, approximately the helicity-dependent difference, proportional to the axial-vector electron

current term mixing with the electromagnetic amplitude,

$$A_{PV} \simeq A_{hel} \simeq \frac{\frac{d\sigma^R}{d\Omega} - \frac{d\sigma^L}{d\Omega}}{\frac{d\sigma^R}{d\Omega} + \frac{d\sigma^L}{d\Omega}} = \frac{|\mathcal{M}_\gamma + \mathcal{M}_Z^R|^2 - |\mathcal{M}_\gamma + \mathcal{M}_Z^L|^2}{|\mathcal{M}_\gamma + \mathcal{M}_Z^R|^2 + |\mathcal{M}_\gamma + \mathcal{M}_Z^L|^2} \simeq \frac{2|\mathcal{M}_\gamma \mathcal{M}_Z^{AV}|}{|\mathcal{M}_\gamma|^2}. \quad (1.22)$$

Inserting the expressions for the matrix elements, and converting from point V and A couplings to momentum-space weak and electromagnetic charge distribution form factors, $F_W(Q^2)$ and $F_Q(Q^2)$, by assuming plane wave scattering in the Born approximation, yielding

$$A_{PV} = \frac{\sqrt{2}G_F Q^2}{2\pi\alpha Z} \frac{g_A^e g_V^N(Q^2)}{Q_{EM}(Q^2)} = \frac{G_F Q^2 |Q_W|}{4\sqrt{2}\pi\alpha Z} \frac{F_W(Q^2)}{F_Q(Q^2)}. \quad (1.23)$$

1.3.3 Form Factor

The form factors in equation 1.23 are obtained from the momentum-space Fourier transform of the spatial charge distributions,

$$F(Q^2) = \frac{1}{4\pi} \int d^3\vec{r} j_0(qr) \rho(r), \quad (1.24)$$

where $j_0(qr) = \frac{\sin qr}{qr}$ is the zeroth order Bessel function and \vec{q} is the 3-momentum [40]. The distributions ρ_p and ρ_n are normalized, such that, using the weak vector couplings $g_V^f = \frac{1}{2}Q_W$ from table 1.1, we have

$$\rho_W(r) = \int d^3\vec{r}' G_E(|\vec{r}' - \vec{r}|) [-N\rho_n(r') + Z(1 - 4\sin^2\theta_W\rho_p(r'))] \quad (1.25)$$

where G_E , for simplicity, represents the Sachs form factors of the various charges, and

$$Q_W = \int d^3\vec{r} \rho_W(r) = -N + (1 - 4\sin^2\theta_W)Z. \quad (1.26)$$

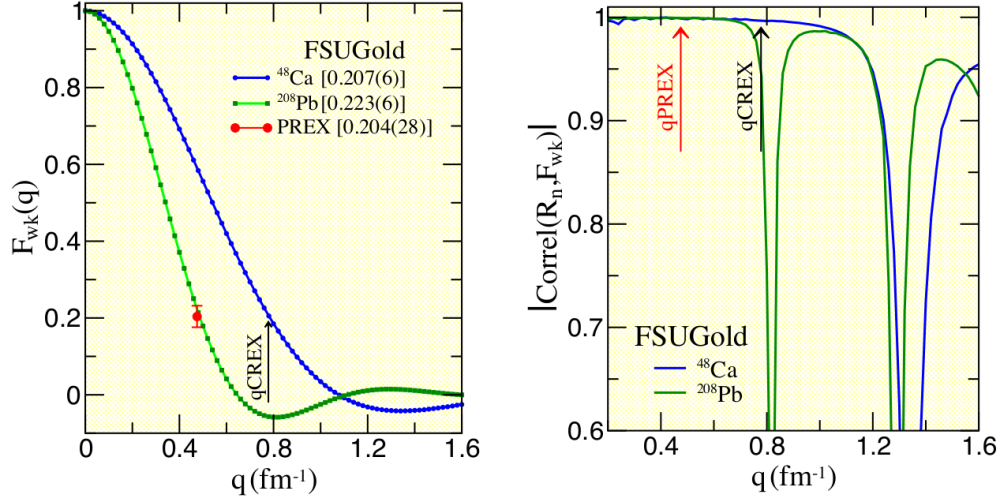


Figure 1.6: Form factor versus momentum transfer (left) and correlation between form factor and the weak skin thickness (right) for PREX and CREX using the FSUGold relativistic mean field model. Reproduced from [1].

Before the asymmetry in equation 1.23 is interpretable, Coulomb corrections must be applied within theoretical models performing the full distorted wave calculations with known electric charge densities, and additional terms must be considered in the charge distributions to account for the strangeness of the nucleons, for axial-vector couplings to meson currents inside the nucleus, and for spin-orbit couplings within the nucleus [40].

The theoretically predicted weak form factors for PREX II and CREX are shown in Fig. 1.6 for a specific nuclear structure model, the FSUGold relativistic mean field (RMF) model, along with the correlation between the neutron radius and the weak form factor [1]. The correlation is not perfect as there exists some uncertainty in the neutron surface-thickness, a_n , parametrization of the charge density, described further in the next section. Extracting the weak charge radius is done by recognizing that the expansion of the form factor in small $|q|$ gives the root mean square (RMS) weak charge radius, $\sqrt{\langle r_W^2 \rangle}$ [20],

$$F_W(Q^2) = \int \left(1 - \frac{(qr)^2}{2} + \dots\right) \rho_W(r) d^3\vec{r}, \quad (1.27)$$

which yields

$$\langle r_W^2 \rangle = -6 \frac{dF_W(Q^2)}{dQ^2} \Big|_{Q^2=0}. \quad (1.28)$$

However, in practice we choose to obtain the charge density and its moments, including the weak and neutron radii and skins, by fixing models to the measured asymmetry and acceptance function from experiment, which correspond to a distribution of the form factor over a range of Q^2 and angle, and then integrating the resulting theoretically-extracted weak charge distribution directly,

$$\langle r_W^2 \rangle = \frac{1}{Q_W} \int d^3\vec{r} r^2 \rho_W(r). \quad (1.29)$$

The weak form factor is the fundamental observable obtained by CREX, and for convenience it can be averaged, linearly to a central value or directly within the theoretical model, and compared with the models' predicted form factor. With the model distributions tuned to match the form factor measurement, they can be compared with each other, integrated to obtain the weak charge and neutron skins for ^{48}Ca , and make further theoretical observations.

The beauty of the PVES method of measuring the form factor is that, although there may be some nuclear structure model-dependence involved in obtaining convenient macroscopic results like the skin thicknesses, the form factor itself is obtained cleanly with very little model-dependence, only a small contribution coming from the meson axial and spin orbit couplings [40, 41]. For CREX, the radius extractions are sensitive to the nuclear structure model-dependent surface-thickness parametrization, meaning that an extraction of the radii will have theoretical systematic uncertainties unless the sensitivity is adequately addressed, and that the observed F_W is useful as a constraint for the surface structure physics of models [12, 36].

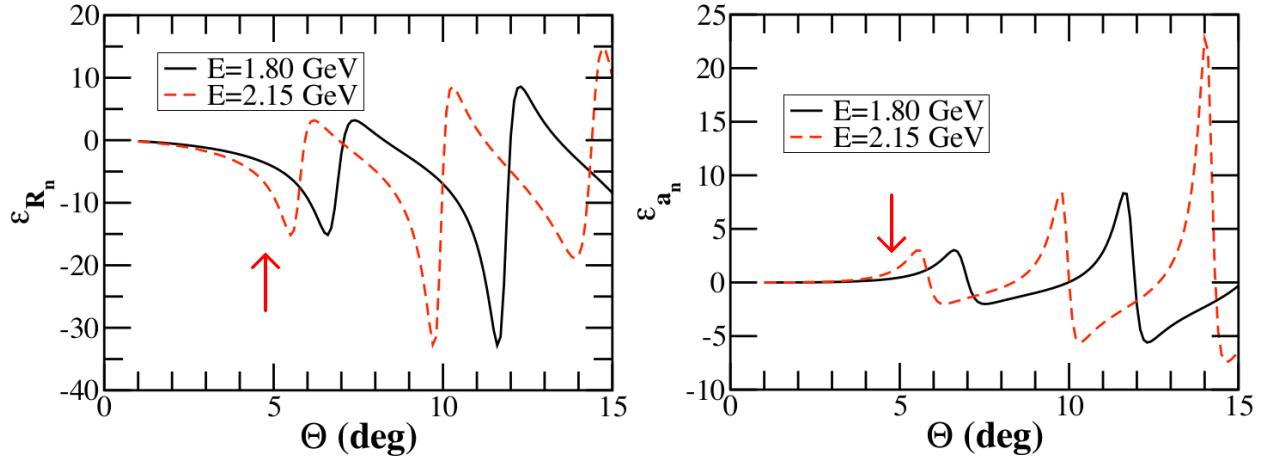


Figure 1.7: Predicted A_{PV} sensitivity $\epsilon_{R_n} = d \ln A_{PV} / d \ln R_n$ to a 1% change in R_n^{48} versus scattered angle (left) and sensitivity to skin thickness, $\epsilon_{a_n} = \epsilon_{a_n} = d \ln A_{PV} / d \ln a_n$, (right) for two possible CREX energies. The SLY4 neutron density was used. The red arrows indicate the approximate average scattering angle for CREX running. Figures adapted from [12].

1.3.4 Figure of Merit

To optimize the measurement of $F_W(Q^2)$ to be sensitive to the isovector skin thickness observable we need to select the optimal kinematics for CREX. The distance scales relevant to measuring the bulk neutron distribution size, over a limited range in Q^2 and optimizing the use of available beam time, are the electromagnetic size of the nucleus, $R_{ch} \sim 0.935 A^{1/3} \simeq 3.4 fm$ from the simple droplet model shown before in Fig. 1.4, as well as the expected scale of the neutron skin thickness, $0.1 \leq R_{skin}^{48} \leq 0.3 fm$, from various models considered in the next section. Considering the deBroglie wavelength relevant for the scattering momentum transfer, $|q|$, where $\hbar c = 197 \text{ MeV} fm$, a $|q| \sim 200 \text{ MeV}$ is needed to probe physics at the fm scale.

There are also limitations on the possible experiment at kinematics placed by the available hardware at JLab. The Hall A HRSs must separate out the first excited state in ^{48}Ca , around $\Delta E_{inel} \simeq 4 \text{ MeV}$, making use of their $\frac{dp}{p} \sim 10^{-3}$ momentum resolution achievable when the

HRSs are tuned to focus the scattered flux for integration. Separating the excited state from the elastic scattering flux with negligible nuclear recoil and radiative energy loss limits the incident beam by $\frac{\Delta E}{E_{beam}} \geq 10^{-3} \rightarrow E_{beam} \leq 4\text{GeV}$. This allows the use of the 1 pass 2.2 GeV JLab CEBAF beam. More significantly, to measure the same Q^2 momentum transfer range at high energy requires measuring a smaller scattering angle. To successfully measure the low-angle scattered electrons with the minimum 12.5° HRSs, a septum magnet must bend them, and for 1 pass 2.2 GeV beam the minimum angle achievable with the available septa magnets is $\sim 5^\circ$.

The CREX measurement only probes $F_W(Q^2)$ at one place in Q^2 . Although an ideal measurement would cover the full range to allow Fourier transforming to get the charge distribution, it is only necessary to make a measurement at one point in order to extract information about the RMS radius because, as seen in equation 1.28, R_n is related to the $Q^2 = 0$ slope of $F_W(Q^2)$, and the slope varies smoothly in the theoretical models. To measure a point that is useful to constrain models we measure close to the diffractive minimum where the F_W slope is large, but far enough away from $Q^2 = 0$ so that $A_{PV} \propto Q^2$ is large enough and $\frac{d\sigma}{d\Omega} \propto \frac{1}{Q^2}$ is not too small to allow a precise statistical measurement. In practice, we define a figure of merit (FOM) that encapsulates the ability to precisely measure a non-zero asymmetry that is sensitive to the isovector relevant R_n within a finite amount of time.

To maximize the FOM we must minimize the uncertainty in the PVES asymmetry,

$$A = \frac{N_R - N_L}{N_R + N_L} = \frac{\Delta N}{N}, \quad (1.30)$$

which is

$$\delta A = \frac{1}{\sqrt{N}} \propto \sigma^{-1/2} \rightarrow \frac{\delta A}{A} \propto \frac{1}{\sqrt{\sigma A}}. \quad (1.31)$$

Minimizing $\frac{\delta A}{A}$ maximizes $\text{FOM} = \sigma A^2$, balancing $\sigma \propto \frac{1}{Q^2}$ and $A \propto Q^2$. Additionally we

consider the goal of isovector sensitivity of the asymmetry, so we define the sensitivity, ϵ_{R_n} , of A_{PV} to a 1% change in the neutron skin thickness,

$$\epsilon_{R_n} = \frac{d \ln A_{PV}}{d \ln R_n} = \frac{R_n}{A_{PV}} \frac{dA_{PV}}{dR_n} = \frac{1}{0.01} \frac{A_s - A}{A}. \quad (1.32)$$

To obtain ϵ_{R_n} we calculate dA_{PV}/dR_n using a model to predict A under normal conditions and stretched A_s . The stretched A_s is calculated by the same model but with a $\lambda \simeq 1.01$, 1% stretched, $\rho_n(r)$ charge density,

$$\rho_n(r) \rightarrow \frac{1}{\lambda^3} \rho_n\left(\frac{r}{\lambda}\right). \quad (1.33)$$

The ϵ_{R_n} calculated in the SLY4 neutron density model is shown for approximately the beam energy and acceptance angle relevant for CREX in Fig 1.7. This shows a peak of $\epsilon_{R_n} \simeq 15$ at the 5° angle for 1 pass 12 GeV CEBAF running at ~ 2.2 GeV, meaning that a $\sim 15\%$ measurement of A_{PV} is sensitive to the neutron RMS radius, R_n^{48} , at the 1% level ($\pm 0.03 fm$), which is accessible in just a few weeks of beam time [12]. Combining these considerations together we have[1]

$$\text{FOM} = \epsilon^2 \sigma A_{PV}^2. \quad (1.34)$$

The CREX FOM is optimized at the $q \sim 0.8 fm^{-1} \rightarrow Q^2 \sim 0.03 \text{ GeV}^2$ scale. This makes CREX remarkably sensitive to the neutron skin compared to PREX II for similar conditions. CREX is 5 times more sensitive due to the larger asymmetry, measured at higher Q^2 , needed to optimize the smaller R_n measurement, and is only hindered by the lower cross section for the smaller ^{48}Ca nucleus, requiring higher beam current and time for experiment statistical precision.

It is possible to estimate the model-dependence of the R_{skin} extraction by parametrizing

Table 1.2: Approximate kinematic parameters for CREX [12].

E	A_{PV}	$\frac{d\sigma}{d\Omega}$	Rate	$\frac{\Delta R_n}{R_n}$
2.2 GeV	2.7 ppm	1.1 mb/str	~ 20 MHz/arm	$\sim 0.3\%$

the model-predicted density in any convenient simplified step-like two parameter function form, for example a Woods-Saxon distribution,

$$\rho_n(r) = \rho_0/[1 + \exp(r - R_n)/a_n)], \quad (1.35)$$

where R_n is the neutron radius and a_n is the neutron skin thickness. In this simplified picture the asymmetry's sensitivity to stretched changes in the a_n skin thickness versus a fixed R_n are studied, shown in Fig. 1.7 computed with the SLY4 neutron density model. CREX is more sensitive to the a_n surface parametrization than PREX II, due both to the larger A_{PV} magnitude and to ^{48}Ca 's $\rho_n(r)$ distribution substantially involving the surface area and depending more on the surface part of the nuclear symmetry energy [12, 36]. The FOM optimized kinematic values for the CREX running are given in table 1.2. This strong sensitivity of A_{PV} near ~ 2.2 GeV to R_n and a_n makes the kinematically optimized CREX $F_W(Q^2)$ observable uniquely suited to constraining the bulk and surface isovector parts of nuclear models which make predictions of the $\rho_n(r)$ arrangement of the excess neutrons in ^{48}Ca , alongside the recent PREX II measurement that independently constrains the bulk symmetry energy.

1.4 Physics Impact

Theoretical models of nuclear matter typically rely on effective field theory (EFT) techniques. EFT is needed to get around the limitations on calculations of the strong interaction

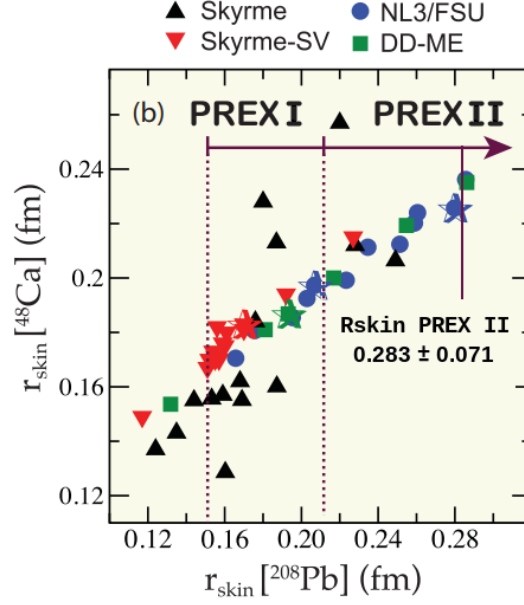


Figure 1.8: Calculations from 48 DFT models of R_{skin}^{208} versus R_{skin}^{48} , including constraints from PREX I and II [2]. Adapted from [13].

using the fundamental quark and nucleon degrees of freedom. These limitations come from the breakdown of perturbation theory, $\alpha_s > 1$, at energy and distance scales relevant for nuclear structure, $E < \Lambda_s \sim 1 \text{ fm}^{-1} \sim 200 \text{ MeV}$. EFT approaches are able to describe the interactions and energy of nuclear structure and make predictions for diverse systems when their parametrizations are constrained by available measurements. The distribution of the excess neutrons in ^{48}Ca is driven by the density dependence of the nuclear EOS symmetry energy, $L = 3\rho_0 \frac{dS(\rho)}{d\rho} \Big|_{\rho=\rho_0}$. The energy balance of placing the excess 8 neutrons in a low-density skin versus in the higher density core of the nucleus drives the thickness of the neutron skin. The constraints placed on nuclear structure models by the measurement of $F_W(Q^2)$ are useful across a broad range of physics from nuclear dipole polarizability (α_D), radioactive isotope beams, heavy ion physics, and up to the scale of neutron stars. We quickly survey several families of theoretical approaches which make predictions for ^{48}Ca and discuss their expectations and motivation for the precise measurement with CREX.

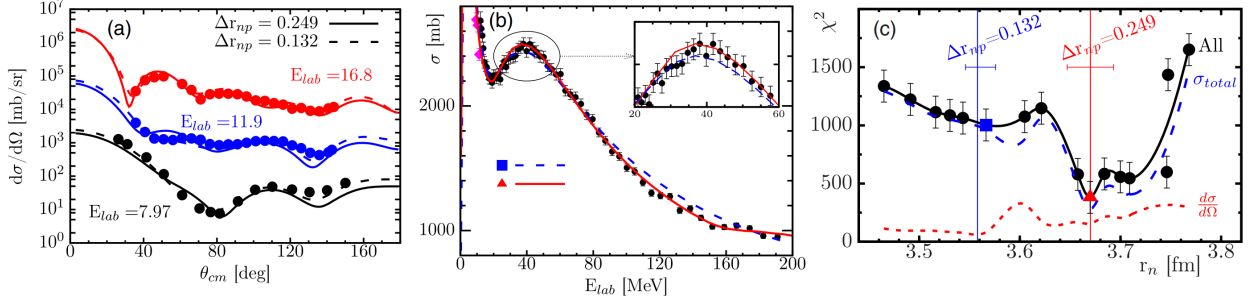


Figure 1.9: (a) Fit of neutron- ^{48}Ca elastic-scattering data to the DOM best-fit (solid curves) and also constrained to match the the *ab initio* $R_{skin}^{48} = 0.132\text{fm}$ results (dashed curves). (b) Similar comparison of the total neutron cross section data, with similar best fit (solid) and *ab initio* result constrained (dashed) lines. (c) The data-fit χ^2 space, indicating the contribution from the elastic scattering data (short dashed) and total neutron cross section data (long dashed) separately, and displaying the *ab initio* value and best-fit values on the plot. Reproduced from [3].

1.4.1 Density Functional Theory

An approach to convert the nuclear many-body problem into a single body problem is density functional theory (DFT). Nuclear DFT makes use of energy density functionals (EDF) to construct self-consistent mean field (SCMF) models of the nucleons and their interactions within the nuclear medium. Two general ways of constructing SCMF models are the non-relativistic and relativistic approaches. An example of non-relativistic models are the Skyrme-Hartree-Fock (SHF) family, which parametrize nuclei in terms of baryon, spin-orbit, and kinetic energy densities, each expressed in terms with vector and isovector forms and having $\mathcal{O}(10)$ parameters that are constrained with $\mathcal{O}(100)$ experiment observables. An example of relativistic models are the Relativistic Mean Field (RMF) family of models, which relate Dirac nucleons that interact under Yukawa couplings to effective-field mesons that in turn interact based on the baryon field densities. The meson field densities are used to derive local scalar and vector potentials for the baryon field interactions, a process which is iterated until self-consistency is achieved. The kinds of effective meson interactions in RMF models

are adjustable, including the possibility of density dependence in the couplings, leading to $\lesssim \mathcal{O}(10)$ parameters, depending on the complexity of the model, that are constrained with the measured binding energies and charge radii of magic nuclei and bulk properties of nuclear matter.

The difference between SHF and RMF models comes primarily through their different treatment of the interaction mechanisms and of the isoscalar-scalar densities, which are independent in SHF and tightly coupled in RMF models [6]. The FSUGold model, whose $F_W(Q^2)$ predictions for PREX II and CREX are shown in Fig. 1.6, includes two additional terms relevant for the nuclear symmetry energy and its density-dependent slope in order to better fit experimental data, at the cost of sensitivity to additional constraints from isovector related observables like R_{skin}^{48} [42]. The FSUGold model yields calculations of the neutron skin thicknesses in ^{208}Pb and ^{48}Ca of $R_{skin}^{208} = 0.21 fm$ and $R_{skin}^{48} = 0.20 fm$, respectively [43]. The results from 48 DFT model calculations of R_{skin} in ^{48}Ca and ^{208}Pb from [13] are shown in Fig. 1.8 along with the PREX II extracted $R_{skin}^{208} = 0.283 \pm 0.071 fm$ result from [2]. A subset of 25 of the models shown yields a model-averaged $R_{skin}^{48} = 0.176 \pm 0.018$. When considering the range of models crossing the PREX II result range and projecting to the CREX prediction axis, a loose estimate of $R_{skin}^{48} \simeq 0.23 \pm 0.03 fm$ is obtained based on the observed correlation.

1.4.2 Dispersive Optical Model

Another approach which builds effective-field potentials relating the interactions of nucleons to nuclear structure and to reaction physics is the dispersive optical model (DOM). The DOM approach builds potentials which include non-local effects by separating the effective nuclear potential into real and imaginary parts, constrained by a causality-enforcing disper-

sion relation. The DOM approach constructs the nucleon self-energy as a Green’s function to describe the dynamics of particles and holes within the nuclear medium [44]. The term “optical” comes from the optical theorem that relates the real and imaginary parts of scattering from a potential, as the DOM approach allows the description of waves’ scattering, transmission and absorption by the real and imaginary potentials, and the term “dispersive” comes from the dispersion relation between the potential’s components.

The DOM approach builds potentials, constrained with hadronic scattering data, that predict cross sections of nuclear reaction processes, especially useful in nuclear reactions with rare isotopes, but which also allow calculations of the neutron skin in ^{48}Ca [45]. Recent results from [3] constrained with elastic scattering and total neutron cross section data suggests a large value of $R_{skin}^{48} \simeq 0.249 \pm 0.023 fm$, as shown in Fig. 1.9, loosely in agreement with the DFT predictions that range from 0.12 to 0.26 fm. However, if instead the DOM results only rely on the elastic scattering data, the χ^2 minimization process would approximately halve the result and bring it into agreement with the results from an *ab initio* theoretical approach, also shown in the figure and discussed next.

1.4.3 Ab Initio models

The *ab initio* theoretical approach uses chiral effective field theory (χEFT) microscopic calculations to access the low-energy behavior of the fundamental strong force degrees of freedom and thereby build fundamental two nucleon (NN) and three nucleon (3N) effective interaction potentials. These potentials can be employed in various ways; a specific approach described in [4] is to build a Hamiltonian from them to describe coupled-cluster single and double (CCSD) particle excitation and hole EFT systems. These coupled-cluster dynamics are used to calculate the 2-body density matrix, which is integrated over the nuclear volume

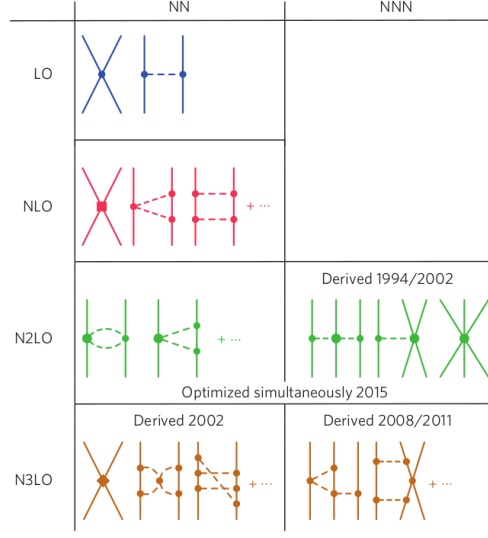


Figure 1.10: Two-nucleon (NN) and three-nucleon (NNN, 3N) chiral effective field theory (χ EFT) interactions at various orders in perturbation theory used to construct potentials in *ab initio* nuclear structure models. Reproduced from [4].

to obtain proton and neutron density distributions and radii that can be compared with experiment. Recent advancements in computational power and the coupled-cluster technique have resulted in calculation complexity significantly reducing, allowing calculations of nuclei as large as ^{48}Ca .

The specific *ab initio* model described in [4], which uses next-to-next-to leading order (NNLO) χ EFT to generate NN and 3N potentials, is NNLO_{sat} . It is constrained with masses and binding energies for nuclei up to $A \lesssim 25$. To evaluate the model systematic uncertainty in NNLO_{sat} , a range of higher order, N3LO, less constrained, $A \lesssim 3$, χ EFT models are explored. The correlation between R_p versus various isovector related observables and the consequent systematic uncertainty spread are shown in Fig. 1.11. The well measured proton-dominated electric charge radius, R_p , crossing the range of χ EFT predicted results provides an estimate of the model's systematic uncertainty, resulting in a calculated $R_{\text{skin}}^{48} \simeq 0.135 \pm 0.015$. The key takeaway from this study is the strong correlation between the dipole polarizability, α_D ,

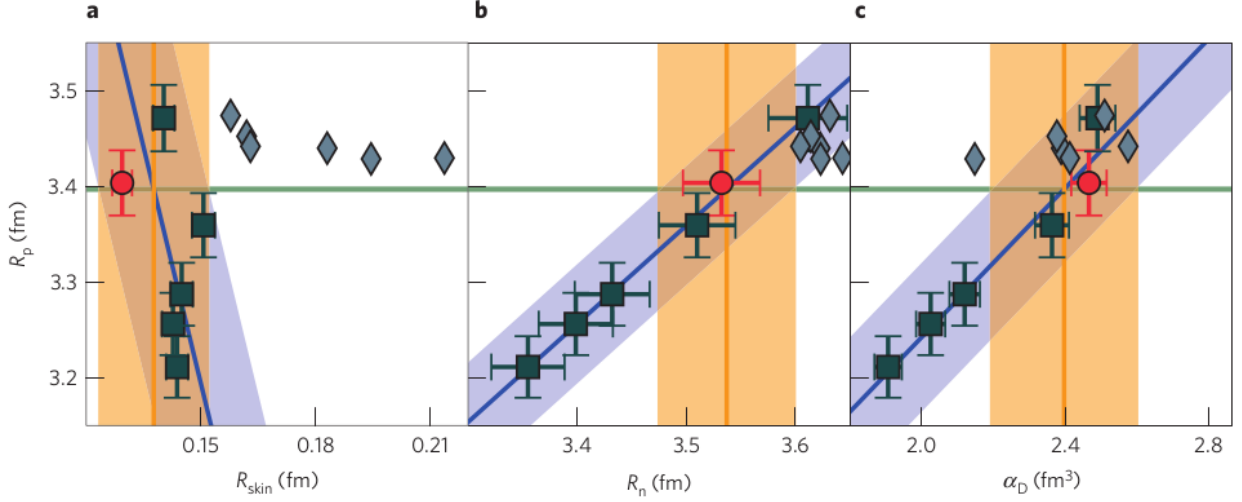


Figure 1.11: Plots showing the χ EFT NN and 3N potential derived $NNLO_{sat}$ (red circle) and N3LO (squares, fit line and error band) model predictions of the proton and neutron radii, neutron skin, and dipole polarizability α_D . The green band is the experimental value of R_p and its intersection with the blue error band from the less constrained N3LO models generates the (orange) theoretical systematic uncertainty band for the predicted isovector sensitive quantities on the horizontal axis. The blue diamond points come from DFT models, including the SLY4 model, and display trends independent from the *ab initio* models, particularly for the R_{skin}^{48} predictions. Reproduced from [4].

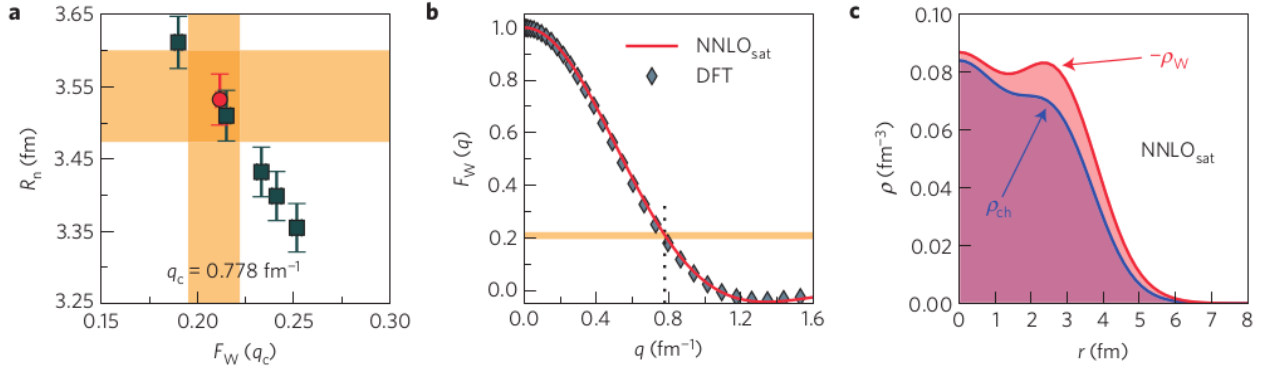


Figure 1.12: (a) Plots showing the χ EFT NN and 3N potential derived $NNLO_{sat}$ (red circle) and N3LO (squares, fit line and error band) model predictions of the neutron radii, taken from Fig. 1.11b, versus and the predicted $F_W(Q^2)$, whose error band is calculated in a similar way. (b) The $F_W(Q^2)$ from DFT and *ab initio* model calculations for the full range of Q^2 , with the proposed CREX kinematic $q_c = 0.778 \text{ fm}^{-1}$ point indicated [4](supplementary) (c). The weak and electric charge densities from the *ab initio* model discussed in the text, indicating a non-trivial neutron skin. Reproduced from [4].

Table 1.3: Theoretical calculation and experimental constraint results for R_{skin}^{48} discussed in the text.

Theory/Model	$R_{skin}^{48} (fm)$
χ EFT - NNLO _{sat} [4]	$\sim 0.135 \pm 0.015$
DFT - FSUGold [43]	~ 0.20
DFT - Avg of 25 EDFs [13]	0.176 ± 0.018
DOM - Neutron $\frac{d\sigma}{d\Omega}$, σ constrained [3]	0.249 ± 0.023
Experiment	$R_{skin}^{48} (fm)$
DFT - Constrained by PREX II [2, 13]	$\sim 0.23 \pm 0.03$
^{48}Ca α_D [14]	$\sim 0.17 \pm 0.03$
^{48}Ca proton scattering [15]	$0.168^{+0.025}_{-0.028}$
^{48}Ca mirror nuclei [46]	0.181 ± 0.10

and the neutron radius, R_n . Another observation is that the neutron skin, R_{skin} is predicted to be small as well as relatively independent of R_p , due to the strong correlation $R_p \propto R_n$ in the χ EFT models, in contrast with the DFT and DOM results discussed before. Predictions of the skin thickness and form factor at the CREX kinematics with NNLO_{sat} are shown in Fig 1.12.

1.4.4 Model Predictions and Hadronic Measurements

These models, which exemplify a subset of the nuclear structure models available, each make predictions of the weak form factor in ^{48}Ca and the neutron distribution and corresponding skin thickness, shown together in table 1.3. In summary, the DOM approach yields a large predicted R_{skin}^{48} when constrained with elastic neutron scattering and total neutron cross section data, which is dominated by the total neutron cross section constraints. The NNLO_{sat} *ab initio* model yields a small skin, consistent within the systematic error of less

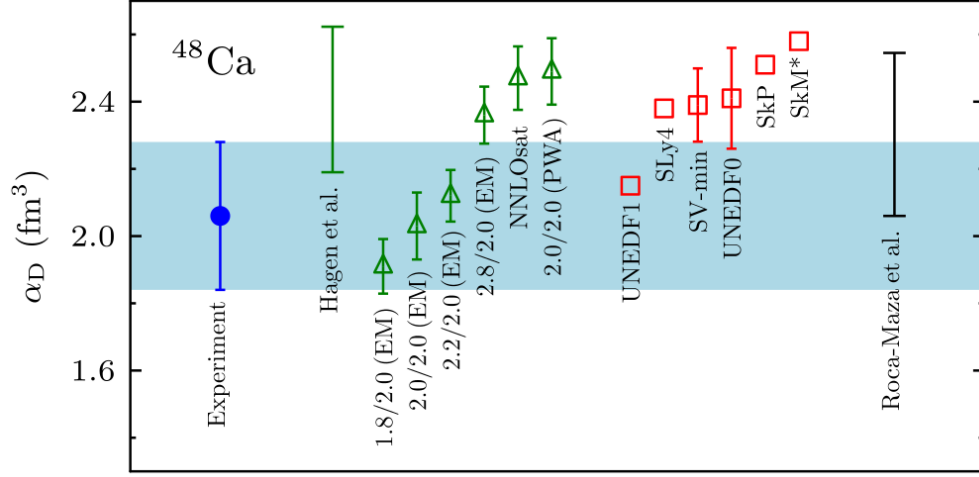


Figure 1.13: Plot showing the experimental result for the electric dipole polarizability of ^{48}Ca from [14] (blue band) alongside model predictions from χEFT (green triangles) and DFT models (red squares). The green bar indicates the χEFT models whose α_D results match the experimental measurement and which are used to predict R_{skin}^{48} , and the black bar is the same for the DFT models. Reproduced from [15].

constrained but higher order N3LO models' ability to match the precisely known R_p radius. And the DFT models span a region in the middle, but with constraints from the recent PREX II experiment pushing the $R_{skin}^{48} \propto R_{skin}^{208}$ correlated estimate towards larger values as well. In terms of the $F_W(Q^2)$ observable, the different theoretical approaches predict the difference between the charge and weak form factors $F_{ch} - F_W$ around the high FOM CREX Q^2 region. The models' calculations of $F_{ch} - F_W$ span a similar range from low to high, following the same trend the R_{skin}^{48} predictions, shown in Fig. 1.14 alongside an arbitrarily placed point with the projected experimental error for CREX [16].

This range of predicted $F_W(Q^2)$ and extracted R_{skin}^{48} represents non-trivial tension between the theoretical approaches which will be illuminated by the CREX measurement. It is valuable to relate the *ab initio* models to DFT the CREX result because there is no microscopic foundation for calculating the DFT models' parameters. The χEFT models represent a microscopic foundation, but are not able to explicitly calculate the DFT model parameters

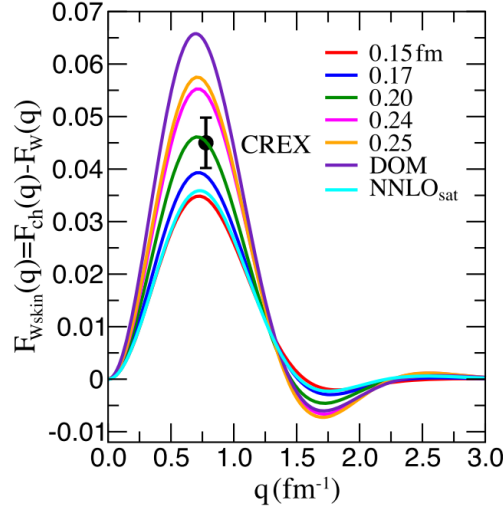


Figure 1.14: The difference in charge and weak form factors of ^{48}Ca vs. q , along with the predictions from relativistic DFT models and the DOM and NNLO_{sat} *ab initio* model discussed in the text. A point is shown for the predicted CREX precision at an arbitrary location. Reproduced from [16].

either, and so measurements described by both provide a bridge. A recent measurement of the dipole polarizability α_D in ^{48}Ca has been reported in [14], shown in Fig. 1.13. When taking only the theoretical models that are consistent with their α_D result to predict a range of skin thickness, the measurement implies $0.14 \leq R_{\text{skin}}^{48} \leq 0.20 \text{ fm}$, the lower range of which is in agreement with the NNLO_{sat} *ab initio* models. Hadronic scattering results using proton scattering are recently reported in [15], which obtain similar conclusions and $R_{\text{skin}}^{48} = 0.168^{+0.025}_{-0.028} \text{ fm}$, and theoretical considerations from mirror nuclei in [46] anticipate $R_{\text{skin}}^{48} = 0.181 \pm 0.010 \text{ fm}$.

These results from hadronic scattering and various theoretical approaches suggest that the measurement of CREX, especially when coupled with the relatively thick neutron skin result from PREX II, will allow for mutual constraints of bulk and surface symmetry energy terms. The measurement of a large neutron skin implies a large, or “stiff” density dependence of the nuclear symmetry energy, as the cost of isovector asymmetry rapidly changes from high at

high density to low at low-density, while a thin neutron skin oppositely implies a soft density dependence and small L value, where the asymmetry cost is similar between high and low densities. PREX II measures a thick skin, $R_{skin}^{208} = 0.283 \pm 0.071 fm$ reported in [2], compared to the averaged predictions from a subset of DFT models of $R_{skin}^{208} = 0.168 \pm 0.022$ reported in [13], which implies a stiffer EOS than expected at densities near nuclear saturation, $L = 106 \pm 37$ MeV [11]. The CREX measurement, along with PREX II and dipole polarizability results will constrain the EOS at densities relevant for nuclei, and provide inputs useful for neutron star physics, as well as radioactive isotopes and heavy ion physics [16, 45, 47].

1.5 Calcium Radius EXperiment

These theoretical considerations make the case clear for a high precision PVES measurement of $F_W(Q^2)$ in ^{48}Ca . Developments in radiation shielding and target design for PREX II have paved the way for success with CREX using the same equipment. The next chapters detail the experimental apparatus and asymmetry analysis, and the final chapter details the extraction of the weak form factor from the experimental data and its theoretical impact.

Chapter 2

Experimental Overview

Parity-violating electron scattering experiments, such as CREX, attempt to measure small asymmetries at the 10^{-6} (*ppm*) scale, whose statistical precision are limited by Poisson counting statistics as

$$\sigma_{APV} \geq \frac{1}{\sqrt{N}}, \quad (2.1)$$

where N is the number of measured scattered electrons. This relationship is not an exact equality due to instrumental noise. To allow the most statistically significant measurement necessary for the proposed CREX $\sim 0.02fm$ scale extraction of the neutron skin R_n for ^{48}Ca , we must design the experiment to run at high rates [1]. The Thomas Jefferson National Accelerator Facility’s (TJNAF, or Jefferson Lab or JLab) Continuous Electron Beam Accelerator Facility (CEBAF) is capable of fulfilling this high rate need [17, 48]. CEBAF is a dual-linac recirculating electron accelerator which produces a “continuous wave” (CW) pulsed beam of electrons for simultaneous delivery to four experimental halls: A, B, C, and D. The CREX experiment ran in Hall A from December 2019 through September 2020, with CEBAF delivering $150\mu A$ of $\sim 90\%$ highly-polarized, one-pass (2.18 GeV), electron beam

Table 2.1: Table of parameters used in CREX running.

Parameter	Value
E	2.18 GeV
Current	150 μ A
Beam Polarization	$\sim 90\%$
Helicity Flip Rate	120 Hz
Target Thickness	$\sim 1.0 \text{ g/cm}^2$
Momentum Resolution	10^{-3}

to Hall A in simultaneous running along with the other halls. A schematic of CEBAF and the experimental halls is shown in Fig 2.1, with an aerial view shown in Fig. 2.2. The experimental parameters for CREX are given in Table 2.1.

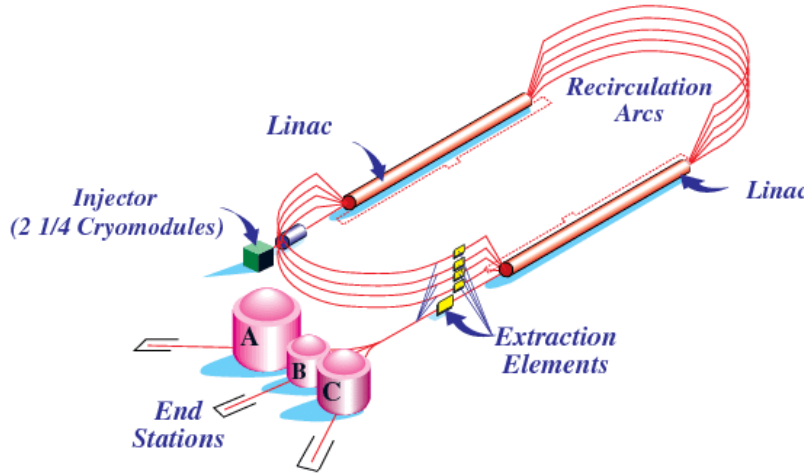


Figure 2.1: CEBAF cartoon, adapted from [17].

The CEBAF electron beam begins its life in the injector via electron photoproduction from circularly-polarized laser light incident on a strained gallium-arsenide crystal cathode and is accelerated through a sequence of superconducting radiofrequency cavities in two parallel linear accelerators with recirculating arcs. After acceleration, the beam is delivered into experimental Hall A via a series of extraction arcs where it is then scattered from the $\sim 90\%$ isotopic purity ^{48}Ca target. The scattered flux is collimated and bent by magnets so



Figure 2.2: Aerial view of the Continuous Electron Beam Accelerator Facility (CEBAF), where CREX takes place.

that CREX measures a small average scattering angle of $\sim 5^\circ$, which maximizes the figure of merit for CREX, the A_{PV} sensitivity to the ^{48}Ca neutron skin, discussed in section 1.3.4. The kinematics are determined and resolved by a custom collimation system and septa magnets and the Jefferson Lab Hall A High Resolution Spectrometers (HRSs).

To maximize N to measure the asymmetry within a reasonable time, a high scattering rate is needed. However, it is not practical or cost effective to implement a detector and data acquisition system that can count such a high rate of electrons individually. We therefore utilize custom integrating detectors and data acquisition (DAQ) to measure the ~ 50 MHz rates of scattered electrons in neighboring helicity windows, while we utilize the standard Hall A VDCs and counting mode DAQ for low-current optics kinematics calibration data collection. This integrating detector system for asymmetry measurements has a non-zero resolution of signal response to incident electrons, as well as electronics and DAQ noise limitations that are all considered.

To achieve the high scattering rate we also approach the limit of scattering intensity,

which requires cooling and radiation safeguards for protecting the ^{48}Ca target, the electronics in the experimental hall, and the general public. The beam produced by the polarized source, injector, and accelerator may carry false left-right helicity-correlated (HC) beam fluctuations, A_{beam} , which are measured in the primary beam for later correction of the scattered and detected beam during the data analysis. These challenges have received substantial scrutiny over the years, as prior generations of PVES experiments have successively pushed previously achieved statistical precision and systematic control limits, which CREX builds upon. This chapter covers the experimental techniques and details the challenges that CREX addresses and the solutions achieved.

The author’s primary contribution to the experiment running is in setting up, optimizing, and maintaining the Parity DAQ and Alarm Handler GUI system for PREX II and CREX running, as well as the final asymmetry analysis, which is described in the next chapter. Due to the proximity of the DAQ system and alarm handling to both the experiment’s hardware and data analysis, the author developed familiarity with most of the experimental methods and hardware systems, motivating their detailed description in this dissertation.

2.1 Injector at Jefferson Lab

CREX proposes to measure the *ppm*-scale helicity-dependent parity-violating asymmetry of polarized electrons scattering from ^{48}Ca with $\sim 1\%$ scale systematic accuracy [1]. To achieve this accurate measurement we require a clean and stable way of changing the helicity state between left- and right-hand polarized electrons. This mechanism must be fast so it is insensitive to slow signal drifts, as well as synchronized to 60 Hz so it cancels power-line noise. Therefore, we utilize a polarized source with a fast laser helicity-flipping Pockels Cell system. To achieve a high degree of systematic control, the polarized source must generate only very

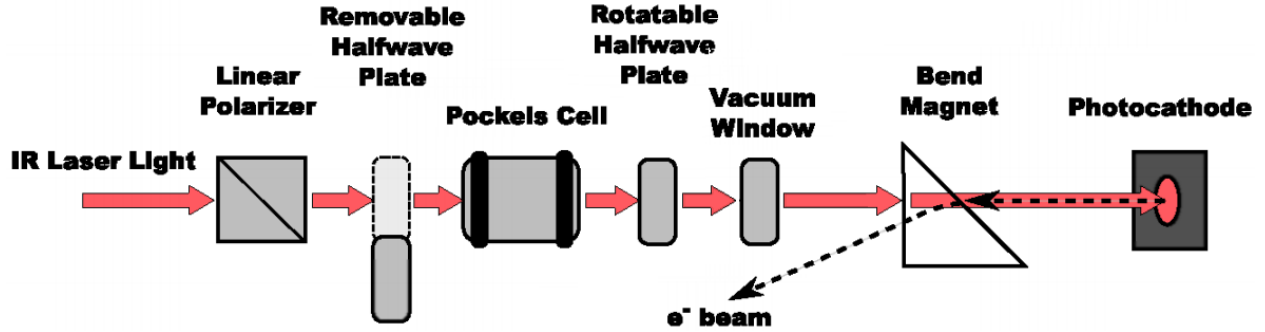


Figure 2.3: Schematic drawing of the injector laser and polarized electron source. Adapted from [18].

small unwanted HC A_{beam} , as they contribute helicity-correlated fluctuations carried within the beam, contaminating the primary A_{PV} measurement from polarized ^{48}Ca scattering, for which corrections must be measured and made.

To mitigate the possibility of HC effects evading direct measurement and correction from configurations of components in the injector, we perform regular slow helicity-reversals that affect different components of the polarized source. Slow reversals ensure that we have similar amounts of data with possible unmeasured HC A_{beam} in opposite-sign contributing configurations, yielding cancellations, and we verify the statistical consistency of the A_{PV} measurement between those various slow-control helicity-reversal configurations as a cross check of their minimal systematic error contribution. There are many components involved in the production of the highly-polarized electron beam, and many of them are capable of generating beam intensity, position, polarization, spot size, and energy HC A_{beam} if not controlled carefully. Fortunately, there are various tools which have been developed for the measurement, control, and correction of these features.

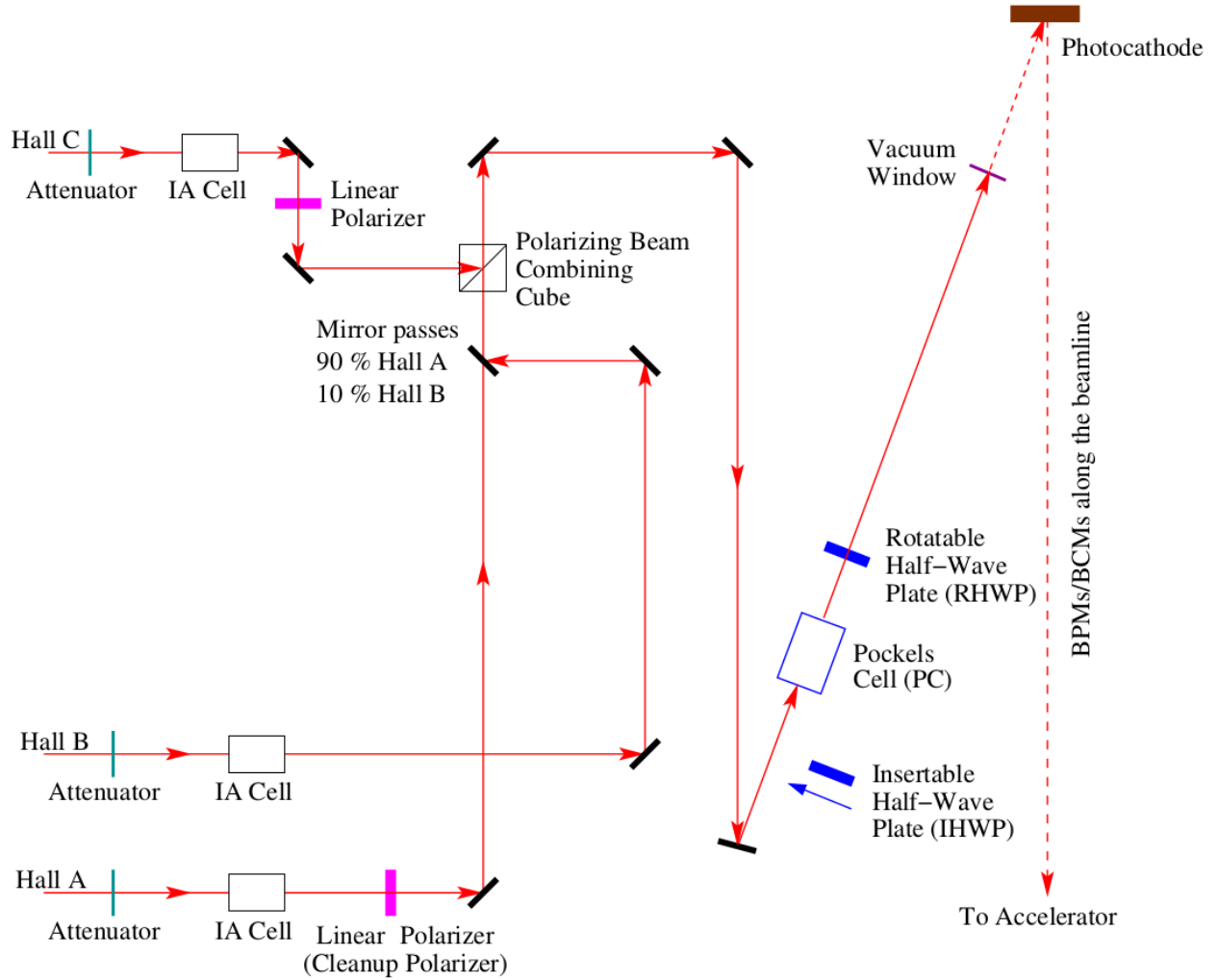


Figure 2.4: Schematic drawing of the CEBAF injector's polarized source. The double Wien system, not shown, is located along the beamline after the photocathode. Reproduced from [19].

2.1.1 The Polarized Electron Source

Polarized electrons are generated in the injector, whose simplified schematic is shown in Fig. 2.3, which consists of a set of lasers passing through optical elements to generate circularly-polarized laser light and electron beams for the four experimental halls simultaneously. The lasers for the halls operate in continuous wave (CW) pulsed mode, out of phase with each other, with the Hall A laser running at 499 MHz bunch pulse timing, such that the four halls (two of the other halls must run at 249.5 MHz) interleave their bunch trains to cover the full 1497 MHz CW timing of the electron accelerator downstream [48]. These lasers shine onto diode optical amplifiers that pass through linear polarizers, which gives substantial control over the source intensity of the beam. The beams also pass through attenuators and an adjustable slit which are used for controlling how much of the beam makes it farther through the injector, and are used for measuring and controlling any interactions between the laser paths or bleed-through from one hall's pulse train to another along the beamline.

The polarized source setup is shown in Fig. 2.4. The lasers pass through linear polarizers and then through a Pockels Cell (PC) which is used to convert from linear to circular polarization. The PC is also used to rapidly flip the helicity state and for fine HC A_{beam} control and minimization. The PC's helicity-control mechanisms and electronics are described in the following sections.

The PC crystal is an electro-optic device whose birefringence is proportional to an applied external electric field. The PC functions as a quarter-wave retardation plate under specific externally applied several kV voltage. This occurs when the primary axis of the PC is aligned along the incident polarization direction, but the birefringent axes are set to $\pm\frac{\pi}{4}$ with respect to that axis, as shown in Fig. 2.6. The externally applied voltage selects a $\pm\frac{\pi}{2}$ phase shift

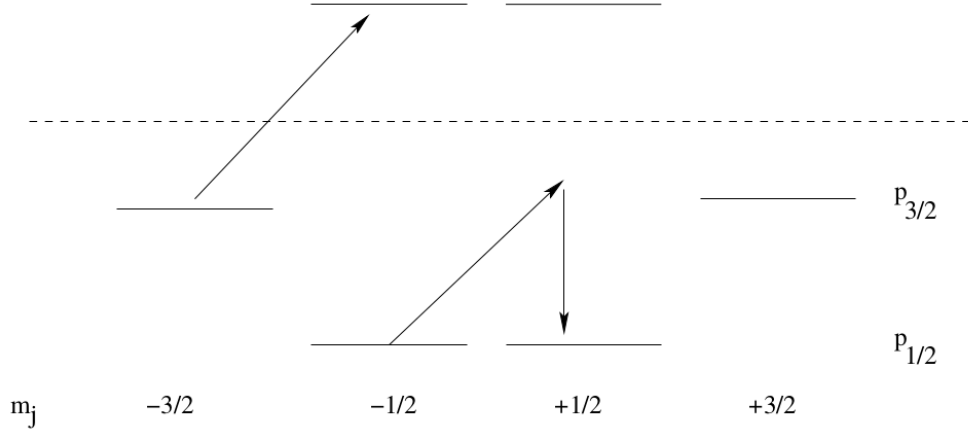


Figure 2.5: Diagram of the strained GaAs crystal's electron band structure and dynamics for one helicity handedness. As a result of breaking the spin-dependent degeneracy it is possible to preferentially promote and eject electrons from the conduction band of a specific helicity, producing a polarized beam. Reproduced from [20].

between them, whose sign \pm is determined by the sign of the helicity generator electronics (discussed below). The birefringent axes being orthogonal converts the incident linearly-polarized light into left- or right-handed circularly-polarized light depending on the PC voltage. Therefore the helicity of the circularly-polarized light is rapidly switched between left and right handedness to generate the opposite helicity polarization states desired for the CREX asymmetry measurement. Recent developments, described in detail in [49], have allowed the ringing and stabilization time scale of the PC to be reduced below the $100\mu s$ level found in traditional Potassium Dideuterium Phosphate (KD*P) crystals to as fast as $8\mu s$ in Rubidium Titanyl Phosphate (RTP) crystals. This is a substantial improvement over prior generation PVES experiments and allows the integrating data acquisition system's (Parity DAQ) signal integration to span up to $\sim 98.3\%$ of the available time per helicity window, discussed further in section 2.8.3.

The circularly-polarized laser beam from the PC passes through a transparent vacuum window and on to a doped GaAs crystal photocathode where the circularly-polarized photons

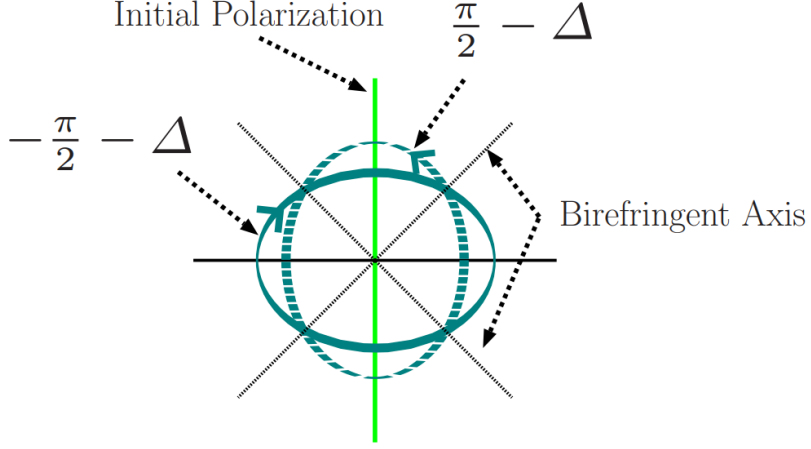


Figure 2.6: Polarization ellipses for the electric field vector of nearly-perfectly circularly-polarized light in the two opposite helicity states. The asymmetric phase shift Δ represents residual linear polarization and is responsible for the PITA effect in devices with linear polarization analyzing power. Reproduced from [18].

generate the longitudinally-polarized electron beam for injection into the accelerator [19, 49]. Due to the dopant in the photocathode, it experiences a strain, which breaks the valence band degeneracy. This broken degeneracy allows polarized incident light to selectively promote electrons to the conduction band, preferentially those of the same spin state, as shown in Fig. 2.5 [18, 20]. The figure shows the result of straining the GaAs crystal, whereby the $p_{3/2}$ and $p_{1/2}$ states separate, allowing the $p_{3/2}$ state to preferentially promote electrons to the conduction band and escape the cathode, thereby inducing a incident-photon's circular polarization dependent on the longitudinally-polarized electron beam. The conduction band excited electrons escape the cathode and are pulled by an electrostatic field to continue downstream into the accelerator.

Before running and after every major configuration change, such as adjusting the GaAs photocathode, we perform standard parameter measurements and optimization to set up the injector beamline to correct for the imperfectly circularly-polarized laser light exiting the PC. Two of the key tools for measuring and minimizing HC A_{beam} not removed by the

injector set-up process are the insertable half-wave plate (IHWP) and rotatable half-wave plate (RHWP). The IHWP will rotate the linear polarization incident on the PC by 90° , which causes the outgoing circularly-polarized light to flip to the opposite handedness [24]. The RHWP allows aligning the axis of any unwanted linear polarization relative to the photocathode’s axis, which is needed for optimal HC beam intensity control.

2.1.2 Slow Helicity Reversals

Due to the possibility of unwanted HC effects coming from any of the injector components bearing an analyzing power to imperfections in beam polarization we utilize the IHWP as a slow helicity-reversal control. Analyzing power is any difference in response or transmission of the beam between the left vs. right helicity states. The analyzing power may respond to or produce HC differences in any photon or electron beam parameter, such as intensity, polarization, spot size, or position. Slow reversals cause a relative polarization flip of the outgoing electron beam’s polarization with respect to the logical helicity signals sent to the PC and the high voltages applied to set the helicity state [19]. The IHWP is taken in and out of the laser beam on a daily time scale, with approximately equal amounts of production data taken in each state. The data collected in one IHWP state is called a “slug,” and each slug corresponds to nearly ~ 6 hours or ~ 3 Coulombs of electron beam on target passing all event cuts. Taking slugs of data with similar statistics and opposite helicity sign provides cancellation of many systematic HC A_{beam} which do not change sign with the reversals, as the physics asymmetry measured in the experimental hall does change sign with the slow reversal. This is especially useful for effects coming from the PC imperfections and signal pickup from its helicity-control electronics, described in the next sections, which are fully independent of the state of the IHWP. We similarly utilize a double Wien magnetic filter

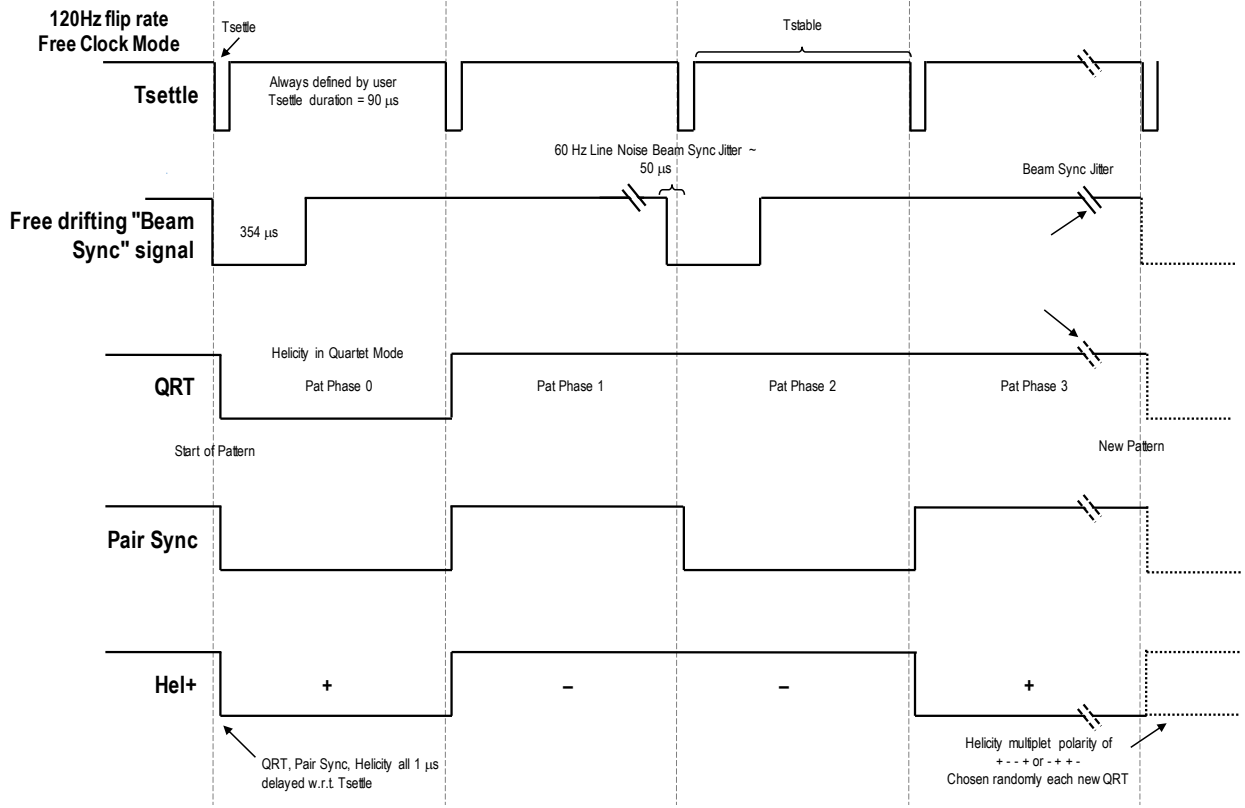


Figure 2.7: Helicity logical signals timing diagram for CREX. This figure shows the four helicity-control signals for CREX 120 Hz “free clock” running, alongside the reference freely floating “beam sync” signal that indicates the starting phase of each 60 Hz power supply oscillation.

to directly flip the polarization of the electrons, described in section 2.2. The double Wien filter similarly functions to independently change the sign of the electron’s polarization state with respect to the logical helicity signals, this time downstream of the electrons’ production by the strained GaAs cathode. Double Wien flips were performed twice during CREX with similar amounts of data collected in each “Wien left” and “right” configuration.

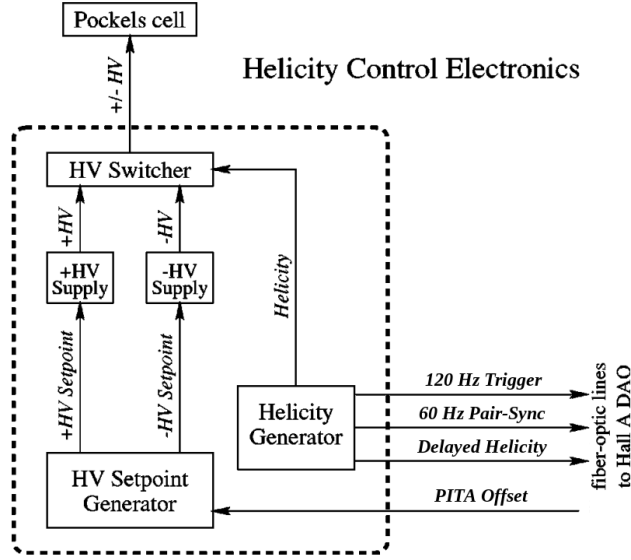


Figure 2.8: Schematic of the helicity-control electronics. The helicity-state logical signal is transmitted via fiber optic cables and determines the high voltage on the Pockels cell. The Pockels Cell and helicity-signal generator are both electrically isolated from the beamline and data acquisition components elsewhere in the laboratory (dashed box). Adapted from [21].

2.1.3 Helicity Signal Electronics

The helicity signals, whose logic is shown in Fig. 2.7 and their connection to the PC shown in Fig. 2.8, are generated in a JLab custom-built logic circuit “Helicity Control Board.” [21, 50] The Helicity Board controls the timing and helicity sequence structure and can be configured via the VME backplane. For CREX running we choose to utilize a quartet helicity pattern with individual helicity state windows at 120 Hz. The helicity state, labelled “Hel+” in the figure, comes in quartet “multiplet” patterns of $+- -+$ or $-+ +-$, where the sign of the first window in the multiplet determines the sign of the entire multiplet as either a $+$ or $-$ multiplet pattern. The sign of each multiplet is determined by the Helicity Board using a 30 bit pseudo-random number generator, where the seed of the pseudo-random pattern can be extracted only if 30 sequential multiplet patterns’ signs are known. The logical

helicity signals themselves are transmitted by light over fiberoptic cables to allow complete ground-isolation of the helicity-generator circuit, reducing the possibility of electronic signal leakage or pickup in other parts of the experiment or in the Parity DAQ.

The goal of the randomly alternating multiplet pattern is to oppositely sample the phase of any 60 Hz power supply line noise that may be carried in the beam, and to cancel that noise in neighboring helicity windows. The pseudo-random selection of multiplet sign and the simultaneous production of both a “Hel+” and “Hel-” copy of the helicity signal within the Helicity Board are designed to cancel any accidental power load or electronic pickup signal that may propagate the information about the helicity from the source into other parts of the accelerator, DAQ or experiment hall. For the same reasons, the helicity signal sent to the experiment’s DAQ is delayed by 8 multiplets, destroying any correlation with the true helicity of the electron beam during that multiplet window, so that the helicity information is unable to affect the DAQ’s measurement. These various precautions provide a high degree of confidence that any asymmetry signals measured in the experiment DAQ are in fact due to random non-HC noise or from real HC signals in the beam and scattered flux, which are discussed below. This confidence is further strengthened by beam-off electronics studies and battery studies of the DAQ performed before experiment running, where small levels of electronics noise are controlled at the few *ppm* level, with no noticeable accumulated HC signal even at the *ppb* scale.

The T_{settle} time, shown with the other helicity signals in Fig. 2.7, is the time where the helicity state is potentially changing or unstable, and therefore serves as a veto signal for the integrating DAQ. For CREX T_{settle} was chosen to be $90\mu s$ to allow the PC ringdown to stabilize and avoid any imperfect polarization flip between neighboring helicity state windows. The minimum time for the ringdown is likely much shorter than $90\mu s$, potentially as short as $8\mu s$ [49], but we chose the larger time scale because it is already very small compared to

the $8.33ms$ scale of the entire 120 Hz helicity windows and also to be conservatively careful while avoiding expending excess effort to monitor the PC system or verify the relative timing between the hall and injector DAQ components. The integrating “Parity” DAQ setup is discussed further in section 2.8.2.

2.1.4 Helicity Correlated Beam Asymmetries

The helicity control system shown in Fig. 2.8 contains an additional feature beyond simple helicity state selection. The PC is able to generate and correct HC A_{beam} that are measured with the Parity DAQ, and this feature is used during CREX to perform real-time HC “charge feedback” as part of the online analysis. Charge feedback manipulates the PC voltages in the injector to correct for HC intensity asymmetries (A_Q) caused by residually linearly-polarized laser incident on the beamline components with a linear polarization analyzing power. It is necessary to control A_Q , because the asymmetry of the beam intensity will directly impact the measured asymmetry of the scattered flux. The correction accuracy of an A_Q measured with current monitors is limited by non-linearity of the monitors, which is at the one percent level, and so we want to intentionally minimize the CREX net A_Q below the 100 *ppb* level such that its systematic error is below the one *ppb* level and contributes negligible uncertainty to the final A_{PV} result. Without any control on A_Q the net measurement could be several orders of magnitude larger and start to contribute non-trivial systematic error. The charge feedback system of CREX is described in the next section.

HC A_{beam} signals can be introduced in a number of ways, including from helicity correlated position and spot size dependences. The most significant HC A_{beam} come from residual linear polarization in the laser from the PC incident on the GaAs photocathode. Although our beam is nearly 99% circularly-polarized, because polarization adds in quadra-

ture to 100%, even a small deviation from 100% circular polarization amounts to a non-trivial amount of linear polarization. The interaction of the residual linearly-polarized portion of the laser light on a beamline element which has an analyzing power (the preferential transmission or interaction with one state over the other) gives rise to the “Polarization-Induced Transport Asymmetry” effect (PITA), whereby these beamline elements drive HC A_{beam} signals. These PITA induced effects account for most of the net HC A_{beam} and must be minimized to avoid contributing large systematic uncertainty to the measured scattered electron flux asymmetries from imperfect measurement and correction.

These effects can be used as a tool within the controllable PC, which can produce intentional helicity-correlated transmission and residual linear polarization for mitigating unwanted PITA elsewhere. The PC, when properly instrumented with external electric fields, provides control over the PITA effect via carefully applied voltages [49]. The residual linearly-polarized light and its helicity dependence, which generate unwanted PITA, can be characterized by writing the phase shift applied to the linearly-polarized light by the PC as

$$\delta^R = -(\frac{\pi}{2} + \alpha) - \Delta, \quad \delta^L = +(\frac{\pi}{2} + \alpha) - \Delta, \quad (2.2)$$

where R and L are the helicity state (handedness) of the circularly-polarized light and α and Δ represent the difference between the actually applied phase shift and the ideal case of pure $\frac{\pi}{2}$ shift, again shown in Fig. 2.6 [18]. If α is non-zero then both helicity states have the same amount of excess phase shift relative to each other, while if Δ is non-zero then the size of the phase shift changes size between the two helicity states, thereby generating a residual linear polarization that changes sign with the helicity change.

As mentioned before, this helicity-dependent residual linear polarization will generate a HC A_{beam} charge intensity asymmetry (the PITA effect) when passing through optical

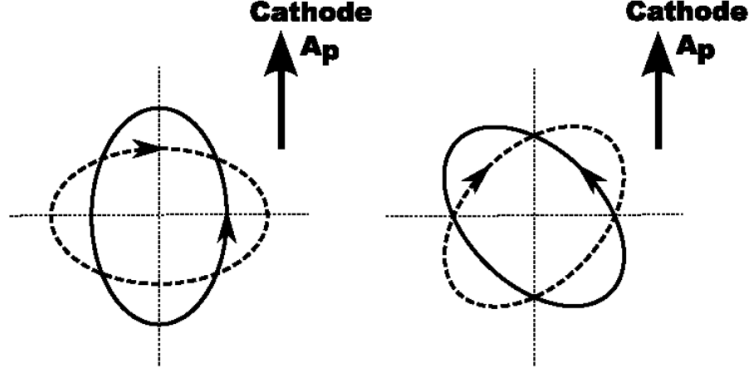


Figure 2.9: Maximal PITA effect sensitivity from the cathode’s analyzing power (A_p) due to residual linear polarization asymmetry between two imperfectly circularly-polarized laser helicity states (left handed, dashed, and right handed, solid, lines) is shown on the left, and the case with minimal PITA effect sensitivity by rotating the axes of the two states’ residual linear polarization to 45° with respect to the cathode’s A_p optical axis is shown on the right. Reproduced from [22].

components with analyzing power to linear polarization, such as the cathode, which develops a linear polarization analyzing power due to the strain it bears. Similarly, any beamline component with static birefringence-induced Δ phase shift independent of helicity state will also generate residual linear polarization, such as the vacuum window and the PC itself, independently of the primary helicity-flipping voltage applied. Because of the tunable nature of the PC, it is possible to mitigate Δ phase shifts within the various beamline components by intentionally setting the PC voltages in a helicity-dependent way to cancel all other sources of Δ phase shifts, and therefore also minimize the PITA effect.

2.1.5 Charge Asymmetry and Feedback

An additional feature of the PITA control afforded by the PC, alluded to already, is the ability to mitigate both static sources of A_Q and to actively perform beam intensity “charge feedback” to drive A_Q close to zero consistently, on few second time scales [21]. Throughout CREX, calibration runs were performed to determine the optimal rotation angle of the

RHWP to align its axis close to 45° with respect to the GaAs cathode’s linear polarization analyzing power axis to generally but not completely minimize A_Q , as in Fig. 2.9. Calibrations are performed to determine the slope of induced PITA asymmetry to the remaining RHWP analyzing power as a function of applied external voltage to the PC. This “PITA slope” is used in an A_Q cancelling feedback correction loop which runs on a 7.5s time scale of measuring A_Q and applying a PC voltage correction to cancel it [19, 22].

By not fully rotating the RHWP to 45° with respect to the cathode, the remaining sensitivity of the cathode’s analyzing power axis with respect to the RHWP rotated incident linear polarization is used to minimize the impact of static imperfections in the PC’s birefringence. This yields a sufficiently large lever arm, both to generate an opposite linear polarization to cancel other sources such as those coming from the birefringence in the vacuum window, as well as to provide the PITA slope for charge feedback [18, 49]. Additionally, because the vacuum window is totally static and independent of the PC’s optical axis, a rotation of the cathode itself is utilized to align its axis with respect to the vacuum window’s in such a way as to effectively cancel it out.

The set point for the PC charge feedback controlling voltage is the “PITA Offset” signal in the figure, which is calculated based on the measured beam A_Q and the necessary external PC voltage to drive it to 0. The PC “PITA Offset” is the voltage calculated by the feedback online analyzer required to negate the measured A_Q during the prior 7.5s interval of data collection. The “PITA Offset” value is transmitted from the Hall A DAQ workstation via the CEBAF EPICs control system, and the voltage to the PC is also ground isolated with respect to the rest of the experiment and the Parity DAQ to avoid any HC signal pickup. There are similar static “U” and “V” voltages applied, not shown in the figure, which determine the necessary helicity-dependent voltages to apply to the PC that mitigate the Δ phase shifts mentioned before.

2.1.6 Position Differences

HC A_{beam} position-dependent differences are produced by spatial gradients in the Δ phase shift found in birefringent injector beamline optical components, or in the analyzing power of the residual linear polarization, or may be produced by other means such as charge asymmetric beam clipping past a position dependent obstruction, and they may impact the measured rates of electron scattering by the ^{48}Ca target [18]. Although the scattering is accepted into symmetric collimation and transported similarly to the left and right integrating detectors, that left-right symmetry is not sufficient to remove all HC A_{beam} . The sharp dependence of the cross section on scattering positions, angles, and energy mean that any fluctuation in the beam will translate with an approximately linear relationship into a HC A_{beam} measurable in the detected scattering rate asymmetry in the integrating detectors.

As mentioned before, these HC A_{beam} are also potential sources of false asymmetries and are a background which must be measured, corrected, and accounted for in systematic uncertainty estimates. Due to the limitations of our instrumentation and calibration techniques for the sensitivity of scattered rate to beam parameters, the uncertainty estimates of HC A_{beam} position dependent differences' contributions to the corrected asymmetry are only in the few % accuracy range and must be kept small to avoid contributing substantial systematic uncertainty. HC position dependent differences from optical elements with Δ phase shift gradients in the injector, as well as spot size asymmetries from the second derivative of Δ , are suppressed by the rotation of the RHWP and tuning of PC voltages to fixed values that minimize the analyzing power, which are determined in dedicated calibration runs. It is possible to utilize the PC for position-dependent HC feedback, similarly to the charge feedback described before, but this was not deemed necessary for CREX. The remaining HC A_{beam} from charge intensity, and beam position, angle, and energy that are not mitigated

by injector studies' optimization and the charge feedback system are carefully measured and corrected, and the study of their impact on the measured scattered flux asymmetry is a primary goal of the asymmetry analysis for CREX, and is discussed in detail in chapter 3.

2.2 The Accelerator, CEBAF

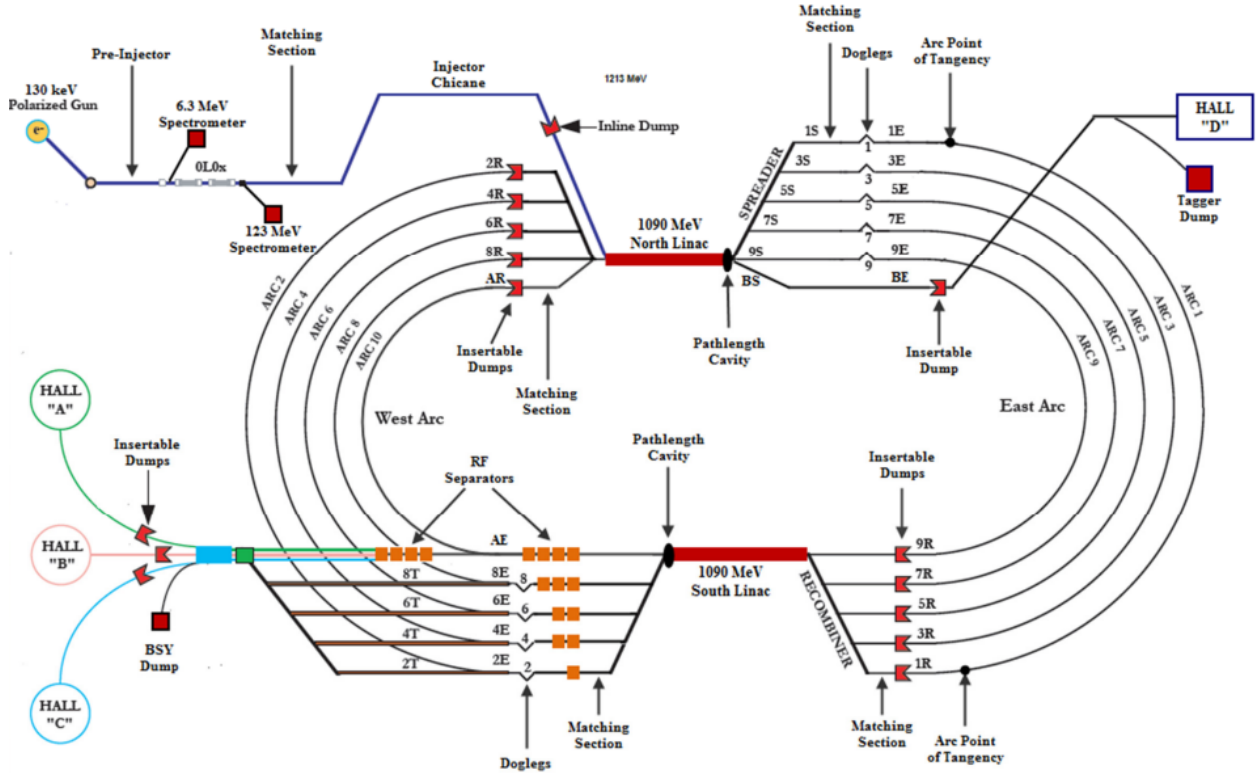


Figure 2.10: CEBAF 12 GeV upgrade design schematic. Reproduced from conference proceedings slide 5 of [23].

The Continuous Electron Beam Accelerator Facility at Jefferson Lab (CEBAF) is a “race-track” design pair of linear accelerators (linacs) and magnetic bending arcs that takes the electron beam produced in the injector, accelerates it to the desired energy, and delivers it to the four experimental halls simultaneously [48]. CEBAF recently underwent an upgrade

from its 6 GeV configuration to the 12 GeV configuration, which included adding additional accelerating cavities, a new fourth experimental hall (Hall D), as well as the upgrades to the injector and polarized source described in the prior sections. CEBAF’s linear accelerators are comprised of the original 6 GeV era superconducting radiofrequency (RF) accelerating cavity cryomodules, called C20’s and C50’s, which give 20 MeV and 50 MeV energy kicks respectively to the electrons per module pass, along with new 12 GeV era cryomodules called C100’s which run at an improved 19.2 MV/m electric field and give 100 MeV per module per pass [51].

The injector provides a starting energy from two C100 cryomodules, yielding 123 MeV, the 20 original C20’s and C50’s run in the 6 GeV era’s optimal configuration, yielding up to 600 MeV energy per linac per pass, and the five new C100’s yield up to an additional 500 MeV per linac per pass. Combined, CEBAF in the 12 GeV era is able to reach around 2200 MeV per pass around the accelerator [52]. The many cavities operate in synchronization with each other, with their relative timing and that of all beamline elements optimized to accelerate and manipulate the electron beam, as determined by the ~ 60 Hz power supply phase “beam sync” reference signal, shown in Fig. 2.7. The beam is composed of the electrons from each pass through the accelerator simultaneously, and the separate passes are split and recombined vertically by dipole and septa magnets in the spreaders and recombiners to pass through the different recirculation arcs based on their momentum, so that they can be separately bent the 180° needed for recirculating into the next linac pass [51].

Matching is the process of tuning various accelerator components, principally the accelerating gradients in each cavity and the magnetic field strengths of optical-tuning quadrupoles, with the goal of “matching” the theoretically modeled accelerator beam parameters. Matching is performed by running a pulsed “tune beam” tied to the “beam sync” signal into insertable beam dumps along the beamline (shown in Fig. 2.10), scattering the beam with

movable wire “harps” to determine its profile and updating the cavity field gradients and quadrupole fields in the matching sections to shape the beam spot size, transverse position and relative energy emittances, and position to get the beam to “match” the simulated CEBAF design parameters [23]. This matching procedure is performed sequentially through areas of the accelerator, starting in the injector, then to the start of each bending arc, and finally into Hall A through the Hall A extraction arc.

Several other “knobs” are available to the accelerator operators to provide clean beam with minimal halo and spot size problems, such as bunch compression in the injector chicane and monitoring of the relative power and phases of all linac cavities. Matching the different components of the accelerator, arcs, and transport into Hall A is an important step for maintaining the beam spot size at the desired level of $\sim 150\mu m \times 150\mu m$ on the target, which is necessary to optimize the heat dissipation in the Calcium, for maintaining the decoupling of the transverse beam motion degrees of freedom that must be measured and used for correcting the measured asymmetry, and for keeping the electron beam halo small to mitigate unwanted backgrounds by minimizing the beam’s emittance due to synchrotron radiation in the accelerating and bending segments of CEBAF. The emittance of the beam is small for the lower passes and becomes dominated by synchrotron radiation driven emittance for the higher passes. The matching process is done as part of commissioning the beam at the start of the experiment and after down times, and matching tuning into Hall A requires collaboration between the experiment shift workers and the CEBAF accelerator operators, as well as online monitoring by both to ensure optimal “parity quality” data collection.

For CREX, $150\mu A$ of CW electron beam is transported through the linacs in their full 12 GeV configuration at one pass through CEBAF, to reach the 2.18 GeV delivered into Hall A. Because CREX operates at one pass, it receives a more stable $\epsilon_{x,y}$ emittance and $\delta p/p$ energy spread than the higher pass beam, at $\sim 0.3nm\ rad$ and $\sim 3 \times 10^{-5}$ respectively

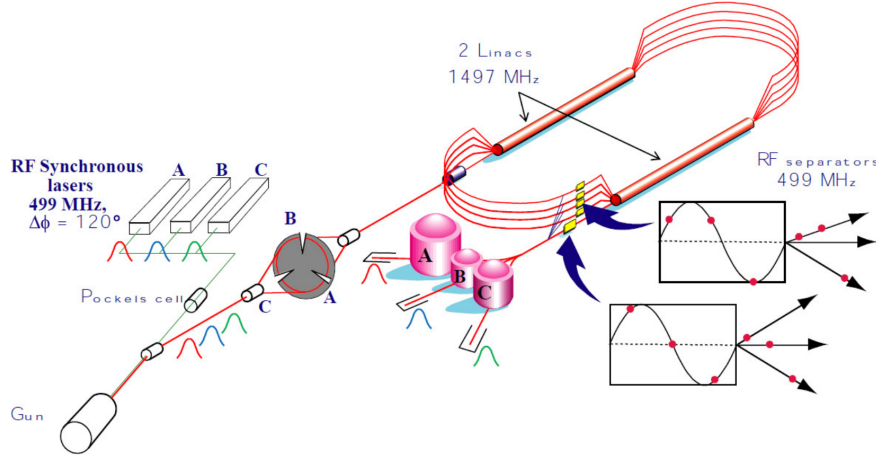


Figure 2.11: Cartoon depiction of the horizontal separator RF-cavity acting on phase and time separated electron beams generated in the injector. Shown on the right are cases of separating or maintaining beams, based on the relative timing of the copper cavities. Reproduced from [24].

[23]. The electron bunches produced in the injector and accelerated to the halls are nearly circular, with spot size of $\sim 80\mu\text{m}$ RMS in the transverse direction and bunch length of $\sim 300\text{fs} \simeq 90\mu\text{m}$ longitudinally [48, 51]. The beam spot is spread out to the desired $\sim 150 \times 150\mu\text{m}^2$ by quadrupoles in the Hall A arc for safe delivery to the calcium targets.

The 1497 MHz beam is made up of the beams for the four halls, separated in time by the interleaved 499 MHz (two of the halls must run at 249.5 MHz) electron bunch-train repetition rate. This temporal and spatial separation, depicted in Fig. 2.11, allows the beams, one beam only for each of the first four passes and all beams for pass five of the accelerator, to be separated into Halls A, B, or C by horizontally deflecting copper cavities and septa magnets [51]. The process of delivering the beam stably onto a small target relies on accelerator energy and position feedback systems involving locks on the target beam positions, the orbit through the accelerator's recirculation arcs and Hall A extraction arc, as well as a fast feedback (FFB) system [20]. The FFB system measures high-frequency oscillations in the beam and injects counteracting signals based on the measured and even predicted (with a

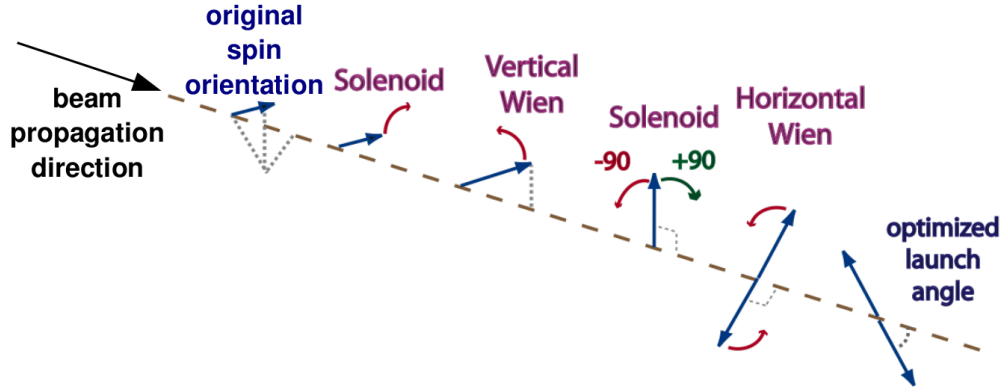


Figure 2.12: Schematic of the double Wien filter in the CEBAF injector, used for optimizing polarization launch angle and for performing slow-control helicity reversals. Reproduced from [19].

so-called “feed forward” system) noise into specialized accelerator components just upstream of the Hall A extraction arc to minimize that noise.

The polarization delivered to the halls is optimized in all halls simultaneously by choosing an ideal electron-spin launch-angle out of the double Wien filter to propagate and precess through CEBAF, whose schematic is shown in Fig. 2.12 [20]. The Wien filters use balanced crossed electric and magnetic fields, where the magnetic field causes the electron spin to precess, and the electric field balances and cancels the deflecting force from the interaction in the magnetic field, as shown in Fig. 2.13. The first Wien filter rotates the electron polarization from the gun in the vertical plane, and two solenoids allow rotating the spin to the right or left horizontal plane, which is what is flipped to the opposite side in the HC A_{beam} “Wien flip” slow-control procedure. From there the second Wien filter rotates the spin to the optimal launch angle [24]. By optimizing the launch angle and linac energy the beam is delivered with high longitudinal polarization to all halls simultaneously. Residual transverse polarization from imperfect launch angle tuning is kept at or below the 1% level and is a potential source of transverse polarized electron scattering asymmetry in CREX. The

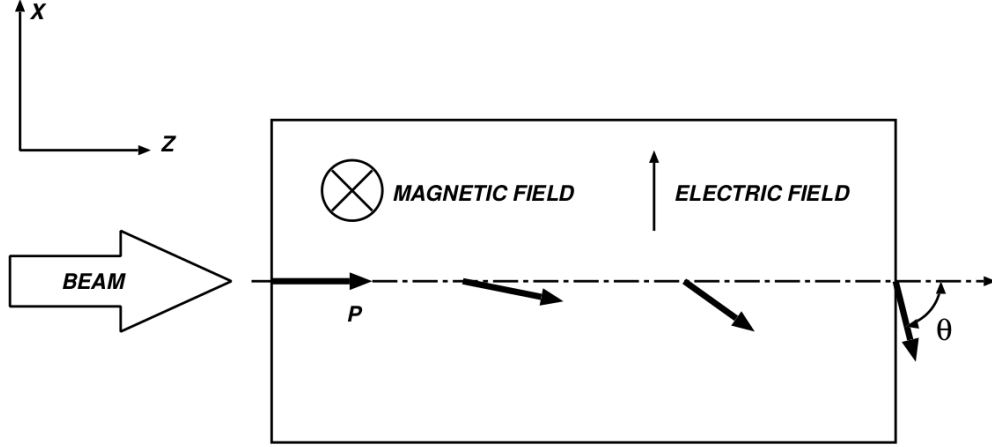


Figure 2.13: Schematic of the crossed electric and magnetic fields in a Wien filter used to rotate the spin but not perturb the trajectory of passing electrons. Reproduced from [25].

launch angle and transverse polarization minimization is checked by dedicated polarization measurements in the injector Mott polarimeter and the polarimeters in each of the halls, and a parasitic measurement of a possible transverse asymmetry in CREX is performed with additional detectors placed in sensitive locations in the CREX detector package.

2.3 Hall A

After acceleration in CEBAF and extraction to the beam switch yard, the electron beam is transported, as shown in Fig. 2.14, through the Hall A arc, which contains beam position monitors (BPMs) and dipole magnets that provide an energy dispersion of 4 meters for measurement and control of the beam position and energy, beam modulation coils for beam motion sensitivity measurements, and harps for accelerator matching. The beam is transported from the arc and into experimental Hall A, where the CREX kinematics and parity-violating asymmetry measurements are performed by scattering the beam on a high isotopic purity ^{48}Ca target and into the HRS spectrometers. Before scattering on the tar-

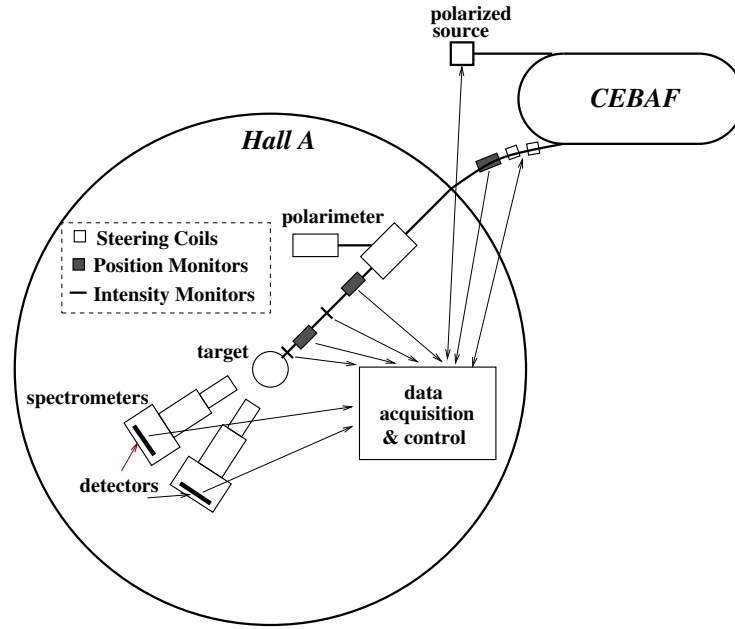


Figure 2.14: Cartoon depicting the beam delivery and monitoring systems of Hall A. Adapted from [21].

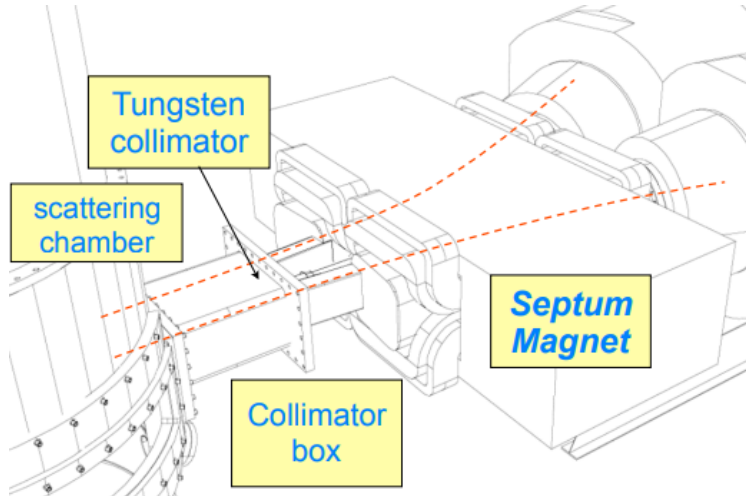


Figure 2.15: Simplified CAD depicting the target scattering chamber on the left, acceptance-defining collimator and septum magnets in the middle, and HRS acceptance on the right.

get, the beam is spread over several mm^2 by a fast raster system and its position and current are measured in dedicated stripline switched-electrode electronics (SEE) BPMs, resonant RF-cavity beam current monitors (BCMs), and newly developed RF-cavity combined BPM/BCMs. The polarization of the beam in Hall A is measured parasitically at high current in a polarized laser cavity Compton scattering polarimeter system, as well as invasively at low current in regular dedicated runs in a polarized iron foil Møller scattering polarimeter system.

The target ladder containing the liquid helium cooled ^{48}Ca production target and another containing water cooled low-current optics calibration targets are contained within a vacuum scattering chamber, which has its front face at 1151.2mm upstream of the “pivot” center of the circular underground experimental hall [26]. Shielding and collimation is placed to absorb unaccepted scattered flux and to minimize radiation to the hall and surrounding environment, and the low-angle scattered and unscattered beam continues unperturbed downstream to the small angle monitors (SAMs) and beam dump. The electrons pass through beamline and acceptance-defining collimators and are bent from the accepted $\sim 5^\circ$ average scattering angle to 12.5° by a custom-built septum magnet. The septum magnets transport the scattered flux into the left-right symmetric high resolution spectrometers (HRSs) comprised of superconducting quadrupole (Q) and indexed dipole (D_n) magnets, which have been operational since May 1997. The target chamber, collimation, septum, and HRS acceptance are shown in Fig. 2.15. The desired four-momentum transfer (Q^2) kinematically-selected scattered flux is accepted by the Q_1 collimator and continues into the HRSs, which are QQD $_n$ Q focusing spectrometers with 2×10^{-4} momentum resolution, $< 2 \text{ mrad}$ horizontal angular resolution, and 4 GeV/c maximum central momentum [30]. For CREX, the HRSs’ magnetic optics are specially calibrated and tuned to transport the elastic peak, separated from inelastic excitations, onto a small focused area in the detector package. Counting mode



Figure 2.16: 15 K gaseous helium cooled “production” target ladder, viewed from downstream. The calcium targets are on the far left in the 1 *cm* diameter top-hat shaped insert plugs. Reproduced from [26].

and integrating mode DAQs record the beam position, intensity, and flux in the detectors in the hut for low-current counting mode optics kinematic calibration measurements and high current integrating mode asymmetry measurements respectively.

2.4 Target Ladder

The target system, described in detail in a forthcoming paper ([27]), is newly designed to be shared between the PREX II and CREX experiments, with the ^{208}Pb and ^{48}Ca targets at different positions along the movable production target ladder, so that the target apparatus and average accepted angle of 5° is the same between both experiments. Due to the need for effective cooling of the large number (12) of lead targets in PREX II receiving $85\mu\text{A}$ of beam and of the calcium targets in CREX receiving $150\mu\text{A}$, the production target ladder is



Figure 2.17: Water cooled “optics” target ladder, viewed from upstream. Reproduced from [26].

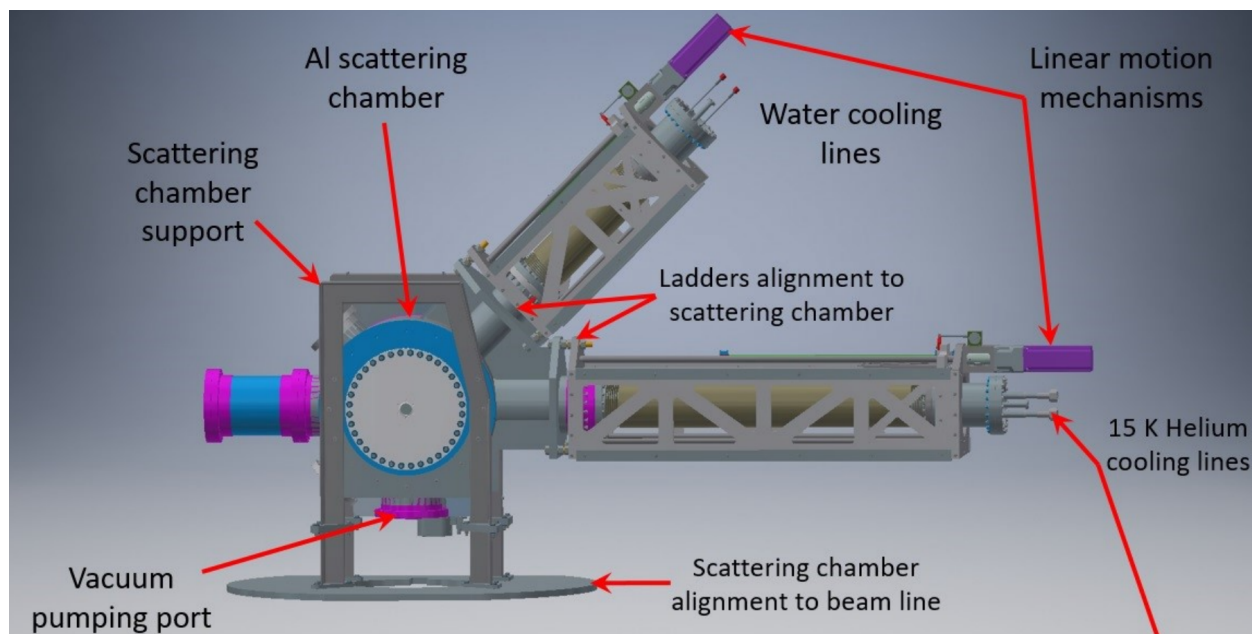


Figure 2.18: Annotated CAD view of the PREX II and CREX target system. Reproduced from [27].

cryogenically cooled, made of Copper, and is separate from the water cooled, low current, optics calibration target ladder. The production and optics target ladders, shown in Figs. 2.16 and 2.17 respectively, are contained within an aluminum target chamber, 60.96cm in diameter, with its z axis 33cm long along the beam axis, with a 9.4cm neck downstream. The two ladders are placed at the same z position, with the production ladder mounted horizontally and the optics ladder at 45° to the horizontal, as shown in Fig. 2.18.

The “cold” production ladder is kept cold by 15 K and 13 atm gaseous helium coolant from the End Station Refrigerator (ESR), controlled remotely by an adjustable Joule-Thomson (JT) valve, while the “warm” optics ladder is cooled by water flowing in a closed loop at 1 GPM or 63.1 g/s which also serves as the material of the water-cell calibration target [26]. The cryogenic coolant flows at 10 g/s, which with the beam at $150\mu A$ on ^{48}Ca accounts for approximately 300 Watts of target heating. Calcium melts at 1115 K, and thermal analysis simulations were performed, determining that under ideal thermal contact with the Copper frame, the target would reach 203 K, while with $200\mu m$ of $\sim 5W/mK$ thermally insulating CaO oxidation layer interfacing with the frame it would only reach ~ 300 K, well below the melting point [27]. Due to an incident on the 18th of January 2020 involving the miss-steering of the electron beam onto the Copper frame at full current, the first ^{48}Ca target was melted, shown in Fig. 2.19, as the heat generated in the Copper frame was dumped into the ^{48}Ca target puck, whose melting point of 1115 K is below that of Copper at 1358 K. This incident led to replacing the ^{48}Ca target and swapping the positions of the ^{48}Ca and ^{40}Ca targets on the ladder.

The targets are removable, to allow servicing the ^{48}Ca target and allow inserting it after PREX II completed running. The copper frame serves as the heat sink for the production target and has the cryogenic helium fed through cooling lines attached to it with 0.25" metal fittings [27]. The calcium target cylindrical pucks are installed within the copper

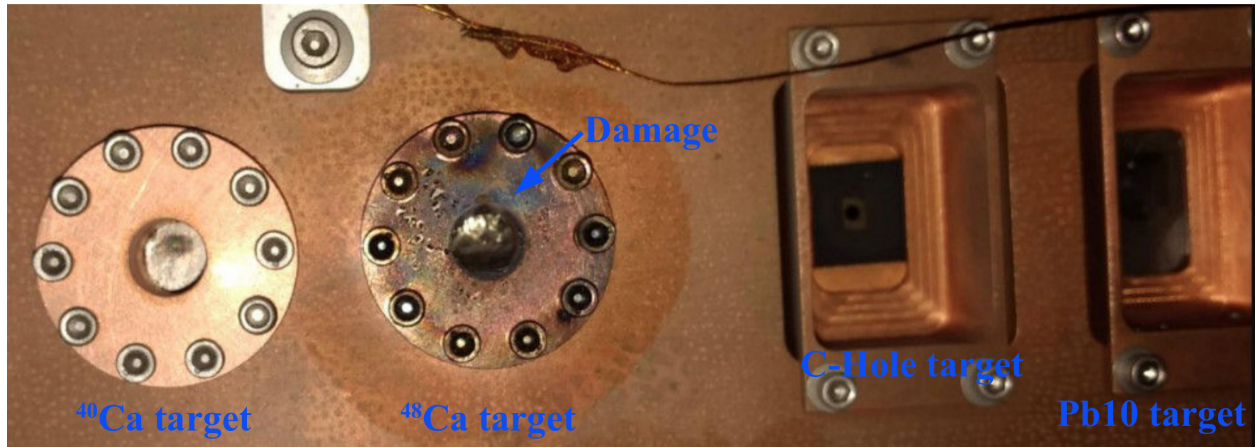


Figure 2.19: The ^{40}Ca (left) and damaged original ^{48}Ca target (middle). A miss-steering event on January 18th 2020 caused the beam to strike the copper frame and dissipate the generated heat by melting the ^{48}Ca target. Reproduced from [28].

ladder heat sink using top-hat style flanges 1cm in diameter. Screws attach the flange to the copper ladder with a strong torque to ensure thermal contact. The second ^{48}Ca target is composed of three smaller pucks, which are contacted together with silver paste (*SPI Silver Paste Plus*), which is also applied on the contact with the flange, to increase the thermal conductivity to the heat sink. Additionally, the second ^{48}Ca target's configuration includes a protective collimator ring made of 90% tungsten, 6% nickel and 4% copper [28] upstream on the flange's face, designed to prevent a second beam miss-steering incident from depositing power as quickly and simultaneously generate sufficient radiation load to the nearby ion chambers to immediately trigger an accelerator fast shutdown (FSD).

Because calcium easily oxidizes, the vacuum is carefully monitored, with alarms raised when it reaches above 10^{-5} atm, and the vacuum gate valves upstream and downstream of the target chamber will close and a nitrogen purge system will kick in to protect the Ca target in the case of a beam line vacuum break. The two independent target ladder linear motion systems are identical systems which use brushed DC servo (BDS) motors with encoder readbacks and an independent pull-string potentiometer for monitoring their positions.

Table 2.2: “Warm” optics target ladder positions and thicknesses. Reproduced from [27].

Target Position	Material	Thickness (mg/cm^2)
1	Pb-natural	61.2 ± 0.5
2	W	17.5 ± 0.2
3	C-graphite	83.3 ± 0.3
4	C-Hole	N/A
5	H ₂ O	1080 ± 20

Table 2.3: “Cold” production target ladder positions and thicknesses. Index 1 indicates the initial configuration and thicknesses before the ^{48}Ca target melting incident, and 2 indicates the configurations afterwards. Reproduced from [27], where the precise carbon-lead-carbon sandwich targets’ descriptions may also be found.

Target Position	Material	Thickness (mg/cm^2)
1, 2	C - Pb-natural - C	$\sim 90 - \sim 600 - \sim 90$
3, 5-13	C - ^{208}Pb - C	$\sim 90 - \sim 600 - \sim 90$
4	C-graphite	445 ± 1
14	C-Hole	N/A
15 ₁	$^{48}\text{Ca}_1$	1016 ± 2
16 ₁	^{40}Ca	1004 ± 2
15 ₂	^{40}Ca	1004 ± 2
16 ₂	$^{48}\text{Ca}_2$	991.5 ± 1.7

The motion systems are housed outside of the vacuum vessel so they can be serviced without breaking vacuum when problems arise. All of the target motion controls, vacuum pressure, and temperatures are controlled and monitored by an input-output controller (IOC) computer in the Hall A access labyrinth, which is remotely controlled by the target operator (TO) in the Hall A counting house.

The lists of production and optics targets are given in Tables 2.2 and 2.3, where the initial ^{48}Ca target, involved in the melting incident, is indexed “1” and the second ^{48}Ca target, on which the bulk of the data was taken, is indexed “2”. The original ^{48}Ca target is a 6% radiation length, 5.72 mm thick and 1.2938 g mass puck with an isotopic enrichment of 95.99% ^{48}Ca , 3.84% ^{40}Ca , and negligible contribution of other impurities. The original

Table 2.4: Second ^{48}Ca target’s three puck components’ thicknesses and isotopic purities. Reproduced from [27].

Nominal Thickness (<i>mm</i>)	Mass (<i>g</i>)	Thickness (<i>mg/cm</i> ²)	Isotopic Enrichment
0.511	0.1067	83.9 ± 0.8	$95.99 \pm 0.02\%$
1.118	0.2461	192.7 ± 0.8	$95.99 \pm 0.02\%$
4.094	0.9116	714.9 ± 1.3	$90.04 \pm 0.13\%$

target was replaced with a sandwich of three thin pucks, whose isotopic purities are listed in Table 2.4 with the primary impurity coming from ^{40}Ca for them as well. The two thin pucks in the second ^{48}Ca target are from the same batch as the first target. The isotopic purity of the ^{40}Ca target is 99.965% [27].

The ^{48}Ca target is the primary target used for production data collection, as well as optics kinematics calibrations at low current. The ^{40}Ca target is used for some commissioning tests, the various lead targets are used in the PREX II experiment, the carbon hole target is used for target ladder positioning and raster checks, and there is a 1% radiation length graphite carbon target which is used for some high current tests due to its high thermal conductivity. The calcium, lead, and carbon targets on the production ladder are also used in dedicated transverse asymmetry measurements. The optics ladder contains thin lead, tungsten, and graphite carbon targets for optics calibrations, as well as a carbon-hole target for ladder positioning and raster size checks, and a water cell target for energy and angle calibrations for the HRSs.

2.4.1 Beam Rastering

Due to the relatively low melting point of the lead targets used in the PREX II and transverse asymmetry measurements, as well as the desire to operate as safely as possible with the calcium targets, it is necessary to mitigate the local heating effects in the target

that are caused by the small $\sim 150 \times 150 \mu m^2$ beam spot. The density of solid lead varies substantially with temperature, by about 0.9% over a temperature difference of 100 K, and therefore localized heating in lead targets causes localized density fluctuations, which contribute noise into the measured asymmetries [26]. To mitigate localized target heating we utilize a fast magnetic raster system to spread the beam across the face of the target, and we also chose to synchronize the rastered frequencies such that each integrated helicity window spans the same spread out pattern.

The Hall A raster magnets' operating frequencies are approximately 25kHz, which was designed and optimized for the original constraint of keeping recirculating liquid targets in Hall A and C from experiencing local beam heating temperature increases above $1^\circ C$ [53]. The raster strafes the beam across the face of the target separately in the X and Y planes, crossing from one side to the other in $20 \mu s$ and with a turning time at the vertex of the pattern of $200 ns$ [53]. We operate the raster at $2 mm \times 2 mm$ for ^{48}Ca at $150 \mu A$ production, using low current runs (called Spot++ runs) on the carbon hole target's circular hole to set the distance scale factor for the raster magnets' current amplitudes. The raster currents needed to achieve the $2 \times 2 mm^2$ raster pattern on the target changed throughout the run due to changes in the tune of the quadrupole magnets along the beamline between the raster magnets and the target. These quadrupole magnets also slightly twisted the square raster pattern into a parallelogram shape due to their focusing effects.

Optimizing the raster magnets' frequencies is an important way to improve the production data quality. During PREX I, initially no special care was taken to synchronize the raster frequencies to the helicity flip rate, and so the temperature-dependent density fluctuations of the lead targets generated residual correlations, shown in Fig. 2.20a, between the asymmetries measured in the independent detectors in the left and right HRSs, even after correcting for position, energy, and current fluctuations in the standard ways [20]. The

raster frequencies were adjusted to integer multiples of the 120 Hz helicity flip frequency, with 120 Hz difference between the two, that is

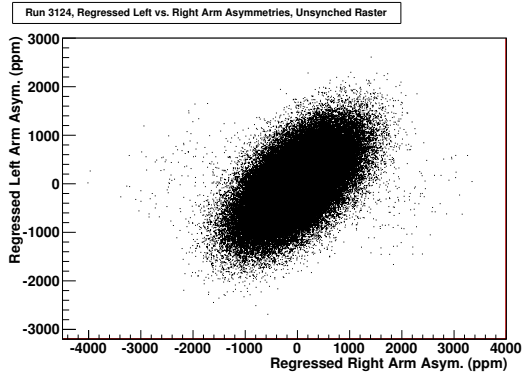
$$f_A = A * f_{hel}, f_B = B * f_{hel}, \quad (2.3)$$

where

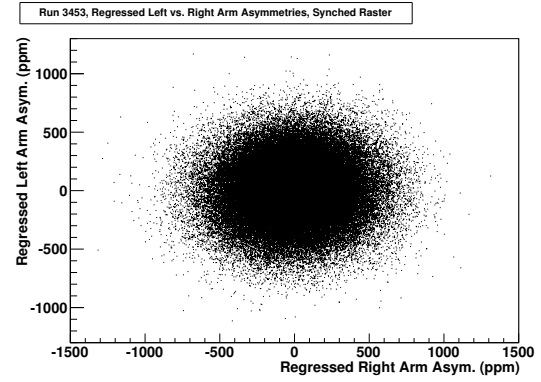
$$C = A - B, \quad (2.4)$$

with C chosen to be $= 1$, and the residual correlations disappeared, as shown in Fig. 2.20b, due to the integration time window $T_{integration} = 1/f_{hel}$ spanning a full trace of the raster's pattern equally in all events included in the asymmetry multiplet. Additionally, by increasing the difference in frequency between the two directions of the raster the pattern spreads out across the face of the target more rapidly and leading to less concentrated heat load, as shown in a simulation of the pattern traced over equal amounts of time with $1 \times f_{hel} = 120$ Hz difference and $8 \times f_{hel} = 960$ Hz difference, such that $C = 8$, shown in Fig. 2.21. This is confirmed with computational fluid dynamics (CFD) simulations which show the reduction in peak and average temperature in the lead targets when using larger differences in frequency for the two raster magnets, shown in Fig. 2.22.

A further realization was made during PREX II commissioning that using multiples of the helicity flip frequency as the difference between the two directions' frequencies where the frequency difference factors into both of the individual frequencies (where C factors both A and B) causes a shorter duration pattern to be repeated multiple times (C times) within the integration window. This can be changed by using raster frequencies that are still multiples of the helicity frequency, but which are not integer multiples of the difference between the two, such that C no longer factors both A and B . The effect of using frequencies which do not have the frequency difference as a factor of each frequency is that the pattern repeats



(a) Unsynchronized raster configuration.



(b) Synchronized raster configuration.

Figure 2.20: PREX I data, showing the left- and right-arm regression-corrected asymmetry distributions. Reproduced from [20]. With the unsynchronized raster there is still some residual correlation between the two detectors' measurements, even after correcting for beam position and energy correlations using linear regression, which go away in the synchronized case.

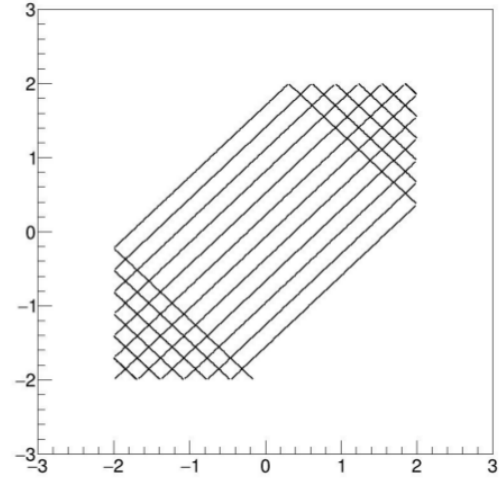
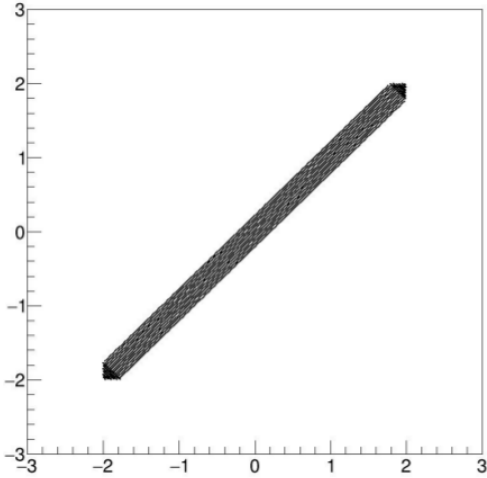


Figure 2.21: Target face area covered by the raster within the same amount of time for a frequency difference of 120 Hz (left) and 960 Hz (right). Reproduced from [26].

after a longer time and more uniformly covers the face of the target, as shown in Fig. 2.23.

The potential improvement in heat spread across the face of the target motivated the use of raster frequencies of $A = 213$ and $B = 205$ times, such that C is large $= 8$ and does not divide A or B , with $f_{hel} = 119.99976$ Hz and the two frequencies $= 25.55994888$ kHz and 24.5999508 kHz respectively for both PREX II and CREX. This choice is responsible for the negligible residual correlation between left and right HRS detectors' asymmetries up until each lead target fully degraded during PREX II and permanent density changes non-uniformly distorted the targets' shape. Dedicated studies investigating the calcium target's stability under changes to the raster, beam current, and raster frequency setup were performed during CREX, using the nearly-pristine ^{40}Ca target with a large $\sim 300 \times 300 \text{ mm}^2$ beam spot size at the end of the experiment out of an abundance of caution. In these studies no clear dependence on current, raster size, or raster frequency was noticeable with standard 5 minute long amounts of data and asymmetry corrections analysis applied.

The raster frequencies are controlled by two independent Agilent frequency generator channels which are synchronized to the helicity frequency by hand. The exact raster magnet frequencies are determined based on the discussion above and tuning them until there is no visible relative phase drift with respect to the 120 Hz f_{hel} "MPS" helicity signal on an oscilloscope. The raster frequency control schematic is shown in Fig. 2.24 [20]. The helicity control board in the injector is capable of running in either free clock mode or in beam synchronized (beam sync) mode. Free clock mode means the individual integration window durations are all identical and their rate, f_{hel} is determined by the clock of the helicity control board, which is in turn determined by the duration of the T_{settle} plus T_{stable} times chosen for the experiment, as shown in Fig. 2.7.

Beam sync mode also sets the individual integration window durations to be identical and determined by the desired rate, but in order to synchronize the helicity flip rate in

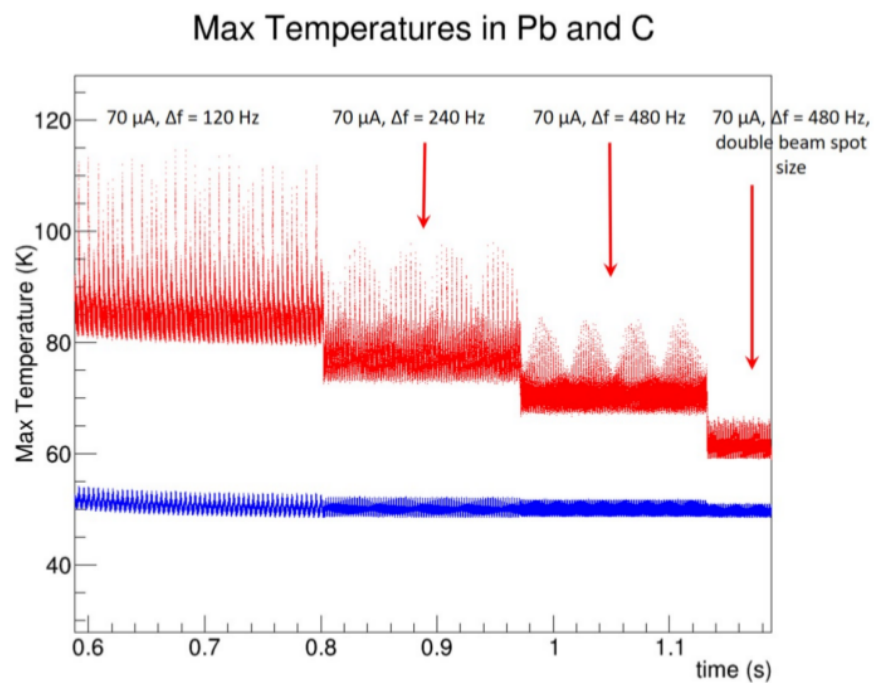
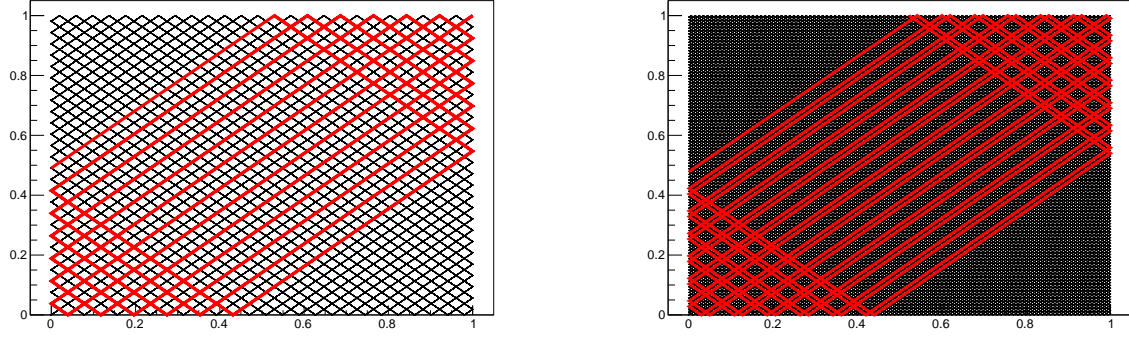


Figure 2.22: CFD simulation results showing the time dependence of the maximum temperature (red) and average temperature (blue) within the PREX II lead targets under various raster frequency and beam spot size conditions. Reproduced from [26].

the polarized source to the 60 Hz power line frequency that drives all equipment along the beamline, beam sync mode triggers each new multiplet (Quartets for CREX) only when the 60 Hz line frequency phase signal called “beam sync” arrives after the end of the previous multiplet. The effect of beam sync mode relying on the power line’s 60 Hz signal to trigger new helicity multiplets is the final T_{stable} time of each multiplet will be a different length depending on the random jitter intrinsic to the timing of the power line’s 60 Hz signal and so the T_{stable} time must be shortened to allow for the most early arriving jittered new beam sync pulse signal, which reduces the ideal integration time by $\sim 45\mu s$ to account for instability in the 60 Hz power line phase. Therefore, because of the need to exactly lock the frequencies of the raster to that of the polarized electron source helicity flip rate and the difficulty of performing the frequency set up procedure described above with the 60 Hz beam sync’s timing jitter, it was decided to set up the polarized source and the raster frequencies relative to each other as precisely as possible with the helicity control board set to free clock mode, choosing the free clock mode helicity-flip rate to match the timing of 60 Hz beam sync as closely as possible.

2.5 Pivot Area

The PREX I experiment was cut short due to radiation problems affecting the experimental controls and vacuum systems: radiation-damage induced failure of a soft O-ring in the connection of the vacuum scattering chamber to the exit beam pipe caused the experiment to end before reaching its statistical goals, and frequent down times due to unshielded radiation disrupting the hall’s electronic control systems caused frequent interruptions to experiment running. As a result, PREX II and CREX have implemented redesigned collimation, cooling and radiation shielding in the pivot area surrounding and downstream of the target, shown



(a) Raster frequencies of 204 and 212 multiples of the helicity flip frequency. (b) Raster frequencies of 205 and 213 multiples of the helicity flip frequency.

Figure 2.23: Simulated raster pattern showing the improvement in target face coverage by going from raster frequencies which are divisible (a) by the difference between them to frequencies which are not (b). In red is a fraction of the pattern to display the trajectories, and in black is one full helicity flip period's pattern to display the change in target face coverage.

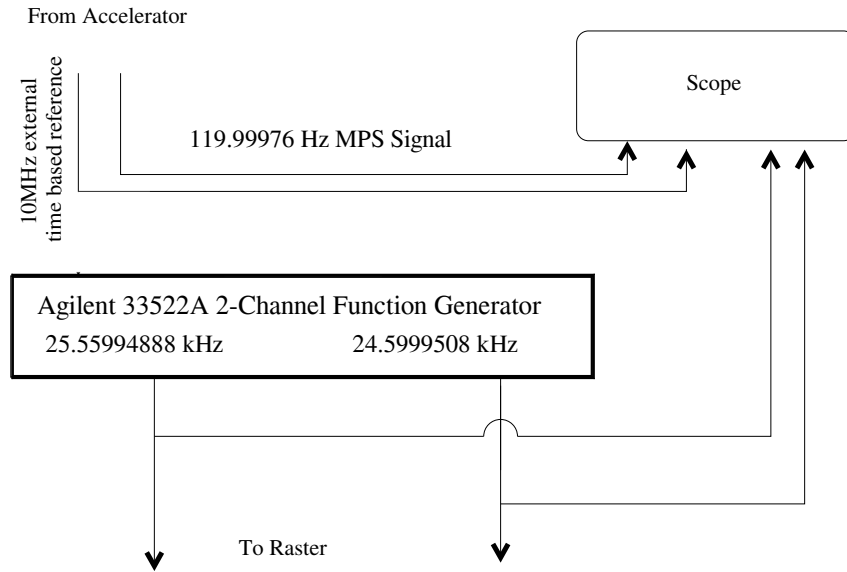


Figure 2.24: Schematic of the raster frequency controls. The 10 MHz signal is used in the injector to give a consistent clock while the measured MPS signal sent from the injector to Hall A over fiber optic cables marks the beginning of new helicity windows and is used to tune the raster frequencies in two independent channels of the Agilent 33522A function generator. Updated and adapted from [19, 24].

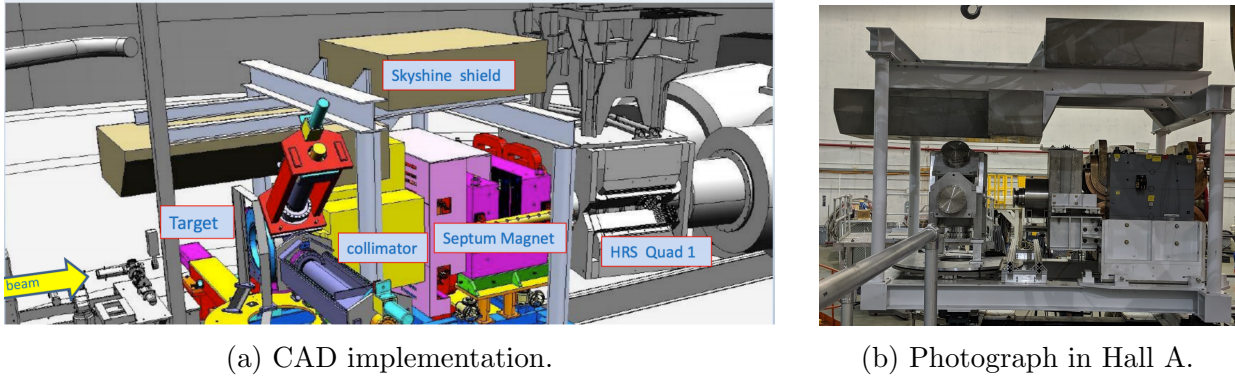


Figure 2.25: CAD snapshot and picture, both taken by Ciprian Gal, of the PREX II and CREX collimation, shielding, and septum magnet systems, along with the target and beam-line components.

in Fig. 2.25.

Both PREX II and CREX share the target system, described above, and they also share the same collimation and magnetic spectrometer system, adding constraints to their design and optimization. Due to the 12.5° minimum angle limitation imposed by the construction of the HRSs, PREX II and CREX utilize a pair of septum dipole magnets to pull the $\sim 5^\circ$ scattered electrons into their 12.5° acceptance defined by custom-built acceptance-defining collimators placed in the Q_1 magnet's openings. The pivot area is also redesigned with all-metal vacuum controls, and special shielding is designed to mitigate neutron damage to the hall's control electronics, as well as to maintain JLab site boundary dose below administrative limits.

2.5.1 Collimation

The central beamline collimator is designed to intercept the low-angle scattered beam that would otherwise interact with material along the beamline without reaching the dump. The electrons stopped by the collimator generate a large amount of photonuclear reaction 0.1-

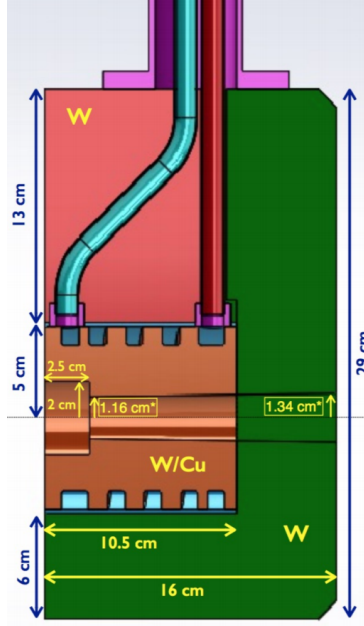


Figure 2.26: CAD cross-section of the central beamline collimator, showing the spiraling water cooling channel and recirculation system.

10 MeV neutrons, whose elastic scattering with nuclei damage the hall's control electronics. Shielding is designed to slow the neutrons until they are thermalized, where they do less damage to electronics, requiring $\sim 20\text{cm}$ of hydrogen rich high-density polyethylene (HDPE) [54]. The central beamline collimator is made of a 30% copper and 70% tungsten alloy and is cooled by a water chiller pumping 1 Gpm, with the water travelling in a spiraling groove around the cylinder, shown in Fig. 2.26. The collimator absorbs $\sim 3000\text{ W}$ and its temperature is carefully monitored to verify its successful cooling and the stability of electron scattering conditions in the target. The front of this collimator is located $\sim 85\text{cm}$ downstream of the target and absorbs all low-angle, 0.78° to 3.0° , scattered electrons which would otherwise interact with beamline components further downstream [54].

Custom-built acceptance-defining collimators are used to define the accepted kinematics of scattered electrons, placed in the entrances to the HRSs in the Q_1 magnet openings.



Figure 2.27: Photograph taken during installation of the Q_1 magnet entrances, with the acceptance-defining collimators, painted blue, installed. Reproduced from [28].

The acceptance definition provided by these collimators is crucial to optimizing the figure of merit and providing the most sensitive extraction of the neutron skin thickness. Therefore the choice of the collimators' acceptance cut must be tuned to satisfy several simultaneous constraints. The acceptance-defining collimators in the two HRS arms must: simultaneously optimize the PREX II and CREX sensitivities to R_n while considering the proposed systematic uncertainties and statistical dilution from detector resolution limitations, $\sigma_{det} \simeq 1.06$ (discussed in section 2.7.3); maintain symmetry between the left and right HRSs to maximize HC A_{beam} cancellations between arms; maintain symmetry in the vertical plane to minimize HC A_{beam} due to beam-position dependent changes in acceptance; maintain hard cuts on minimum and maximum polar angle θ , while simultaneously optimizing those angles to be most sensitive for R_n extractions for PREX II and CREX; minimize the rate far from the central ray with low θ chamfer cuts, both to avoid interception with downstream HRS components and to optimize the transport through the HRS optics; and insensitivity to one mm scale machining and alignment tolerances.

The acceptance-defining collimators, shown in Fig. 2.27, are designed using Monte Carlo GEANT4 simulations of the detector, acceptance, and HRS magnetic optics, which use theoretical model predictions of asymmetry, weak form factor (F_W) and neutron radius (R_n) versus kinematic variables to estimate the sensitivity (S), where S is defined as the model predicted fractional change of asymmetry (A) for a 1% change in R_n and is dimensionless. The relationship between A , R_n , and S comes from the model predicted F_W that describes the neutron distribution in ^{48}Ca . The distributions of S and A are predicted within the Monte Carlo, and averaging over the entire acceptance is used to optimize the chamfer cuts and θ bite cuts for the acceptance-defining collimators to maximize sensitivity [1, 2]. Because the measured asymmetry depends on kinematic parameters such as the momentum transfer Q^2 , maximizing the measurement sensitivity is done by sampling the A and F_W distributions across kinematic ranges such that the average scattering-rate weighted asymmetry is maximally sensitive to the shape of F_W and therefore comparisons between experimentally measured kinematic and asymmetry distributions and model predictions maximally pin down the theoretical model's predictions, minimizing the uncertainty on extracted R_n . Simultaneously optimizing $\frac{\delta R_n}{R_n}$ for both PREX II and CREX results in a goal of average central accepted angles of 5.13° and 4.985° respectively [55, 56]. This procedure was done using a GEANT4 Monte Carlo package utilizing differential cross section, asymmetry, and sensitivity in [57]. The CREX kinematics optimization differs from that of ^{208}Pb . CREX achieves a lower average angle for accepted elastically-scattered electrons than PREX II by setting the septum magnetic field to be 5% higher than the level needed to match the PREX II kinematics.

Additionally, an insertable sieve collimator with a distinct pattern of holes is used during low-current data collection to provide calibration data for magnetic transport reconstruction [20]. Comparing predicted trajectories to the measured sieve hole positions constrains the

magnetic transport reconstruction and verifies our understanding of their trajectories. Estimation of residual inaccuracies in track reconstruction is used to bound the certainty of our kinematic acceptance function, used in model comparisons with the measured asymmetry, discussed further in chapter 4.

2.5.2 Shielding

As mentioned before, PREX I was statistics starved due to radiation-induced control electronics failures and soft O-ring vacuum problems, which motivates the improvement of radiation control in the hall by a factor of at least 10 for PREX II and CREX, in addition to needing to maintain control of the radiation dose at the JLab site boundary for administrative limits and public health concerns [54]. Radiation load is high due to the elastic cross section, where the Z^2 dependence is a strong factor relative to other lower Z experiments typically performed in Hall A. To mitigate radiation damage we design and add shielding to the entrance to the Hall A dump to mitigate splash-back, to the sides of the HRS electronic controls, to the controls near the beamline upstream of the target, and around and above the target and collimator.

We also redesign the small angle monitors' (SAMs) size and vacuum insert tubes to minimize radiation load to the HRSs and change the target area vacuum system to use more radiation hard metal in all connections. To slow the large number of neutrons generated in the collimator we place concrete and $\sim 20cm$ of high-density polyethylene (HDPE). The geometry of the various shielding pieces are determined by Monte Carlo simulations done in GEANT4 and FLUKA, optimizing to sufficiently minimize radiation to the hall electronics and sky-shine to the JLab site boundary while also minimizing expense and weight. The target area shielding is shown in CAD in Fig. 2.25a and as built in the hall in Fig. 2.25b.

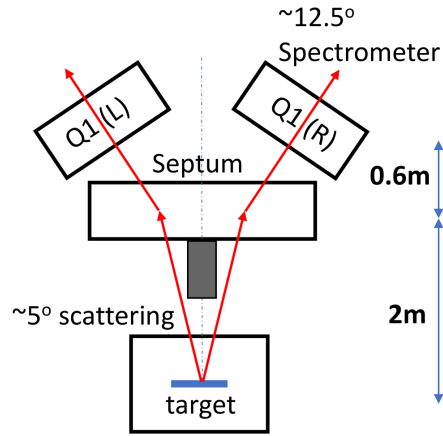


Figure 2.28: Schematic diagram of the septum magnet bending $\sim 5^\circ$ scattered electrons into the acceptance-defining collimators at the HRSs minimum 12.5° angle. Reproduced from [29].

This radiation shielding was successful in both PREX II and CREX, as the control electronics in the hall performed sufficiently well to avoid substantial down times and the site boundary radiation dose was kept well below the annual administrative limits.

2.5.3 Septum Magnet

To achieve the small $\sim 5^\circ$ central angle scattering we use a set of identical, independently powered, septum dipole magnets. The septum magnets are made of three regular conducting dipole coils and are placed between the central beamline collimator and the Q_1 magnets of the HRSs. A schematic is shown in Fig. 2.28. The HRSs are constrained to a minimum angle with respect to the beam axis of 12.5° by their physical size, and so these magnets on the left and right side of the beam generate dipole fields pointing up and down, respectively, to bend the low-angle electrons into the HRSs acceptance. The septum magnets are normally conducting to avoid problems with superconducting magnets due to radiation near the beamline and downstream of the collimator. The septum magnets are driven by two independent power supplies set to 801.248 A, cycled first to 900 A whenever powered

on to mitigate hysteresis, and are cooled with a water chiller system pushing water through channels within the coils of each magnet.

2.6 High Resolution Spectrometers

CREX is designed to measure the parity-violating asymmetry from elastically scattered electrons off of the ^{48}Ca nucleus, which requires the ability to cleanly separate the electrons scattered elastically from those scattered inelastically or involving any other reaction products or processes and to measure their kinematics accurately for extracting the F_W physics observable information. Consequently we use the high resolution spectrometers (HRSs) in Hall A, which are two identical sets of superconducting magnets in a QQD_nQ orientation of $\cos(2\theta)$ quadrupoles and a gradient-indexed bending dipole [30]. The HRSs are designed to bend the scattered electrons upwards towards the ceiling of the hall, and are able to achieve a 12.4 m dispersion at the focus and a momentum resolution of $\frac{\delta p}{p} \sim 10^{-4}$, which is reduced to $\sim 10^{-3}$ by the custom tune of CREX. The left (right) HRS can span from 12.5° - 130° (12.5° - 150°) along the horizontal plane in the hall, moving on tracks on the floor, and are both set to their minimum of 12.5° for CREX. Both HRSs are designed to accept ± 30 mrad horizontally with 0.5 mrad resolution, and ± 60 mrad vertically with 1.0 mrad resolution [30]. A schematic of the HRS magnet design is shown in Fig. 2.29 and a drawing of the HRS along with the rest of Hall A is shown in Fig. 2.30.

By utilizing a vertical bend in the spectrometer we decouple first-order effects from target length. The first quadrupole, Q_1 , serves to focus the scattered flux in the vertical plane, which is associated with the dispersive (recoil electron's energy) direction, and the 6.6 m long gradient indexed ($n = -1.25$) dipole provides additional focusing and bends the scattered flux by 45° to the detector package at the top of the HRS [20]. This designed

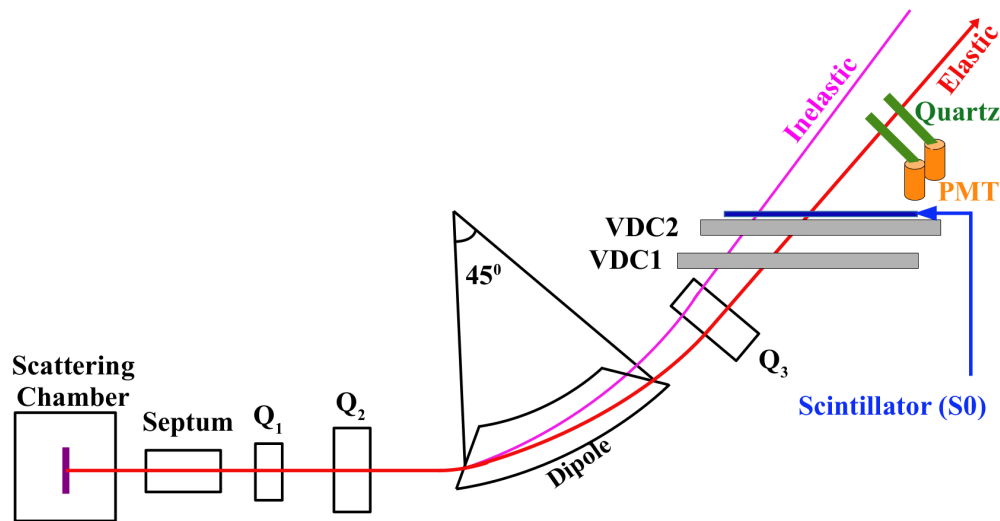


Figure 2.29: Cartoon of the layout of the HRS magnetic transport and momentum spectrometry in Hall A, also showing the detector systems used for optics and asymmetry measurements. Reproduced from [28].

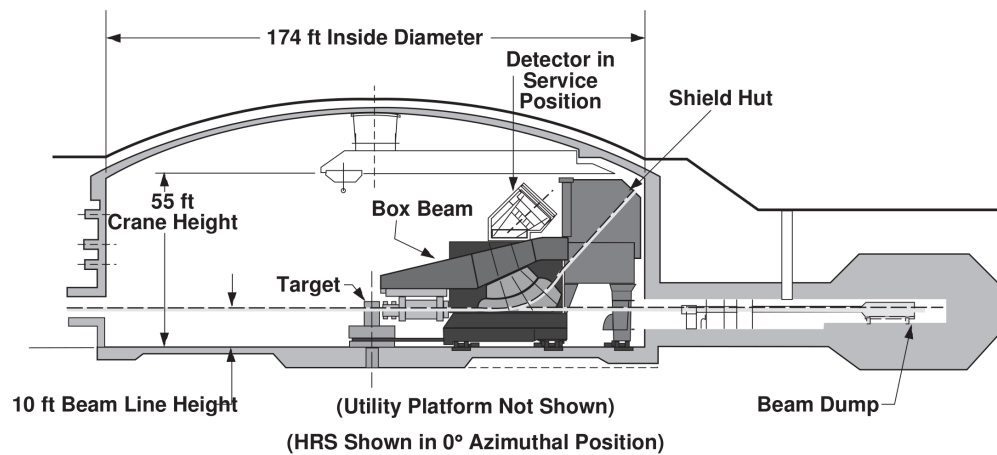


Figure 2.30: Drawing of the HRS along with the rest of Hall A and the beam dump, to scale. Reproduced from [30].

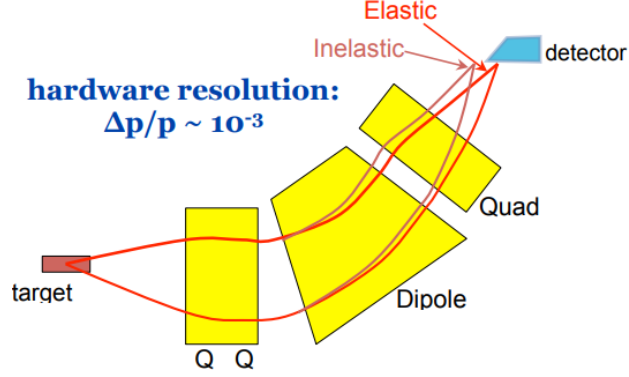


Figure 2.31: Cartoon of the HRS optics system, from Kent Paschke, showing the focusing feature of the QQD_nQ HRS magnet setup and the separation of inelastic states from the primary detector.

bending angle is the result of a compromise between high energy resolution and capital costs. The quadrupoles immediately before and after the dipole, Q_2 and Q_3 have identical field maps and provide focusing in the transverse scattering plane, which is used to decouple angle and position sensitivities.

Because the nuclear mass energy of ^{48}Ca is much higher than the incoming 2.18 GeV beam energy, the elastically scattered electrons lose a negligible amount of momentum to the nuclear recoil and are therefore scattered with outgoing energy very close to the beam energy and with decoupling between scattered angle and energy. As a result of these decouplings, it is possible to simultaneously focus the scattered flux at the detector plane in both position and energy so that the elastic scattered flux is separated spatially from inelastic states. The magnetic fields are tuned based on Monte Carlo simulation of the optics and measurements of the scattered flux in the tracking detectors at the top of the HRSs; a result of that optimization, the HRSs focus the elastically scattered electrons into the primary integrating detector while resolving the energy and spatially separating the inelastic states at lower energy outside of the detector, as shown in the cartoon in Fig. 2.31.

The superconducting magnets are cooled with a combination of liquid N_2 and Helium

from the ESR, and their magnetic fields are measured and maintained with dedicated control systems in the hall. The quadrupoles are monitored with Hall probes and the dipole fields are measured with Hall and NMR probes. The left HRS dipole’s NMR probe failed during CREX, so the field control lock system does not function and we control its field by watching the Hall probe value and monitoring the electric current powering the magnet. Because the Hall probe is not stable over time, we rely on regular optics calibration runs to keep track of the location of the focused elastically-scattered peak in the detectors to be sure of the stability of the system. These detector alignment calibration runs are performed using an additional set of “downstream” detectors in the detector package to save time, which supplement the dedicated high statistics runs with the primary “upstream” detectors that are used for extracting the kinematic Q^2 distributions [28].

2.7 Detector Package

Charged particle detector systems are housed within shielding huts at the top of both HRSs, including a custom installed gas electron multiplier (GEM) tracking and integrating detector system and the standard HRS vertical drift chamber (VDC) and counting mode triggering package [30]. To protect from ionizing and radio-frequency radiation backgrounds, the detector systems are housed within a shielding hut along with their data acquisition systems and high voltage controls. The shielding hut, shown in Fig. 2.30, is made of a 10cm thick steel frame, 5cm of lead shielding, and 40cm to 100cm of concrete shielding, which keeps the radiation load inside at manageable levels. The detector stack can be wheeled out of the shielding hut for installation and maintenance. A CAD drawing of the movable support structure and all of the detector systems within the HRS is shown in Fig. 2.32.

The VDCs and GEMs for electron tracking function in counting mode only and use

scintillator detectors for triggering on individual particles. Integrating “main” detectors are placed with the upstream detector 1.3m downstream (above) the first VDC plane. Additionally the detector package contains “ A_T ” background detectors identical in design to the main detectors, and both the main and A_T detectors may be used in counting mode or integrating mode by changing the cables connected to the two separate DAQs. The main detectors placement in the detector package is finely controlled remotely with a stepper motor motion control systems, giving X (dispersive), Y (transverse), and θ_X degrees of freedom for commissioning the detectors and optimizing their collection of the focused electron flux.

2.7.1 Vertical Drift Chambers (VDCs)

The VDC systems in the identical HRSs are each composed of two identical VDC detector planes, used for electron track reconstruction in counting mode data collection. The VDC’s track information is used for optics calibration studies, elastic peak alignment checks, and for extracting the kinematics of the particles at the target and the Q^2 measurement used in the acceptance function extraction [30]. The VDC chambers are $2118mm \times 288mm$ in active area, composed of one U and one V planes of sense wires at 45° to each other and aligned along the Hall A horizontal axis, which is 45° with respect to the scattered flux trajectories, as shown in Fig. 2.33. The lower of the two VDCs is placed so that its lower wire plane is as close to the design HRS focal plane as possible, the U and V planes are 26mm apart vertically, and the upper VDC chamber is 335mm above the first. The upper VDC is also offset in the dispersive direction so that the central ray from the HRS passes through the middle of both chambers. Each VDC plane has 368 $20\mu m$ diameter sense wires with 4.24mm spacing.

Charged particles traversing the VDC gas will ionize molecules as they pass, and those

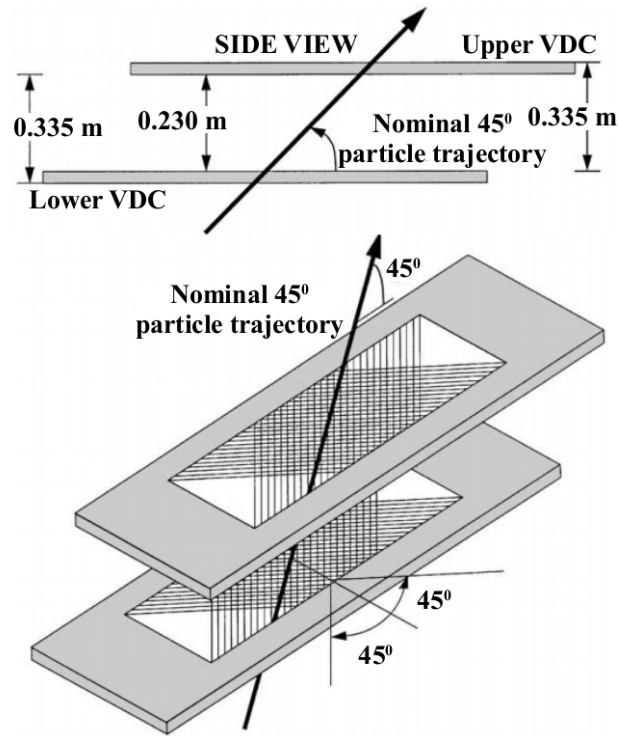


Figure 2.33: Schematic views of the Hall A HRSS' VDC chambers (not to scale). Reproduced from [28] and [30].

ions will be pulled towards the sense wires and pushed away from the cathode surfaces that are kept at a negative high voltage. As the ions are pushed away from the cathode and towards the wires, they encounter the $1/r$ electric potential around the wires and are drawn in faster, generating an ionization cascade, and the positive ions are pushed away from the wire. This induces a negative signal in the wire which is read by the DAQ and used in the spatial and timing analysis of tracks [24]. For CREX, the VDC chambers are filled with a 50/50 mixture of argon and ethane and the potential is set to -3500 V [28]. The scattering rate is limited due to high voltage of the cathode planes and the possibility of sparking if the gas medium is too ionized, with a maximum safe electron flux of 2 kHz/mm^2 , and noticeable tracking efficiency loss above 0.1 kHz/mm^2 , which requires the use of low beam current and careful monitoring, limited in the other direction by the need to maintain beam current above $1 \mu A$ for beam position monitor reliability. Gas electron multiplier (GEM) detectors are also installed in the detector package for PREX II, but are not used for CREX due to the sufficient capabilities of the VDCs to measure the scattering from ^{48}Ca at low beam current.

2.7.2 Trigger Scintillators

CREX uses two scintillator paddles in each HRS to trigger the counting mode measurements, called S0 and S3. S0 is a $185\text{cm} \times 25\text{cm} \times 1\text{cm}$ organic plastic scintillator with a PMT on each of the long ends. S0 is installed directly above and parallel to the VDCs, with the long side in the dispersive direction [28]. S3 is a set of three plastic paddles, each $71\text{cm} \times 9\text{cm} \times 1\text{cm}$ with one PMT on one side for each, with 1cm of overlap between them along their lengths. S3 is installed downstream of (above) the detector package, and used to trigger in logical OR mode between the three PMT signals [28]. Electrons passing through the organic plastic paddles generate isotropic scintillation light, which propagates to the

PMT and generates a signal which is processed and read by the DAQ through carefully-tuned PMT high voltage and discriminator logic.

2.7.3 Integrating Cherenkov Detectors

CREX intends to use the weak interaction to measure the weak charge distribution of ^{48}Ca , probing the neutron distribution. Due to the small strength of the weak interaction we rely on its violation of parity symmetry to measure asymmetries, cancelling the leading electromagnetic interaction dependence and giving us sensitivity to the electromagnetic and weak interaction's interference, as described in section 4.1. Because of the expected small *ppm* level of the parity-violating asymmetry, to achieve a high counting statistics precision $\sigma_{A \text{ stat}} = \frac{1}{\sqrt{N}}$, where N is the number of detected electrons, it is necessary to measure as many electrons as possible. Our detectors that measure asymmetries at high scattering rates must therefore possess several features: support of GHz scale event rates, radiation hardness, high linearity and resolution, and insensitivity to low-energy backgrounds. While the GHz scale rate of PREX II drives the high rate limitation, CREX's ~ 28 MHz rate still requires attention to these features.

The solution to these needs is to integrate the high rate scattered flux using the detection of internally reflected Cherenkov (DIRC) radiation in fused silica (quartz) tiles generated by normally incident electrons and measured by high-linearity PMTs. High-purity Spectrosil 2000 fused-silica quartz is good for Cherenkov light generation and detection because its index of refraction is ~ 1.5 at the 300nm Cherenkov peak, with total internal reflection (TIR) at $\sim 43^\circ$ and a Cherenkov light cone opening angle at $\sim 46^\circ$, as shown in Fig. 2.34. This optimal index of refraction causes the Cherenkov light generated from normally incident charged particles to propagate to the 45° beveled cut where they escape to the

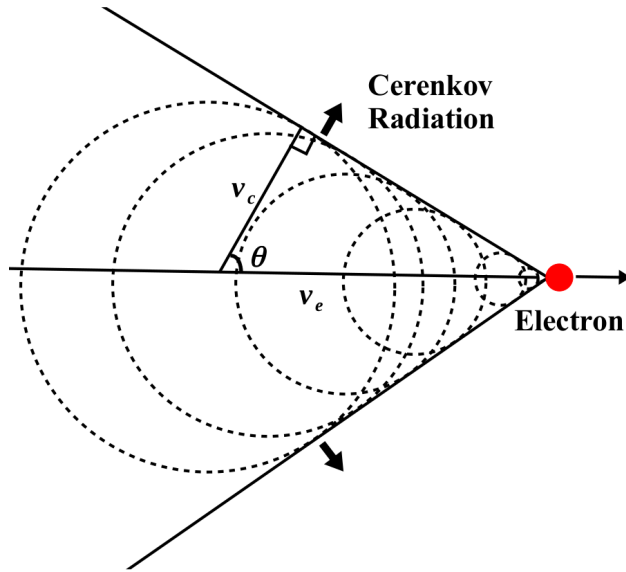


Figure 2.34: Schematic of the Cherenkov cone produced by relativistic charged particles ($\beta \sim 1$) in fused silica quartz, with a Cherenkov emission angle of 46.6° . Reproduced from [28].

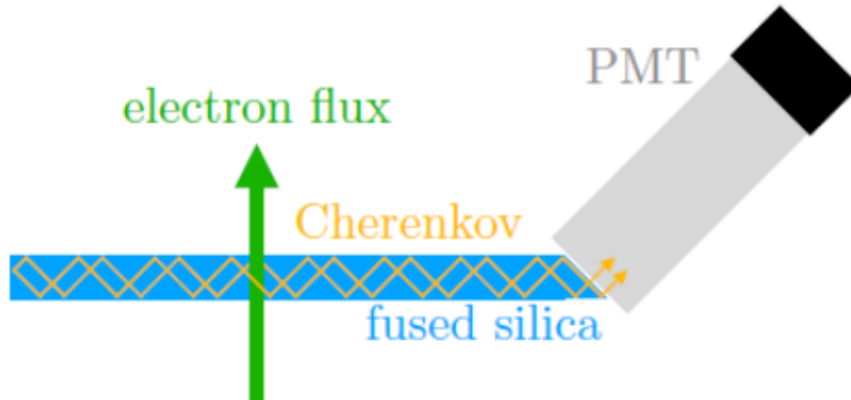


Figure 2.35: Cartoon, drawn by Tyler Kutz, of the detection of total internal reflected Cherenkov light (DIRC) in the CREX detector design.

PMT face, as shown in Fig. 2.35. Because Cherenkov light is only generated when a charged particle passes through the material at $v \geq c/n$, the kinetic energy required is $E \geq m_0 c^2 \frac{n}{\sqrt{n^2-1}}$. With an index of refraction of $n = 1.5$ the detectors are insensitive to non-relativistic particles whose β is below $\frac{1}{n} \simeq 0.66$ and $E_{\text{kinetic}} \leq 0.34 m_0 c^2$, which when coupled with the low-recoil elastic scattering and high resolving power of the HRSs provides a very clean measurement of elastically scattered electrons. A non-zero RMS spread of the distribution of photoelectrons (PEs) for each electron passing through the detector reduces the statistical precision $\sigma_{A \text{ stat}} = \frac{1}{\sqrt{N}}$ to

$$\sigma_{A \text{ measured}} = \frac{1}{\sqrt{N}} \times \sqrt{1 + \left(\frac{\sigma_{PE}}{\langle PE \rangle} \right)^2}, \quad (2.5)$$

where σ_{PE} is the single electron PE distribution's RMS and $\langle PE \rangle$ is the mean, which comes from propagating the uncertainty caused by the non-zero PE distribution RMS for one incident electron through the distribution predicted for a high rate of measured electrons. The RMS of the distribution of PEs can be parameterized as a Gaussian part from counting statistics, inversely proportional to the thickness of the quartz, and a Landau tail term coming from showering processes in the material, proportional to the thickness of the quartz. We optimize the PE resolution $\simeq \frac{\text{RMS}}{\text{Mean}}$ of the integrating detector by changing the quartz thickness, thicker to maximize Cherenkov rate but thinner to minimizing showering, using a dedicated optical physics simulation in GEANT4 benchmarked with data collected at the MAMI Mainz and SLAC test beam facilities.

Optimizing the resolution reduces the effective loss of counting statistics, which for the CREX detector set up using 5mm thick quartz is $\frac{\text{RMS}}{\text{Mean}} \sim 25\%$, as shown in Figs. 2.36 and 2.37, amounts to a factor of 1.03 increase in PMT signal width relative to idealized counting statistics, and therefore only leads to an acceptable equivalent 3% loss in asymmetry statis-

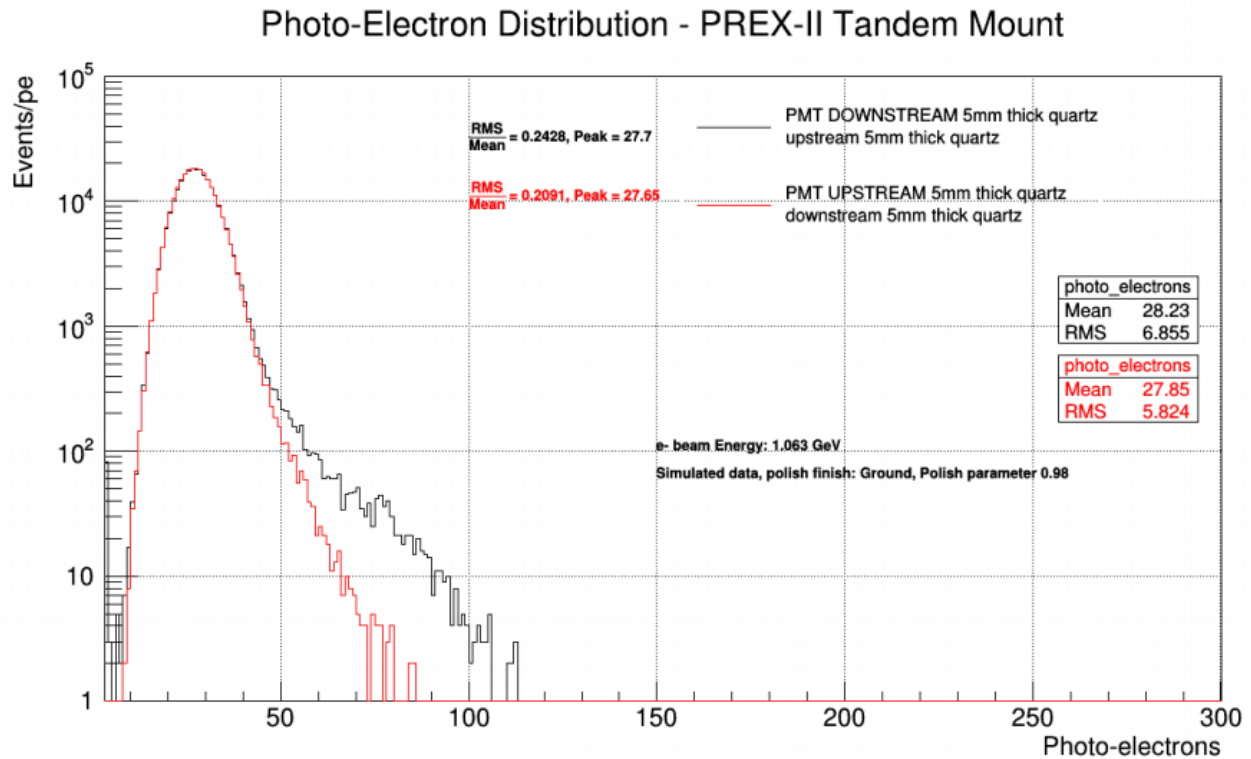


Figure 2.36: Example single electron photoelectron (PE) spectrum for the upstream (red) and downstream (black) CREX detectors using 5mm thick fused silica (quartz) Cherenkov radiator tiles. The downstream detector's spectrum has a more significant tail due to charged particle showering (delta rays) generated in the upstream quartz.

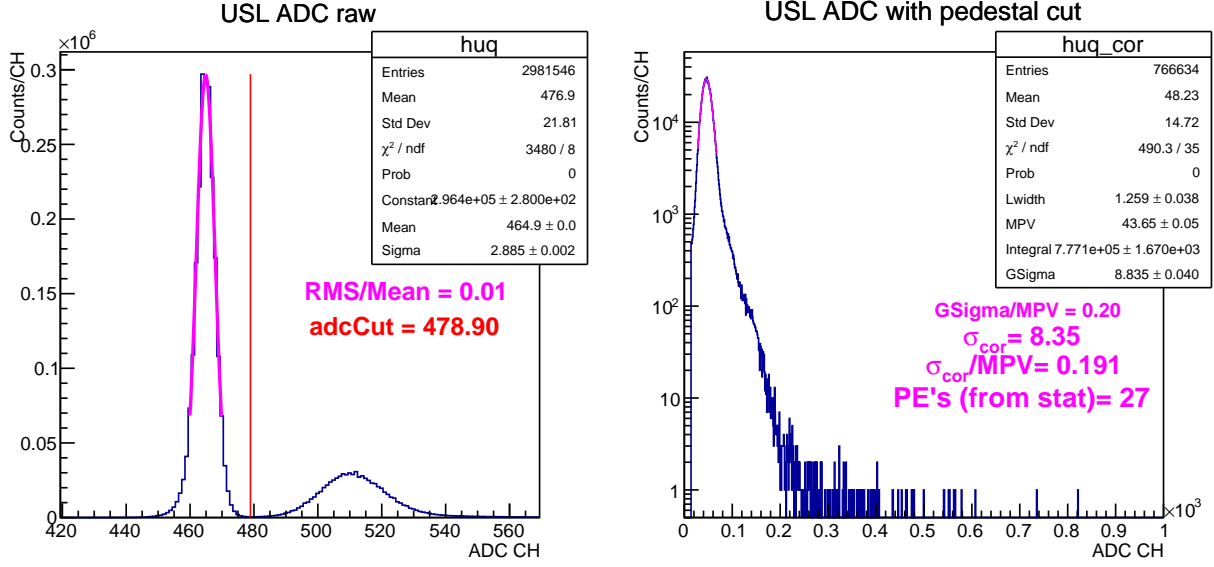


Figure 2.37: Pulse height spectrum from single electron tracks in the upstream integrating detector taken during CREX, analyzed by Devi Adhikari. The left figure shows the raw signal, including the pedestal peak which is fit with a Gaussian and subtracted in the figure on the right.

tical precision. This detector optimization also considers the need to minimize non-linearity in the PMTs due to the high light levels they see during PREX II running, which resulted in selecting 5mm thick pieces of quartz for the integrating detectors for both experiments. We use Hamamatsu R7723Q 2 inch PMTs and special studies were performed by the ISU parity group to optimize the PMT voltage divider, high voltage settings, and I-to-V pre-amplifier resistance to achieve a $\sim 10^{-3}$ non-linearity limit [28]. We utilize a 5mm thick, 3.5cm wide, 16cm long piece of quartz with a 45° beveled cut at the face of the PMT cathode and extending to the end of the 5cm long and 3.5cm wide elastic peak scattered flux distribution to facilitate TIR of the Cherenkov light onto the PMT with minimal loss. The PMT cathode is a near-UV sensitive quartz-window to optimize the light collection from the 300nm peak of the Cherenkov light spectrum. CREX saw a PMT cathode light level of 0.13nA , allowing a high voltage $\sim 900\text{ V}$ and I-to-V pre-amplifier resistance of $2\text{ M}\Omega$, which keeps the detector

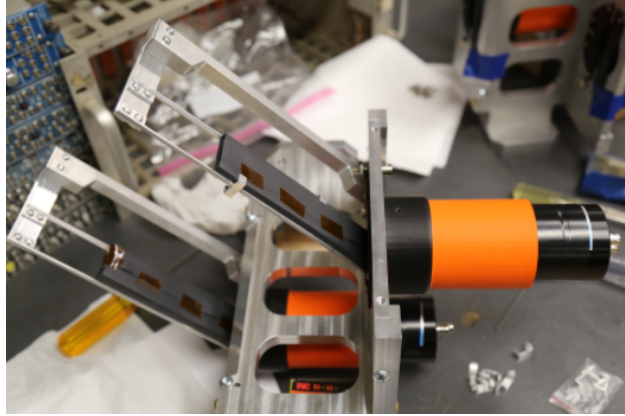


Figure 2.38: Photograph, taken by Dustin McNulty, of the tandem mounted “main” integrating fused silica (quartz) Cherenkov detectors. The plastic and Kapton covering is not shown. The black paper around the quartz is only for light tightness and is in loose contact to avoid affecting the optical properties of the quartz.

nonlinearity at a small level $\sim 10^{-3}$ [28].

Two identical integrating upstream and downstream “main” detectors are attached to the tandem mount, shown in Fig. 2.38, which allows translation and rotation of the detectors to optimize their interception of the elastic peak flux. Both detectors are encased inside 3-D printed light-tight plastic and Kapton film housings. The downstream detector is left in the counting mode configuration to facilitate regular checks of the alignment of the elastic peak with respect to the detectors and of the clean separation of the inelastic excited states from the quartz tile’s acceptance. Each detector package also has two background monitoring “ A_T ” detectors, further downstream from the main detectors and controlled with independent motion control systems in X and Y. These detectors are identical to the main detectors but placed in a different configuration, determined by Monte Carlo simulations, described in [58], to maximize sensitivity to possible transverse asymmetry (A_T) from residual transverse polarized scattering in the target and provide a background correction.

2.8 Data Acquisition

We have both counting mode and “parity” integrating mode DAQ systems, which operate independently of each other, and also independently of the DAQ systems for the Compton and Møller polarimeters in Hall A. The counting DAQ is used for track reconstruction and rate measurements used in optics calibration, kinematic information extraction, and HRS commissioning data collection at low beam current with the VDCs and quartz detectors. The integrating DAQ is used for measuring the integrated signal from the quartz detectors in the HRSs, the small angle monitors (SAMs), beam current monitors (BCMs), and beam position monitors (BPMs). The integrating DAQ is also responsible for controlling the beam modulation (BMOD) system used for measuring the integrating detectors’ sensitivities to beam motion. Both DAQ systems utilize the JLab designed CEBAF On-line Data Acquisition System (CODA) [59]. The data is sent over JLab’s ethernet network to a remote Linux workstation where it is built into local memory by a CODA event builder (EB), stored within an event transfer (ET) system to which multiple user-defined online analysis processes can be attached, and finally written to disk by a CODA event recorder (ER) for subsequent analysis.

2.8.1 Counting DAQ

The counting mode DAQ uses the standard Hall A system, including VME and NIM signal logical processing modules and readout electronics. Trigger configurations involving the logical AND and OR of scintillators S0 and S3 are described in detail in [28]. The main quartz detectors are not involved in the trigger, as it is not necessary to focus on their signals. Additionally, hardware limitations from designing the detectors to optimize for high rate integration mode means they only produce a small signal for individual

electron tracks in the low current running, and the process of splitting the signal to send it to the DAQ readout channels and trigger logic simultaneously further degrades the signal to the point that single electron signals cannot be cleanly separated from the pedestal for use in triggering. When the trigger scintillators' signals pass thresholds and meet the logical conditions defined in the trigger system, the counting DAQ reads the data from the modules and processes it through the CODA system.

2.8.2 Integrating DAQ

The primary design goal of the integrating DAQ is to avoid dead-time from traditional approaches that try to count the high rate of electrons needed to make a precise asymmetry measurement [60]. The high flux of electrons produces Cherenkov light in the quartz which is detected by the PMT, whose output anode current is converted to a voltage by the custom QWeak-designed I-to-V pre-amplifier [31]. The voltage signal from the quartz detectors, BPMs, and BCMs are then integrated in custom QWeak-designed analog to digital converters (ADCs) [31] triggered by a single “Macro Pulse Signal” (MPS) global trigger for each helicity window. The helicity signals are generated by the helicity control board in the injector, as described in section 2.1.3, and are distributed to the various DAQ components. A schematic of the main integrating detectors signal chain is shown in Fig. 2.39.

The integrating DAQ is spread across the laboratory to measure the helicity-correlated detector signals with minimal cable length to mitigate noise and impedance problems [61]. There are four primary DAQ systems, located in the injector, Hall A counting house (CH), and the left and right HRSs, each of which contains NIM and VME crates for producing and distributing trigger information, housing the ADCs, and reading out the modules with VME based VxWorks or Linux Input/Output controller (IOC) single-board computers, referred

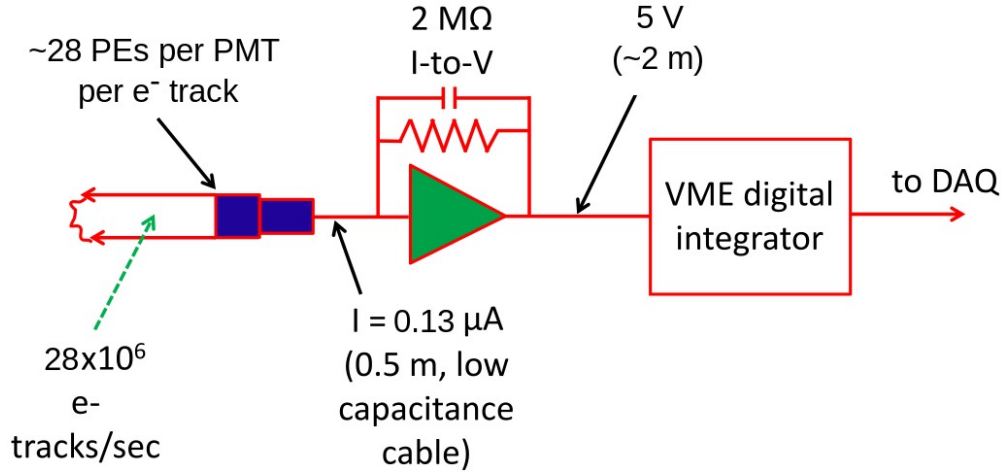


Figure 2.39: Schematic of the integrating quartz detector signal chain, from PMT to pre-amplifier to ADC integrator. Adapted from [31].

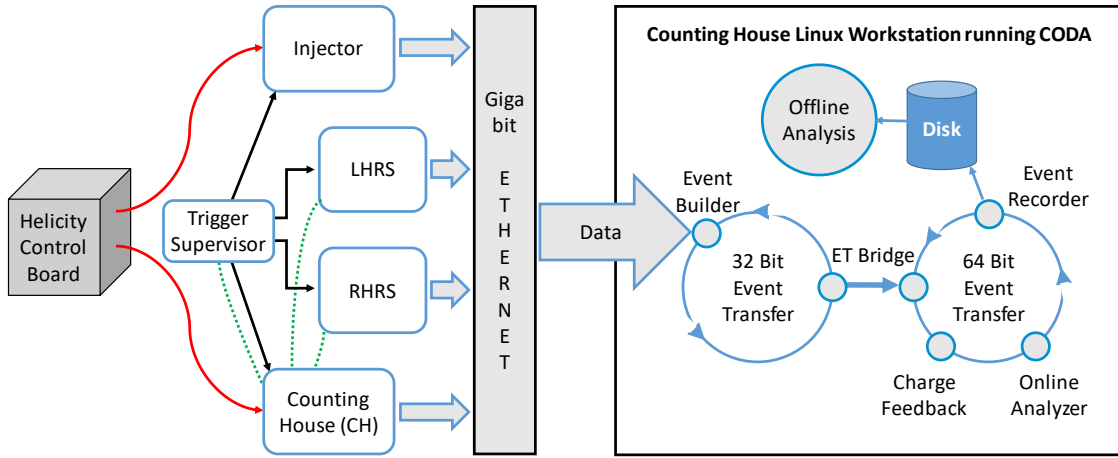


Figure 2.40: Schematic diagram of the integrating DAQ. The helicity information (red) is transported by fiber optic cables from the helicity control board to the injector and CH integrating DAQs. The CH DAQ generates copies of the helicity information, integration gate and latch signals, and the MPS based trigger for itself and the HRSs and TS (green). The TS initiates the DAQ readout with a global shared trigger (black arrows). The data (light blue) is extracted by each ROC and sent via gigabit ethernet to the Hall A Counting House Linux workstation where it is processed by CODA to be used in online and offline analyses.

to as Read Out Controllers (ROCs). The DAQ systems are all controlled by a central Linux workstation in the Hall A counting house which runs the CODA Run Control (RC) system. The central RC system receives data from the VME crates through JLab's ethernet network and processes it with CODA 2.6.2's event builder, transfer, and recorder systems, with the addition of a event transfer bridge program to convert the CODA events to 64 bits from the 32 bits generated in the CODA 2.6.2 EB. Attached to the 64 bit ET system are two online analysis systems for controlling beam charge asymmetry feedback and for monitoring the data in real time. A schematic of the DAQ systems and their relationships to each other is shown in Fig. 2.40.

Each of these four DAQ systems are independent but are used in a combined mode for PREX II and CREX. A fifth VME crate, located in the Hall A counting house alongside the primary counting house DAQ crate, contains a Trigger Supervisor module (TS) which distributes the synchronized MPS trigger to the other four crates and governs the CODA data reconstruction. This fifth crate also contains a custom Data Tagger (TS Tagger) module which monitors the synchronization between the injector, counting house, and two HRS VME crates. The trigger and CODA data production synchronization is monitored and verified using several monitoring techniques throughout the experiment, including the TS Tagger module described further later, and the scaler synchronization check system is described in detail in appendix C of [61]. Data runs are limited to one hour, so that the CODA data files and analyzed output files do not exceed reasonable size limits, and to minimize the amount of potentially lost beam time in case of the failure of any DAQ component.

The analog signals from the quartz detectors and beam monitors are read by the QWeak ADCs, which were extensively tested before the experiment. Several ADC channels went bad between run periods and were replaced with spare modules and repaired for use by the JLab electronics group as spares. The helicity logical signals, trigger information, and vari-

ous signals involved in the BMOD system and synchronization checking system are handled in additional boards which are located in each of the four DAQ systems. The four systems contain similar modules, designed to provide complete independence and modularity when needed, so that the failure of one component would have negligible consequences on the experiment. The various features of the DAQ systems and modules are explained in the following sections, and the processing of the data obtained with the DAQ for online monitoring and the offline asymmetry data analysis are described in chapter 3.

2.8.3 Integration Triggering

As described in section 2.1.3, the helicity signals are generated by the helicity control board in the polarized source. These signals are transmitted via fiber optic cables, to maintain ground isolation, to the integrating DAQ systems in the injector and in the Hall A counting house where they are converted to NIM logical signals and read into the data-stream by dedicated VME modules. The primary trigger signal generated by the helicity control board is the MPS, which is on, set to a logical “true,” $1\mu s$ before the helicity changes, and is held true for $90\mu s$ to allow time for the PC to settle. CREX runs at 120 Hz, and with helicity windows $8.33ms$ long, splitting the MPS pulse into the $90\mu s$ T_{settle} and $8244\mu s$ T_{stable} periods. There is also a “pair sync” signal which simply alternates between true and false for alternating events and does not contain any vital information, and a multiplet “QRT” pattern synchronization pulse, which is set to true for the duration of the first helicity window of each quartet pattern.

The helicity control board sends a delayed helicity signal to the DAQs, delayed by 8 integration windows, to provide additional isolation from the true helicity information. The helicity state itself is determined by a 30 bit random number generator which determines

the polarity of the first helicity state in a quartet to be $+$ or $-$, with the remaining three states following to complete a quartet pattern of $+- -+$ or $-++-$ respectively. The helicity signals read by the DAQ in the injector are used to inform the parity analysis of the helicity information, while the helicity signals received in the Hall A counting house are read into the CH DAQ as a redundant backup copy and for further distribution to the two HRS integrating DAQ systems and others, such as the Hall A polarimeter DAQ systems.

The triggering and integration gate distribution is handled separately in the injector and CH DAQ systems, with the CH signals relayed to the HRS systems via patch panel connections. The primary MPS T_{settle} signal is used to trigger a VME HAPPEX Timing Board, designed specially by JLab for the HAPPEX experiments [61]. This HAPPEX Timing Board produces a signal labelled GMN, which serves as the integration gate signal to control the JLab custom-built HAPPEX 18 bit ADCs' sample and hold routine. These 18 bit ADCs were in place and read out by the HRS and CH DAQ systems during PREX II and CREX, but no signals were plugged into their channels and they served only as hot spare backup ADCs which were never used.

The GMN trigger signal is determined by a delay length counted relative to the input MPS trigger T_{settle} and an integration gate length, which are both configured remotely by the Linux workstation in the counting house and span the integrated data, as shown in Fig. 2.41. The trigger timing is handled separately for the various ADC and scaler modules to avoid problems with DAQ read out processing data from the previous event.

A read out controller (ROC) single-board computer controls each VME crate and is responsible for executing the CODA Read Out List (ROL). The ROL defines the routine for the ROC to interface with the other modules in the VME crate to read the data stored in their memory buffers through the VME backplane and send it over the ethernet network to the CODA systems running in the central Linux workstation in the counting house. The

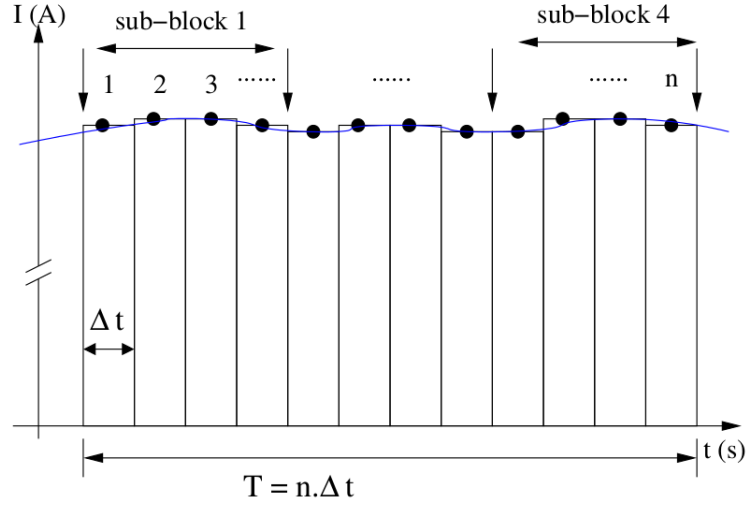


Figure 2.41: Schematic representation of the $\Delta t = 2\mu s$ sampling of analog signals, digitized by 18 bit QWeak ADCs. The samples are summed in four sub-blocks and a full sum for each helicity state. The input signal fluctuations are exaggerated to show the significance of the sampling process. Reproduced from [32].

ROL processes take some time to read each board, which are organized within the program and trigger timing to avoid errors. The ROC's ROL routine is triggered by a JLab designed trigger interface (TI) board that can run in either standalone or combined mode governed by a trigger supervisor (TS). For CREX we use the TS, which is triggered by a single ended ECL copy of the T_{settle} signal, to coordinate the simultaneous triggering of the four DAQs' ROC's ROL routines. The TS passes the trigger signals through a newly designed custom TS Tagger module, which generates an additional random 4-bit number for each event and sends it along with the primary MPS signal from the TS to each DAQ systems' TI board along the unused triggering channels. This additional information is used to tag contemporaneous events to verify the synchronization of the four crates. The TS and TS tagger signals are sent via fiber optic cables to the injector crate to achieve negligible signal delay and degradation.

2.8.4 Integration Sampling

The primary ADCs for CREX are the custom QWeak ADC boards (VQWK), designed at the TRI University Meson Facility (TRIUMF) for use in the QWeak experiment [31, 32]. The VQWK ADC channels begin their integration after a programmable internal “gate delay,” chosen to be $10\mu s$, after the external trigger signal in order to prevent the internal signal processing electronics from being affected by the external NIM pulse integration gate start. The external VQWK trigger is set to $80\mu s$ after the start of T_{settle} so that the additional $10\mu s$ internal gate delay causes the ADCs to begin integrating at the start of the T_{stable} signal, which was checked with dedicated runs testing the variable offsets of these parameters and NIM timing gate generators. The VQWK ADCs sample the input signal every $2\mu s$ and integrate the samples into four sub-blocks for each integration window, as shown in Fig. 2.41.

The integration time for the VQWK is determined by the number of samples, which is a programmable number set within the ROL tuned to cover as much of the T_{stable} part of the helicity window as possible. Although the available T_{stable} time is $8244\mu s$, we choose to not integrate the final $51.33\mu s$ to allow changing the helicity frequency from free clock to beam sync mode. As described in section 2.4.1, when the helicity control board is driven in beam sync mode, the 60 Hz beam sync signal has some jitter between neighboring windows, typically at the $\sim 35\mu s$ scale, determined from monitoring the signal on an oscilloscope. Although we run the DAQ in free clock mode for all of the production running, to simplify the setup and to avoid the possibility of integrating the signal of a following helicity window while running in beam sync mode, we choose to shorten the integration window for the ADCs to stop $\sim 50\mu s$ before the next T_{settle} signal arrives. The timing of sampling the integrating mode analog signals is shown in 2.42. The integrating DAQ was set up identically for PREX

II and CREX running, with the exception that PREX II runs the latter majority of its data collection in octet mode, with $+ - - + - + + -$ or $- + + - + - - +$ patterns, at 240 Hz, performing 503 VQWK ADC samples per block with a correspondingly reduced HAPPEX Timing Board GMN integration window.

The VQWK ADC electronics are designed to measure the high rate signal with minimal noise contribution from the electronics chain, depicted in Fig. 2.39, as demonstrated by the negligibly small asymmetry RMS of only ~ 6 ppm from a fixed voltage battery signal, shown in Fig. 2.43. The integrating detectors' interface with the custom-designed QWeak I-to-V pre-amplifiers and ADC board electronics are described in further detail in Appendix C of [32] and its references. In addition to the QWeak ADC channels we also utilize a SIS3801 Scaler for reading some channels, which are first passed through a voltage-to-frequency converter (V2F) whose output is a rate of pulses proportional to the input voltage. These scaler channels are used with some additional instrumentation in the injector, the synchronization check system, and BMOD function generator readbacks. The complement of the GMN signal from the HAPPEX Timing Board is used as a veto to prevent scaler counting during the T_{settle} time, and the GMN signal is tuned to end at the same time as the QWeak ADC internal integration time described above, so that the signals are exactly comparable and the scaler can be used in a similar way to the integrating ADCs.

The $\sim 50\mu s$ non-integrated window at the end of the GMN signal, in addition to providing the freedom to switch between free clock and beam sync helicity timing, also serves the purpose of providing a buffer for the HAPPEX Timing Board's triggering, which requires more than $\sim 20\mu s$ of dead time to reset, during which new triggers are ignored. Even after removing the T_{settle} and end buffer times, the integrated time of the ADCs and scalers amount to $8192\mu s$, which is 98.3% of the total helicity window.

Two other scalers are used for reading the helicity state information, latching the de-

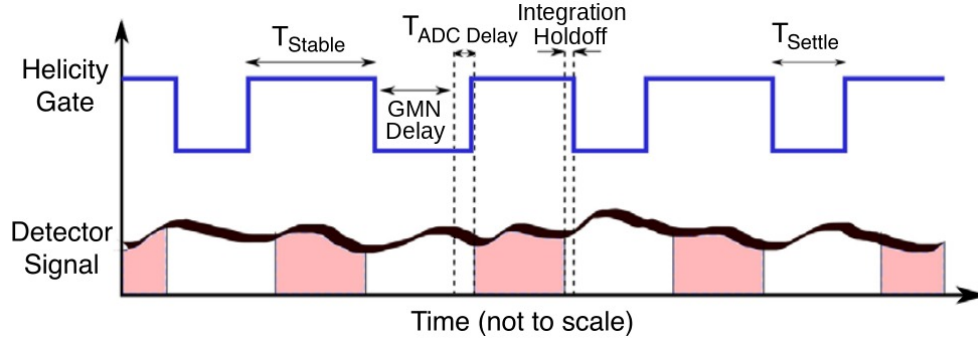


Figure 2.42: Schematic representation of the ADC and scaler integration timing for CREX. The $10\mu\text{s}$ VQWK internal delay and integration gate with $\sim 50\mu\text{s}$ integration holdoff at the end are shown. The signal fluctuations are exaggerated to show the significance of integration. Adapted from [31].

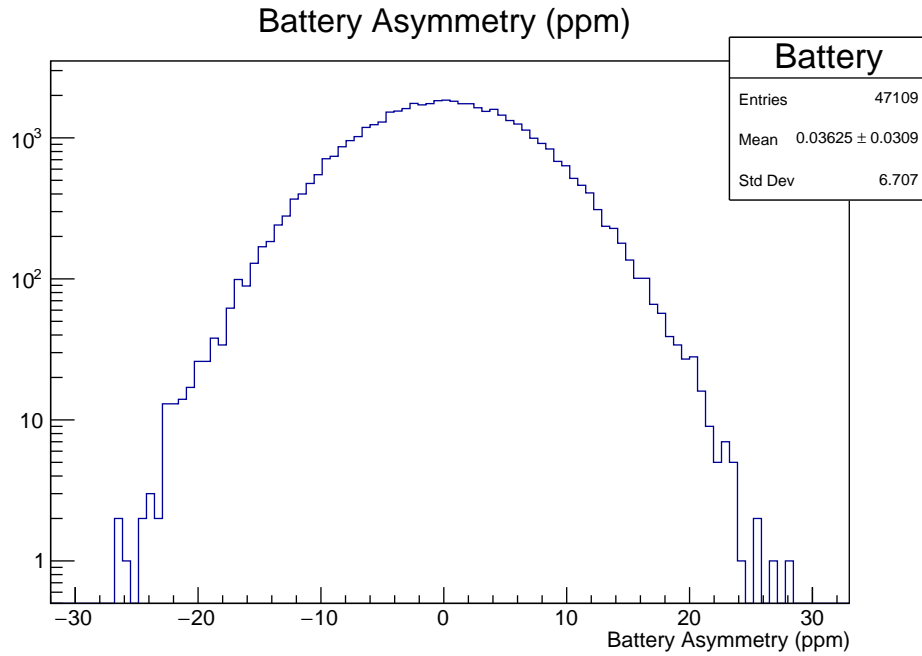


Figure 2.43: Battery asymmetry distribution from run 5408 at the beginning of CREX, showing the RMS ("Std Dev" in the statistics box) stability of the QWeak ADC channels at the few ppm level.

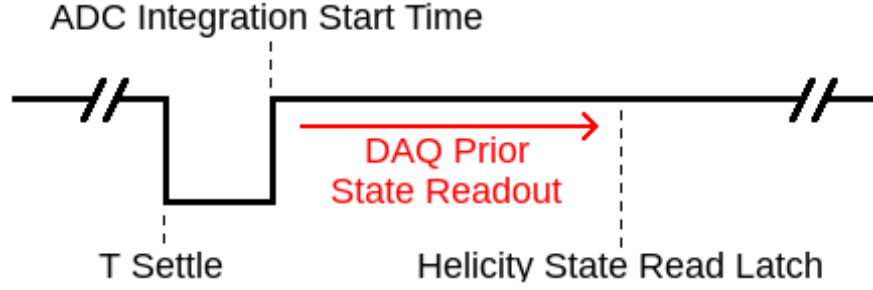


Figure 2.44: Diagram showing the delayed helicity state read latch signal timing, delayed after the beginning of the integration. This is done so the CODA DAQ process can read the the prior helicity state information and store it in memory, before the latching scaler (FLEXIO or STR7200) reads the current state. The delay is $\sim 150\mu s$, to allow sufficient time for the CODA read out list (ROL) to safely finish reading all prior helicity state data.

layed helicity and QRT states within the window and storing them in the data-stream. We primarily use a STR7200 Scaler in the injector DAQ system to latch and store the helicity information, whose latching trigger is set at a time after the module has its previous helicity state information read out by the ROC's ROL, as shown in Fig. 2.44. A redundant helicity state read is performed in a similar way by JLab designed FLEXIO boards, and this is done in each DAQ crate independently as a redundant check and additional synchronization verification.

The FLEXIO module in the CH crate also serves to send an output trigger for the BMOD function generator. The timing of the BMOD system trigger is defined by a program running in the counting house Linux workstation and the BMOD 15 Hz ramping frequency is set to start in time with the helicity windows' starting at T_{settle} . Offline analysis reveals that the variable computation time inside of the DAQ computers causes neighboring BMOD coils ramps to sometimes start with a different phase offset with respect to the quartet helicity pattern. The relative phase determines how much of the BMOD sine wave position fluctuations are canceled in the asymmetry calculation. Maintaining control over this relative phase may be desired for future experiments, which could improve the timing of this system

by instead aligning the BMOD ramping signal with the QRT signal to ensure consistent relative timing of beam modulation and helicity multiplets.

2.9 Beam Monitors

Beam monitors are a critical component of any PVES experiment, as they are used to set up reproducible and stable beam delivery, to help determine the kinematics of the experiment, to tune away and measure and correct for HC A_{beam} , and to measure and remove noise with fast feedback. The monitors are capable of measuring the HC A_{beam} for every helicity window and are used to measure and remove dependence on HC intensity asymmetries (A_Q) by normalizing the detected yield with the beam current,

$$y = Y/Q, \quad (2.6)$$

where Y is the signal yield in the detector measured by the DAQ in Volts, Q is the beam current in μA , and y is the current-normalized detector yield, thus removing the dependence of scattered rate on beam intensity. Calculating the detected asymmetry with the normalized detector yield y then removes the beam intensity asymmetry, A_Q , assuming $y_+ \simeq y_- = y$, as

$$A_{raw} = \frac{y_+ - y_-}{y_+ + y_-} \simeq \frac{\Delta y}{2y}, \quad (2.7)$$

which to first order is

$$A_{raw} \simeq \frac{\Delta Y}{2Y} - \frac{\Delta Q}{2Q} = A_{rate} - A_Q. \quad (2.8)$$

The scattered rate measured in the detectors, A_{rate} , also depends on the energy and angle of scattering from the target into the acceptance-defining collimator, and so we must calibrate

the change in detector signal due to helicity-correlated position and energy changes. This is done by measuring the sensitivity of the detector to natural beam motion fluctuations and to dedicated dithering of the beam using the Beam Modulation (“BMOD” or “dithering”) system. The calibrated sensitivities are used to correct the asymmetry measured in each helicity multiplet by the detector as a function of the measured HC position and energy differences. Following up on the removal of beam intensity asymmetries from the scattered rate asymmetry in the detectors through detector signal normalization, we can measure and remove the correlated position and energy-dependent fluctuations by assuming they are linearly related

$$A_{det} = A_{raw} - A_{correction} = \frac{\Delta Y}{2Y} - \frac{\Delta Q}{2Q} - \sum_i C_i \Delta x_i, \quad (2.9)$$

where C_i are the linear correction slopes calculated by measuring the correlation coefficients between the Δx_i HC position and energy differences and A_{raw} . All of the HC differences and asymmetries are measured and corrected for each multiplet to reveal any residual correlations or instrumental problems, although the corrections can also be made on the asymmetry distributions to arbitrary order in the distribution moment expansion. After correction through either technique, the resulting asymmetry distribution is dominated by statistical fluctuations and is ready for physics interpretation.

Hall A contains multiple beam monitors sensitive to the beam intensity, position, and energy, as well as a “Fast Feedback” (FFB) system for actively correcting for < 80 Hz noise and power line 60 Hz harmonics [62]. The BMOD system is used to drive energy and position fluctuations of the beam (dithering the beam) to calibrate the correlation between beam parameters and the scattered flux measured by the detectors. The various beamline components involved in monitoring and calibrating the beam motion are shown in Fig. 2.45. The position and current monitors’ values are reported to the CEBAF EPICS system on

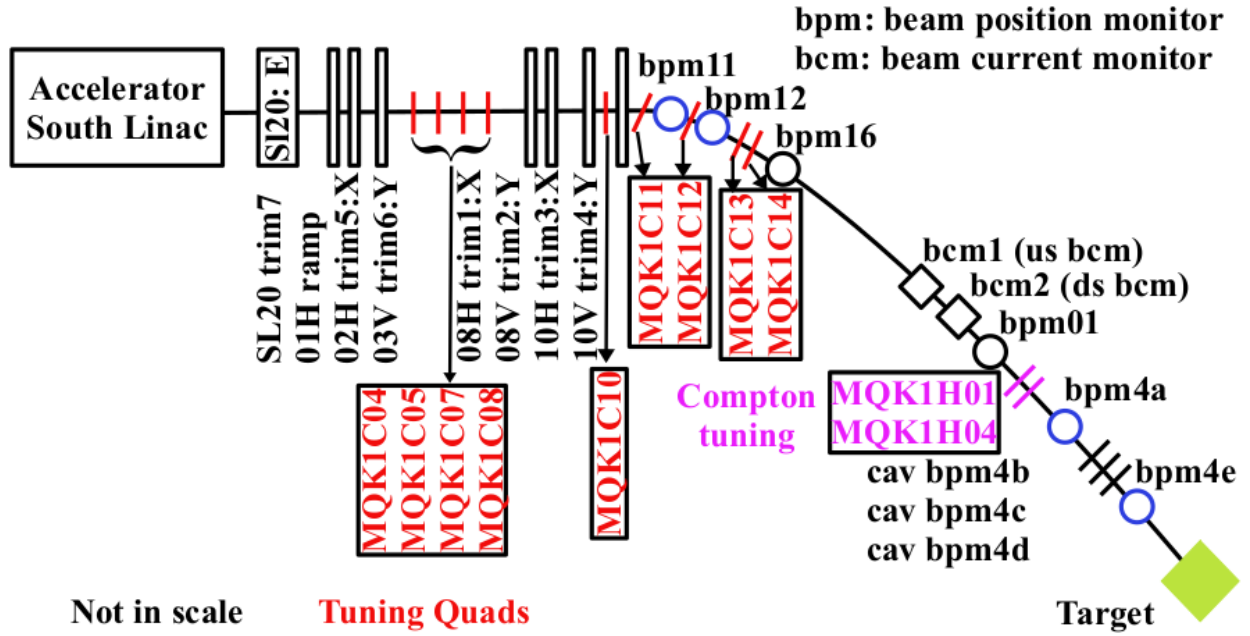


Figure 2.45: Schematic of the Hall A beamline monitoring and beam modulation hardware, along with approximate locations of the current monitors and beam optics tuning quadrupole magnets. The modulation coils are indicated by their “trim” control systems, with trim 7 dithering energy in the final cavities of the south linear accelerator, measured in BPMs 11 and 12, trims 1, 3, and 5 dithering the X position, and trims 2, 4, and 6 dithering the Y position of the beam, measured in the hall BPMs 1, 4A, and 4E. Reproduced from [28].

second time scales for use in beam set up and delivery, and also have their analog signal outputs sent to the integrating and counting mode DAQ systems to be used in the analyses.

2.9.1 Position

To measure the position and angle of the beam on the target we use beam position monitors (BPMs) placed along the beamline. The primary BPMs for CREX are the stripline switched electrode electronics (SEE) BPMs that are generally implemented in CEBAF. CREX uses these BPMs instrumented in several places along the beamline in Hall A, and in the Hall A beam transport arc, to independently measure the beam position at locations with sensitivity to different elements of the beam transport optics tune, intended to cover the five dimensions of vertical and horizontal position and angle of incidence on the target, along with energy. The BPMs used in CREX are labelled using the CEBAF nomenclature; the BPMs most sensitive to energy fluctuations, named 1C11 and 1C12, are located in the Hall A arc, where energy shifts cause changes in the position; those in the transport region into the hall are named 1C16 and 1H01, and the BPMs several meters upstream of the target and downstream of the beam profile tuning quadrupole magnets are named 1H04A and 1H04E.

Additional BPMs are located within the Compton polarimeter's chicane and are used when tuning the beam delivery to the hall and for analyzing the Compton polarimetry data. BPMs are located within the injector and are used in calibrating the PC and setting up the polarized source to minimize HC A_{beam} during dedicated injector beam studies. In addition to the stripline SEE BPMs CREX also utilizes three cavity BPMs (named 1H04B, 1H04C, and 1H04D), which use radiofrequency cavities tuned to the 1497 MHz CW frequency to measure the position of the beam, as well as the beam intensity. The cavity BPMs were

primarily used for low-current calibration runs and are not relied on for measuring the high current production-mode data. The monitor names in the CEBAF naming convention are often abbreviated, only using the final numbers and letters to distinguish them from each other.

The stripline SEE BPMs measure the position of the beam using four wire-antennas labelled XP, XM, YP, and YM, with X and Y referring to the horizontal and vertical directions and P and M referring to the plus and minus sides of these axes. The antennas are rotated 45° with respect to the horizontal-vertical X-Y plane to avoid synchrotron radiation from the bending of the beam in the horizontal plane. The antenna's response is proportional to the distance from the beam, and their gains are set in an automated way to maintain a stable sensitivity and signal size, changing the gain inversely with the beam current passing through the monitor. The energy sensitive BPMs in the Hall A arc are operated in fixed gain mode to avoid problems caused by the FFB system. The signal from each antenna is sampled and integrated using a switched electrode technique, and the resulting signal is sent from the sample and hold cards to the integrating DAQ where they are measured as voltages in the VQWK ADCs.

The absolute scale of the position measurement is determined by the geometry of the antennas, such that the calculated position is proportional to the wire signals relative measurement of the beam times a fixed constant, $k = 18.76mm$, which is the same for both axes and all SEE BPMs at JLab, and is used to convert from relative scale into units of mm . The X and Y axis positions are extracted from the complementary wire measurements with the following relation:

$$X = k \times \frac{XP - XM}{XP + XM}, \quad Y = k \times \frac{YP - YM}{YP + YM}, \quad (2.10)$$

and the horizontal and vertical positions are obtained by rotating those positions back into

the hall coordinate system, $X_{hall} = \frac{X-Y}{\sqrt{2}}$ and $Y_{hall} = \frac{X+Y}{\sqrt{2}}$. The BPM signals are used in the analysis and correction of HC A_{beam} , described in detail in Chapter 3, both for measuring the sensitivity to BMOD beam dithering and for measuring the correlations between HC A_{beam} and the asymmetry of the scattered flux in the main detectors, A_{raw} .

2.9.2 Beam Intensity

The beam intensity is measured by several dedicated BCMs, whose independent measure of the beam intensity allows a clean removal of intensity HC, A_Q . The BCMs used for CREX are the “Unser” parametric current transformer and two radio-frequency (RF) cavity monitors, labelled upstream (US) and downstream (DS) analog (AN) BCMs, “BCM AN US” and “BCM AN DS.” The “Unser” BCM is used for an initial calibration of the beam current scale factor from the monitors [63]. The Unser BCM is relatively noisy and unstable on minute-timescales, but it is highly linear and stable on short time scales, and so is used to calibrate the RF-cavity BCMs’ pedestals with dedicated current ramp runs [64].

The pedestal calibration runs to calibrate the RF-cavity BCMs with respect to the Unser intentionally measure the beam off signal before and after each current point in the ramp to mitigate minute-timescale drifts in the Unser’s pedestal. Pedestal calibrations are discussed more in section 3.1. The two RF-cavity BCMs are resonant at the 1497 MHz CW frequency of the accelerator and have their RF signals processed by a 1 MHz down-converter box near the beamline. The 1 MHz down-converter sends its output signal upstairs to another processing box in the Hall A counting house, which in turn connects its output voltage signals to the integrating DAQ. The upstream BCM is used for the integrating detector normalization for all of CREX running, and the multipletwise difference (“double difference” or “DD”) between the asymmetries of the two analog BCMs is used to estimate the monitors’ resolution.

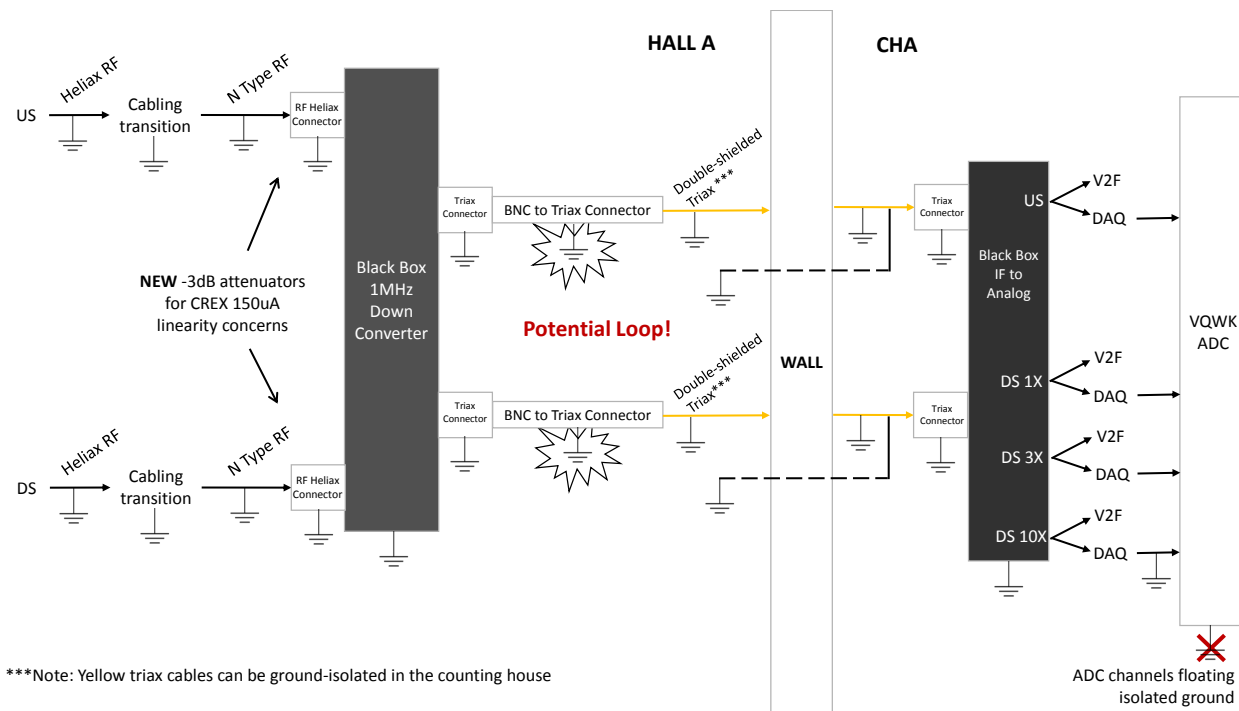


Figure 2.46: Schematic diagram of the upstream (US) and downstream (DS) analog (AN) beam current monitors' (BCM) signal chain and cabling.

The BCMs are located on the beam line upstream of the target, with the Unser and two RF-cavity BCMs sharing a temperature-controlled box. The temperature controls were not operating perfectly during the run, and so the current calibration performed before PREX II running was no longer valid during the CREX run, but this few percent inaccuracy in calibration scale factor has no effect on the asymmetries measured due to the accurate pedestal calibrations. The cabling of the BCMs is a potential source of RF pickup through ground loops, as the cables are not ground isolated at each step from the beamline to the counting house integrating DAQ, but the long cables from the hall to the counting house are RF shielded “triax” cables and the integrating DAQ ADC channels do have a floating ground, so the possibility of picking up HC radiofrequency signals in a full loop is mitigated. A diagram of the BCM system and their cabling is given in Fig. 2.46.

There is a BCM in the injector (BCM “0l02”) which is included in the injector integrating DAQ setup and used for injector commissioning and tuning. In addition to the BCM signal chain shown in the figure, there is also a digital sampling signal processing chain, which is not relied on in CREX because the signal latency and instrumental resolution are not as good as the analog signal chain, not matching the main detector integrating PMT latency as well as the analog signal chain does. The BCM and detector latency are measured using pulsed “tune” beam from the accelerator and looking at the signals on oscilloscopes as well as with few-sample integration windows in a special DAQ configuration to measure the slowly drifting line synchronized tune beam pulse as it passes the fixed frequency integration windows. The cavity BPM systems’ current measurements are not relied on for similar reasons, and because they were set up primarily to assist with low current studies.

Due to the higher current running point of CREX, at $150\mu A$, relative to PREX II, at $85\mu A$, the input signal strength is modified by adding 3dB attenuators on the inputs to the 1 MHz down-converter in the analog signal chain to bring the full current running signal into

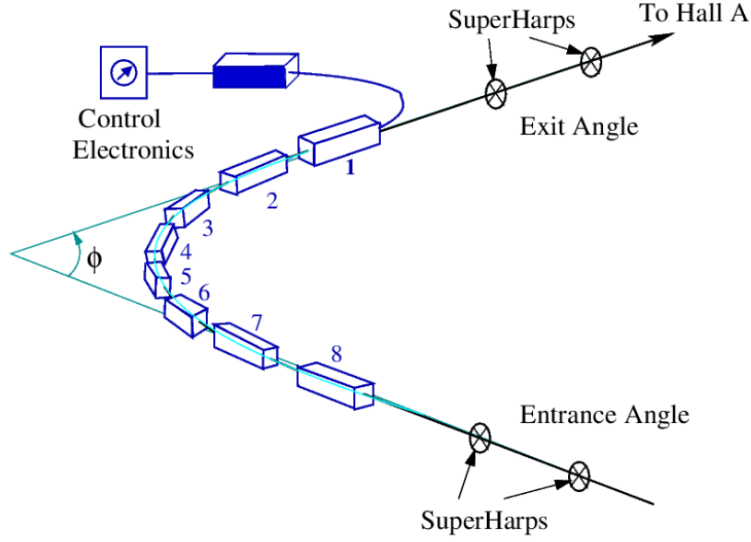


Figure 2.47: Schematic diagram of the Hall A arc magnets and super harps used in the arc energy measurement. Reproduced from [24].

the same linear response range of the system for both experiments. This procedure ensures that the linearity of the BCM system is at the sub-percent level so that it contributes negligibly to the final systematic uncertainty.

2.9.3 Energy

The beam energy is measured both online with beam position monitors in the bending arcs and offline with a dedicated measurement of the Hall A arc's magnetic field integral and the response of the beam. The arc energy measurement is performed by measuring the field integral of the bending dipoles in the arc and by measuring the deflection of the beam from changes in beam energy using harp scans. Because the harp scans are a destructive measurement, this procedure is not done frequently. The precision of the arc energy measurement is around $\delta p/p \simeq 2 \times 10^{-4}$ [24]. The energy measured with this method for CREX is 2182.79 MeV \pm 0.04 stat \pm 1.09 systematic [63, 65]. The Hall A arc and its instrumentation relevant

for the arc energy measurement are shown in Fig. 2.47.

In a similar way of relating positions and magnets to measure the beam energy, the “Tiefenback” energy measurement uses the current readbacks from the Hall A arc dipole magnets and the BPM position readings along the arc to estimate the energy, relying on the passive instrumentation calibrated by the arc energy measurement. The “Tiefenback” energy measurement is used in the FFB system and in the tuning of the accelerator after down times. Due to electronic noise and monitor resolution, the precision of this measurement is around $\delta p/p \simeq 1 \times 10^{-3}$.

The FFB system measures beam motion across a range of frequencies and drives the beam to cancel periodic noise, particularly in the frequency range of 0 to 80 Hz and for the first twelve power line 60 Hz harmonics [62]. Because the dispersion of the beam through the Hall A arc by the bend magnets is approximately $4m$, any position fluctuations around the most sensitive area (where BPM 12 is located) are related to energy fluctuations. The FFB system can modulate the energy of the beam using an energy vernier of RF-cavities at the end of the south linac of CEBAF [20]. At BPM 12 in the Hall A arc, a change in beam energy by 10^{-5} corresponds to $40\mu m$ of beam motion. The FFB system suppresses these energy fluctuations down to $\sim 20\mu m$ when it is working correctly, which is limited by BPM measurement noise [62]. During the final part of CREX data collection, after the Summer shutdown, the FFB system behaved poorly, even driving substantially worse noise in the Y direction in the Hall A arc and beamline BPMs, and so after a few days of unsuccessful commissioning efforts, the FFB system was turned off and the energy stability was monitored with careful attention to dedicated counting mode measurements of the elastic peak in the HRSs, the BPM-based Tiefenback measurement, and occasional manual changes by the accelerator operators. Additionally, when intentionally modulating the beam, as discussed in the next section, the FFB system must be paused, to avoid driving the system to cancel

the signal intentionally sent to dither the beam energy.

2.9.4 Beam Modulation

The position and energy fluctuations, the Δx_i from Equation 2.9, are measured for each helicity window and each multiplet with all of these monitors, and the correlation coefficients and their resulting C_i correction slopes are determined by calibrating the detectors' responses to beam motion. We measure the correlations between the detector and monitors with two independent methods: regression and dithering (referred to equivalently amongst the collaboration as beam modulation, BMOD, or dithering). In regression analysis, HC “multipletwise” position differences' correlations to the detector asymmetry and the C_i slopes are determined by multivariate linear regression. This regression acts on the intrinsic beam motion and noise measured in the BPMs HC position differences (diffs) and main detector scattering rate asymmetries. In dithering analysis, the helicity window “eventwise” beam position amplitude correlations to the detector response yield and C_i slopes are calculated from the beam's position and energy modulated amplitudes' sensitivities with respect to the separate modulation coils. Regression, dithering, and a combination of the two which constrains regression with dithering sensitivity information included using the Lagrange multipliers technique are all discussed in detail in section 3.5.

The linear regression correlation analysis relies on natural beam motion to determine the correlation coefficients and regression correction slopes between the detectors and monitors, but there is no guarantee that the beam delivery through the monitors is able to fully independently measure each degree of freedom of the beam interacting with the target and collimated acceptance definition. Beam modulation intends to break any possible natural beam motion correlation degeneracy or inadequate target response phase space coverage by

independently dithering all of the position and energy degrees of freedom, performing the modulation with independent coils at different times and at different positions along the Hall A arc beam delivery profile, and measuring the dithered beam position response at different locations along the beamline. Energy modulation is achieved using the same energy vernier as the FFB system, where the energy is dithered across a mm scale range at BPM 12. Six magnetic coils along the Hall A arc modulate the beam position, three horizontally and three vertically. At least four of the coils are used to independently span the parameter space of the beam interacting at the target in X and Y position and θ_X and θ_Y angle. The redundant leftover coils in X and Y are used to explore the dependence of the sensitivity measurement on the coil selection and to evaluate the residual sensitivity of the corrected detector response to the redundant coils, which will be discussed further in section 3.6.1. The beam modulation hardware and beam monitors along the Hall A beamline are detailed in Fig. 2.45.

The beam modulation process involves a “supercycle” containing multiple cycles for each coil of dithering the beam at $\sim mm$ distance scales in the X, Y, and energy sensitive BPMs at 15 Hz. After cycling one coil several times the supercycle waits a few seconds before moving to the next of the six modulation coils and lastly to the energy vernier. The amplitude of modulation is tuned by hand by the system experts to prevent too-large beam position fluctuations on the target while maintaining sensitivity to the independent degrees of freedom. The beam modulation supercycle lasts for more than a minute, requires FFB to be temporarily paused, and is repeated every ten minutes during production running. If the beam trips during a supercycle then it is abandoned and the ten minute wait timer is restarted, which has the unintended consequence of producing more partial supercycles with only the first few coils and less overall data with the later coils and energy modulation, which comes last among the cycles in each supercycle. Beam modulation accounts for approximately 5%

of the production data and both the event-to-event cuts and the modulation amplitude are tuned to allow the data to be included in the final data-set, which is discussed in section 3.7.

The integrating DAQ in the counting house controls the supercycle timing, by sending a signal to the function generator and trim cards in the beam switch yard (BSY) service building. The integrating DAQ also measures the linear ramp signal in multiple ways to have a metric of the beam modulation phase for use in offline analysis. The relative phase of the beam modulation ramp to the helicity quartet phase is not controlled, as mentioned previously, which causes the HC position difference calculation across the cycles to have a random phase relation, sometimes maximally cancelling and other times maximally driving a large position difference from the sinusoidal dithering of the beam. The analysis of the beam modulation data for CREX is described in detail in section 3.5.2. Ultimately, the measured detector response to monitor HC beam parameters are used to cancel the HC A_{beam} carried within the electron beam allowing a clean corrected A_{PV} extraction with small ($\sim 1\%$ level) systematic uncertainty.

2.10 Small Angle Monitors

Small angle monitors (SAMs) are placed downstream of the target at low $\sim 0.5^\circ$ angle to monitor the high-rate forward scattered flux. Eight identical detectors are placed with circular symmetry and are collectively sensitive to the position fluctuations of the scattered beam and any sources of noise in the hall. The SAM design uses a small quartz piece, similar to the main detectors', close to the beam with a reflective air-core light guide, flushed with dry air to prevent mirror degradation, which funnels the Cherenkov light to the PMTs [28]. The signal processing chain is very similar to the main detectors, going from PMT to pre-amplifier to VQWK ADC for helicity window integration and asymmetry measurement,

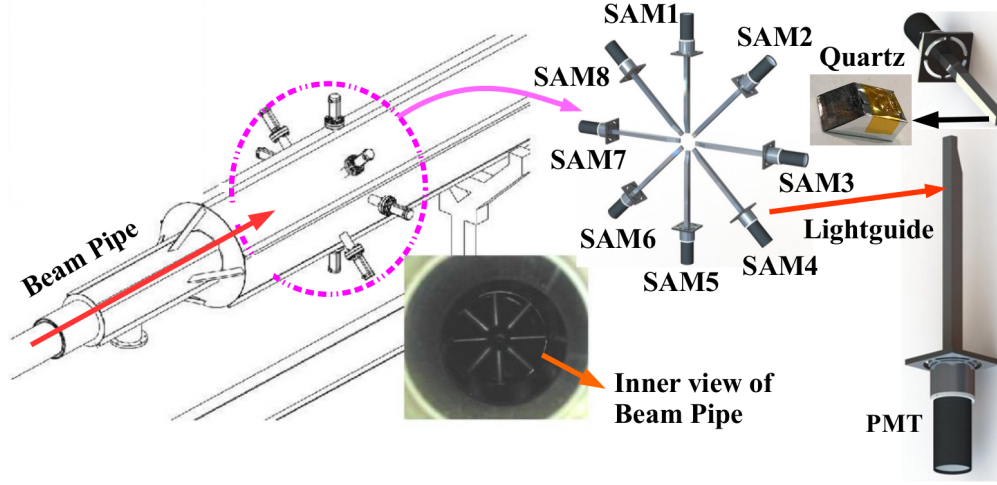


Figure 2.48: Images of the SAMs implemented in CREX. On the left is an engineering drawing of the SAM placements in the beamline, showing the PMTs protruding from the vacuum insert tubes. In the middle is a beam line view of the vacuum inserts protruding into the beamline. On the right are CAD views of the SAM PMT, quartz, and light guide design. Reproduced from [28].

though due to the very high rate at low-angle, PMT non-linearity limits the precision of the SAMs. Images of the SAMs design and implementation are shown in Fig. 2.48.

The SAMs are a tool for monitoring the limits of HC A_{beam} contributions: by measuring the high-rate low-angle flux with low statistical fluctuations, the bulk of the signal RMS width, especially after correction slopes are applied, must come from noise contained within the beam or from electronics sources. This noise floor indicates the minimum statistical measure possible, around the $50ppm$ multipletwise asymmetry RMS level, which corresponds to a much higher rate than the main detectors in the HRSs measure, which have around $1000ppm$ asymmetry RMS for each detector for CREX. The SAMs are able to reveal potential HC A_{beam} or fluctuations in scattered rate that the lower rate main detectors are unable to see, are used to verify the relative quality of the correction slopes, and are sensitive to the noise floor of the BPM and BCM monitors as well.

Because the SAMs are at such a low-angle, close to the beamline, they serve as a source

of re-scattering and radiation into the hall. This re-scattering is especially dangerous for the HRS magnet electronics, which are housed very close to the SAMs position along the beamline. As such, additional shielding was placed on the sides of the HRSs and the SAM vacuum inserts, quartz dimensions, and light guides were redesigned using GEANT4 simulation by the author for PREX II and for CREX separately. The SAM geometry is redesigned to allow maintaining the low-angle and high-rate measurements but without too much of a radiation load in the hall for each experiment. The previous SAM design with a cylindrical and thick vacuum insert was replaced with a shorter system with a thin tipped spherical end cap at the end of a thinner cylindrical vacuum insert, and a thinner piece of quartz only $6mm$ thick and $13mm$ long. As a result, the goals of radiation load in the hall, HRS magnet stability and SAM performance were met.

2.11 Polarimetry

The measured asymmetry is diluted by the imperfect polarization of the incoming electron beam

$$A_{det} = P_e A_{phys} \quad (2.11)$$

where P_e is the fractional longitudinal polarization of the electron beam, $P_e = \frac{N_p - N_{ap}}{N_p + N_{ap}}$ with N_p the number of electrons with spin parallel to the intended longitudinal polarization and N_{ap} the number of electrons with the anti-parallel polarization, and A_{phys} is the asymmetry from the polarization-dependent physics interaction of electrons in the target. The A_{phys} extraction from the measured and HC A_{beam} corrected A_{det} then corresponds to extrapolating how large of an asymmetry would have been measured if the N_{ap} number of electrons had not carried the opposite sign and cancelled out the N_p electrons' scattered asymmetry.

This extraction works on the HC A_{beam} corrected A_{det} which no longer carries any effects depending on the fractional polarization magnitude, other than the physics asymmetry from scattering in the target. The beam polarization is measured in the injector during the beam set up and spin launch angle optimization with an invasive Mott polarimeter, and is measured in Hall A constantly with a parasitic Compton polarimeter and periodically with an invasive Møller polarimeter.

Transverse polarization may also be present at the few percent level, and it may contribute an azimuthally-dependent scattering “Transverse” asymmetry background, A_T , which is covered in detail in [58]. To mitigate its contamination in the A_{PV} measurement we also make a dedicated measurement of A_T with the beam set to fully transverse polarization to determine the magnitude of the transverse asymmetry, and we make a parasitic contamination limiting measurement of the degree of azimuthally-dependent measured asymmetry with the difference between the two HRS detectors measured asymmetries and with the four strategically placed auxiliary “ A_T ” detectors near the main detectors in each HRS.

2.11.1 Injector Mott Polarimeter

The Mott polarimeter is located in the injector after electrons have reached 5 MeV and measures the polarization of the electron beam through scattering on an unpolarized, high Z , $0.1\mu m$ thick gold target at large angles $\sim 172.6^\circ$ [21]. A CAD drawing of the Mott polarimeter is shown in Fig. 2.49. The differential cross section depends on the beam polarization through the interaction of the electron’s spin scattering on the magnetic field of the unpolarized high Z nucleus induced by their relative motion

$$\sigma(\theta) = I(\theta)[1 + S(\theta)\vec{P}_e \cdot \hat{n}]. \quad (2.12)$$

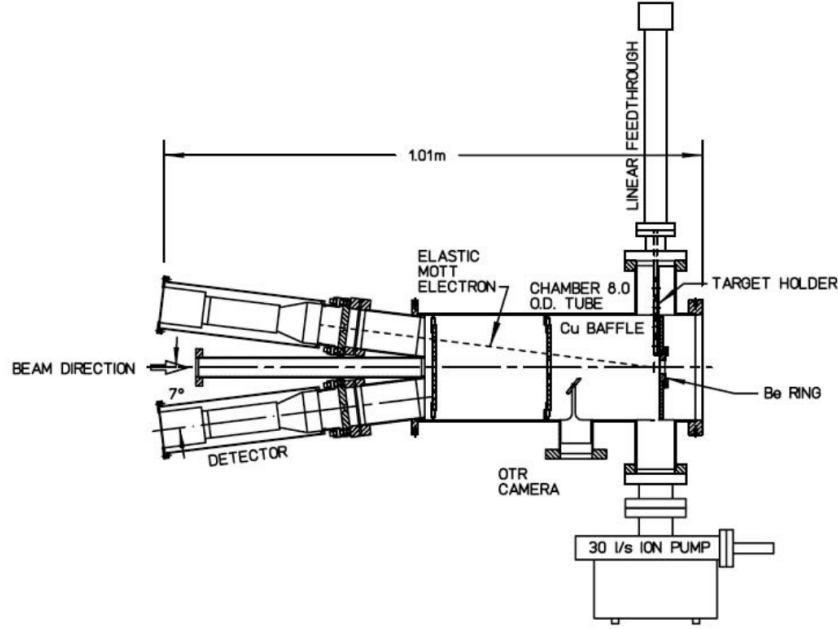


Figure 2.49: CAD drawing of the Mott polarimeter in the 5 MeV region of the injector. Reproduced from [25].

In the differential cross section $S(\theta)$ is the “Sherman” function, or the polarimeter’s analyzing power, and $I(\theta)$ is the spin-averaged scattering rate. Taking an asymmetry between the electrons scattered to the left and right,

$$A(\theta) = \frac{N_L - N_R}{N_L + N_R} \quad (2.13)$$

allows cancellation of the scattered rate from the measurement and leaves us with just the Sherman function and beam polarization,

$$A(\theta) = P_e S(\theta) \quad (2.14)$$

The Sherman function is well known for the injector Mott polarimeter, and the polarization in both transverse directions is measured [25]. In this way the total magnitude of the polar-

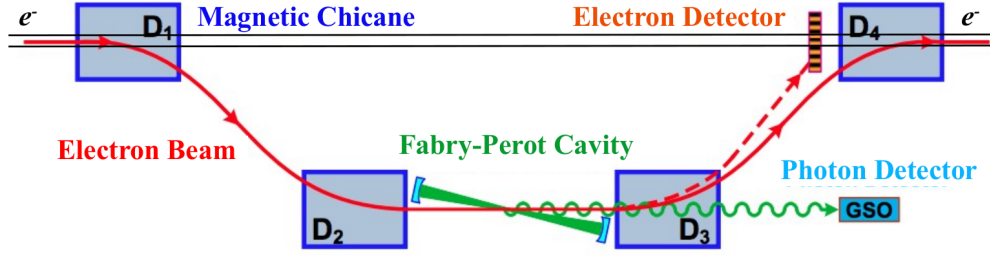


Figure 2.50: Schematic drawing of the Compton polarimeter in the Hall A beamline. Reproduced from [28, 33].

ization is measured. The launch angle in the injector is optimized for the chosen accelerator energy and the spin precession resulting from the recirculation arcs by using the polarimeters in the halls to simultaneously measure the magnitude of the longitudinal polarization, along with the transverse polarization measurement in the injector. This process is called a “spin dance,” and is performed when bringing the accelerator back online by ensuring that the full magnitude of the polarization measured by the Mott polarimeter, to within one or two percent, is delivered as longitudinal polarization in all of the halls.

2.11.2 Compton Polarimeter

The Compton polarimeter uses Compton scattering of the incident electron beam on a polarized laser “target” ($e^- + \gamma \rightarrow e^- + \gamma$) to measure the scattering rate asymmetry and therefore the polarization of the electron beam [33, 66]. The Compton asymmetry is related to the beam polarization as

$$A_c = P_e P_{laser} A_a \quad (2.15)$$

where A_c is the Compton scattering rate asymmetry, P_e is the polarization of the electron beam, P_{laser} is the polarization of the laser light, and A_a is the theoretical analyzing power of the Compton polarimeter under perfect polarization conditions, which is several percent.

The Compton polarimeter, whose schematic is shown in Fig. 2.50, consists of a four-dipole magnetic chicane bend which pulls the electron beam away from the standard Hall A beam-line and onto a laser table system, with dedicated collimation and BPMs, for optimizing the electron beam scattering through the prepared laser light.

The Compton laser system uses a Nd-YAG laser to produce $1064nm$ infrared light which is passed through a PPLN frequency-doubling crystal to convert the light to $532nm$. The scattering rate of the electron beam with light is very low, which allows CREX to run the Compton polarimeter simultaneously with production running. To amplify the scattering rate, so that a statistically significant measurement of the polarization can be made over the course of a few hours, the laser light is passed into a Fabry-Perot amplifying cavity with a feedback system to cause the laser light to constructively interfere and generate a power of upwards of $1kW$ within the scattering region. With this amplified laser in place, about a 10^{-9} fraction of the electrons are scattered, where the electron and photon both scatter downstream and are measured in dedicated electron and photon detector systems. The unscattered beam continues through the chicane and into the hall, unperturbed, for use in CREX.

The electron detector was not operational for CREX, so the primary measurement comes from the photon detector, which is a Gadolinium Orthosilicate (GSO) crystal scintillator dry-mount (without any optical grease or light guide) coupled to a PMT [28]. The upstream beamline components are a non-trivial source of background signals from beam scraping and halo scattering bremsstrahlung and synchrotron radiation, and so lead collimation and scanning finger scintillators are put in place to mitigate these backgrounds. Careful beam steering and Compton scattering rate optimization is regularly performed with the assistance of the accelerator operators and careful Compton data quality monitoring, which are important for the minimization of systematic errors and background contamination subtraction.

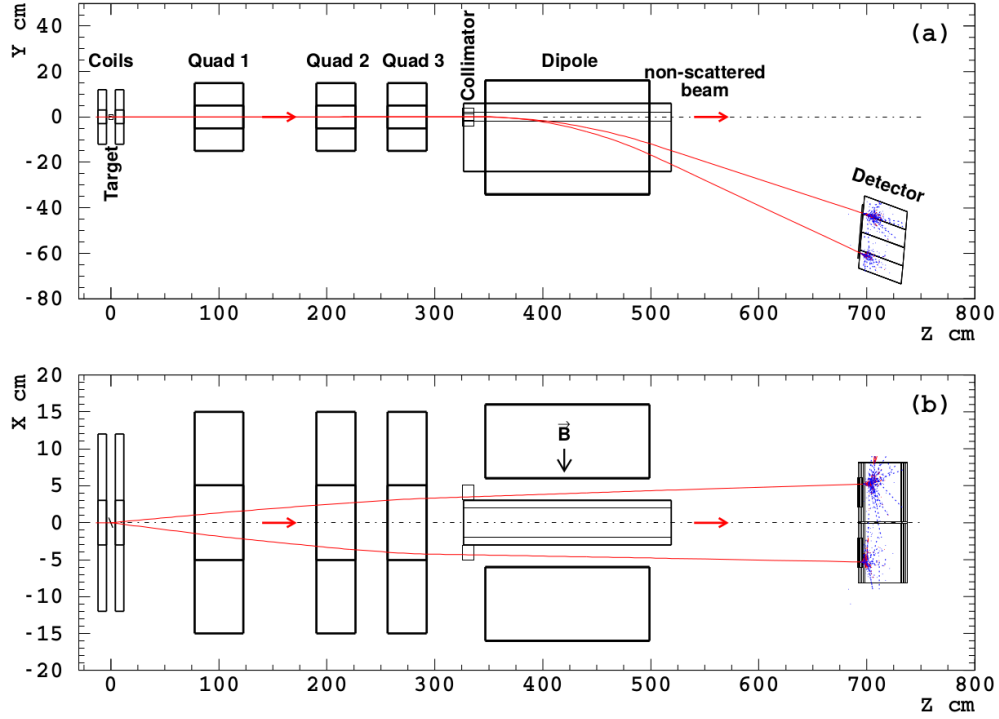


Figure 2.51: CAD schematic of the Møller polarimeter in Hall A. Reproduced from [21].

2.11.3 Møller Polarimeter

The Hall A Møller polarimeter uses a magnetically-polarized thin iron foil target to perform Møller scattering ($e^- + e^- \rightarrow e^- + e^-$) of the incident beam with the polarized electrons in the iron to measure the beam polarization,

$$A_m = \vec{P}_b \cdot \vec{P}_{Fe} A_{zz} \quad (2.16)$$

where A_m is the Møller coincidences scattering asymmetry, P_{Fe} is the iron target polarization, and A_{zz} is the analyzing power for longitudinally-polarized scattering which is known from theoretical calculations and Monte Carlo simulations.

The Møller polarimeter needs to achieve low systematic error to satisfy requirements

for the CREX A_{PV} measurement. To improve accuracy, a high magnetic field of several T generated by a Helmholtz coil surrounding the target is used to saturate the polarization of the iron foil target, which removes much of the iron foil polarization uncertainty. Multiple iron foil thicknesses are used to determine measured asymmetry dependence on thickness and study the impact of potential wrinkles in the thin foil.

The Møller polarimeter spectrometer system is composed of collimation, three focusing quadrupole magnets and the beamline bending dipole; it transports the coincident Møller scattered electrons into matching calorimeter and scintillator detectors on each side of the beam line, and the asymmetry of coincidences is the measured A_m used to extract P_e . A schematic of the Hall A Møller polarimeter is shown in Fig. 2.51. Substantial improvements to the existing Monte Carlo and its use in systematic studies of tuning the Møller spectrometer for the PREX II and CREX experiments allow a robust comparison of the measured asymmetry with predictions and optimizing the magnet tune to minimize the uncertainty on A_{zz} , leading to a small systematic error at the $\sim 1\%$ level.

Møller polarimetry measurements require low beam current, around $1\mu A$, to minimize target heating and radiation load in the hall, and they require redirecting the beam onto the separate Møller target apparatus and are therefore invasive to CREX production running. Møller measurements take around four hours to complete, as well as a similar amount of time to ramp the magnets before and after the measurements. The measurements are performed approximately every two weeks throughout the experiment, but due to the beamline bending dipole magnet having problems with quenching, a portion of CREX running is not covered adequately by Møller measurements and Compton measurements are used to compare with Møller results and provide full coverage of CREX.

2.12 Experimental Summary

With all of these measurements and handles for controlling the electron beam production, delivery, scattering, and asymmetry analysis, CREX is well prepared to make a systematically controlled and statistically significant measurement. The data quality and the offline data analysis are described in the following chapter.

Chapter 3

Data Analysis

To precisely extract A_{PV} and the weak form factor (F_W) from the data produced by the finely tuned injector, beamline, polarimeters, and Hall A described before, it is necessary to understand and correct for sources of false asymmetry and to provide estimates of their corrections and systematic uncertainties. This chapter goes into the details of processing the data, calculating helicity-correlated beam corrections, and evaluating their systematic uncertainties for the CREX asymmetry result. Detailed discussions of the corrections and systematic uncertainties from polarization, kinematics and acceptance function, and transverse polarization are covered in the dissertations of other students collaborating on CREX.

CREX ran from December 6, 2019 until September 18, 2020 with several down times and the operations restrictions imposed by the onset of the COVID-19 global pandemic. The experiment ran in production mode at $150\mu A$ beam current, with hour-long DAQ runs that are later subdivided into miniruns each containing five minutes worth (9000 multiplets) of “good” asymmetry data. “Good” here is determined by applying cuts to the helicity events to focus only on the stable beam current and position running conditions, within the range of calibration applicability. After all cuts CREX measured 85.5 million good multiplets

contained within 8527 miniruns over 1386 production DAQ runs.

The data are extracted from the DAQ modules and saved to raw data files by the CODA system running on the Hall A Counting House DAQ workstation computers, is analyzed and turned into partially calibrated and corrected asymmetry data online by the JAPAN analyzer, and afterwards is carefully analyzed using offline analysis programs and scripts to optimize cuts, produce calibrations, and optimize the beam corrections. Slow-control flips of the sign of the scattered electron asymmetry with respect to the helicity control electronics are performed by changing the laser circular polarization direction with an insertable half waveplate (IHWP) after 6-8 hours of good data collection, which form “slugs” of data with the same sign, and by performing a double Wien flip of the electron spin direction after several weeks, which was done twice over the course of the experiment. Every week dedicated calibration runs are performed to provide measurements of the PITA slope for use in the charge feedback system and of the pedestals for the BPMs, BCMs, SAMs, and detectors in the HRSs. After the event cuts and pedestals are applied, the calibrated raw asymmetry data is available as the starting point for corrections and systematic uncertainty estimates.

The raw asymmetry data must be corrected for helicity-correlated beam asymmetries (HC A_{beam}) to remove beam current and position fluctuations. This is done both to remove false asymmetry backgrounds from the measurement and to remove excess noise from the asymmetry distributions so that their widths correspond closely to counting statistics and can be used to find statistical weights for averaging asymmetries across the experiment. Other background asymmetries are measured and contribute corrections and systematic uncertainty to the extracted physics asymmetry, A_{phys} , and the kinematics and acceptance function are used to extract and provide systematic uncertainty limits for the weak form factor, F_W , whose interpretation is the subject of the following chapter.

3.1 Pedestal Calibration

To obtain accurate measurements of the helicity-correlated detector asymmetries and position differences it is necessary to calibrate the monitors and DAQ channels that read them out for dark current signals that produce a “pedestal” baseline and subtract them from the detector yields. The pedestal shifts the signal, S^{phys} , measured in the DAQ as

$$S_{R(L)}^{meas} = S_{R(L)}^{phys} + S^{ped}, \quad (3.1)$$

such that measured asymmetries in the DAQ depend on their pedestal as

$$A_{meas} = \frac{S_R^{meas} - S_L^{meas}}{S_R^{meas} + S_L^{meas}} = \frac{S_R^{phys} - S_L^{phys}}{S_R^{phys} + S_L^{phys} + 2S^{ped}}. \quad (3.2)$$

To remove the pedestal contribution from measured asymmetries we correct the measured helicity event yields in the raw data decoding, using pedestals measured with dedicated calibration runs that correspond to the same run conditions. To monitor the changes in detector and DAQ pedestals and provide the optimal run-ranging for pedestal application and averaging, calibration runs are performed on a weekly time-scale, as well as whenever the detectors experience significant configuration changes. These calibration runs are performed in several ways, with separate dedicated runs each focusing on the BCM calibration, the PMT-based detectors (the main detectors, auxiliary A_T detectors, and SAMs), and the BPMs.

We first calibrate the primary BCM to the Unser, described in section 2.9.2, to establish a connection to zero current beam-off for the primary BCM. Then we calibrate the other BCMs and the PMT-based detectors with a faster current ramp against the primary BCM, and also calibrate the BPMs using a separate current ramp where the BPMs are switched to fixed

gain mode at full $150\mu A$ current to obtain pedestals for the four wires. Independently, the beam-off pedestal value is tracked, monitored and compared with the current ramp derived pedestals for the PMT-based detectors.

Inaccurate calibration of the pedestals contribute error to the extracted signal, $S_{L,R}^{extracted} = S_{L,R}^{meas} - S^{ped} - \delta S^{ped}$, where δS^{ped} is the pedestal error, which leads to modified scaling of the extracted $A_{extracted}$ due to applying pedestal corrections,

$$A_{extracted} = \frac{S_R^{extracted} - S_L^{extracted}}{S_R^{extracted} + S_L^{extracted}} = \frac{S_R^{phys} - S_L^{phys}}{S_R^{phys} + S_L^{phys} - 2\delta S^{ped}} \simeq A_{phys} + \delta A_{ped}. \quad (3.3)$$

A fractional pedestal uncertainty $\frac{\delta S^{ped}}{S^{phys}}$ linearly impacts the scale of measured asymmetry to first order, so we make efforts to reduce the calibration error as much as possible.

We monitor the stability of the pedestals and estimate a pedestal error from its uncertainty compared to the full scale of the signals to estimate a systematic uncertainty in the detected asymmetry. PMT-based detectors and BPMs wire signals all depend on the beam current, and so inadequate calibrations of any of the pedestals will show up as residual correlations between the different detectors, and dedicated runs with large Pockels Cell induced PITA asymmetry are used to monitor residual correlations scales, in addition to their primary purpose of determining the PITA slope for use in the online charge feedback.

3.1.1 Unser

Pedestals are determined by comparing the current response of detector signals to the highly linear Unser beam current monitor. However, the Unser is quite noisy and its beam-off pedestal is unstable on minute time scales, so it is difficult to use it to calibrate everything precisely. As a result, we use the accurate but imprecise Unser monitor to calibrate the precise but inaccurate RF Cavity BCMs, so that they can then be used to calibrate the rest

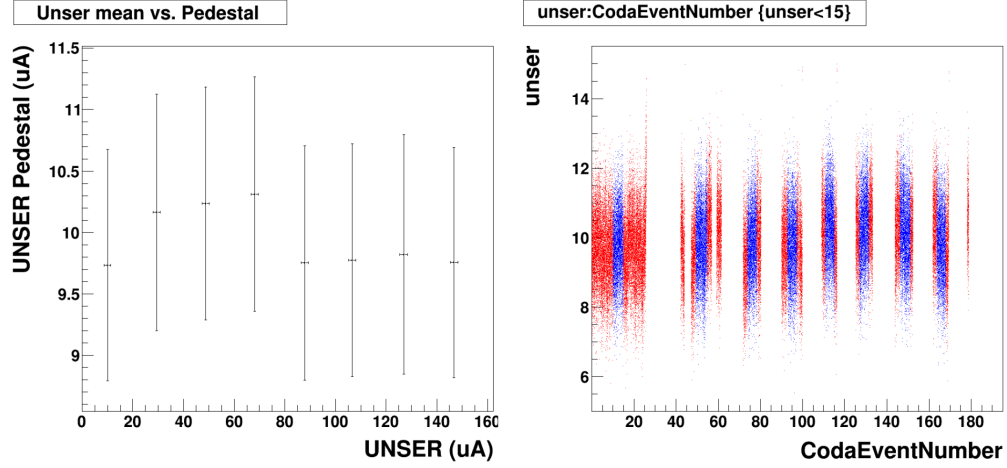


Figure 3.1: Example Unser relative calibration data showing the beam-off pedestal values for the Unser on the left, with their cleaned source distributions on the right. The cleaned data is shown in blue and the red data is cut to provide a stable pedestal with no beam-on data included. The RMS of the data in the blue distribution is used as the uncertainty for the Unser pedestal, on the left, and its uncertainty is propagated to the points used in the Unser relative pedestal calibration fit shown in the next figure.

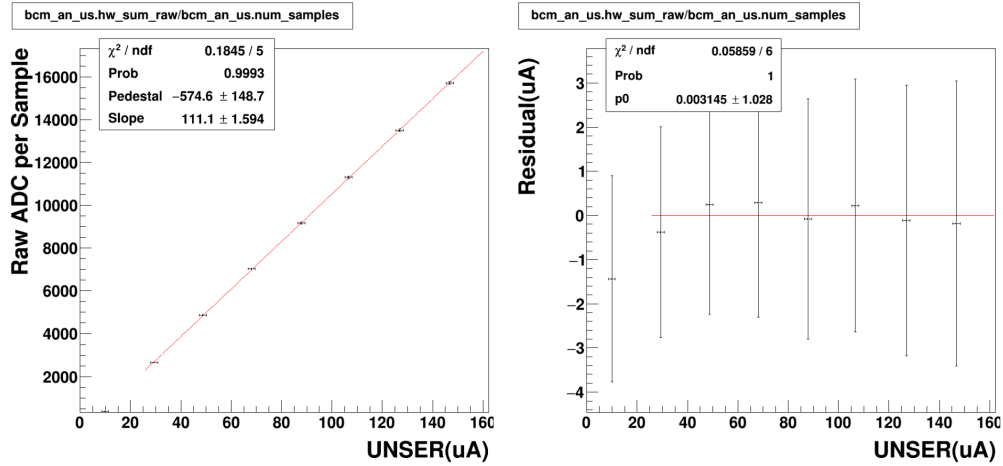


Figure 3.2: Example Unser relative calibration fit for the BCM AN US pedestal on the left, and residuals of the fit on the right. The Unser relative calibrations use the RMS of the beam-on and beam-off data as the uncertainty in the mean values and Unser's subtracted pedestal, shown in the previous figure.

of the detectors. The BCM versus Unser calibration procedure involves taking minute scale quantities of data with no target in place, alternating between beam-off and beam-on, with the beam-on data stepping upwards by $10\mu A$ for each new point in the pedestal calibration ramp between the beam-off periods. To extract the pedestal, a first-order polynomial linear fit is performed between the BCM and Unser. Due to the slow drift of the Unser’s beam-off pedestal, it is necessary to fit the response not across all events, but instead to form average quantities for each fixed current step and to subtract the local pedestal of the Unser for each step calculated from the neighboring beam-off data.

A clean Unser pedestal is obtained for each step by cutting away data from the beam ramping up and down, as shown in Fig. 3.1. The mean values for each step are computed from a histogram of the current for both monitors during that step, and the uncertainty for each step is taken from the RMS, because the Unser contains a substantial amount of non-statistical fluctuations. The BCM pedestal calibrations relative to the Unser, an example of which is shown in Fig. 3.2, are fit over the range of reasonable linearity for the BCMs, which is taken to be from $25\mu A$ to $150\mu A$ for CREX. Studies scanning the low range limit of the fit do not see a significant impact from it on the results. The pedestal extraction fits do not account for quadratic non-linearity in the BCMs, as we only intend to extract the dark current corresponding to beam off for use in the pedestal correction and non-linearity is considered as an additional source of systematic error.

3.1.2 BCMs and BPMs

We choose to use the upstream analog BCM (referred to as “AN US”) as the reference BCM calibrated relative to the Unser, as it displays the most stability across the run and has a more similar latency to the PMT detectors than the digital BCMs do. Because BCM AN

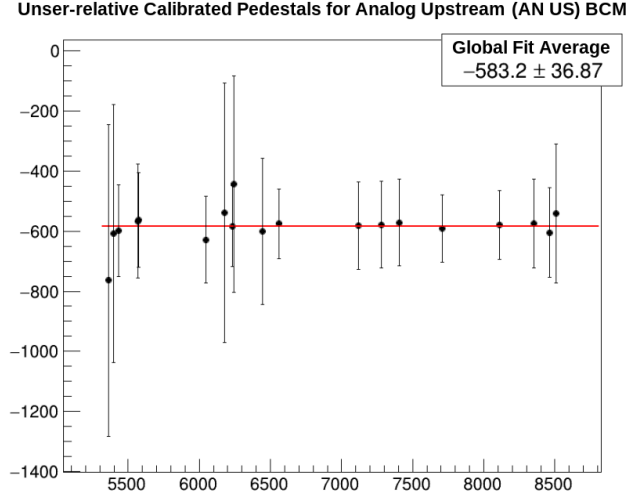


Figure 3.3: Global average of the Unser-relative pedestals for the normalizing BCM AN US.

US shows a stable pedestal across the experiment, we take its pedestal from a global average across all of the Unser-relative calibration runs, which is shown in Fig. 3.3. Averaging the pedestal over all of the calibration runs also gives us more certainty in the extraction of its pedestal relative to the noisy Unser. PREX II had more sub-segmentation in the choice of normalizing BCM and pedestal, caused by limitations in the BCM hardware, which were resolved before CREX ran.

All of the other monitors, the analog and digital BCMs, cavity BPMs, stripline BPMs, and PMT-based detectors, are then calibrated with respect to the normalizing BCM AN US. These calibration fits come from additional pedestal calibration runs where the fit is performed similarly to the Unser-relative calibration runs but each current step's point error is taken from the current step histograms' RMS/\sqrt{N} . This is different from the Unser-relative case of only using the RMS because the normalizing BCM AN US is much less noisy than the Unser during the steps. An example fit of the upstream left (USL) PMT-based main detector typical of the current ramp pedestal calibrations, is shown in Fig 3.4. For the BPM calibration runs the target is taken out of the beam for safety and the beam is ramped

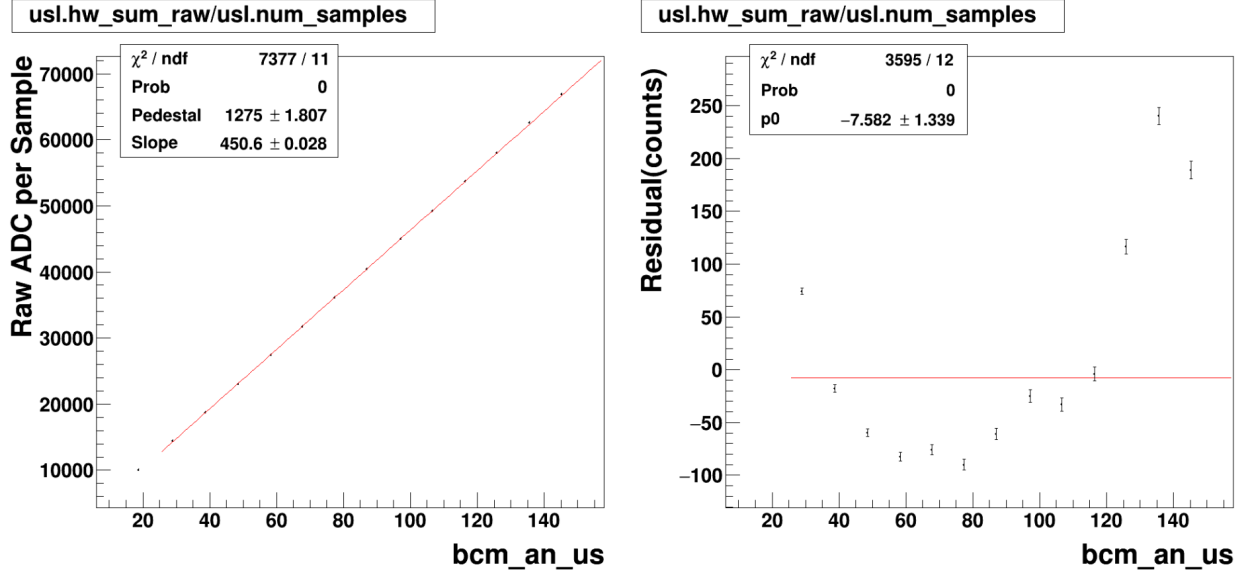


Figure 3.4: Example Normalizing BCM AN US-relative calibration fit for the USL main detector pedestal on the left, and residuals of the fit on the right. The Normalizing BCM AN US-relative calibrations use the RMS/\sqrt{N} of the beam-on data as the uncertainty in the mean values.

in several steps while the BPMs are left in fixed gain mode so that the response is relative to their gain setting at full $150 \mu\text{A}$ current. The BPM pedestals are segmented across the experiment based on when each calibration run was taken.

The BCMs, cavity BPMs and PMT-based detectors are calibrated using current ramp runs taken with the target in place and under nominal production conditions, so that the PMT-based detectors' responses are useful. The cavity BPM pedestals are segmented based on when each calibration run is taken, but the analog downstream and digital BCMs are segmented only once, based on a noticeable shift in the pedestal after the summer downtime. Segmentation of pedestals across the run is done by averaging the pedestals obtained from each calibration run together, with the segmentation corresponding to the two main run periods, before and after the COVID shutdown at run 7500. An example of an averaged pedestal for the digital downstream (referred to as “DG DS”) BCM for the pre-COVID

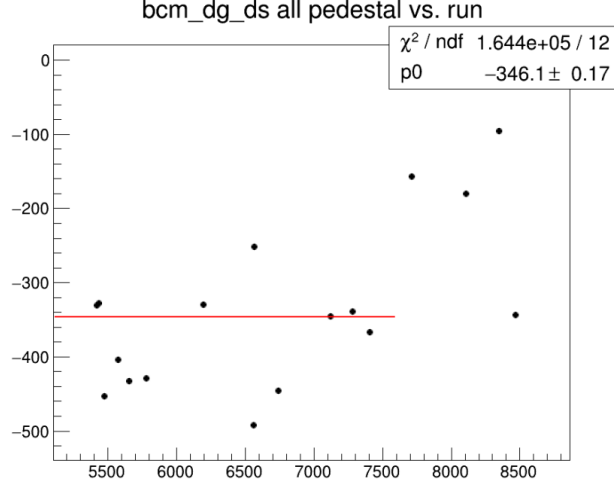


Figure 3.5: Global average over the first run period of CREX of the Normalizing BCM AN US-relative pedestals for BCM DG DS.

shutdown period is shown in Fig. 3.5. The segmented pedestal map files and analysis scripts are contained within the JAPAN analysis software GitHub repository and detailed descriptions of the analysis are contained within the PREX collaboration electronic logbook. All of the algorithms and fit procedures are shared between PREX II and CREX, except for the choice pedestals of PMT-based detectors, described in the next subsection.

3.1.3 PMT-Based Detectors

The PMT-based detectors, the SAMs, auxiliary A_T detectors, and main integrating detectors (the upstream left and right detectors, referred to as “USL” and “USR”), are calibrated as discussed in the prior section, but because their non-linearity is known to be very small from bench-top studies performed at ISU, described in [28], and we have sufficient data with the beam off, we choose to utilize the pedestal value obtained by directly measuring the ADC level with the beam off. The status of the beam current is determined using the digital downstream BCM, which is most capable of determining the difference between very

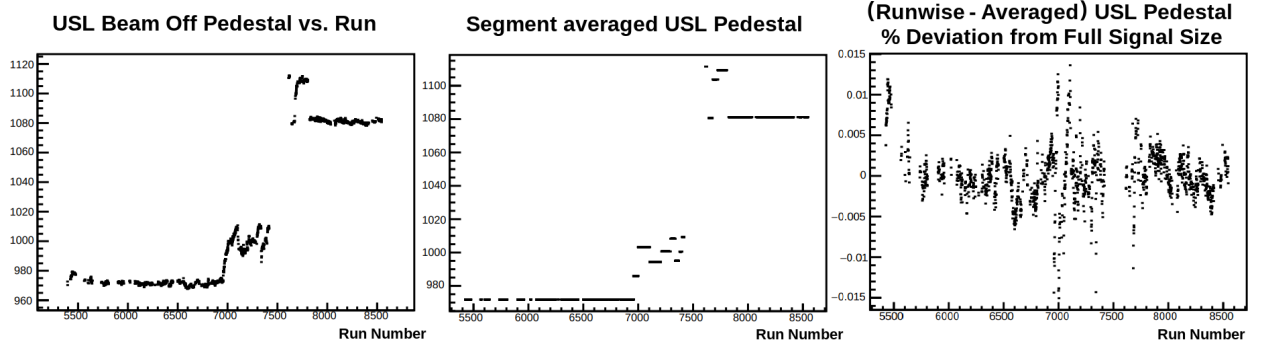


Figure 3.6: Beam-off pedestals measured for each run in CREX (left), their stable-segment averages (middle), and the percent deviation from the full beam-on signal size of the difference between the stable-segment averaged and run-wise beam-off pedestals (right). The effect on precision of averaging is seen to be minimal, well below the 0.1% level.

low and completely off levels of beam current, which the analog BCMs are incapable of distinguishing. These beam-off pedestals are similar below the percent level to the pedestals obtained through the current ramps, and are stable over several day time scales. To provide pedestals relevant to each time period, averages over the run-wise calculated beam-off pedestals are performed, and the deviation from the average is very small, below the 0.1 percent level, within these averaging segmentations. Choices for splitting the averaging of beam-off pedestal are made for each detector individually by looking at the behavior of the beam-off pedestal versus time by eye, and the quality of the segmentation is verified with plots of the deviation, as for the case of the USL main detector shown in Fig. 3.6. The beam-off pedestals are obtained similarly for the auxiliary A_T detectors and the SAMs.

3.2 Normalized Asymmetry

As discussed before in section 2.9, the raw detector asymmetry contains noise contributions from the helicity-correlated beam intensity and position fluctuations. The beam current (or “charge”) asymmetry directly affects the measured yield and raw asymmetry,

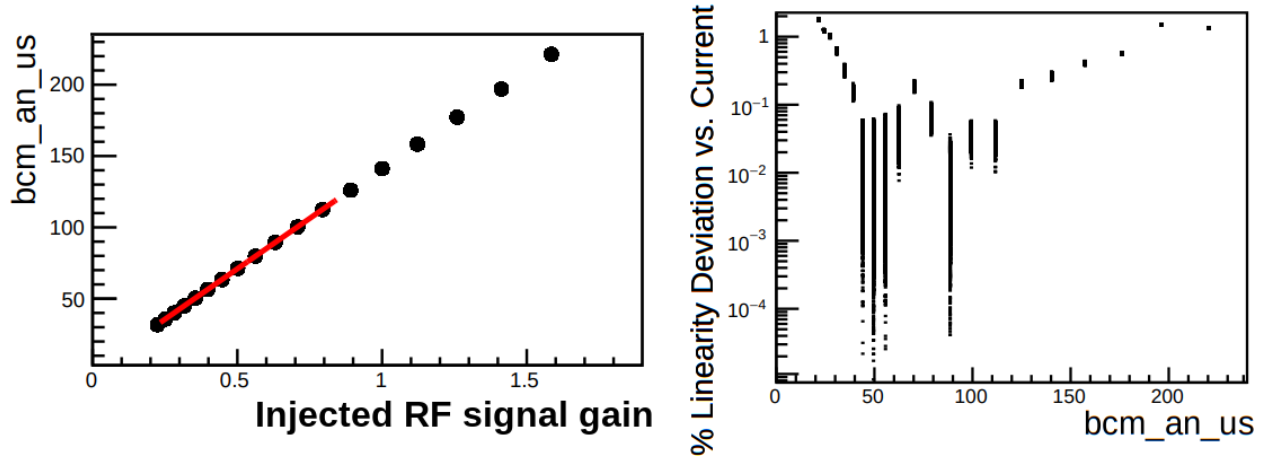


Figure 3.7: Plots showing the response of the normalizing BCM AN US versus injected RF signal on the left, and the percent deviation from the linear fit across that range on the right. RF injection tests were performed before CREX to optimize the signal input into the analog BCMs' 10 MHz down-converter box to maximize the linearity in the CREX current range around $150\mu A$. The non-linearity measured in these RF injection scans is approximately at the 0.3% level.

and so we normalize the detected signal, Y , by the beam current, Q , within each helicity integration window,

$$y = Y/Q, \quad (3.4)$$

removing the dependence of scattered rate on beam intensity. Calculating the detected asymmetry with the normalized detector yield y then removes the effect of the beam intensity asymmetry, A_Q , simplifying with $\langle y \rangle_+ \simeq \langle y \rangle_- = \langle y \rangle$ yields

$$A_{raw} = \frac{y_1 - y_2 - y_3 + y_4}{y_1 + y_2 + y_3 + y_4} = \frac{\langle y \rangle_+ - \langle y \rangle_-}{\langle y \rangle_+ + \langle y \rangle_-} \simeq \frac{\Delta y}{2\langle y \rangle}, \quad (3.5)$$

where Δ indicates the average helicity-correlated difference and $\langle \rangle$ indicates averaging over the four events within the quartet. To first order this is

$$A_{raw} \simeq \frac{\Delta Y}{2\langle Y \rangle} - \frac{\Delta Q}{2\langle Q \rangle} = A_{rate} - A_Q. \quad (3.6)$$

With the pedestals properly accounted for in the calculations of charge Q and yield Y , we are able to consider the impacts of non-linearity and pedestal error on the raw asymmetry.

The systematic uncertainty due to non-linearity in the PMT detectors' measurement of the scattered rate is at the 0.3% level, as discussed in [28]. The systematic uncertainty in the normalizing BCM AN US due to non-linearity and pedestal error is at the 1% level. This limit is determined by looking at the measured non-linearity from an RF injected signal scan performed before CREX ran, shown in Fig. 3.7, which shows agreement at $150\mu A$ at around the 0.3% level with a power-law fit to the RF injected signal. Additionally we have uncertainty due to the global Unser-relative pedestal's uncertainty, shown in Fig. 3.3, relative to the ~ 16100 ADC channels at $150\mu A$ full scale BCM signal, where $37/16100$ ADC channels corresponds to a $\sim 0.3\%$ level uncertainty.

We use comparisons between the available analog and digital BCMs asymmetries, taken as double differences, to check for over-correction of the normalizing BCM by the charge feedback system. The charge feedback system operates on the charge asymmetry in the feedback BCM, which for CREX is the same as the normalizing BCM, and it is possible that the feedback system may pick up on instrumental noise and over-correct the device. The double difference comparisons with other BCMs provide confidence in the central value of the normalizing BCM AN US at the $\sim 1ppb$ level. The effects of BCM and PMT pedestal and non-linearity systematic uncertainties on the measured A_{raw} are determined after the data-set is finalized through the event cuts, discussed in the next section. The systematic

uncertainty is from the false asymmetries and non-linearities are calculated as the fraction of the weighted-averaging asymmetry. The weights correspond to the statistics of the main detector asymmetry, which are made available by removing the remaining position dependent HC A_{beam} noise from A_{raw} , and is the topic of the remainder of this chapter.

3.3 Cuts

Preparing a cleaned data-set for asymmetry analysis requires careful monitoring of every event and the application of helicity event level “event cuts” to remove data taken under non-ideal electron beam, experimental hardware, or DAQ running conditions. Cuts are handled by the data decoder, “Just Another Parity ANalyzer” (JAPAN) which is discussed in detail in sections 3.6 and 4.2 of [67], and are only applied on the event level data, to avoid any biasing of the asymmetry results computed at the multiplet level. The data considered for cuts includes the raw readout from the DAQ modules, including DAQ hardware error metrics, and also the beam current and position of the beam, after pedestal corrections are applied. The current and position cuts use calculations on moving “event rings” to determine the average location and RMS jitter of the beam. The mean and RMS are compared to limits that define comfortable and stable running conditions. The cuts throw out data failing these stable condition checks, and to ensure insensitivity to measured asymmetries to remain unbiased, all calculations are performed on time scales much longer than the 30 Hz multiplet.

We place limits on the beam current to ensure viability of the pedestal calibrations and consistence of statistical weight for each multiplet, on the beam positions to ensure stability of the corrections and to avoid including any copper scattering contamination from hitting the target ladder, and on the CODA data-stream itself to ensure perfect performance from

all of the DAQ components. Each type of cut that fails for each helicity event sets a bit in the affected device’s specific error code variable and, for cuts affecting devices included in the global data-set cut, sets a bit in the global “ErrorFlag” 32-bit integer variable. The primary devices included in the global level cut are the BPMs along the beamline and in the Hall A arc for position stability, the normalizing BCM AN US for beam current cuts and BCM AN DS for comparisons with it, and the main integrating detectors and the auxiliary A_T detectors for ADC hardware error checks. The full list of bits corresponding to cuts is given in table 4.5 of [67] and the code is available in the JAPAN GitHub repository [68].

The logic, mathematics, and criteria for the choice and implementation of the chosen cuts were initially developed by the Ohio University group and the process of monitoring the data quality and fine tuning the cuts involved the dedicated efforts in online and offline data analysis and data cleaning of all the graduate students working on both PREX II and CREX. Due to the dependence on subsequent steps in the analysis, the inclusion of beam modulation active data is discussed at the end of this chapter in section 3.7, but it is included in the data-set and it is important to note that the development of cuts on the beam positions and the tuning of the beam modulation system intentionally considered the need to allow frequent dithering of the beam while passing the cuts without relaxing the quality of the cuts or of the dithering calibrations.

3.3.1 Current Monitor Cuts

The BCM current readout is used to determine when the beam is on and cut away data immediately preceding a beam trip, during a beam trip, and for a few seconds after the beam has recovered to full current. Over the course of CREX the production beam current level and the trip recovery ramp rate vary, being adjusted by the accelerator operators. We

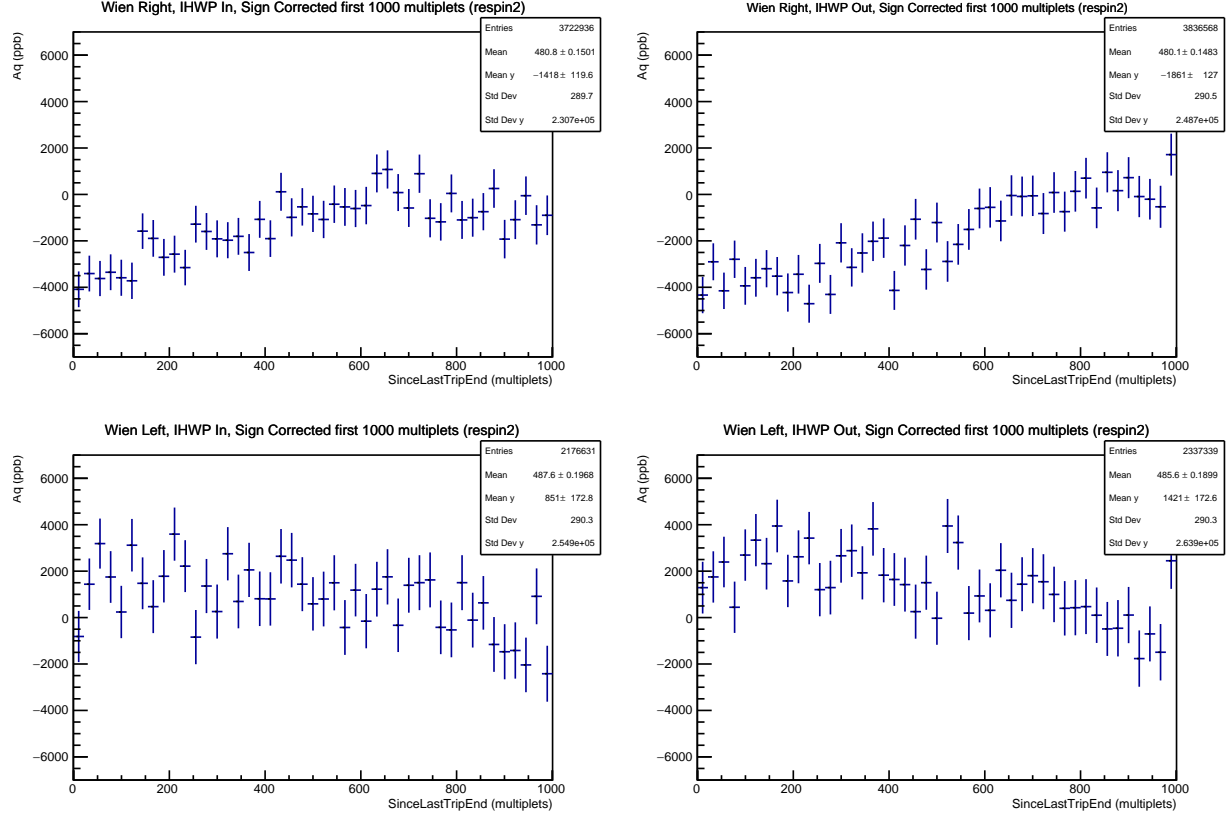


Figure 3.8: Plots showing the cumulative bias in the beam intensity asymmetry following beam trip recoveries, separated into the four states of the IHWP and Wien across the experiment. The beam trip recovery cut used in the online charge feedback analyzer is an additional 1000 events (250 multiplets) too long compared to what is used in the offline analysis, and these 250 multiplets are not included in the online charge feedback correction calculations and do not have corrections applied to them. The following 250 multiplets, starting at multiplet 250, are included in the correction calculations and begin to receive corrections based on the running feedback analyzer's event loop calculation including data from before the beam trip began. The third set of 250 multiplets, starting at 500, are fully corrected by the calculation made on the second set of 250 multiplets, and show a trend closer towards average null charge asymmetry. The effect changes sign under the Wien flip, indicating that it comes from a systematic effect in the Pockels Cell related to the beam ramping back to full current.

choose to keep the beam trip threshold current approximately $30\mu A$ below the running level, typically $120\mu A$ relative to $150\mu A$, and to remove the 1000 events, corresponding to nearly eight seconds of data, following the return to the running level.

Due to a mistake with the JAPAN cut map files during CREX running, the beam trip recovery extent cut length was accidentally left at 2000 events in the charge feedback engine, corresponding to the 240 Hz PREX II running set-up. As a result the online feedback analyzer for CREX 120 Hz running did not account for an additional 1000 events after each beam trip in its calculation of the PITA-based charge feedback loop. This data was not considered in the feedback calculation and did not have any corrections applied by charge feedback, but it is included in the offline analysis data-set by correcting the beam trip recovery extent cut to be only 1000 events long. As a result of the Pockels Cell's systematic induced PITA effect following current ramps, there is a non-trivial bias in the measured charge asymmetry after each beam trip from these 1000 events in the corrected-cut data-set. The bias in the charge asymmetry as a result of the too-long cut and inactive charge feedback is seen in an aggregate plot of the charge asymmetry versus time for data immediately following beam trip recoveries, shown in Fig. 3.8. This effect in the Pockels Cell changes sign with the double Wien flip change of the electron spin direction, which serves to cancel most of the magnitude of this effect across the full data-set, as similar amounts of data were taken in each Wien flip state and the too-long beam trip recovery extent cut was in place in the online charge feedback analyzer for the entire experimental run.

In addition to the beam current threshold used to determine beam trips, we also implement a cut on the beam current stability. The stability cut checks an event ring spanning 200 events, calculates the RMS of the events in the ring, and if the RMS is above the threshold level, cuts out the entire ring of events. Single event jumps in the gain of one of the analog BCMS occasionally occur, which requires the application of a global cut on the difference in

beam current measured between the upstream and downstream analog BCMs at the $0.15\mu A$ level. This BCM difference cut removes only a few dozen events across the run, but is needed to ensure the reliability of the BCM hardware.

3.3.2 Position Monitor Cuts

Similarly, cuts are placed on the BPMs' wires and calculated positions. We place upper limit cuts on each of the four BPM wires for the BPMs near the target, BPMs 1H04A, 1H04E, and 1H01, and in the energy sensitive region of the Hall A Arc, 1C11, and 1C12, to remove data taken near the BPM system's saturation level. Cuts are placed on the beam positions to remove data that could contain scattering from the edges of the ^{48}Ca target where the Copper target holder and frame could contaminate the asymmetry measurement, as well as to remove data with unstable beam positions that may add unwanted noise and instability to the measured rates.

The position excursion limits are typically cut at the $1mm$ level, to maintain confidence that the $2 \times 2\text{ mm}^2$ rastered beam is placed on the center of the ^{48}Ca target. Stability and "burp" cuts, calculated in the same way as the beam current cuts, are typically placed with $\sim 0.7mm$ limits on both of the calculated X and Y positions of the two target BPMs, 1H04A and 1H04E, and, when deemed necessary, upper and lower position limit cuts are placed. Upper and lower position cuts are sometimes placed on the energy sensitive BPM, 1C12, when deemed necessary to remove short energy jumps. Many of the beam position excursions are slow drifts that do not trigger the stability or burp cuts and they require cutting with event range cuts placed by hand, and the choice of limits for each of the position cuts changes across the data-set as beam conditions change. Due to the non-negligible impact of small changes in the pedestal, described in [69], we avoid placing upper and lower limit cuts on

the BPM directions and typically resort to event range cuts placed by hand.

3.3.3 Data Stream Cuts

Additional cuts monitor the quality of the data produced by the Parity DAQ, checking for hardware and software failures in the ADCs and issues with helicity decoding. The JAPAN analyzer checks each ADC channel every helicity event for failure, performing checks of whether the ADC has saturated, if number of samples recorded matches the set number, if the integrated “hardware sum” across the integration matches the sum of the four sub-blocks’ integrals, if the ADC’s event counter has incremented properly, if the ADC returns the same value twice in a row, or if the ADC reads out an uninitialized 0. These data-stream cuts ensure that every event in the data-set corresponds to correctly measured quantities, and also serve as checks of the health of the ADC modules, which occasionally develop broken parts and are replaced with spares. The global ErrorFlag cut variable also contains a bit corresponding to the beam modulation system actively modulating, in addition to dedicated variables containing the beam modulation coil status and ramp phase.

The ErrorFlag event cuts are also responsible for monitoring the helicity decoding and keeping the value of the additive blinding factor secret. The blinding factor is randomly chosen and adds with the same sign as the combined IHWP and Wien polarization flip relative to the helicity state in the Pockels Cell, and so any accidental changes in the polarization sign in the middle of a run, which happened during a handful of runs, must be thrown out of the data-set. If there is a change in the blinding factor or the electron’s polarization sign due to changes in the target position or IHWP state during a run, which are determined by reading their values from the EPICs system, the remainder of the run fails the blinding factor checks and fails the global cuts. The ErrorFlag event cut also monitors the decoded

helicity and cuts away the 30 multiplets of data at the beginning of the run when the helicity sequence seed is being determined or whenever a faulty helicity state is read out and the seed must be determined again.

3.3.4 Additional Cuts

Although the event cuts implemented in JAPAN are good at removing beam trips and many substantial position fluctuations, as mentioned before it is sometimes necessary to remove a range of events by hand when the motion is slow or below the threshold needed to allow the beam modulation active data to pass the cuts. Some runs contain HRS magnet trips midway through the run. When any of the HRS magnets trip we ramp the beam off and try first to bring the magnet back online, but if the magnet requires repairs and technicians are not available immediately then we simply take data with one arm running. For runs with mixed amounts of one and both HRS active data we remove the one arm running data with an event range cut. For the three times during CREX where only one HRS is available we split the one arm only run-ranges into their own slugs.

A total of 14 runs correspond to good production but are outside of the range of good calibrations or show questionable hardware behavior that is not easily removed with cuts; these runs are labelled as suspicious and are not included in the final data set. In total, 24 runs are included in the data-set with only one HRS arm active: slugs 124 and 143 are right arm only and slug 191 is left arm only. Incidents including suspicious conditions surrounding the ^{48}Ca melting incident and DAQ synchronization or helicity read out failures are also removed from the data-set.

3.3.5 Data After Cuts

The parity runs are labelled as production by the shift crew and have their quality marked during the prompt online analysis by the expert analysis shift worker and again later in the day by the weekly analysis coordinator (WAC). The runs are considered several more times and the cuts and pedestals are tuned in daily meetings led by the WACs during the experiment run and in weekly meetings during the offline analysis after the experiment. The offline analysis passes through two “respin” iterations, where pedestals and cuts are optimized and the data-set and corrections analysis are finalized. At each stage in this process we store the run labels and descriptions of the quality of the data and critical variables in the “Parity Violating Data Base” (PVDB), which is a PREX II and CREX specific implementation of the “Run Control Data Base” (RCDB) software maintained by various experimental groups at Jefferson Lab [70]. The finalized run-lists for PREX II and CREX are both available at hallaweb.jlab.org/rcdb, where PREX II spans the run range from 3000 to 5000, and CREX spans from 5000 to 8560.

CREX ran for several months, collecting 1386 hour long runs that pass all cuts, with 8527 total miniruns containing 87 million multiplet passing cuts, listed explicitly in table 3.1, with about a third of the beam availability time during those good runs failing cuts, not including the runs with data that is deemed unusable or when no beam is available. Because of the large amount of data, some of the noisy beam conditions and faulty hardware issues that we cut from runs when we see them are included in the later steps of the analysis and were only noticed when taking a final look at the data-set. To avoid performing another respin of the data-set we choose to simply remove these 16 miniruns, listed in table 3.2, corresponding to the few periods where data is included that should be cut [35].

Table 3.1: CREX data quantities after cuts.

Runs	Miniruns	Good Multiplets	Cut Multiplets
1386	8527	86840789	47003320

Table 3.2: Table of miniruns cut after the final analysis respin due to missed beam position and hardware problems [35].

Run	Minirun	Run	Minirun
6564	4	7211	4
6567	2, 4	7889	0
6571	3, 4	7942	5
6593	2	8036	2
6983	8	8240	1
7149	6	8549	0, 1, 4

3.4 Raw Asymmetry

With the pedestals, charge normalization and cuts all in place we have a clean dataset with a measured A_{raw} corresponding to the observed asymmetry in scattered rate in the main detector. Not all multiplets measure the scattered asymmetry with the same statistical precision. Due to the nature of integrating measurements, the only reliable way to determine the relative statistics of asymmetry measurements is from the width of the asymmetry distribution, which is why we give so much attention to maintaining stable beam conditions and strict data quality cuts. It is possible to extrapolate the approximate integrated rate from the PMT detectors' output raw voltage yield or from the relative beam currents, but both of these are susceptible to changes in the gain of the PMTs and BCMs, which are known to drift over the month timescales of the experiment. The measured asymmetry distribution widths however contain non-statistical fluctuations as long as HC A_{beam} noise is present. The beam current HC A_{beam} is corrected out of the A_{raw} measurement by the charge normalization procedure described above, which is possible because the charge asymmetry A_Q

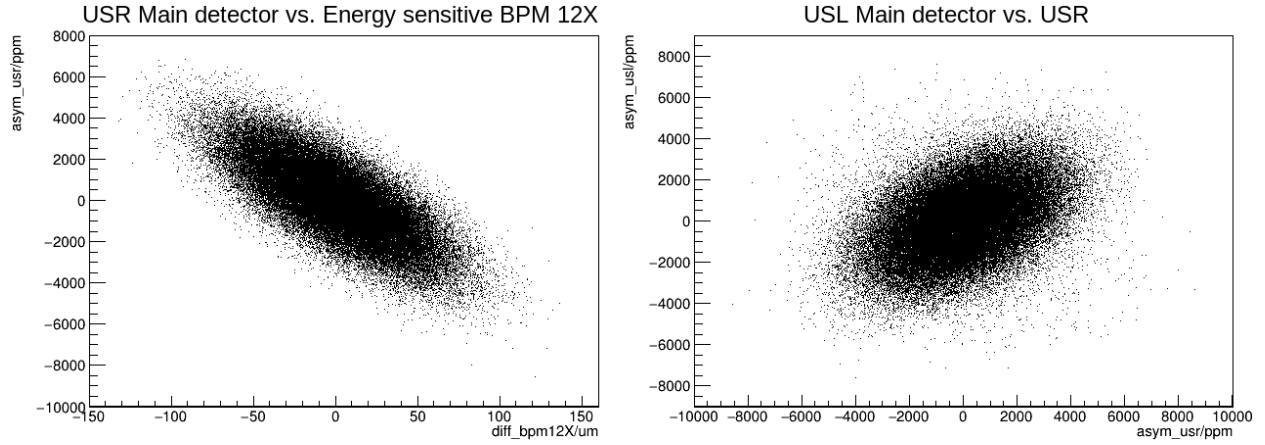


Figure 3.9: Correlations between the USR main detector asymmetry and the energy sensitive BPM 12X, left, and between the USL and USR main detectors, right.

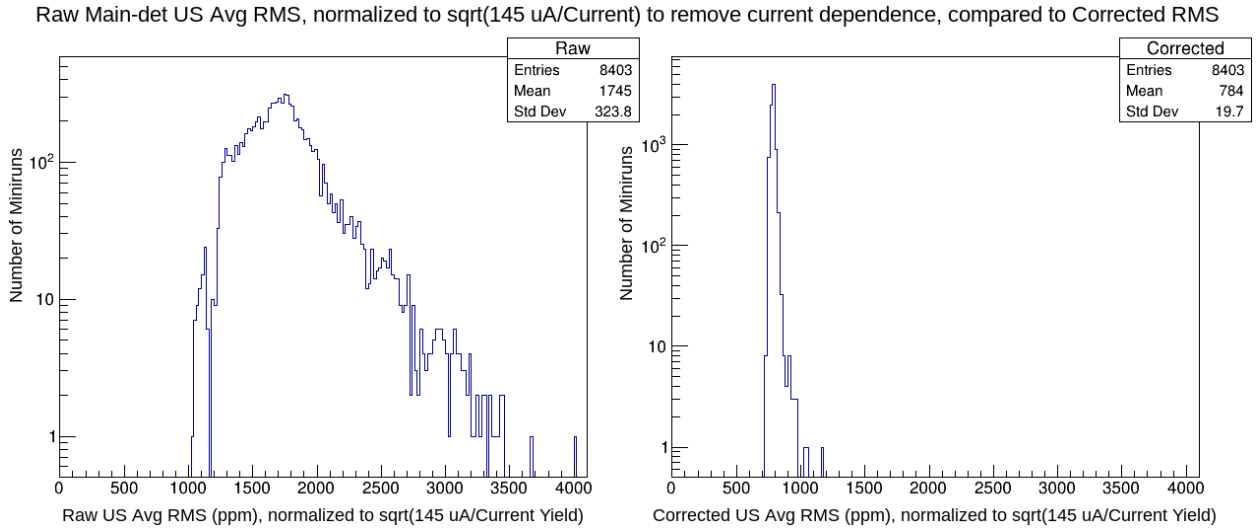


Figure 3.10: Display of the spread in the raw asymmetry RMS (left) compared with the stable and smaller corrected asymmetry RMS (right). The spread in the raw asymmetry RMS does not correspond to counting statistics, but rather comes from changing amounts of beam position noise and changes in measured rate's position sensitivity over the course of the experiment.

is uncorrelated, to first order, with the beam positions and energy. This decoupling of A_Q and beam parameters is due to the sufficient calibration of BPM pedestals and because the superconducting RF accelerator cavities have high Q and very little resistive load, mitigating beam current loading effects on the accelerated energy.

We correct for the energy and position dependent HC A_{beam} based on the correlations between the scattered rates and measured beam positions, which is the topic of the remainder of this chapter. An example of the A_{raw} correlation with BPM HC position differences and the correlation of raw USL with USR are shown in Fig. 3.9. The improvement in asymmetry widths across minirun timescales between the raw, uncorrected distributions and the beam position correlation corrected distributions is shown in Fig. 3.10.

The corrections and asymmetry distribution widths are calculated for the minirun timescales, corresponding to 9000 good multiplets, or five minutes of cumulative data that passes cuts, to provide consistent quantities of data and a fast enough time scale to ensure beam condition stability in the corrections analyses. The HC A_{beam} fluctuations are removed from the asymmetry distribution at the multiplet level through the beam position corrections and the ideal corrected distribution widths come from counting statistics alone, with a small amount of dilution from the integrating detectors' finite resolution, as described in section 2.7.3. With the statistically determined asymmetry distributions we get the asymmetry for each minirun from the unweighted histogram mean and uncertainty for each minirun. The j 'th minirun's mean is the mean value of the unweighted histogram, and the uncertainty on the mean is

$$\sigma_j = \frac{\text{RMS}_j}{\sqrt{N_j}}, \quad (3.7)$$

where RMS_j is the root mean square distribution standard deviation of the j 'th minirun's corrected asymmetry distribution of N_j multiplets. The RMS represents the distribution

width corresponding to the fundamental $\delta A = \frac{1}{\sqrt{N}}$ counting statistics uncertainty of each multiplet. Maintaining stable beam conditions keeps the rate in the main detectors stable, so that the RMS of the minirun distribution reflects the counting statistics uncertainty in each multiplet equally. The uncertainty on the minirun distribution mean provides the statistical weights,

$$w_i = \frac{1}{\sigma_j^2}, \quad (3.8)$$

which are needed to perform a weighted average to get the experiment's average asymmetry and other observable values.

With these minirunwise-corrected asymmetry means and weights, the weighted average asymmetry is calculated as

$$\langle A \rangle = \frac{\sum_j w_j A_j}{\sum_j w_j}, \quad (3.9)$$

and the uncertainty on the weighted average is

$$\sigma_{\langle A \rangle} = \frac{1}{\sqrt{\sum_j w_j}}. \quad (3.10)$$

These weighted averages can be calculated over ranges corresponding to slugs or other useful time-scales, and weighted averages can be performed in the same way across the larger time scale averaged values, using their weighted mean errors in the weights,

$$w_k = \frac{1}{\sigma_{\langle A \rangle_k}^2}. \quad (3.11)$$

The HC A_{beam} position dependent corrections, described in the following sections, are critical for achieving statistical asymmetry distribution widths for this averaging approach. The results of weighted averages for the various beam parameters, corrections, and final corrected

asymmetry values for CREX are discussed towards the end of the chapter.

3.5 Beam Corrections

The insufficiency of A_{raw} distribution widths for use as statistical weights and the possibility of non-zero accumulated HC A_{beam} backgrounds prompt the use of corrections to remove them at the multiplet level. Position, angle, and energy motion in the beam affect the cross section of scattering from the target and into the acceptance, driving changes in the measured rates that generate asymmetry fluctuations not coming from the counting statistics of the parity-violating electron scattering process we are investigating. Beyond non-statistically limited noise, the experiment-averaged position differences may contribute non-trivial contributions to the measured asymmetry that must be removed. Position measurements with the BPMs in the energy sensitive Hall A Arc and with BPMs near the target span the space of those position, angle, and energy fluctuations correlated to the main detector's signal. The detector-BPM correlations are used to derive first order correction slopes relating measured HC position differences to corrections to the A_{raw} distribution at the multiplet level, as

$$A_{det}^i = A_{raw}^i - A_{correction}^i = A_{raw}^i - \sum_j C_j \cdot \Delta x_{ji}. \quad (3.12)$$

where A_{raw} is the uncorrected raw asymmetry, C_j are the correction slopes, and Δx_{ji} are the helicity-correlated position differences for the j th monitor and i th helicity quartet,

$$\Delta x_{ji} = \frac{x_{1ji} - x_{2ji} - x_{3ji} + x_{4ji}}{4} = \frac{\langle x \rangle_{ji}^+ - \langle x \rangle_{ji}^-}{2}. \quad (3.13)$$

However, simple calculations of the correlations between the beam differences and the detector asymmetries are insufficient. Beam motion is also correlated between the various

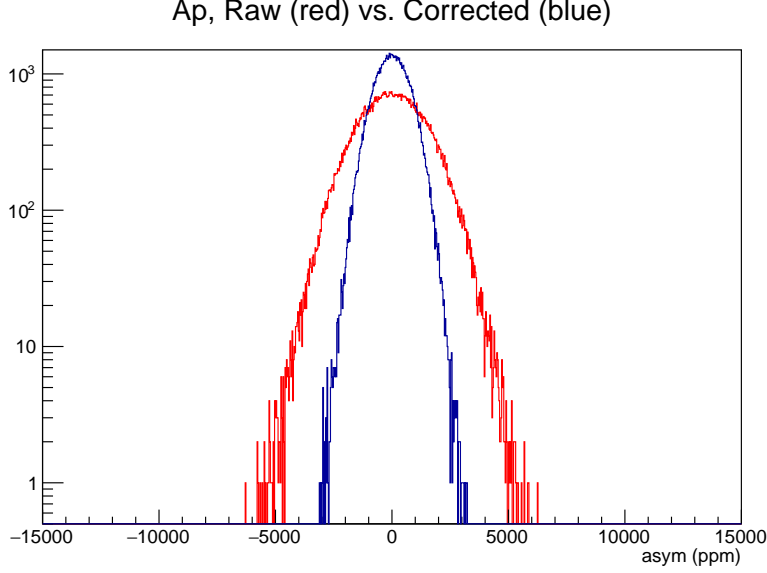


Figure 3.11: Display, for one representative run, of the spread in the raw asymmetry RMS (red) compared with the stable and smaller corrected asymmetry RMS (blue) corresponding approximately to the counting statistics distribution width, displaying the power of and necessity for performing beam corrections.

position monitors which make correlated measurements of the beam at different places along the beamline and are sensitive to couplings between the position, angle, and energy degrees of freedom in the accelerator system.

Prior PVES experiments have developed several techniques for calculating correction slopes from the BPM-detector correlations, which include multi-variable linear regression, beam modulation or dithering, and a new technique using Lagrange multiplier mathematics to incorporate constraints from both regression and dithering simultaneously, referred to as regression or “reg”, dithering or “dit” or “BMOD”, and Lagrange or “lagr” analyses, respectively. The Lagrange analysis was developed by Tao Ye in [67] for analyzing the PREX II data-set, where the GHz scale scattering rates pushed the limits of the BPMs resolution, necessitating a way to combine information from the multipletwise calculated regression correlations and the independently calibrated dithering data. The analysis of the

CREX data-set is described in the remainder of this section, which builds on the techniques of PREX II and prior PVES experiments to provide accurate HC A_{beam} corrections with small systematic uncertainty.

Correction slopes are calculated from correlations between the BPMs and the detectors. Linear regression calculates the correlations between the HC differences in the stochastic beam noise and motion versus the detected scattering asymmetry, measured at the multiplet level. Dithering calculates the correlations at the event level between the intentionally modulated beam position amplitudes and the detector yield responses, both relative to the independent modulations in separate dithering coils. Finally, the Lagrange method combines the correlation information from both regression and dithering.

Multiple correlation and slope calculation configurations are valid for each of these analysis techniques, including the use of different subsets and combinations of BPMs and beam modulation coils. The choice of BPMs and coils used in each technique is optimized to cover the full phase space of motion, requiring at least five independent beam position measurements to span the five degrees of freedom in X and Y position, X and Y angle, and energy. The BPM and coil choices are optimized to provide the most sensitivity to and to allow for comparisons between the correction slopes generated by the analysis techniques, which is used to evaluate the systematic error on the beam corrections. Because of changes of the beam optics over day and week timescales and of the scattering rate sensitivities to changes in beam delivery on minirun timescales, several degrees of segmentation and averaging are employed to guarantee the accuracy of the corrections. The power of beam corrections to remove beam jitter and random noise is shown in Fig. 3.10 across the entire experiment, as well as in Fig. 3.11 for one run.

3.5.1 Regression

Multivariate linear regression uses natural beam motion to measure the correlations between beam monitors and the detectors. The correction slopes are fit in a multivariate linear regression least-squares χ^2 minimization. This minimization process involves multiple correlated parameters, between the monitors and detectors by design, but also between the monitors which measure the beam at different locations along the beamline and therefore measure correlated position fluctuations. To simultaneously minimize the χ^2 for all of the monitors we perform a matrix inversion of the multipletwise-averaged covariance square matrix between the monitors and covariance vector for each detector. This allows obtaining correction slopes for all beam monitors simultaneously. The χ^2 minimization optimizes the correction slopes of equation 3.12, where

$$\chi^2 = \frac{1}{N} \sum_i^N \frac{(A_{raw}^i - \sum_j C_j \cdot \Delta x_{ji})^2}{\sigma_i^2} \quad (3.14)$$

for N multiplets, and we simultaneously minimize the χ^2 distribution with respect to the C_j slopes such that

$$\frac{\partial \chi^2}{\partial C_j} = 0, \quad (3.15)$$

for all monitors. As long as each multiplet measurement included in the calculation is sampled from the same underlying statistical distribution, the σ_i^2 are all equal and factor out of the χ^2 distribution. This need for a stable statistical sampling drives much of the need for stable beam conditions from event cuts and hand-tuned data quality selection discussed previously, and of the definition of ~ 9000 multiplet long miniruns used in the regression calculations.

Working out the constraints from equations 3.14 and 3.15, which is done in detail in [67]

amounts to a matrix equation relating the covariance vector of the detector signal versus monitors,

$$\vec{A}_{cov}^j = \frac{1}{N} \sum_i^N [A_{raw}^i \Delta x_{ij}], \quad (3.16)$$

to the square covariance matrix of monitors,

$$\mathbf{X}_{cov}^{jk} = \frac{1}{N} \sum_i^N [\Delta x_{ij} \Delta x_{ik}], \quad (3.17)$$

times the vector of slopes,

$$\vec{A}_{cov} = \mathbf{X}_{cov} \vec{C}, \quad (3.18)$$

which is solved by matrix inversion to provide the regression slopes, \vec{C} . Due to BPM monitor resolution limitations from instrumental noise the slopes are diluted somewhat, though the MHz-scale rates measured in CREX do not require the slopes to correct the distribution with as high a degree of accuracy as in PREX II. Nonetheless, false correlations due to shared electronic noise and slope dilution leads to inaccuracy in the slopes. Because of these concerns, in the next sections we utilize BPM monitor basis diagonalization to mitigate the slopes' correlations and make use of additional calibration data and correction techniques in the dithering and Lagrange analyses, which utilize explicit beam modulation to measure detector correlations with the beam monitors with difference systematic concerns.

3.5.2 Dithering

Correction slopes are also obtained from the dithering sensitivities generated in the beam modulation system, described in section 2.9.4. This intentional wiggling of the beam is done in the horizontal, vertical, and energy directions, performed at different positions along the beamline in the Hall A Arc, which are independent from and attempt to decouple the

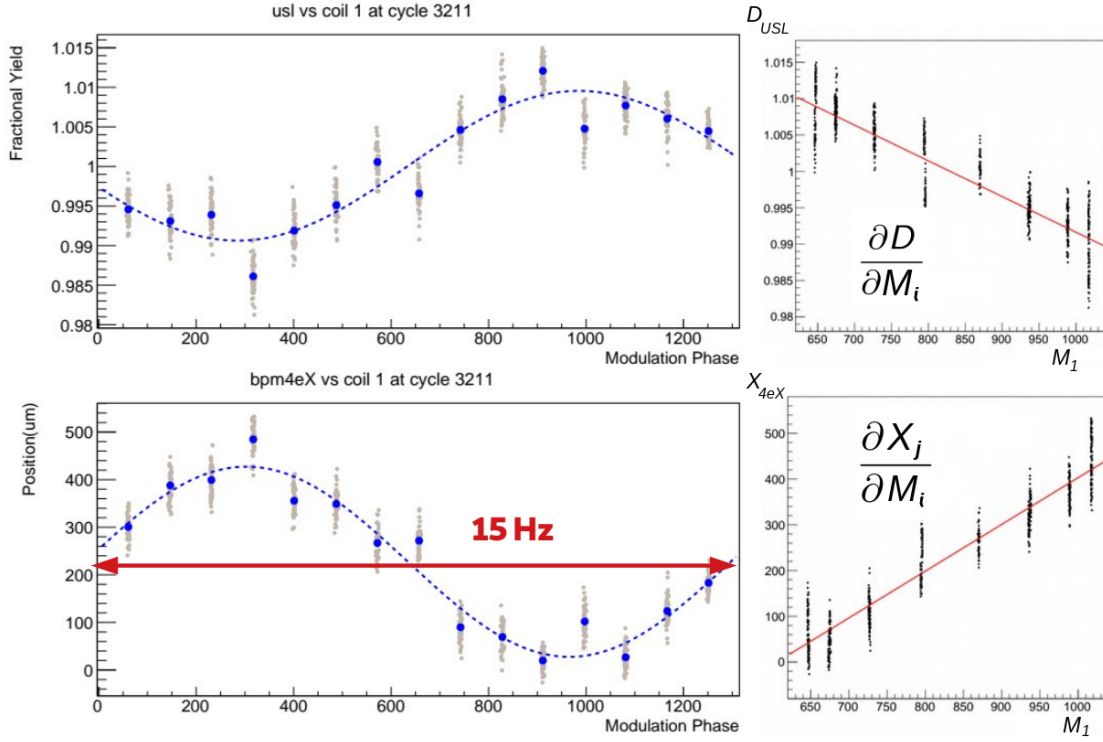


Figure 3.12: An example of beam modulation data accumulated over many cycles of modulation for the horizontally dithering coil 1. The USL main detector and one of the X sensitive BPMs responses as a function of modulation phase are shown on the left, and the correlation sensitivity response versus the modulation amplitude are shown on the right.

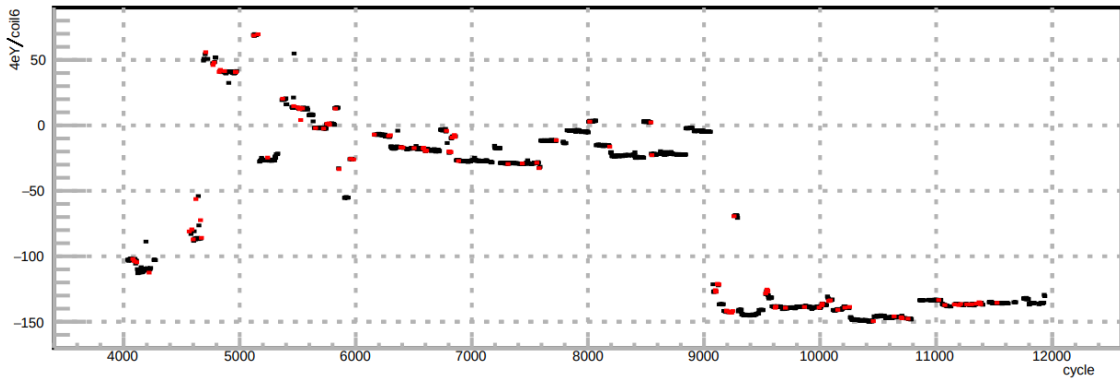


Figure 3.13: BPM 4eY sensitivity to coil6 throughout the CREX run, as an example of the changing dithering sensitivities. Red data points are removed due to insufficient data for slope calculations or are removed by hand.

natural beam motion degrees of freedom. The beam is dithered through many cycles for each modulation coil at 15 Hz to make the measurements independent from the dominant 60 Hz line noise and provide a statistically significant measurement. The beam motion and any resultant detector yield change are correlated to the modulation coil amplitudes, allowing an independent measure of the correlations between beam monitors and the detectors, with the correlations to the coils as intermediaries, as

$$\frac{\partial D}{\partial M_i} = \sum_j \frac{\partial D}{\partial X_j} \frac{\partial X_j}{\partial M_i}, \quad (3.19)$$

which amounts to a matrix relationship of the detector and BPM sensitivities to the coils and the correction slopes,

$$\left(\frac{\partial D}{\partial M_i} \right)_{n_{coils} \times 1} = \left(\frac{\partial X_j}{\partial M_i} \right)_{n_{coils} \times n_{BPM}} \left(\frac{\partial D}{\partial X_j} \right)_{n_{BPM} \times 1}, \quad (3.20)$$

where $\frac{\partial D}{\partial X_j}$ are the C_j dithering correction slopes, D is fractional detector response, M_i are the modulation coil amplitudes, and X_j are the beam positions. The partial derivatives of the detector and BPM responses to the coil amplitudes are the dithering sensitivity measurements, which are obtained from linear fits to the distributions of the helicity event yields of these quantities for each beam modulation set of cycles. The sensitivities to each modulation coil are calculated independently, looking only at the data while that coil is active, and the many 15 Hz cycles taken successively are combined together in this fit to increase the precision. An example of the dithering response and sensitivity calculations is given in Fig. 3.12. The relationship in Equation 3.20 is solved by matrix inversion for the correction slopes as

$$\left(\frac{\partial D}{\partial X_j} \right) = \left(\frac{\partial X_j}{\partial M_i} \right)^{-1} \left(\frac{\partial D}{\partial M_i} \right). \quad (3.21)$$

The detector sensitivities are obtained from the fractional detector response, where

$$D = \frac{y}{2\langle y \rangle}, \quad (3.22)$$

where $\langle y \rangle$ is the beam current-normalized detector yield, from equation 3.4, averaged over the events included in the modulation cycle [67]. This fractional detector sensitivity definition is necessary because the asymmetries we correct are fractional responses as well.

In total there are seven modulation coils that can be used for calculating correction slopes and the matrix inversion works when the number of BPMs used is equal to the number of coils. It is possible to use more coils than BPMs, in what is called over-constrained dithering analysis, but we choose to use only five coils and five BPMs to give a full coverage of the potential five beam motion degrees of freedom and have two coils for additional cross checks later. Coil 7 is the energy vernier, the other odd numbered coils drive horizontal motion, and the even numbered coils drive vertical motion. The determination of which coils best optimize the sensitivities, avoiding matrix singularity that breaks the invertibility of equation 3.21, is done regularly during data collection with the online analysis tools. The choice of five BPMs and five coils remains consistent across the CREX experimental run; we use BPMs 1X, 4eX, 4aY, 4eY, and 12X, and coils 1, 3, 4, 6, and 7, which are shown before in Fig. 2.45. This selection leaves coils 2 and 5 as redundant modulations for evaluating residual sensitivity, discussed later in section 3.6.1. The modulation coils' amplitudes are also monitored and are modified as needed to maintain sensitivity while avoiding triggering the beam position event cuts, typically driving the modulation amplitude at the $\sim 100\mu m$ level. The modulation data included in the sensitivity calculations also must pass the event cuts described before so that the data used to measure the sensitivities reflect the standard running conditions and are safe to include in the final data-set.

Two problems which face the dithering analysis in CREX are the prevalence of incomplete beam modulation supercycles within DAQ runs, where a supercycle is the sequence of modulation cycles from all seven coils, and the frequent sensitivity changes due to the beam delivery optics. The modulation supercycles are performed approximately every 10 minutes if the beam is available and span nearly two minutes, and so it is common for the beam to trip off in the middle of a supercycle, leading to many runs with incomplete supercycles, especially during unstable beam delivery periods. To mitigate the impact of beam trips on the dithering analysis we choose to calculate the sensitivities for each coils' modulation from the data contained in all supercycles within each hour-long DAQ run, and then one set of correction slopes are calculated for the entire run. In this way calibration data for the coils that modulate while the beam is available are not thrown away if just one of the other coils fails event cuts within a supercycle, but are merged with data from neighboring supercycles in the same run. This increases the available amount of data compared with treating each supercycle separately, improving slope calculation precision and improving the coverage of changes in the sensitivities over time.

Even with the runwise calculation of dithering sensitivities, still some runs fail to measure a sensitivity for all of the coils needed to make a calculation due to unstable beam conditions or the modulation system being inactive, and a handful of runs yield problematic outlier dithering measurements that are investigated and removed from the data-set by hand when necessary. Thus the question arises of which dithering slopes should be used to correct data without a full calibration measurement. The strategy employed for CREX is to perform an unweighted average of the runwise calculated slopes for all runs within run-ranged segments and to use the average slopes for all of the runs in that segment. Averaging the slopes both allows correcting runs without successful runwise slope calculations and smooths out the noise in the slope calculations over time, both of which may introduce some systematic

inaccuracy to the corrections. Therefore, to minimize correction inaccuracy, the run-ranging of segments is chosen to group runs together that share similar beam delivery optics and running conditions, which is done by carefully investigating the supercyclewise and runwise sensitivities and slope trends over time.

Segments are defined with delineations whenever a noticeable change in the dithering sensitivities or slopes appears at the cycle or run level, and by looking at the experiment log book and other diagnostic information for runs without clear indications in the dithering data. An example of the runwise sensitivities across CREX for one BPM sensitivity is shown in Fig. 3.13, which displays the characteristic \sim day timescale of changes in beam delivery optics tune in the beamline between the modulation coils and the target BPMs. The segmentation selection and data pruning is done manually, and the chosen run-ranges and removed cycles are given in Appendix A.1. The segmentation does not consider slug run-range definitions, as the slugs in CREX are not all continuous in time and often span changes in beam tune.

3.5.3 Eigenvector Beam Monitor Basis

We now have two different methods of measuring the correlations between the detector and beam motion and calculating slopes for correcting A_{raw} with the BPMs, which are compared in Fig. 3.14. The two approaches are sensitive to the correlations in the beam motion between the BPMs in different ways and they have different sources of systematic error, resulting in the different slope calculation results seen in the figure. This combination of ambiguity and systematic differences makes it difficult to directly compare the corrections or easily estimate the systematic uncertainty in the methods. As a result, we choose to rotate the beam monitor basis set from a BPM basis into one which diagonalizes the beam

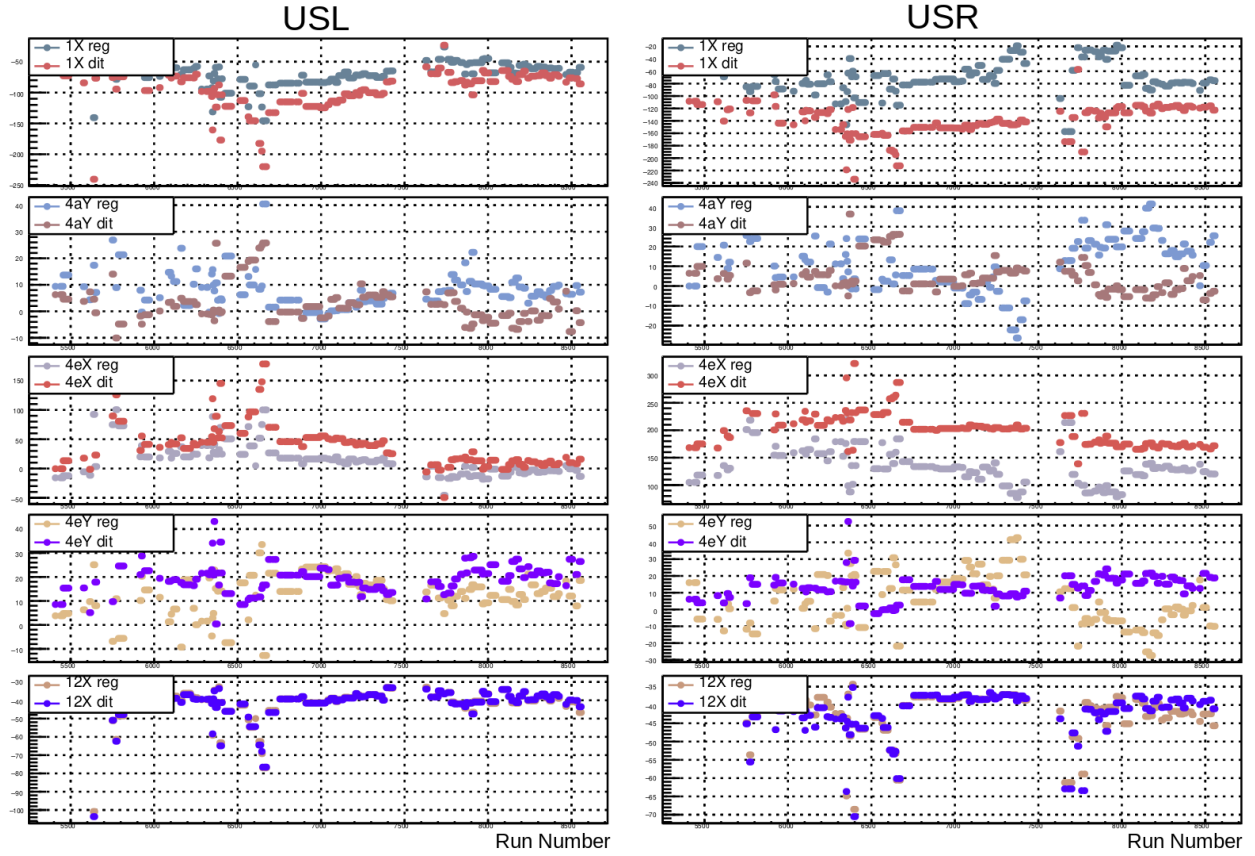


Figure 3.14: Plots showing the dithering-segment averaged slopes for each BPM from the 5 BPM regression and dithering analyses. The slopes do not match between the two analysis methods due to differences in their correlations and systematics.

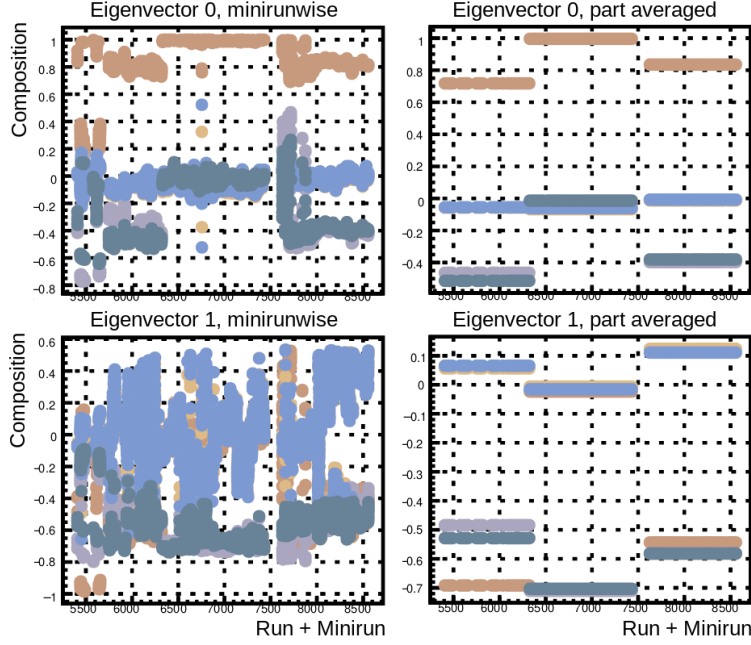


Figure 3.15: Two example eigenvector composition calculations for each minirun (left) and averaged across the three “part” optics tune segmentations of CREX (right).

motion correlations so that the slopes can be more easily compared.

To orthogonalize the beam monitors’ correlations we diagonalize the BPMs covariance matrix, from equation 3.18, by eigenvalue decomposition. The eigenvalues are the square of the RMS jitter of the rotated eigenvector monitors [67]. To maintain consistent rotated eigenvector monitor (referred to as “evMon”) identities across changes in the beam optics tune and BPM correlations, we calculate the eigenvalue decomposition for each five minute minirun and sort the evMons based on their vector distance to the averaged evMons, updating the average with each minirun. We then rank the eigenvectors based on their averaged RMS noise in decreasing order, which amounts to ranking the eigenvectors by their eigenvalue magnitudes.

Because CREX has three clear segmentations in the beam delivery optics tune we choose to separate the eigenvector definition sorting and ranking into those three time periods and

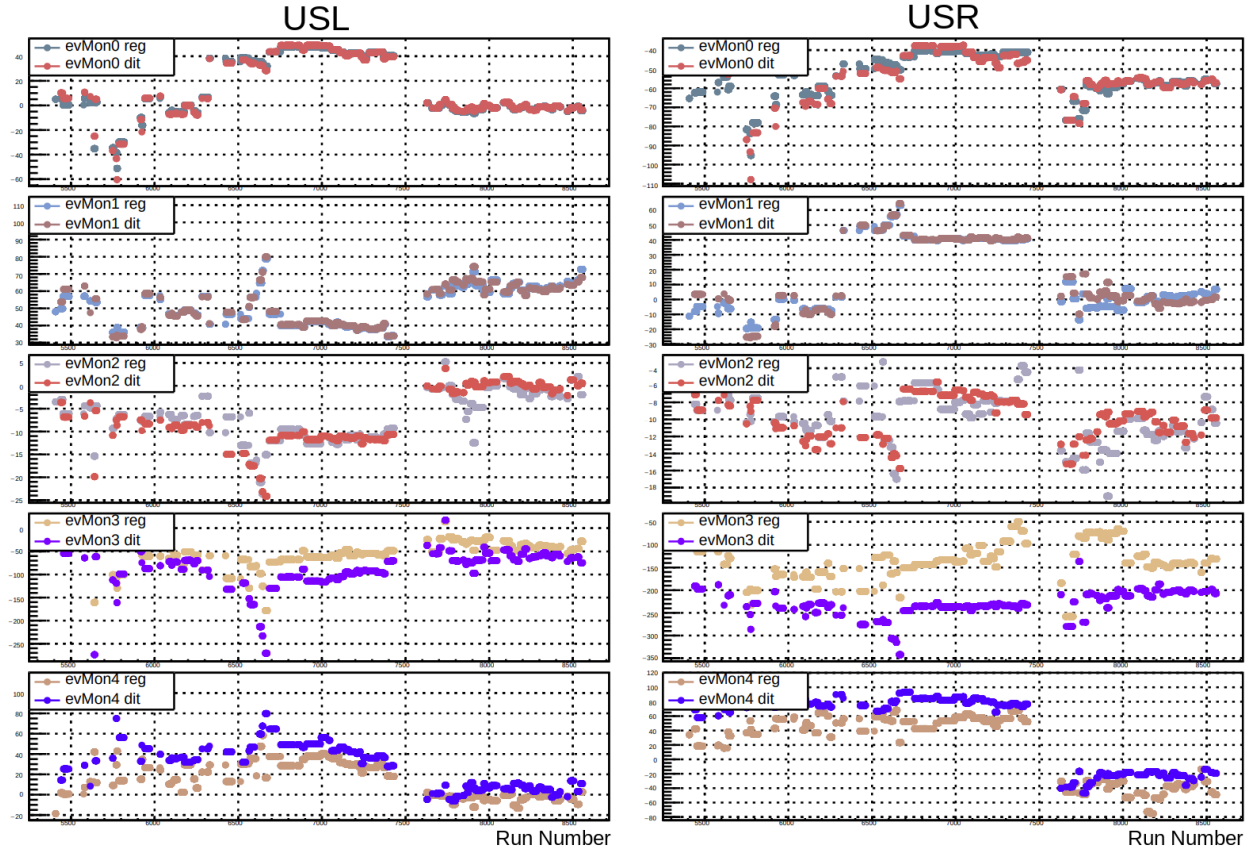


Figure 3.16: Plots showing the dithering-segment averaged slopes for each BPM from the 5 eigenvector monitor regression and dithering analyses. The slopes are in better agreement than the plain BPM basis set correction slopes, but still do not totally match.

to treat subsequent evaluations of the corrections independently between them. Additionally, because of the substantial degree of noise in the eigenvectors definitions over time we choose to perform a flat average of the eigenvector compositions over these three separate segments, referred to as “parts.” We renormalize the averaged eigenvectors so each of their magnitudes in the BPM basis adds in quadrature to 1 and the slopes calculated with them maintain units of $\text{ppm}/\mu\text{m}$, which requires only a small scale factor at the few percent level, but this does mean the eigenvectors are no longer guaranteed to be exactly orthogonal to each other as is the case for the minirunwise results. Finer scale averaging segmentation does not provide noticeable benefit in terms of deviations of the minirunwise eigenvector compositions from the averaged values. An example of the averaged definitions for two evMons across the three parts of CREX is shown in Fig. 3.15, the evMon average position differences and RMSs are given in table 3.4, and the detailed eigenvector definitions and choices in their ranking and averaging are given in Appendix A.2.

The regression and dithering correction slopes calculated in the eigenvector basis are shown in Fig. 3.16, which appear to successfully bring the two correction methods into closer agreement, but there is still some non-trivial disagreement between analysis techniques. In order to provide additional data to better span the phase space of beam motion correlations we use more BPMs in the eigenvector basis set, expanding from the 5 BPMs to 12, including BPMs 4eX, 4eY, 4aX, 4aY, 1X, 1Y, 16X, 16Y, 12X, 12Y, 11X, and 11Y. Because of the limit on the number of independent monitors being \leq the number of modulation coils used in the dithering analysis and the possibility of more correlation among the correction slopes from the additional BPMs, an alternative to the standard dithering and regression techniques is required. A method is needed that can combine regression and dithering constraints into one analysis that allows the use of regression and dithering calibration measurements from many position monitors simultaneously, which is the topic of the next section.

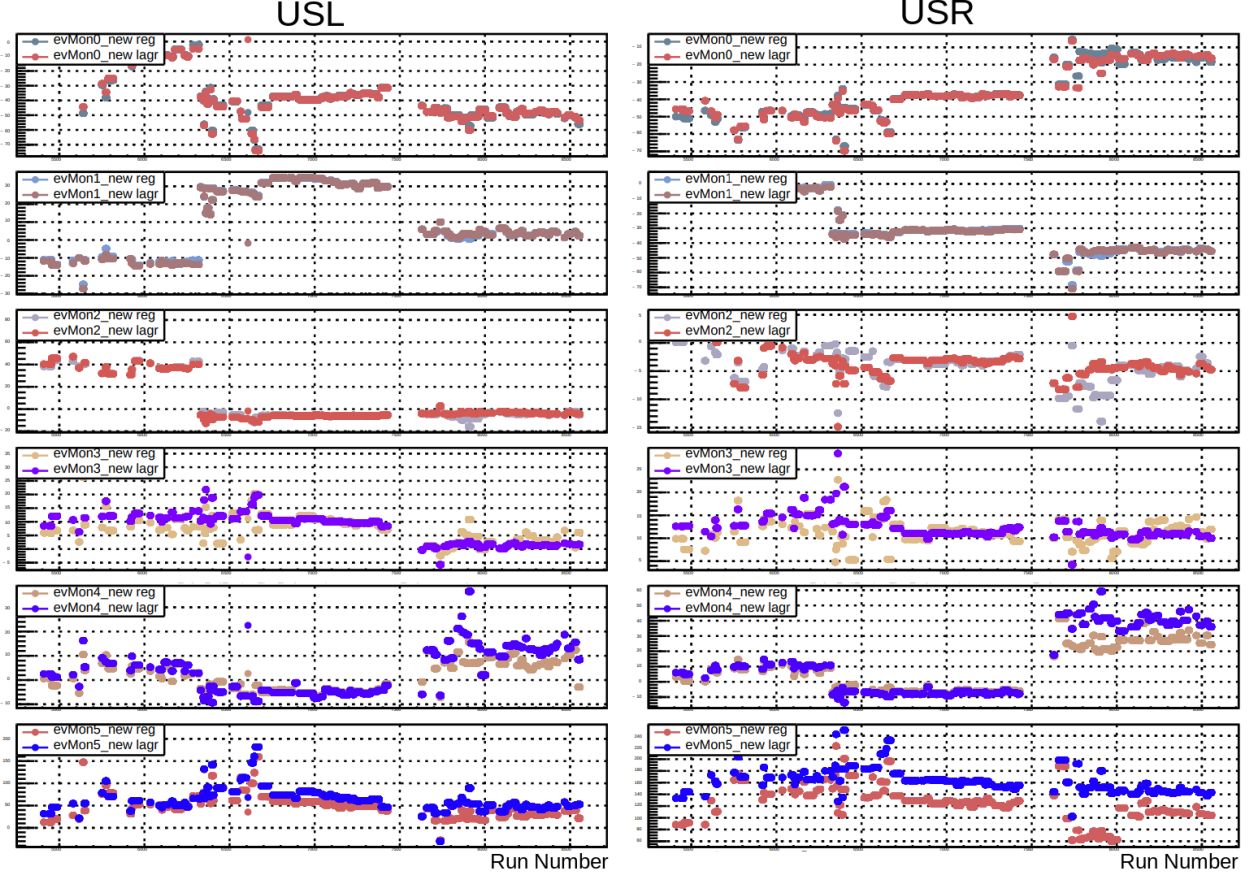


Figure 3.17: Plots showing the USL and USR main detector dithering-segment averaged slopes for each BPM from the 12 eigenvector monitor regression and Lagrange analyses. The segment averaging of the slopes is done to simplify the visual display, though both regression and Lagrange analyses both calculate slopes for each minirun.

3.5.4 Lagrange Multiplier Analysis

To obtain systematic uncertainty estimates we need to produce slopes which span the full range of beam motion and are comparable between analyses. The 5 BPM and 5 eigenvector analyses provide similar results for the CREX dataset, but in order to be careful and confident in the accuracy of our results we desire to perform comparable regression and dithering analyses that use more eigenvector monitors than are available in the standard 5 modulation coils dithering analysis. We therefore use the 12 evMon basis set to perform

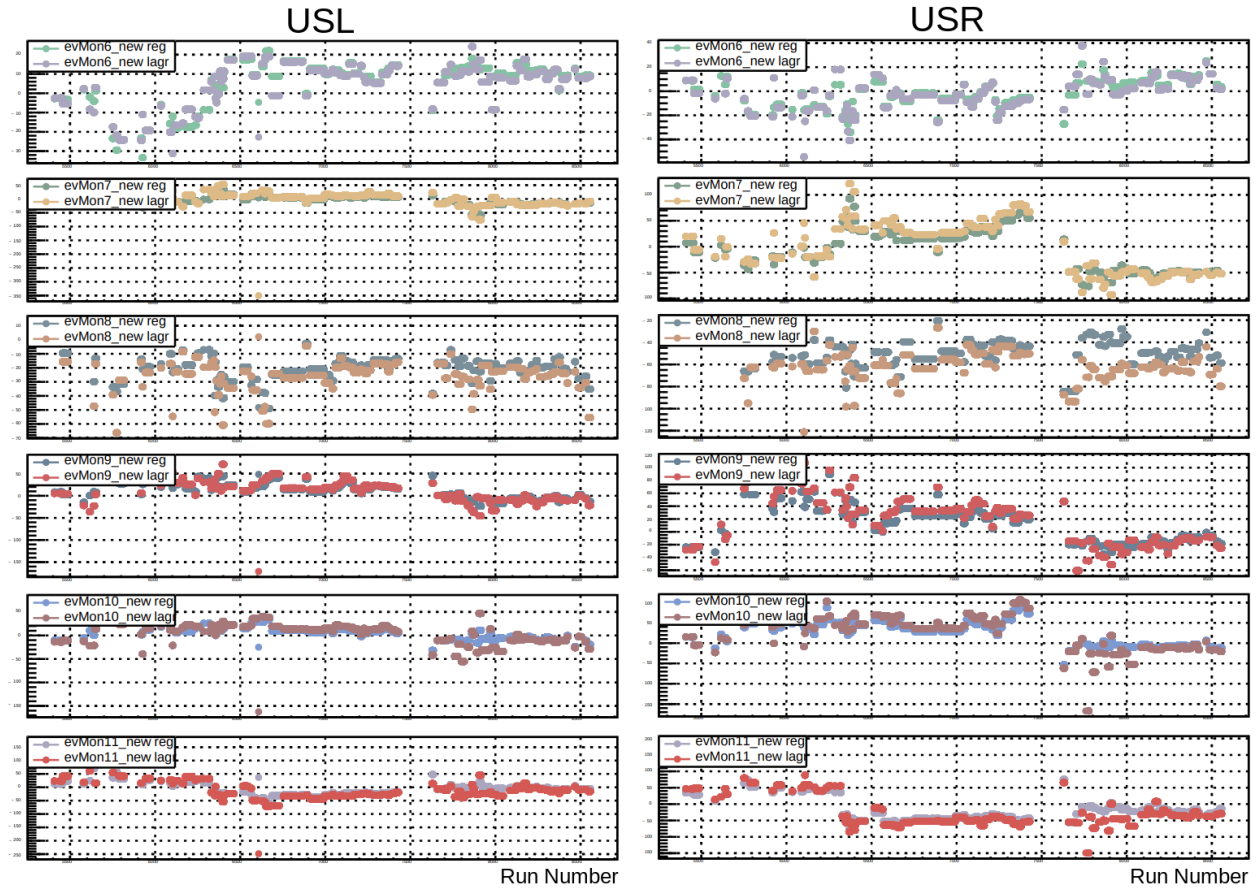


Figure 3.18: The same as Fig. 3.17 but for the six eigenvectors with smaller RMS jitter.

linear regression and the Lagrange multiplier analysis technique pioneered by Tao Ye for the PREX II analysis [67]. The Lagrange multiplier analysis technique combines the χ^2 minimization from linear regression plus Lagrange multipliers for the dithering sensitivity constraints, combining equations 3.14 and 3.19 as

$$\mathcal{L} = \chi^2 + \sum_i^5 \lambda_i \left(\sum_j \frac{\partial D}{\partial X_j} \frac{\partial X_j}{\partial M_i} - \frac{\partial D}{\partial M_i} \right) \quad (3.23)$$

where $\frac{\partial D}{\partial X_j} = C_j$ are the correction slopes, and recall the χ^2 over N multiplets from the linear regression analysis is

$$\chi^2 = \frac{1}{N} \sum_k^N \frac{(A_{raw_k} - \sum_j (C_j \cdot \Delta x_{kj}))^2}{\sigma_j^2}. \quad (3.24)$$

Simultaneously minimizing this Lagrangian with respect to the slopes and Lagrange multipliers,

$$\frac{\partial \mathcal{L}}{\partial C_j} = 0, \quad \frac{\partial \mathcal{L}}{\lambda_i} = 0, \quad (3.25)$$

yields a matrix relation which is solved for the correction slopes. The slopes are calculated for each minirun, as is done with the regression analysis, using segment averaged dithering sensitivities as the Lagrange multiplier constraints, averaging across the runwise dithering sensitivity calculations with the same beam delivery optics tune segments described in the dithering analysis above. The difference between the 12 evMon regression and Lagrange analyses slopes is shown in Fig. 3.17 and 3.18. The slope disagreements are proportional to the calculated Lagrange multiplier values, equal to the residual dithering sensitivities that are corrected by the regression slopes, and inversely proportional to the eigenvalue of the eigenvector monitor, which enhances the difference in those with smaller monitor RMS spread and less contribution to the overall corrections [67].

This 12 evMon Lagrange multiplier analysis, along with the others mentioned before, is

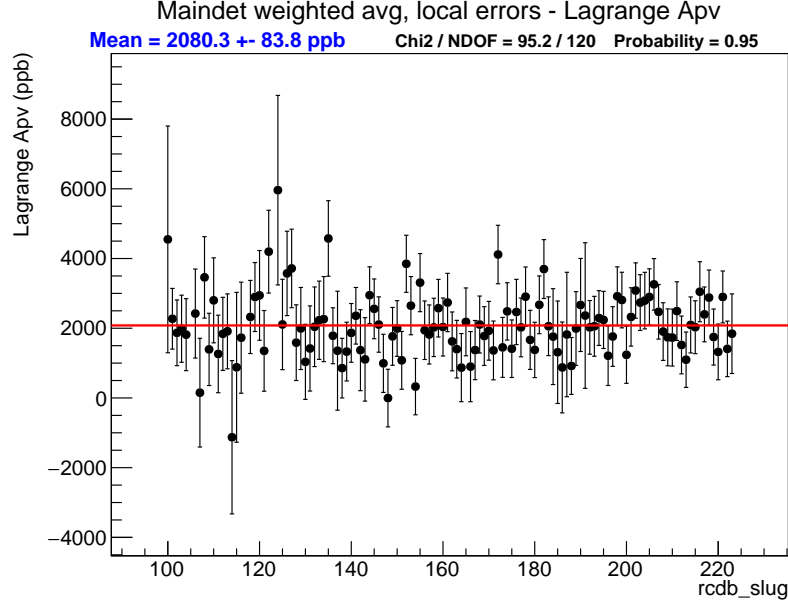


Figure 3.19: Grand-averaged 12 evMon Lagrange corrected main detector A_{det} versus slug number.

done for the main detectors, the left (USL) and right (USR) A_{raw} signals, and the average (US Avg) and double difference (US DD) multiplet-level combinations as well. The “main detector” (or “main det”) asymmetry used for the grand-averaged A_{raw} and corrected for A_{det} is the US Avg combination

$$A_{US\ Avg} = \frac{A_{USL} + A_{USR}}{2}, \quad (3.26)$$

which is an unweighted average sum of the asymmetries measured in both HRSs for each helicity multiplet, and A_{DD} is the average difference. Calculating corrections from the US Avg asymmetry provides cancellation of HC A_{beam} that are correlated between the nearly identically symmetric HRSs. Any remaining asymmetry between the measurements made by the two arms is considered in the kinematic extraction of the acceptance function and applied as a correction to the corrected US Avg A_{det} . For runs where one HRS is inactive,

which occurs for around 1.5% of the data collected, the asymmetry used for the main detector definition is whichever arm's asymmetry is valid.

The blinded 12 evMon Lagrange corrected main detector A_{det} for CREX is 2080.26 ± 83.77 ppb, where the error bar is only from the corrected asymmetry distributions' $\frac{\text{RMS}}{\sqrt{N}}$ statistical uncertainties considered in the weighted grand average. The slug-averaged corrected asymmetry is shown in Fig. 3.19, and the estimate of systematic uncertainty from beam corrections is discussed in the following section.

3.6 Uncertainty on the Beam Corrections

The beam corrections obtained by the various analysis techniques are subject to different systematic effects and limitations which must be considered in the systematic uncertainty estimate. In the following sections we investigate the quality of the corrections using various methods.

3.6.1 Residual Sensitivities

The residual dithering sensitivities of the corrected data to the beam modulation coil responses provide an estimate of the uncertainty in the corrections. The residual dithering sensitivities, R_i , for the main detectors are obtained for each dithering coil by using the calculated slopes, C_j , to correct the detector sensitivities with the measured position sensitivities, as

$$R_i = \frac{\partial D}{\partial M_i} - \sum_j C_j \frac{\partial X_j}{\partial M_i}. \quad (3.27)$$

These are calculated for each coil from the runwise dithering sensitivities corrected by the minirun-wise calculated 12 evMon Lagrange multiplier analysis correction slopes described

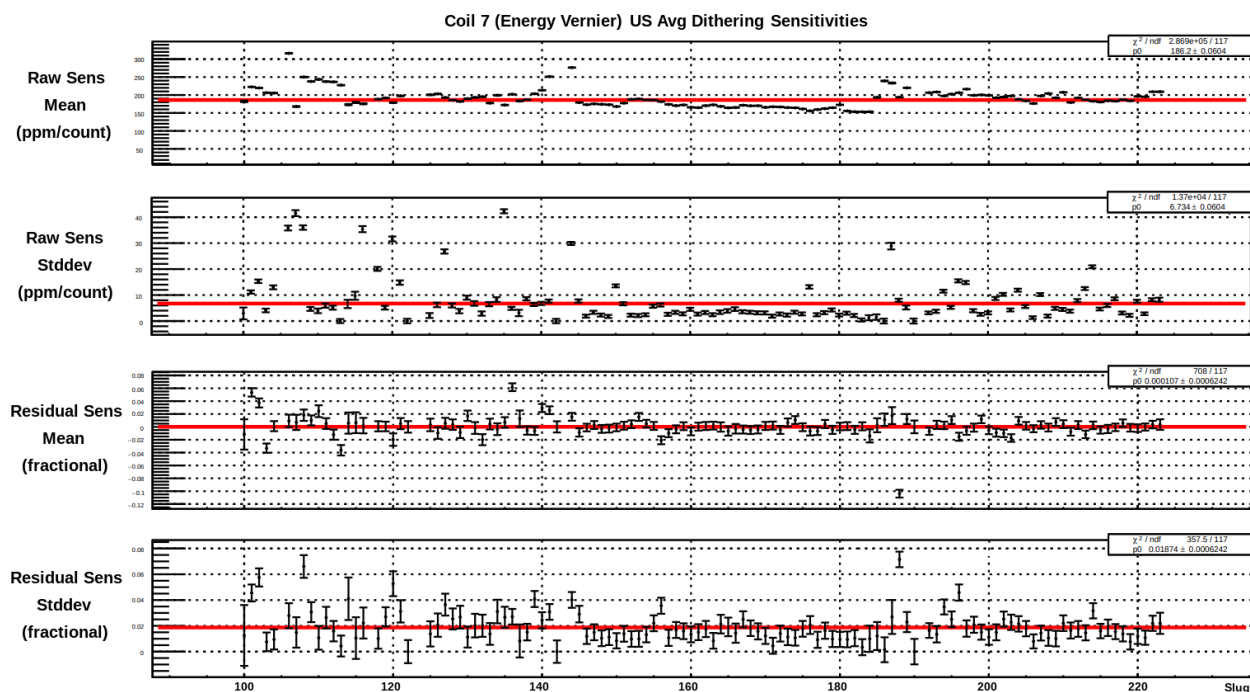


Figure 3.20: Example of dithering sensitivities and residuals showing the raw (top two) and residual (bottom two) US Avg sensitivities to the dithering energy modulation, with the mean and standard deviation shown for each slug. The fits give the experiment-averaged sensitivity mean and standard deviations, used to evaluate the systematic uncertainty in the corrections.

Table 3.3: Table of fractional residual dithering sensitivity RMSs, given in percent, from the 12 evMon Lagrange corrections for USL, USR, and US Avg main detectors. Coils 1, 3 and 5 are horizontal (X) modulation directions, coils 2, 4 and 6 are vertical (Y) modulation directions, and coil 7 is the energy (E) vernier. Coils 2 and 5 are not included in the Lagrange multiplier constraints, and are used to cross check the sufficiency of correction slopes, and are shown in red. The X coils have small raw sensitivities in the US Avg, due to cancellation of sensitivity between the HRS arms, yielding large fractional residuals.

Fractional Residual per detector (self weighted):									
	USL Stddev			USR Stddev			US Avg Stddev		
Coil	Part 1	2	3	1	2	3	1	2	3
X Coil 1	1%	1%	1%	1%	1%	1%	13%	10%	16%
X Coil 3	3%	1%	2%	3%	1%	3%	23%	8%	16%
X Coil 5	3%	1%	2%	3%	1%	3%	19%	10%	26%
Y Coil 2	7%	7%	9%	7%	5%	7%	6%	4%	5%
Y Coil 4	5%	4%	4%	5%	4%	3%	6%	3%	3%
Y Coil 6	16%	7%	3%	15%	9%	3%	12%	7%	3%
E Coil 7	8%	2%	10%	2%	1%	1%	3%	2%	2%

before, which are obtained with the constraints provided by the stable beam tune segment averaged dithering sensitivities.

The 12 evMon Lagrange multiplier analysis slopes precision for removing beam motion is estimated by looking at how well they capture the detectors dependence on beam motion. This is estimated by how much the R_i deviate from zero and by how similarly well controlled the R_i are from the redundant modulation coils that are not included in the C_i slopes calculation. To estimate the accuracy of the correction slopes we look at the fractional residuals and focus on their standard deviation spread as a way to estimate the slopes' precision limitation, where the fractional residuals r_i are the fraction of the residual over the raw sensitivities,

$$r_i = \frac{R_i}{\frac{\partial D}{\partial M_i}}. \quad (3.28)$$

When using fractional residuals we must look at USL, USR, and US Avg independently to

get the full picture, as the X direction coils sensitivities largely cancel in the US Avg detector and make the fraction's denominator too small to be useful. To provide a scale for weights in the averaging, the uncertainties for the r_i come from propagating the raw detector and evMon sensitivities' statistical uncertainties for each run through equation 3.28, giving less weight to the sensitivities computed with less modulation data.

The residual means are very close to zero, and so the spreads of the fractional residuals are used to estimate the precision of the beam corrections. The standard deviations of the fractional residuals over the three evMon definition parts of CREX are given in table 3.3, which shows good control of the X (odd numbered) and Y (even numbered) modulation coil and the energy vernier (number 7) residuals at around the 5% level. The redundant coils 2 and 5, which are not included in the slope calculation constraints, are commensurate in scale with the included coils, providing additional confidence in the precision of the corrections.

An example plot of the raw and fractional residual sensitivities for the dominant US Avg main detector energy sensitivity, averaged on the slug timescale, is shown in Fig. 3.20. In this plot the residual sensitivity mean calculation and the points' error bars instead come from propagating the uncertainties through the main detector statistics-weighted average calculation, described in the next section, which gives a result very similar to the runwise sensitivity error weighted results in the table. The standard deviation error bars in this plot are taken from the mean calculation, shown here to give a sense of the relative statistical weight for each slug and not intended to convey the precision of the calculation. From the scale of the fractional residual distributions' RMSs in table 3.3 and the similarity in scale of the redundant coils to the coils used in the analysis we see that the beam modulation data is adequately utilized by the Lagrange analysis corrections, with the precision for each modulation coil better than the $\sim 5\%$ level.

3.6.2 Weighted Average

With the Lagrange analysis beam corrections adequately removing the background HC A_{beam} and beam motion noise carried in the incident beam we now have corrected A_{det} distributions for each minirun corresponding to counting statistics limited measurements of the scattered asymmetry. To calculate average quantity contributions corresponding to the corrected A_{det} we use the statistical error bars $\sigma_i^{stat} = \sigma_{Ai}$ per minirun as variance weights,

$$w_{Ai} = \frac{1}{\sigma_{Ai}^2}, \quad (3.29)$$

where the σ_{Ai} error bar is obtained from the sample variance for each minirun. Because the beam conditions are stable over the five minute minirun time scale and all measurements thus sample the same distribution, we have

$$\sigma_{Ai} = \frac{RMS_{Ai}}{\sqrt{N_i}}. \quad (3.30)$$

and RMS_i^{det} is the counting statistics distribution width, $RMS = \frac{1}{\sqrt{N}}$, determined by the scattering rate into the main detectors after beam corrections. Here N_i is 9000 multiplets for most miniruns, except for runs with only one minirun, which are kept only if the minirun is more than \sim one third of the full length, and for the final minirun of each run which is always less than 18000 multiplets. Using the A_{det} statistical weights to calculate the amount of some other quantity, Γ , measured alongside A_{det} assumes that the multiplet distribution of A_{det} is uncorrelated with Γ . This is true for all quantities measured in CREX down to the level of the beam monitors' instrumental precision of a few ppm, which are much smaller than the A_{det} distribution RMS of ~ 775 ppm.

The uncertainty of the weighted average is obtained through error propagation, the com-

putation of which is shown explicitly for instructive purposes [71]. Again recall the definition of weighted average,

$$\langle \Gamma \rangle = \frac{\sum_i^n w_{Ai} \Gamma_i}{\sum_j^n w_{Aj}}, \quad (3.31)$$

for n miniruns across the experiment and statistical weights w_{Ai} . Then the uncertainty on $\langle \Gamma \rangle$ is

$$\sigma_{\langle \Gamma \rangle}^2 = \delta \langle \Gamma \rangle^2 = \sum_i^n \left(\frac{\partial \Gamma}{\partial \Gamma_i} \right)^2 (\delta \Gamma_i)^2 = \sum_i^n \left(\frac{w_{Ai}}{\sum_j^n w_{Aj}} \right)^2 (\sigma_{\Gamma_i})^2 \quad (3.32)$$

Moving terms around and simplifying, we get

$$\sigma_{\langle \Gamma \rangle} = \sqrt{\frac{1}{\sum_j^n w_{Aj}}} \sqrt{\frac{\sum_i^n w_{Ai}^2 \sigma_{\Gamma_i}^2}{\sum_j^n w_{Aj}}} \quad (3.33)$$

then, recalling that the weighted mean standard error for the asymmetry is

$$\sigma_{\langle A \rangle} = \sqrt{\frac{1}{\sum_i^n w_{Ai}}}, \quad (3.34)$$

and that the Γ distribution's uncertainties can be expressed as weights $w_{\Gamma_i} = \frac{1}{\sigma_{\Gamma_i}^2}$, and reorganizing terms, we get the grand average's mean standard error

$$\sigma_{\langle \Gamma \rangle} = \sigma_{\langle A \rangle} \times \sqrt{\frac{\sum_i^n w_{Ai} \frac{w_{Ai}}{w_{\Gamma_i}}}{\sum_j^n w_{Aj}}}. \quad (3.35)$$

This amounts to rescaling the main detector statistical uncertainty by a weighted average of the ratio of weights,

$$\left\langle \frac{w_A}{w_\Gamma} \right\rangle = \frac{\sum_i^n w_{Ai} \frac{w_{Ai}}{w_{\Gamma i}}}{\sum_j^n w_{Aj}}, \quad (3.36)$$

which makes intuitive sense for performing a weighted average while carrying along the Γ measurement precision information in $w_{\Gamma i}$. Then, we can rescale the statistical weights by a constant to simplify computations of weighted means and mean errors to get the same results with fewer steps, as

$$w'_{Ai} = \frac{w_{Ai}}{\left\langle \frac{w_A}{w_\Gamma} \right\rangle}, \quad \sigma'_{Ai} = \sigma_{Ai} \sqrt{\left\langle \frac{w_A}{w_\Gamma} \right\rangle}. \quad (3.37)$$

Using these rescaled weights and errors allows one to skip some steps and compute the experiment grand averages of quantities using the corrected distribution σ_{Ai} statistical error bars quickly and easily in two steps: by performing a weighted average first of the ratio of weights, as in equation 3.36, and then of Γ using $\left\langle \frac{w_A}{w_\Gamma} \right\rangle$ to rescale the uncertainties or weights, whose grand average standard error $\sigma_{\langle \Gamma \rangle} = \sqrt{\frac{1}{\sum_i^n w'_{Ai}}}$ is automatically equal to the explicit calculation of $\sigma_{\langle \Gamma \rangle}$ from equation 3.35 while the mean from equation 3.31 is the same regardless of any constant rescaling factor on the weights. The three easiest ways to perform a general weighted average in ROOT, in order from most effort to least, are to explicitly sum the terms, to perform a polynomial-0 (constant) fit with a TGraphErrors using the σ_{Ai} or σ'_{Ai} errors, and to fill a TH1 histogram using the w_{Ai} or w'_{Ai} weights and then obtain the mean from the TH1 mean and the mean error from the $\sqrt{\frac{1}{\text{TH1 integral}}}$, where the integral sums the total weight, as in equation 3.34.

We use this to calculate the grand statistics-weighted averages for most quantities that

need to be compared to the final average $\langle A_{det} \rangle$, starting with $\langle A_{raw} \rangle = 2026.81 \pm 189.88$ ppb, which should be compared to the corrected $\langle A_{det} \rangle = 2080.26 \pm 83.77$ ppb. The asymmetry measurement's statistical precision is greatly improved by removing the HC A_{beam} with the Lagrange multiplier correction slopes. The slopes provide a net correction of 53.45 ppb and reduce the statistical error substantially, but we must also consider the possible systematic uncertainties from error in the correction slopes themselves. The average evMon position differences and average correction slopes are given in tables 3.4 and 3.5, and the corrections for each monitor, as well as the weighted average RMS and the weighted mean standard error, which is calculated from the slope \times the monitor errors as the σ_T , are given in table 3.6. The weighted mean errors for the corrections per monitor are non-trivial compared to the 83.77 ppb $\sigma_{\langle A \rangle}$, but their statistical precision contributions are already included within the minirunwise-corrected A_{det} distributions, and so these correction distribution errors are not that useful. The systematic uncertainty in A_{beam} should come from the uncertainty in the correction slopes alone, which is estimated in the following section.

3.6.3 Differences Between Correction Methods

In order to provide a sanity check that the $\sim 5\%$ accuracy in correction quality estimate from the well-behaved Lagrange residual sensitivities is reasonable, we look at the scale of disagreement between regression and Lagrange corrections. This is done based on the disagreement in slopes and corrections per monitor, and the disagreement between the grand-averaged corrections overall. The monitors with dominant position differences and noise above the monitor resolution are the first five or six, and the scale of disagreement in slopes, given by the ΔC columns in table 3.5, in terms of mean and RMS of the slope differences, is only at the few percent level for each of the slopes with non-trivial

Table 3.4: Main detector statistically-weighted averages of the 12 eigenvector monitors HC differences vs. CREX parts. The mean and error are in units of nm while the RMS is in units of μm . The eigenvectors are ranked by their eigenvalue magnitudes, corresponding to the monitor RMS size.

Diffs	Part 1			Part 2			Part 3		
evMon	Mean	σ	RMS	Mean	σ	RMS	Mean	σ	RMS
0 (E)	-12.0	11.1	39.5	0.2	6.2	38.5	0.8	4.4	23.8
1 (X)	1.9	5.2	18.9	8.9	2.9	18.6	6.3	10.7	59.3
2 (Y)	-2.8	6.2	21.4	-1.4	2.5	15.4	-5.5	5.2	15.6
3	-4.9	1.8	6.3	-0.6	1.4	8.2	-9.3	4.3	10.4
4	-1.3	0.5	1.8	0.02	0.2	1.6	1.2	0.7	1.7
5	-1.4	0.7	2.4	0.1	0.2	1.2	0.2	0.6	2.7
6	0.01	0.4	1.4	-0.1	0.1	0.6	-0.1	0.1	0.7
7	0.6	0.4	1.4	0.1	0.1	0.6	0.2	0.2	1.0
8	0.2	0.2	0.8	-0.02	0.1	0.4	0.1	0.1	0.6
9	0.4	0.3	1.1	0.1	0.1	0.4	0.2	0.1	0.5
10	0.04	0.3	0.9	0.04	0.1	0.4	0.2	0.2	0.5
11	0.2	0.1	0.5	-0.005	0.1	0.4	-0.1	0.1	0.5

Table 3.5: Main detector statistically-weighted averages of the 12 evMon Lagrange multipliers analysis slopes for the US Avg main detector vs. CREX parts, in units of $ppm/\mu m$. The average slopes are shown along with the average difference between Lagrange and regression slopes ΔC , and the RMS of that difference.

Slopes	Part 1			Part 2			Part 3		
evMon	Mean	ΔC	ΔC RMS	Mean	ΔC	ΔC RMS	Mean	ΔC	ΔC RMS
0 (E)	-30.3	0.5	2.7	-39.8	-0.3	0.7	-33.0	-0.5	2.2
1 (X)	-7.7	-0.7	1.5	-0.3	-0.2	0.6	-21.1	0.3	1.3
2 (Y)	18.9	0.4	2.0	-4.9	-0.2	1.5	-4.0	1.7	3.1
3	13.3	3.4	3.8	11.2	0.6	3.7	6.1	-0.8	3.4
4	7.2	2.3	2.4	-6.3	-1.0	1.6	27.2	9.8	7.9
5	110.8	18.5	17.2	121.8	26.3	12.5	98.8	36.1	21.9
6	-10.5	-0.1	9.1	2.6	-1.0	2.9	8.3	-1.6	7.2
7	-7.8	2.3	18.3	27.6	8.8	6.8	-37.5	-2.7	14.3
8	-36.7	-5.3	10.0	-39.9	-6.1	4.0	-45.5	-12.0	12.3
9	36.1	9.6	25.6	27.3	5.9	5.7	-15.7	-4.0	13.9
10	23.9	2.8	17.1	37.1	7.9	5.9	-17.7	-10.4	26.9
11	45.8	11.9	22.1	-41.7	-7.6	8.1	-24.5	-15.6	25.6

Table 3.6: Main detector evMon corrections vs. CREX part, main detector statistics weighted. The correction standard error is calculated by using the slope \times evMon multipletwise difference mean error, propagated through the average calculation, with main detector statistical uncertainties as weights. The mean and error are in units of ppb, while the RMS is in units of ppm.

Corrections	Part 1			Part 2			Part 3		
evMon	Mean	σ	RMS	Mean	σ	RMS	Mean	σ	RMS
0 (E)	-482.8	276.0	1212.9	61.8	232.7	1534.1	-0.9	124.7	792.4
1 (X)	22.3	38.3	145.1	3.8	16.2	32.8	164.0	218.7	1252.8
2 (Y)	52.2	88.6	432.8	-7.3	11.2	78.1	-46.7	8.5	70.3
3	65.4	18.0	84.3	9.1	11.7	93.7	49.4	5.1	62.4
4	9.6	4.6	14.6	-1.2	2.1	10.9	4.4	5.4	38.3
5	162.9	58.0	266.1	-10.9	22.2	152.3	-9.3	33.3	269.8
6	-0.1	6.3	24.3	1.5	1.5	8.3	2.4	2.1	10.8
7	5.4	7.3	32.2	1.5	2.8	19.5	-15.4	6.3	36.3
8	7.1	8.2	31.3	-2.1	3.1	18.0	0.0	4.2	24.9
9	-12.4	12.2	45.7	-3.0	2.2	12.9	-9.2	2.5	12.2
10	-2.0	6.5	25.8	-1.6	2.6	18.0	9.3	2.6	17.0
11	-7.3	7.5	26.3	0.2	2.8	15.4	6.2	3.0	15.8

contributions. For example, the magnitude of the correction difference and fluctuations are small for the dominant evMon 0 even in the most noisy part, part 1, of CREX at $0.5 \text{ ppb/nm} \times -12.0 \text{ nm} = -6.0 \text{ ppb}$, and are also small for the noisier evMon 5 in part 1, at $18.5 \text{ ppb/nm} \times -1.4 \text{ nm} = -25.9$, which may still cancel with other monitors and which is well below the grand average standard error of 58 ppb. The correction for the lowest-ranked evMons from 6 to 11, with the least noise in the monitors, are generally in agreement with zero due to their small grand-averaged position differences.

The deviations in slopes and correction amounts between the regression and Lagrange analyses are generally small, and the larger-scale RMS spread of the dominant evMon 0 position difference is well above the electronics noise level of $0.4 \mu\text{m}$ that limits the lowest-ranked evMons, which gives confidence to its non-zero correction. Additionally, comparing the grand-average corrected A_{det} between the 12 evMon regression and Lagrange and the 5

Table 3.7: A_{det} grand weighted averages, using the 12 evMon Lagrange analysis σ_A as weights, from the 5 evMon regression and dithering and 12 evMon regression and Lagrange analysis techniques. The uncertainty on the correction amount is obtained through $\delta A_{beam} = \text{adding } 5\% \times \text{the grand-averaged corrections per monitor in quadrature separately over the three eigenvector definition parts of CREX.}$

Technique	$\langle A_{det} \rangle$ (ppb)	Δ Lagr	σ_{stat} (ppb)	$\langle A_{beam} \rangle$ (ppb)	RMS (ppm)
5 evMon Reg	2083.80	3.5	84.0	57.03 ± 6.1	777.3
12 evMon Reg	2081.60	1.3	83.8	54.76 ± 5.6	774.8
12 evMon Lagr	2080.26		83.77	53.45 ± 5.44	775.1
5 evMon Dit	2085.20	4.9	84.2	58.43 ± 6.5	779.2

evMon regression and dithering analysis methods, shown in table 3.7, indicates agreement in the grand-averaged asymmetry at the 5 ppb level. All of these considerations lead to a high degree of confidence that a small, $\sim 5\%$, systematic uncertainty on the correction slopes per stable eigenvector definition averaging part of CREX is conservative and appropriate.

3.6.4 Systematic Error Estimate

The uncertainty on the net correction, which is the sum of the corrections from all of the monitors, is obtained from the quadrature sum of the uncertainties in the corrections. The systematic uncertainty estimate of $\frac{\delta C}{C}$ for each evMon slope is the only contribution for each correction, as the uncertainties from the evMon's position distribution widths are already included in the corrected A_{det} widths, yielding

$$(\delta A_{beam})^2 = \sum_i^{\text{evMons}} (\delta C_i \cdot \Delta x_i)^2 = \sum_i^{\text{evMons}} \left(\frac{\delta C_i}{C_i} \cdot C_i \cdot \Delta x_i \right)^2. \quad (3.38)$$

Table 3.8: Main detector evMon corrections vs. CREX part, main detector statistics weighted, as in table 3.6, while also showing the sum and uncertainty in the sum of corrections per evMon averaging part and statistically-weighted grand average. All units are ppb.

12BPM Eigenvector Lagrange Analysis ($\frac{\delta_{\text{slope}}}{\text{slope}} = 5\%$)			
evMon	Part 1	Part 2	Part 3
0 (E)	-482.8	61.8	-0.9
1 (X)	22.3	3.8	164.0
2 (Y)	52.2	-7.3	-46.7
3	65.4	9.1	49.4
4	9.6	-1.2	4.4
5	162.9	-10.9	-9.3
6	-0.1	1.5	2.4
7	5.4	1.5	-15.4
8	7.1	-2.1	0.0
9	-12.4	-3.0	-9.2
10	-2.0	-1.6	9.3
11	-7.3	0.2	6.2
A_{beam}	-179.6	51.9	154.4
σ_{beam}^{syst}	25.9	3.2	9.0
Part weight	15.6%	47.5%	36.9%
Grand Average $\langle A_{beam} \rangle$	53.45 ± 5.44 ppb		

Table 3.9: Blinded main detector asymmetry and net correction per evMon averaging part of CREX and the statistically-weighted grand average A_{det} and A_{beam} correction final results. All units are ppb.

Part	A_{det}	Weight	σ_{det}^{stat}	$A_{beam} \pm \sigma_{beam}^{syst}$
1	2157.68	15.65%	211.77	-179.65 ± 25.9
2	1992.07	47.48%	121.58	51.89 ± 3.2
3	2160.94	36.88%	137.95	154.37 ± 9.0
Net	2080.26		± 83.77	53.45 ± 5.44

Then, assuming the same degree of accuracy $\frac{\delta C_i}{C_i} = 5\%$ for all of the slopes, we have

$$\sigma_{beam}^{syst} = 5\% \cdot \sqrt{\sum_i^{\text{evMons}} (C_i \cdot \Delta x_i)^2}. \quad (3.39)$$

The A_{beam} corrections and uncertainties are calculated for each eigenvector definition averaging part of CREX, and the grand average is calculated using the main detector statistical weighted average approach, using the σ_{beam}^{syst} as the uncertainties propagated through the averaging. The corrections and uncertainties for the three parts of CREX and the grand-averaged A_{det} result are given in tables 3.8 and 3.9. The blinded final 12 evMon Lagrange multipliers analysis corrected detector asymmetry is

$$\boxed{\langle A_{det} \rangle = 2080.26 \pm 83.7 \text{ (stat)} \pm 5.44 \text{ (syst) ppb.}}$$

3.6.5 Statistical Quality

To verify that the beam corrections quality matches the claimed systematic precision of $\sim 5\%$ leading to the small beam corrections systematic error $\sigma_{beam}^{syst} = 5.44$ ppb, we cross check that the corrected A_{det} and beam monitor distributions exhibit statistical behavior indicative of successfully removing all HC A_{beam} , although this does not guarantee systematic control. These checks verify that CREX achieves an asymmetry measurement corresponding to statistical fluctuations, with a lack of uncorrected features. The BCM and PMT detector non-linearities and their impacts on the measured A_{det} are considered as well.

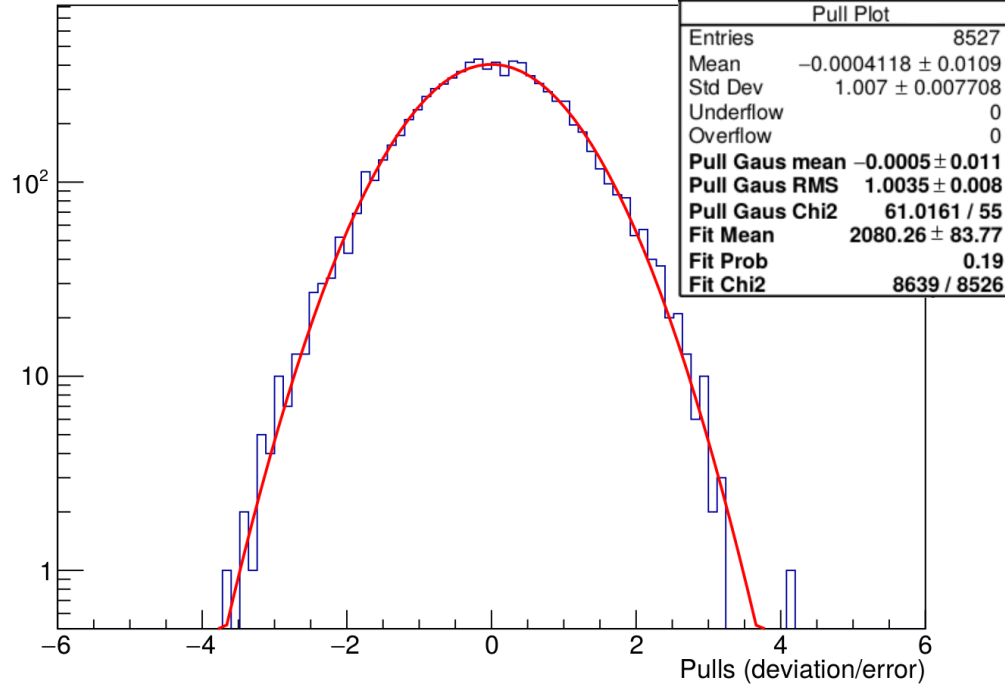


Figure 3.21: Pull plot of the minirunwise grand-averaged 12 evMon Lagrange multipliers analysis corrected A_{det} .

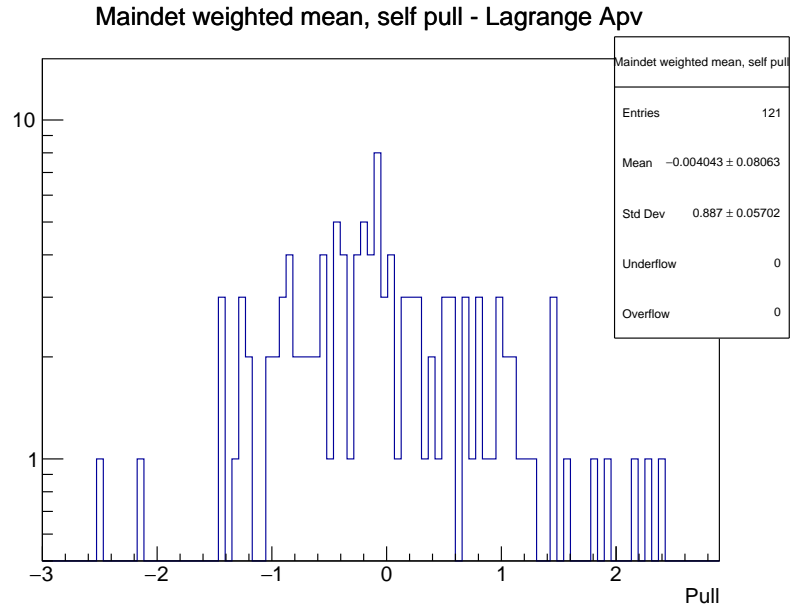


Figure 3.22: Pull plot of the slugwise grand-averaged 12 evMon Lagrange multipliers analysis corrected A_{det} .

Table 3.10: Main detector grand-averaged 12 evMon Lagrange multiplier analysis corrected A_{det} and correction, as well as χ^2 results from performing the average over different timescales, each of which are the result of weighted averages with their constituent miniruns' $A_{det\ i}$ and $\sigma_{det\ i}$. The asymmetry and uncertainties are given in units of ppb, and the RMS is in ppm. The reduced χ^2 are close to 1 for all averaging time scales.

$\langle A_{det} \rangle$	σ_{stat}	$\langle A_{beam} \rangle$	RMS	Minirun χ^2	Slug χ^2	Pitt χ^2	Slow χ^2
2080.26	83.77	53.45 ± 5.44	775.1	8639 / 8526	95.2 / 120	19.6 / 23	3.1 / 5

Statistical Behavior and Pull

The CREX data displays behavior consistent with counting statistics at all averaging timescales. The weighted average calculations have reduced χ^2 metrics which are close to unity. The lack of strong outliers and the consistency with normally-distributed data gives confidence that all HC A_{beam} have been successfully removed and that the minirunwise error bars from the $\frac{RMS}{\sqrt{N}}$ used as weights in the global fits do in fact reflect statistical precision. The statistical quality of the data and uncertainties used in the grand averages is checked by calculating the distribution of the points' statistical pull. The pull for any measured quantity Γ is defined as

$$P_{\Gamma i} = \frac{\Gamma_i - \langle \Gamma \rangle}{\sigma_{\Gamma i}}, \quad (3.40)$$

where the uncertainty $\sigma_{\Gamma i}$ comes from the uncertainty in the measurement of Γ and the average $\langle \Gamma \rangle$ is the main detector weighted average.

For data distributions that are determined solely by counting statistics, as should be the case for the corrected A_{det} measurement, the pull distribution over the data set should correspond to a Gaussian with a mean of 0 and RMS of 1. An example of the pull distribution from the A_{det} grand average over the slugwise and minirunwise calculated A_{det} values and uncertainties are given in Figs. 3.21 and 3.22, which display nearly perfect correspondence with the ideal case expectation. A multipletwise plot of the corrected A_{det} asymmetries is

shown in Fig. 3.23, showing the Gaussian quality of the data over ~ 5 orders of magnitude. The data are all thoroughly checked, as described in section 3.3.4, and the tails in the multiplet plot are due to small issues with brief fluctuations in the beam delivery that evade cuts and which are verified to have negligible impact on the minirunwise results, and the multipletwise distribution’s large tails are symmetric about zero, due to the pseudorandom helicity flip pattern.

The grand-average pull distributions and χ^2 values for the grand-averaged A_{det} , performed both directly with the constituent data points from the miniruns and from the minirunwise averaged slug, Pitt, and slow-control flip timescales, are given in table 3.10. The definition of “Pitt” was developed by Mark Pitt and corresponds to an average over approximately four neighboring slugs with similar amounts of alternating IHWP state data in them. A discussion of the slow-control flips within Pitts as metrics of unmeasured HC A_{beam} is given in section 3.6.5. The definitions of the Pitts for the 121 slugs of CREX and plots of the various timescale A_{det} averages and pull distributions are given in Appendix A.3.

Correction Disagreement Pull

The difference between the 12 evMon Lagrange multiplier and regression correction analyses’ grand-averaged A_{beam} are given before in table 3.7, but we can also investigate the statistical behavior of the difference in corrections. To obtain statistical information we calculate the difference in the corrections at the multiplet level and take the RMS of the distribution to correspond to a statistical measure of the quality of the corrections which takes into consideration all correlations amongst the correction slopes and eigenvector position monitors. Figure 3.24 shows the means and mean errors, from their RMS/\sqrt{N} , obtained from the minirun calculated histograms of the multipletwise difference, and the grand average and pull plot using those errors.

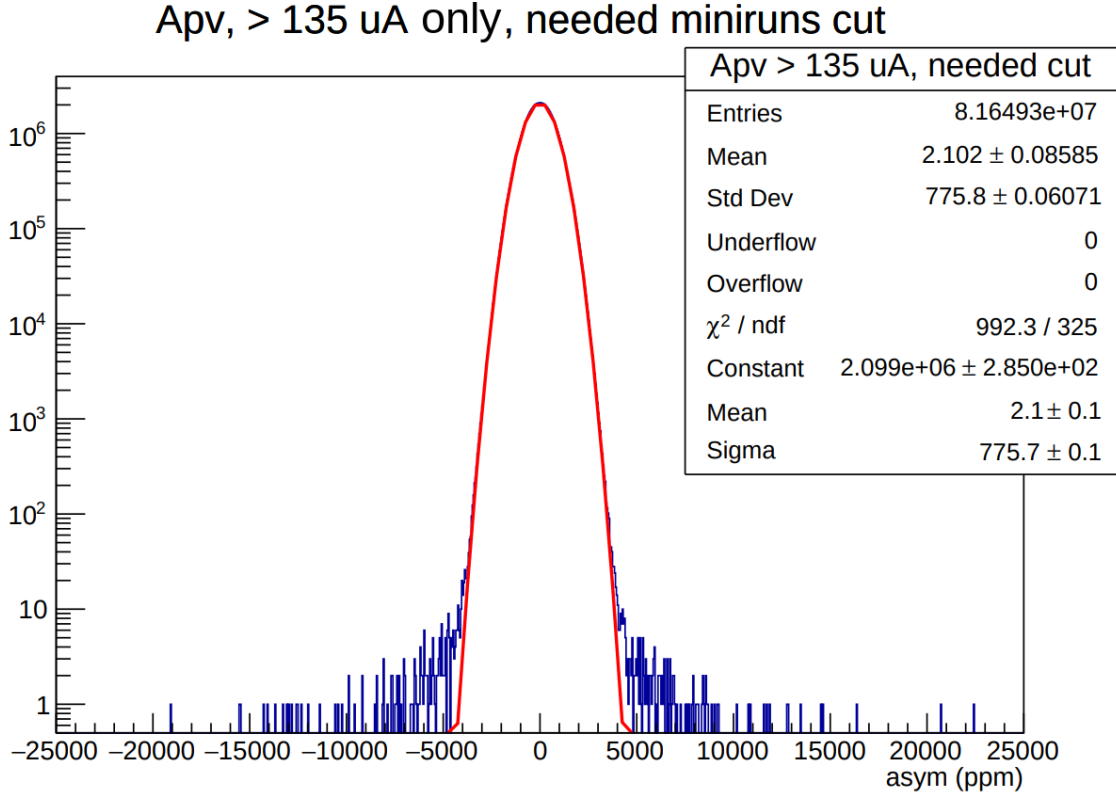


Figure 3.23: Multipletwise asymmetry distribution, “mul plot,” of the 12 evMon Lagrange multipliers analysis corrected A_{det} . The distribution is Gaussian for ~ 5 orders of magnitude, and the tails are primarily due to occasional noise in beam delivery that evades cuts and have no effect on the Gaussian fit σ compared to the distribution standard deviation. A cut is applied for this mul plot to only include data with both HRSs active and with beam current close to the optimal $150\mu A$ level, which removes 4×10^6 events, corresponding to only 5% of the data.

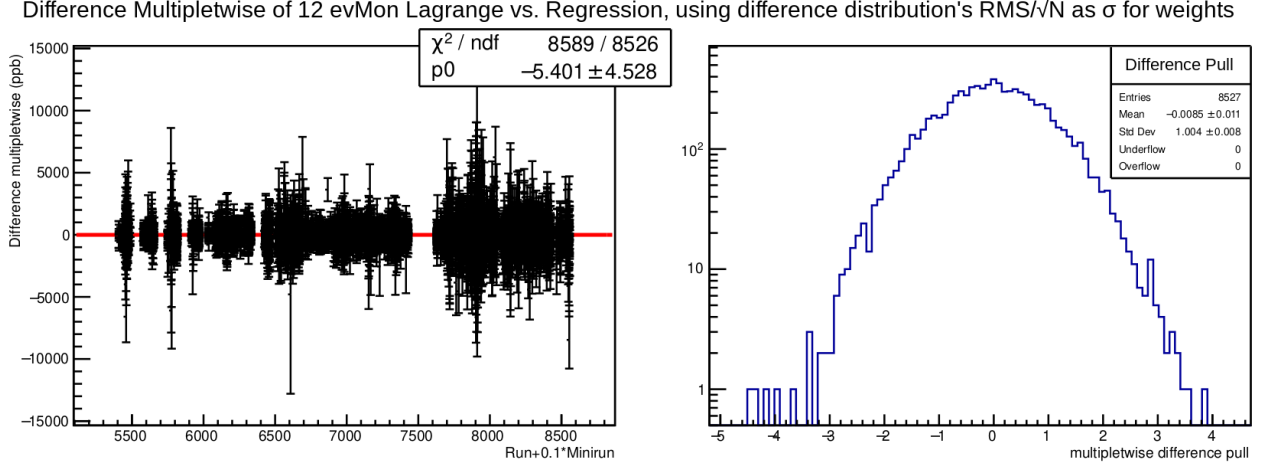


Figure 3.24: Differences between 12 evMon Lagrange multipliers analysis vs. regression corrected A_{det} averaged over miniruns, where the difference distribution is obtained from the multipletwise distribution. The uncertainty used in the weighted average weights comes from the multipletwise difference distribution's RMS/\sqrt{N} widths. The pull distribution is very close to the statistical ideal.

The grand average, using the difference mean errors in the weights, is approximately zero within the error and is uncertain at the ~ 5 ppb scale, while the grand average multipletwise difference that uses the main detector statistical uncertainty in the weights has a grand-averaged mean error of 8.4 ppb. The scale of the multipletwise difference also rests at the ~ 5 ppb scale and the pull plot behaves remarkably statistically, indicating that the combined disagreement between the slopes behaves approximately like random noise. Additionally, the disagreement between the grand-averaged A_{det} results for the various analysis techniques given in table 3.7 are all below the ~ 5 ppb level as well. Taken together these all further support the claimed systematic uncertainty estimate upper limit on A_{beam} .

Slow-Control Backgrounds

The HC A_{beam} corrections made with the charge normalization and position correction slope calculation methods described in this chapter exclusively focus on detector scattering

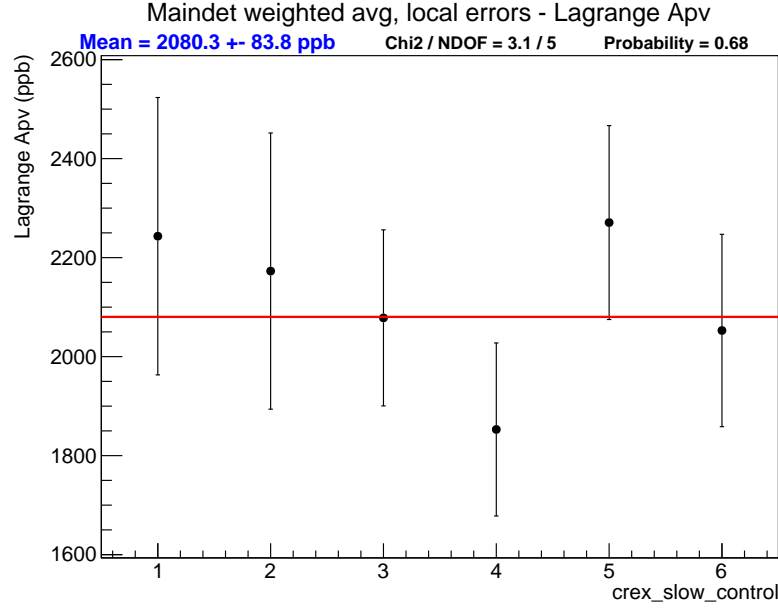


Figure 3.25: Weighted mean.

Figure 3.26: 12 evMon Lagrange multipliers analysis corrected A_{det} vs. slow-control flip timescale minirun averages. Numbers 1, 3, and 5 are IHWP In, 2, 4, and 6 are IHWP Out. 3 and 4 are both Wien Left and the others are Wien Right.

Table 3.11: Slow-control flip timescale A_{det} averaged over miniruns.

IHWP x Wien	Mean	σ_{stat}	Weight	χ^2	Miniruns	χ^2/NDOF
1	2243.28	280.16	8.94%	793.83	741	1.07
2	2172.82	279.00	9.02%	708.52	763	0.93
3	2078.28	177.80	22.20%	1861.08	1902	0.98
4	1852.87	174.79	22.97%	2113.26	2013	1.05
5	2270.86	195.89	18.29%	1546.16	1524	1.02
6	2052.80	194.31	18.59%	1613.95	1584	1.02

rate asymmetries that are linearly correlated with helicity-correlated parameters measured with dedicated devices elsewhere in the beam. However, it is possible for the Pockels Cell or other components in the injector with analyzing power to generate higher-order helicity-correlated asymmetries, such as beam spot size asymmetry. Additionally any electronics which are sensitive to the true helicity state electronics signals that drive the Pockels Cell may accidentally pick up the true helicity signal and contaminate their measurement. Cancelling these possible unmeasured and uncorrected HC backgrounds signals is the goal of the frequent IHWP changes of the laser polarization and less frequent double Wien flips of the electron polarization.

CREX measures nearly equal amounts of statistics in the four combinations of IHWP in and out and Wien flip right and left. The averages over miniruns for each of the six distinct states, where the Wien flip right data is separated across the Spring and Summer experiment periods, appear to behave statistically, with the $\text{IHWP} \times \text{Wien flip}$ averaged A_{det} points lying normally-distributed around the grand average, shown in Fig. 3.26. The χ^2 of the weighted mean is consistent with counting statistics, rejecting the alternative hypothesis of false asymmetry contributions or non-statistical behavior of A_{det} over slow-control timescales with a probability of 68%.

The statistically consistent behavior of the slow-control average A_{det} points indicates that there are no noteworthy uncorrected HC A_{beam} , but another check is to investigate the slow-control flip canceling null asymmetries, which is easily done with the Pitt timescale averages. Calculating a “null” asymmetry is done by treating the opposite IHWP flip states with equal weight without correcting for the IHWP dependent change in helicity sign relative to the Pockels Cell’s unchanged input helicity electronics. A “null” Pitt asymmetry is obtained by independently calculating the weighted average using the main detector uncertainty as weights, for the two IHWP states separately for each Pitt and then averaging the two states

together with equal weight,

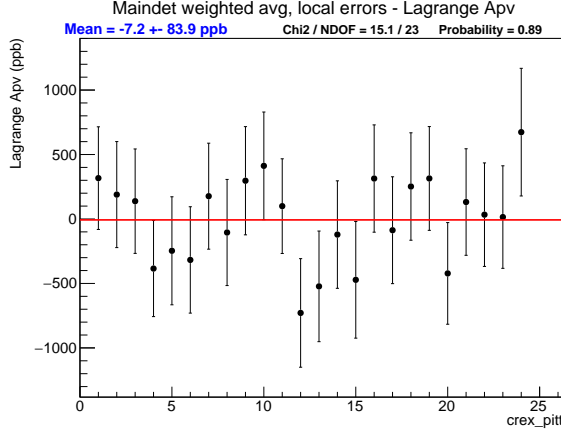
$$A_{\text{null Pitt}} = \frac{A_{\text{IHWP Out}} - A_{\text{IHWP In}}}{2}, \quad (3.41)$$

and propagating the uncertainty through the equally weighted average in a similar way to the discussion before, just with $w_i = 1$ for both states in the null Pitt average. The Pitt definitions are tuned, given in Appendix A.3, to include nearly equal amounts of each IHWP state, where possible, to ensure that the null Pitts are sensitive to differences in A_{det} between IHWP states when weighted equally. Additionally, the choice of changing the sign of the $A_{\text{null Pitt}}$ with the Wien flip illuminates the cancellation due to that slow-control flip.

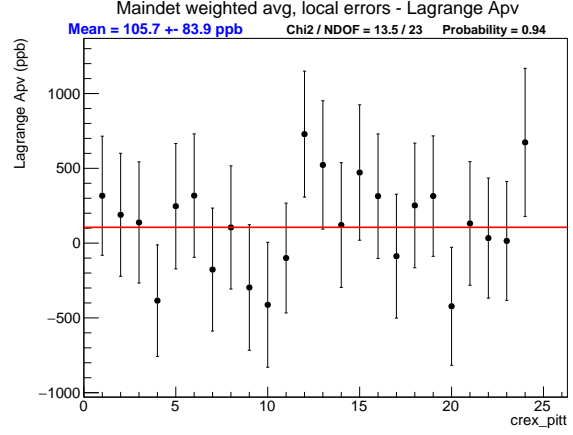
The null Pitt grand averages for changing and not changing the sign with the Wien flip are given in Fig 3.27. The grand average null Pitt with a sign multiplication for the Wien flips is 105.7 ± 83.9 ppb, indicating that a statistically insignificant amount of HC A_{beam} that changes sign with the IHWP flip is present. The grand average null Pitt with no sign multiplication for the Wien flips is -7.2 ± 83.9 ppb, which is consistent with zero and indicates that the uncorrected HC A_{beam} that changes sign with the IHWP slow-control helicity flips do not change sign with the Wien, and that there are no Wien-dependent HC A_{beam} that fail to cancel out in the grand average.

Helicity-Correlated Beam Asymmetry Analysis

A final check on the scale of HC A_{beam} backgrounds is to verify their cancellation with slow-control flips in the grand-averaged position differences. The part averaged eigenvector monitor differences are shown before in table 3.4, but another check is to calculate the HC positions and angles which are obtained from the geometry of the BPMs near the target, and the fractional energy difference, $\delta p/p$. The positions and angles on the target are calculated



(a) Without Wien, with IHWP sign flips.



(b) With Wien, with IHWP sign flips.

Figure 3.27: 12 evMon Lagrange multipliers analysis corrected $A_{\text{null Pitt}}$ vs. Pitts. Each null Pitt average equally weights the IHWP In and Out state data and looks at the disagreement between them to illuminate IHWP dependent HC A_{beam} . The null Pitt average without a sign multiplication between the Wien states also cancels any HC A_{beam} which are not affected by the Wien, to the degree that there are similar amounts of Wien Right and Left data across the experiment.

Table 3.12: Table of weighted average helicity-correlated target and energy beam parameters across the CREX Wien flips.

Wien	Weight	X (nm)	Y (nm)	θ X (nrad)	θ Y (nrad)	E ($\delta p/p$)
Right 1	17.9%	1.6 ± 3.7	-2.4 ± 2.0	-0.26 ± 0.17	-0.11 ± 0.12	$-2.0 \pm 2.0e^{-9}$
Left	45.2%	-4.1 ± 1.6	0.3 ± 1.1	0.08 ± 0.04	-0.02 ± 0.10	$0.32 \pm 1.5e^{-9}$
Right 2	36.9%	-2.8 ± 4.1	-0.2 ± 1.7	-0.06 ± 0.09	-0.28 ± 0.17	$0.84 \pm 1.9e^{-9}$
Weighted Average		-2.6 ± 1.8	-0.4 ± 0.9	-0.03 ± 0.05	-0.13 ± 0.08	$0.09 \pm 1.0e^{-9}$

as

$$\Delta X(Y) = \frac{\Delta x_{4eX(Y)} - \Delta x_{4aX(Y)}}{D/L} + \Delta x_{4aX(Y)}, \quad (3.42)$$

where $D = 4.083$ is the distance between BPMs 4A and 4E and $L = 5.725$ is the distance between BPM 4A and the target center. The angle is calculated as

$$\Delta \theta_{X(Y)} = \frac{\Delta x_{4eX(Y)} - \Delta x_{4aX(Y)}}{D}, \quad (3.43)$$

and the fractional energy is calculated as the energy sensitive BPM relative to the energy dispersion calibration

$$\Delta \delta p/p = \frac{\Delta x_{12X}}{4m}. \quad (3.44)$$

The average kinematic parameters calculated from the multipletwise distributions of these combinations of BPM monitors, given in table 3.12, show that there are no significant helicity-correlated beam parameters with large central value relevant for scattering in the target, either after the IHWP cancellations in the Wienwise averages or in the grand-averaged results. This matches the conclusion that the 5% uncertainty applied per monitor correction slope gives a net uncertainty similar in scale to the observed nm scale beam parameters, and so even if we missed the net HC A_{beam} at this level of precision, the final asymmetry would not be clearly affected.

The beam current charge asymmetry A_Q is well controlled, even though it is known to have a Wien-dependence as a result of the improperly set up charge feedback engine data cuts during production running, described in section 3.3.1. The Wien-averaged A_Q is non-trivial, shown in table 3.13 and Fig. 3.28, but is adequately removed from the A_{raw} measured asymmetry. The BCM AN US monitor measures the A_Q contribution to A_{det} with a $\sim 1\%$ accuracy, limited by the pedestal precision and monitor linearity discussed before, leading to

Table 3.13: Table of weighted average raw and corrected detector asymmetry and A_Q across the CREX Wien flips.

Wien	Weight	A_{raw} (ppb)	A_{det} (ppb)	A_Q (ppb)
Right 1	17.9%	2460.15 ± 391.95	2207.90 ± 197.69	-94.1 ± 69.6
Left	45.2%	1871.06 ± 278.39	1963.65 ± 124.64	148.1 ± 40.1
Right 2	36.9%	2006.57 ± 335.29	2160.94 ± 137.95	-376.3 ± 38.7
Weighted Average		2026.81 ± 189.88	2080.26 ± 83.77	-88.8 ± 26.2

an A_{raw} systematic uncertainty contribution of $0.88ppb$ after the Wien-dependent A_Q cancels in the grand average. A beam-trip recovery cut check like that shown in Fig. 3.8 is also done for the position differences, and no effect is seen, meaning the online set-up of the charge feedback system and the change of beam-trip recovery cuts does not impact the position differences.

Raw Asymmetry Accuracy

Finally, the A_{raw} scattering rate asymmetry measured in the main detector PMTs is slightly degraded by the detector resolution and is affected by the detector non-linearity. For CREX, as a result of the relatively lower scattering rate than in PREX II, the limitations on PMT high voltage (HV) for balancing linearity at low HV and saturation at high HV are not as strict, and offline benchtop measurements determine a nonlinearity, $\frac{\delta S}{S}$, at the production running HV setting below the $\sim 0.3\%$ level when combined with the pedestal precision discussed in section 3.1 [28]. The measured PMT asymmetry includes the A_Q contribution in the measurement itself, both given in table 3.13, giving the uncertainty in the measured raw asymmetry of

$$\sigma_{A_{raw}}^{nonlin} = \frac{\delta S}{S} \times (A_{raw} + A_Q) = 0.003 \times (2026.8 - 88.8) = 5.8ppb. \quad (3.45)$$

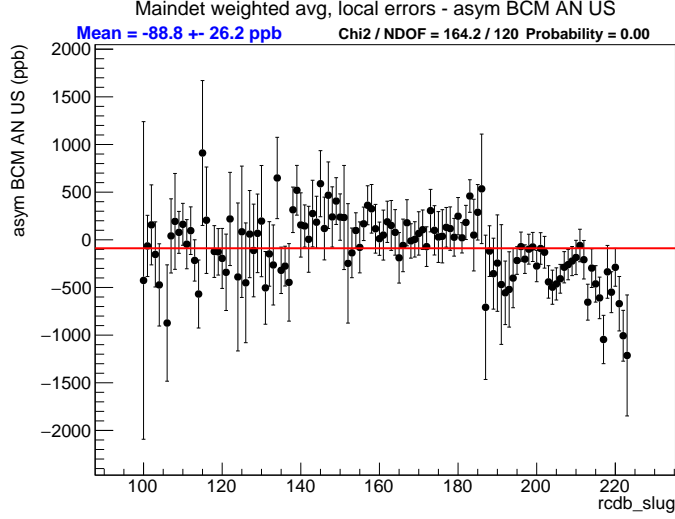


Figure 3.28: Slugwise charge asymmetry A_Q across CREX. The non-trivial Wien-dependence in A_Q due to the improperly set charge feedback engine cuts during production running is visible to the eye. The χ^2 and fit probability are non-statistical because of the Wien-dependent trip-recovery A_Q and also because the charge asymmetry distribution is intentionally driven, non-statistically, to zero with the feedback system during production running.

3.7 Including BMOD Data

All of the results shown so far are data that include the BMOD active calibration data in the cuts, corresponding to adding $\sim 5\%$ more statistics to the data-set. Because of the scale of the modulations it is not guaranteed that this data maintains the same quality as the non-modulating data, as we intentionally tuned the modulation amplitudes and the cuts so that the modulation is on a similar scale to the natural beam motion and is not cut by any of the burp, trip, stability, or limit cuts. We want to include the BMOD active coil active data into the data set to increase the statistical power, and the quality of the BMOD active included results discussed already indicates that doing so is not harmful, but it is worthwhile to compare the BMOD active to inactive data-sets as an additional quality check.

The corrections per eigenvector monitor and net correction disagreements between re-

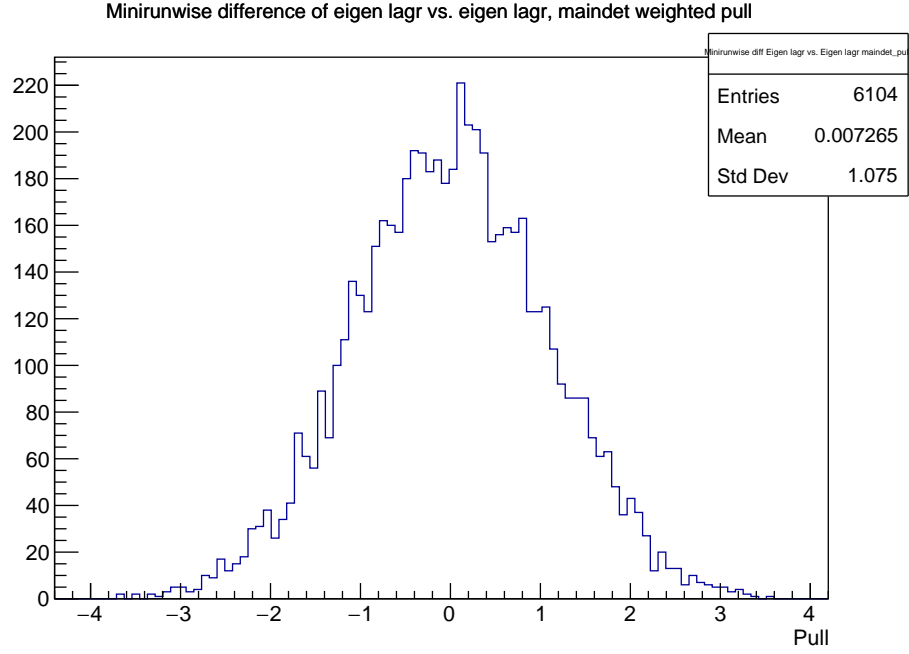


Figure 3.29: Pull plot of the difference in corrected A_{det} between the BMOD active and inactive cut data-sets within each minirun containing BMOD calibration data. This shows the well behaved statistical behavior and independence of the BMOD active vs. inactive data within each minirun.

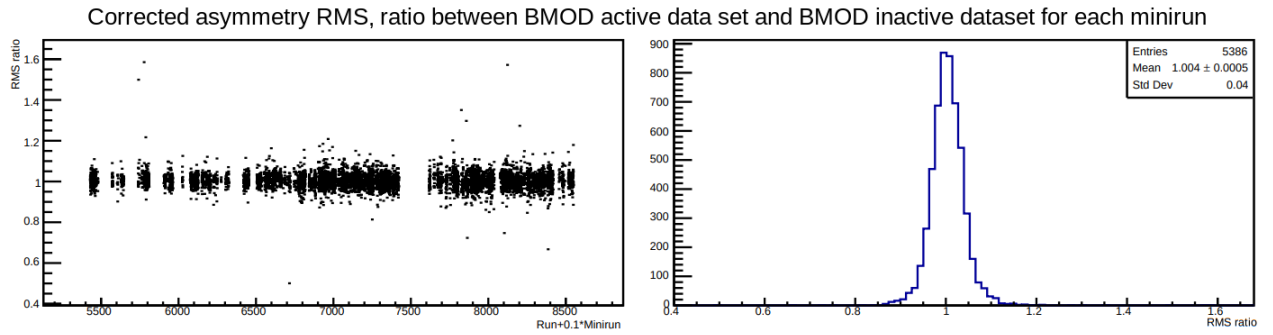


Figure 3.30: Minirunwise (left) and histogram (right) showing the ratio of the corrected A_{det} RMSs of the BMOD active vs. inactive data, indicating their consistent and statistical behavior within each minirun.

gression and the Lagrange multipliers analysis are checked at the minirun and slug levels by comparing the scale of disagreement between the BMOD active and inactive data-set cuts, and all of the metrics fall within acceptable statistical limit expectations. Notably, the difference in measured asymmetry between the two cuts for all miniruns that include BMOD calibration data behaves well, with a pull plot of that difference consistent with counting statistics noise, shown in Fig. 3.29. Similarly, the ratio of the corrected A_{det} distribution RMSs between the two cuts is stable and centered on unity for all miniruns that contain BMOD calibration data, shown in Fig. 3.30.

This conclusion is true for the Lagrange multipliers and dithering analysis techniques, which is expected due to them explicitly including the calibration data in their slope calculations. However, the regression analysis does not adequately correct the BMOD active data for all modulation coils across CREX. This is both due to the BMOD calibration data not being included explicitly in the regression slope calculations and due to the occasional phase shift between the 15 Hz BMOD cycle versus the quartet helicity pattern. The occasional phase shift causes the regression widths to get bigger for the X and Y coils sometimes, particularly during the third part of CREX while the fast feedback system was inactive, but the Lagrange multipliers and dithering analyses are unaffected by this. The phase shifts could have been avoided, and should be in future experiments, by setting the modulation cycle to begin explicitly at the start of multiplets, rather than only at the start of helicity events.

3.8 Beam Corrections Confidence

Taken together, these slow-control helicity flip cancellations, good statistical behavior, and small scales of corrections analyses systematic limitations combine to support the claimed 5% uncertainty estimate for correction slopes with effectively no remaining unmeasured or

uncorrected HC A_{beam} . The resulting 5.44 ppb uncertainty in the applied beam corrections represent a conservative 5% upper limit on the systematic uncertainty.

Chapter 4

Conclusion

This chapter concludes the discussion of the CREX measurement of PVES from ^{48}Ca by describing the steps for extracting A_{PV} from measurements of the detector asymmetry, beam polarization, scattering kinematic variables, and various backgrounds. This is followed by a report of the weak form factor extracted from the measurement and an overview of the steps required to obtain additional nuclear properties. We conclude with a brief review of the theoretical impacts of the CREX measurement and the future prospects for nuclear structure measurements with PVES.

4.1 Parity-Violating Asymmetry

The corrected detector asymmetry, A_{det} , described in the previous chapter, requires more analysis to obtain the measured parity-violating asymmetry result, A_{PV}^{meas} , and its uncertainty,

$$A_{PV}^{meas} = \frac{1}{P_b} \frac{A_{corr} - P_b \sum_i f_i A_i}{1 - \sum_i f_i}, \quad (4.1)$$

Table 4.1: Table of error contributions for the CREX A_{PV} measurement.

Contribution	Absolute [ppb]	Relative [%]
Polarization Magnitude	13.13	0.49%
Horizontal A_T	12.66	0.48%
Vertical A_T	0.89	0.03%
Q^2 Acceptance Function	23.93	0.9%
Rescattering	0.49	0.02%
A_{beam} Beam Correction	6.89	0.26%
A_{raw} Detector Non-linearity	7.36	0.38%
^{40}Ca Background	8.76	0.33%
A_Q Charge Correction	1.12	0.04%
Inelastic Contamination 2^+	18.94	0.71%
Inelastic Contamination $3^-(1\text{st})$	10.19	0.38%
Inelastic Contamination $3^-(2\text{nd})$	3.59	0.13%
Total Syst	39.51	1.49%
Total Stat	106.07	3.99%
Total	113.19	4.25%

where P_b is the beam polarization, the A_i and f_i are background asymmetries and their contamination fractions, and

$$A_{corr} = A_{PMT} - A_{BCM} - A_{beam} - A_T - A_{nonlin} - A_{blind} \quad (4.2)$$

is the corrected asymmetry, where the $A_{PMT} - A_{BCM} = A_{raw}$, $A_{raw} - A_{beam} = A_{det}$, and A_{nonlin} terms are the asymmetries discussed in the previous chapter. The various corrections and uncertainties on the final A_{PV}^{meas} are listed in table 4.1, yielding a final parity-violating asymmetry of

$$A_{PV}^{meas} = 2658.6 \pm 106.07 \text{ (stat)} \pm 39.51 \text{ (syst)}. \quad (4.3)$$

The transverse asymmetry correction A_T comes from the beam normal single-spin asymmetry, which has a non-trivial analyzing power for ^{48}Ca . The A_T correction comes from contributions from possible vertical and horizontal transverse polarization of the beam generating azimuthally-dependent asymmetries in the main detectors that do not cancel perfectly due to some asymmetry in the left-right HRS and detector configurations. The transverse asymmetry correction and systematic uncertainty is the primary topic of [58] and the dedicated measurement of its analyzing power in various targets, including ^{48}Ca , is reported in a forthcoming letter.

The blinding factor is an additional term added to each measured A_{raw} multiplet within the analyzer, in order to blind the final asymmetry and avoid human bias during the data taking and analysis processes. The blinding factor is chosen using a fixed seed string for all runs during CREX, which is selected randomly from a ± 900 ppb box, which is approximately 10 times larger than the anticipated A_{det} statistical uncertainty. After the analysis is completed the blinding factor, $A_{blind} = -255.70923$, is unblinded and removed, yielding the final A_{corr} measured helicity-dependent asymmetry.

The electron beam polarization, P_b , dilutes the parity-violating scattering asymmetry. The average polarization across the run is measured parasitically with the Compton polarimeter primarily, averaged with the periodic Møller polarimeter measurements. The average beam polarization is $87.09 \pm 0.39\%$, which affects the asymmetry and uncertainty contributions to A_{PV}^{meas} described in the previous chapter because they are helicity-state dependent.

Additionally, there are parity-violating asymmetries that arise from the ^{40}Ca impurity contribution to the ^{48}Ca target, rescattering within the HRS, and inelastic excitations in ^{48}Ca , all of which contribute potential background dilutions to A_{PV}^{meas} which must be subtracted based on their dilution fractions, f_i , times their asymmetries, A_i . The effect of the ^{40}Ca dilution is small, due to the similarity of its asymmetry to ^{48}Ca . The rescattering dilution, measured with dedicated calibration runs, is insignificant. The inelastic background dilution fractions, discussed in detail in [40], are measured, and their asymmetries are the subject of a forthcoming letter [34]. Finally, the extraction of the scattering kinematics, described further in the next section, includes various uncertainties in the determination of the acceptance normalization, which are dominated by the ability to reconstruct the track scattering angles at the target with measurements in the HRSs.

4.2 Model Extraction

The A_{PV}^{meas} result depends on the Q^2 momentum transfer of the scattering, calibrated and determined in dedicated counting mode measurements,

$$A_{PV} \simeq \frac{G_F Q^2}{4\pi\alpha\sqrt{2}} \frac{Q_W}{Z} \frac{F_W}{F_{ch}}, \quad (4.4)$$

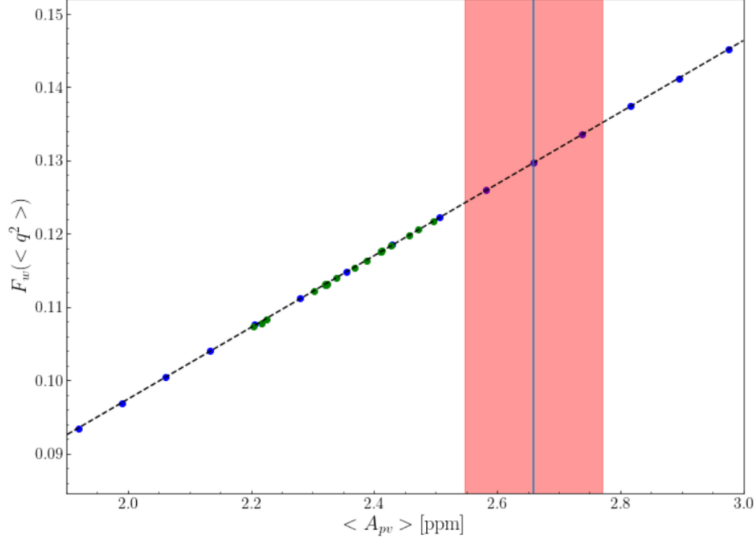


Figure 4.1: Plot of the weak form factor calculated with various relativistic and non-relativistic DFT models at the average $\langle Q^2 \rangle = 0.0297 \text{ GeV}^2$ for CREX. The red band shows the experiment $A_{PV}^{meas} = 2658.6 \pm 113.2$ ppb intersecting a linear fit line to the F_W points, extracting $F_W(\langle Q^2 \rangle) = 0.1297(55)$.

where $Z = 20$ and $Q_W = 26.0728$. A precise interpretation of the experiment's result requires nuclear structure models to calculate the $A_{PV}^{model}(Q^2)$ corresponding to the kinematics that CREX measures. The finite acceptance of the HRSs is defined by the collimators and is studied with calibrated magnetic optics counting mode track reconstruction and Monte Carlo simulations. The acceptance function, $\epsilon(\theta)$, is the probability distribution for electrons to reach the detector as a function of the scattering angle θ , directly related to Q^2 in elastic scattering. The acceptance function is being prepared for publication in a forthcoming letter with the CREX results. From the acceptance function it is possible to extract the model predicted A_{PV}^{model} for nuclear charge distributions obtained from nuclear structure models over the accepted Q^2 distribution,

$$\langle A_{PV}^{model} \rangle = \frac{\int d\theta \sin \theta A_{PV}(\theta) \frac{d\sigma}{d\Omega}(\theta) \epsilon(\theta)}{\int d\theta \sin \theta \frac{d\sigma}{d\Omega}(\theta) \epsilon(\theta)}, \quad (4.5)$$

which can be directly compared to the experimentally measured A_{PV}^{meas} . The acceptance function is obtained by matching the measured magnetic transport extrapolated kinematic distributions at the target with a tuned Monte Carlo simulation. The distribution downstream of the target is produced in the simulation, including radiative corrections and the simulated experiment geometry. With the simulation matching the experimental data, the fundamental scattering vertex information, accessible with the calibrated Monte Carlo data, is tabulated in a probability distribution versus θ scattering angle. The average $\langle Q^2 \rangle$ for CREX is $0.0297(2)\text{GeV}^2$ with an incident beam energy of 2182.5 ± 1.5 MeV, and average scattering angle of $4.51(2)^\circ$. The uncertainty in the Q^2 acceptance function is included in the error table as a contribution to the A_{PV} result.

To adequately model the dynamics of electrons scattering from the ^{48}Ca target, theoretical models must utilize an electric charge distribution, $\rho_{ch}(r)$, constrained by elastic scattering data, calculate the weak charge distribution, $\rho_W(r)$, and incorporate distorted wave scattering Coulomb distortions and contributions from the nuclear spin-orbit coupling interaction [41, 57]. Several other terms which are known to have only small impacts on the charge distributions, but which must still be considered, are the strangeness contribution to the weak charge and axial-vector interactions from meson exchange and possible mixed parity states in the ground state of the nucleus [40].

Theoretical models calculate the weak charge distribution, $\rho_W(r)$, from which incident electrons scatter and compute its Fourier transform to obtain the weak charge form factor,

$$F_W(q = \sqrt{Q^2}) = \frac{1}{Q_W} \int d^3r \frac{\sin(qr)}{qr} \rho_W(r), \quad (4.6)$$

which is then used to calculate $\langle A_{PV}^{model} \rangle$. For convenience, a two parameter symmetrized Fermi function is used to parameterize the charge density in terms of a weak charge radius

and weak skin thickness,

$$\rho_W(r) = \rho_0 \frac{\sinh(c/a)}{\cosh(r/a) + \cosh(c/a)} \quad (4.7)$$

where c is the radius related parameter and a is the skin thickness parameter [72]. This charge density parametrization conveniently yields exact moments, where the RMS weak radius is $\langle R_W^2 \rangle = \frac{3}{5}c^2 + \frac{7}{5}(\pi a)^2$, allowing determination of the theoretical uncertainty, introduced by dependence on the model-determined skin surface thickness parametrization, for the weak charge radius extraction. The DFT family of models only yield preliminary results for the $F_W(\langle Q^2 \rangle)$ value at the moment of writing, and require additional work before reporting the RMS weak charge radius and continuing to extract the neutron radius and skin results.

With the model-calculated form factor and cross section integrated over the CREX acceptance function to get A_{PV}^{model} they compare to the measured A_{PV}^{meas} . Preliminary work with the family of DFT models extracts a $F_W(\langle Q^2 \rangle) = 0.1297(55)$, corresponding to a difference in charge and weak form factors of $F_{ch} - F_W = 0.0233(55)$. This result is obtained by plotting the predicted F_W for various non-relativistic and relativistic DFT models versus their predicted asymmetry, shown in Fig. 4.1, and projecting from the measured asymmetry onto the F_W linear fit. This is possible due to the linear relationship between the two in the approximate equation 4.4 and the small range of Q^2 integrated in the acceptance function. This result is preliminary and indicates that a $R_{weak}^{skin} \sim R_n^{skin}$ measurement at the $\pm 0.025 fm$ level is achievable. This family of preliminary DFT model results require more work before weak charge distribution results can be reported, and the other kinds of nuclear structure models, described before in section 1.4, will need to follow similar steps to make comparisons between them.

4.3 Neutron Skin

Once nuclear structure models report weak charge distribution results, they take the measured RMS weak charge radius, R_W , and extract the RMS point neutron radius, R_n , by expressing the electromagnetic and weak charge densities in terms of their particle content. This process is done in great detail in [41], which includes the spin-orbit interaction contributions to both the electromagnetic and weak form factor calculations. The spin-orbit contributions to the weak skin for the NL3 and FSU DFT models are determined in [41] to be $\sim +0.03 fm$ when compared to calculations that do not consider it, which is similar in scale to the projected experimental uncertainty in the extraction. The spin-orbit contribution to the weak skin is also calculated for the *ab initio* models in [4] and is found to be very similar, about 10% smaller of an effect than in the DFT models, highlighting the importance of its inclusion in the weak and neutron skin extractions.

A simplified version of the R_n extraction from R_W starts with expressing the charge densities in terms of their particle contents, which is achieved by folding the charge form factors of the proton and neutron particles with their point density distributions over the nucleus, $\rho_p(r)$ and $\rho_n(r)$ respectively,

$$\rho_{ch}(r) = \int d^3r' ZG_p^E(r')\rho_p(|\vec{r}-\vec{r}'|) + NG_n^E(r')\rho_n(|\vec{r}-\vec{r}'|), \quad (4.8)$$

and

$$\rho_Z(r) = 4 \int d^3r' ZG_p^Z(r')\rho_p(|\vec{r}-\vec{r}'|) + NG_n^Z(r')\rho_n(|\vec{r}-\vec{r}'|), \quad (4.9)$$

where $G_{p,n}^{E,Z}$ are the charge form factors for the proton and neutron, equal to the Fourier transforms of the electromagnetic and weak charge distribution of the particles [40]. The weak charge form factors of the proton and neutron particles are composed of their electric

form factors, with equal contributions from strangeness to both,

$$G_p^Z = \frac{1}{4}[Q_W^p G_p^E + Q_W^n G_n^E - G_s^E], \quad (4.10)$$

and

$$G_n^Z = \frac{1}{4}[Q_W^n G_p^E + Q_W^p G_n^E - G_s^E], \quad (4.11)$$

and with no contribution from the magnetic form factors for a spin zero nucleus. The densities are normalized to 1

$$\int d^3r \rho_p(r) = 1 \text{ and } \int d^3r \rho_n(r) = 1, \quad (4.12)$$

and the charges of the nucleons and nucleus are [34]

$$Q_{EM} = \int d^3r \rho_{ch}(r) = +Z = 20, \quad (4.13)$$

$$Q_W = \int d^3r \rho_W(r) = Q_W^p Z + Q_W^n N = -N + (1 - 4 \sin^2 \theta_W)Z = 26.0728. \quad (4.14)$$

From these relations we obtain the mean square radii, where the point proton and neutron mean square radii are

$$R_p^2 = \frac{1}{Z} \int d^3r r^2 \rho_p(r) \text{ and } R_n^2 = \frac{1}{N} \int d^3r r^2 \rho_n(r), \quad (4.15)$$

the particle mean square charge radii and the strangeness mean square radius are

$$r_p^2 = \int d^3r r^2 G_p^E(r) \text{ and } r_n^2 = \int d^3r r^2 G_n^E(r) \text{ and } r_s^2 = \int d^3r r^2 G_s^E(r), \quad (4.16)$$

and the nuclear charge mean square radii are

$$R_{ch}^2 = \frac{1}{Z} \int d^3r r^2 \rho_{ch}(r) \quad \text{and} \quad R_W^2 = \frac{1}{Q_W} \int d^3r r^2 \rho_W(r). \quad (4.17)$$

Using these relations, equations 4.8 and 4.9 yield

$$R_{ch}^2 = R_p^2 + r_p^2 + \frac{N}{Z} r_n^2 + \text{SO terms}, \quad (4.18)$$

and

$$R_W^2 = \frac{1}{Q_W} [-N R_n^2 + Q_W^p Z R_p^2 + (-N + Q_W^p Z) r_p^2 + (N Q_W^p - Z) r_n^2 - (N + Z) r_s^2] + \text{SO terms}. \quad (4.19)$$

The point proton and neutron RMS radii and skin thickness are then easily obtained using the limits on the strangeness radius and the known electromagnetic charge and particle mean square radii from prior experiments, combined with the model extracted weak radius from the CREX result. Spin orbit, strangeness, and meson exchange current (MEC) corrections are small but should be considered in order to make accurate comparisons between the measured Weak form-factor and theoretically calculated nucleon distributions.

4.4 Physics Implications

Although the neutron skin information from various models is not yet available, the form factor information is enough to begin evaluating the impact of the CREX result. The preliminary difference in the electromagnetic and weak charge form factors at the CREX $\langle q \rangle = 0.875 fm^{-1}$ is obtained with the DFT family of models, where the charge form factor is obtained by parametrizing the existing experimental data [34] and the weak form factor,

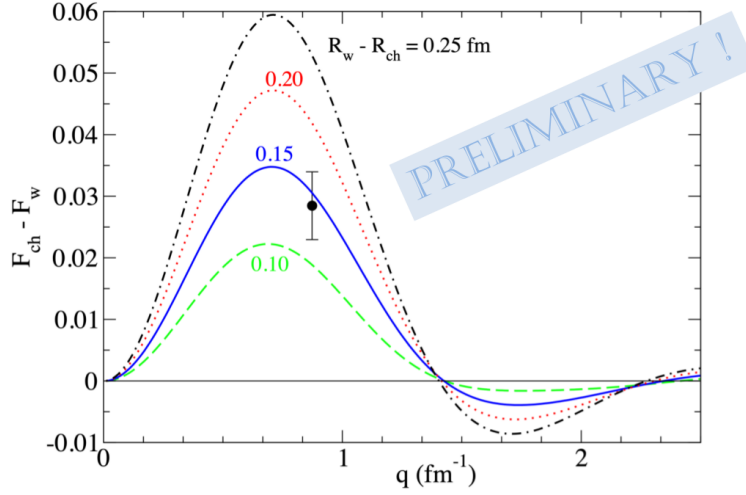


Figure 4.2: The electromagnetic charge form factor minus the weak charge form factor for the ^{48}Ca nucleus as a function of $q = \sqrt{Q^2}$. The curves show the calculated difference in form factors for a family of nuclear structure models corresponding to different weak charge RMS radii over a range of relevant skin thicknesses, which are labelled next to each curve. The CREX result is shown as a point with the experimental error bar [34].

shown in Fig. 4.1, is obtained for several relativistic and non-relativistic DFT models and compared with the experimental A_{PV}^{meas} . The various model calculated $F_W(\langle Q^2 \rangle)$ values are strongly correlated with $\langle A_{PV} \rangle$, with the linear fit line shown in the figure, allowing the family of models to extract $F_W = 0.1297(55)$ corresponding to the observed A_{PV} value. This extracted result differs from the calculated $A_{PV} \sim 2.5$ ppm prediction of the FSUGold DFT model, instead using the family of models to obtain the relationship between F_W and A_{PV} , and provides a useful benchmark connection to the model calculated charge densities.

The difference in form factors, $F_{ch} - F_w$, obtained in this way is shown in Fig. 4.2 [34]. This figure includes preliminary results of the model calculated form factor difference as a function of Q^2 which correspond to electromagnetic and weak charge distributions that yield a range of skin thicknesses. The skin thicknesses calculated by the *ab initio* NNLO_{sat}, FSUGold DFT, and the DOM models, previously discussed in section 1.4, predict a thin $\sim 0.135(15)fm$, intermediate $\sim 0.176(18)fm$, and thick $\sim 0.249(23)fm$ skin, respectively.

From the preliminary result displayed in the figure we see that there is substantial tension with some models. The charge distribution which produces results that match the measured A_{PV} indicated by the point on the plot is compatible with a smaller skin corresponding much more closely to models which predict an $R_{skin}^{48} \sim 0.15 fm$, such as the *ab initio* NNLO_{sat} model, than it does to those which predict a larger $\sim 0.25 fm$ skin, such as the DOM approach.

Similarly it is possible to compare the calculated form factor difference within the same models for both ^{48}Ca and ^{208}Pb and look at the mutual agreement of the models extracted results from both PREX and CREX. This is done for a family of DFT models, shown in Fig. 4.3, which indicates tension at the 90% level with the preliminary results. The DFT models used that are consistent with the PREX measurement yield a thicker skin and larger form factor difference, but the models consistent with the CREX measurement are thinner. The model results may differ due to statistical fluctuations in our data, or the tension may indicate that the DFT models used are not sufficient to characterize the physics at both the larger, volume dominated scale of the ^{208}Pb nucleus and the medium sized and more surface dominated scale of the ^{48}Ca nucleus. The *ab initio* model approach, when constrained by the CREX measurement, may then be useful for informing the medium mass scale physics for the DFT and DOM model approaches.

4.5 Future Prospects and Concluding Remarks

CREX and PREX together provide tight constraints on nuclear structure models across a range of theoretical techniques. These experiments provide valuable input for parametrizing the isovector parts of the nuclear equation of state, with consequences for dense nuclear matter across many orders of magnitude, from medium mass nuclei up to neutron stars.

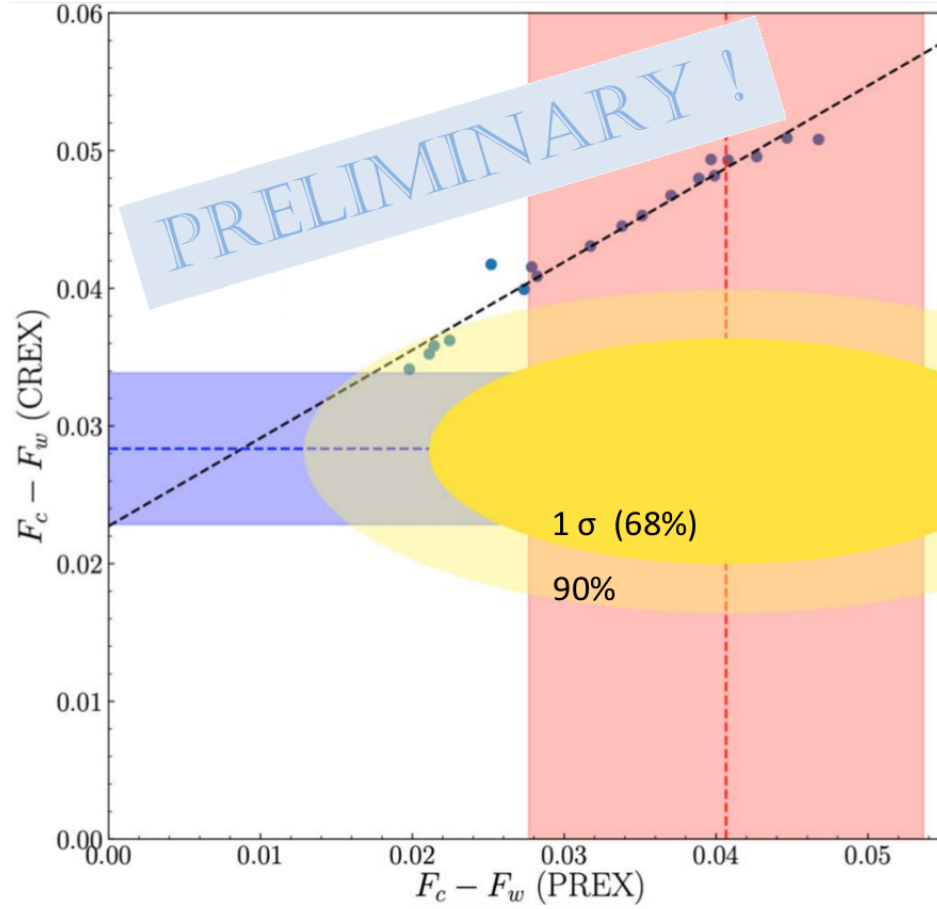


Figure 4.3: The difference in electromagnetic charge form factor minus the calculated weak charge form factor result from a family of relativistic and non-relativistic DFT models for CREX versus that of PREX. The model calculation for both experiments' results are plotted, and the values consistent with the experimental results are shown in the red (PREX) and blue (CREX) bands. The yellow ellipses show the 1σ and 90% confidence levels of the overlap region for the two experiment results [34].

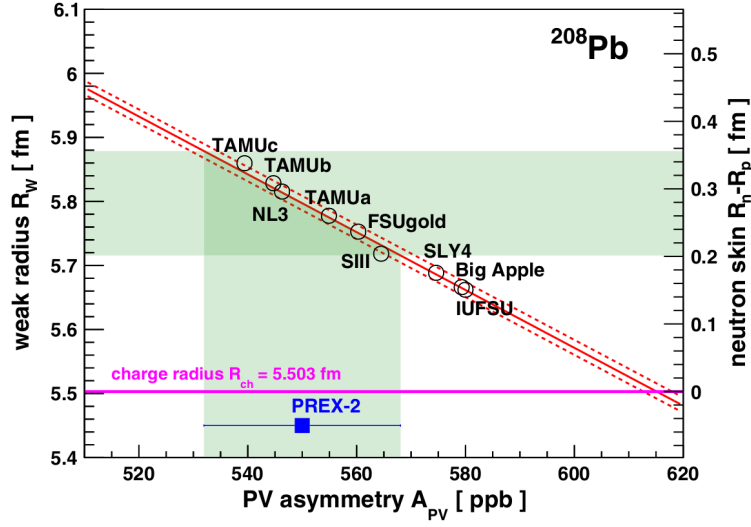


Figure 4.4: The extracted weak radius (left) and neutron skin (right) for the ^{208}Pb nucleus with the experimental electromagnetic charge radius and the PREX II asymmetry result shown. The theoretical uncertainty in the skin extraction is determined by the spread in the correlation of the models' predictions versus A_{PV} and the central value and experimental uncertainty are obtained by projecting the experimental asymmetry result to the fit line. Reproduced from [2].

Because the theoretical models parametrize both the charge radius and the charge surface thickness, as described in section 4.2, the CREX radius extraction includes some model uncertainty due to the possible range of surface thicknesses within the nuclear structure models. It is possible to further constrain the surface thickness with additional measurements at other momentum transfer points, which is discussed in detail in [12] and proposed as a possible measurement with the MAMI facility in a recent letter [36].

It is important that models which are capable of describing the ^{48}Ca nucleus do make calculations corresponding to the CREX measurement using its acceptance function. Obtaining the weak and neutron skin thicknesses can be done, but in order to evaluate the model-dependent uncertainty in its extraction it is necessary to evaluate the spread of the model calculations and their dependence on the surface thickness parametrization. An ex-

ample of this process done for the PREX II result is shown in Fig. 4.4, which plots the model calculated weak radius and neutron skin thickness results versus the calculated A_{PV} values. The theoretical model uncertainty is taken as the spread of the points about the linear fit line, corresponding to the average deviation from the fit of the collection of models. This process may be done with any family of models to provide theoretical model uncertainty estimates. For the PREX result shown in the figure, the model uncertainty in R_{skin}^{208} corresponds to $\sim 16\%$ of the size of the experimental uncertainty, but it is expected to be a larger effect for CREX, as the surface thickness parametrization is more important for the more surface-dominated medium size nucleus [36]. Additionally, CREX will require additional care to treat the spin-orbit correction properly, as its contribution is expected to be similar in size to the experimental error bar.

Another proposed PVES experiment that will probe the neutron structure of nuclei is MREX, the Mainz Radius EXperiment, that is possible with the upcoming P2 experimental apparatus at the MAMI Mainz facility [16]. MREX proposes to measure the neutron skin in ^{208}Pb with twice the precision of PREXII, and will be able to measure a second ^{48}Ca Q^2 point, sensitive to the neutron surface thickness, complementary to this reported CREX result. The systematic uncertainties of the hadronic probe nuclear scattering results described in section 1.4 are also informed by the CREX measurement, as systematic uncertainty from strong interaction physics is insignificant for PVES, but the hadronic probes suffer from substantial model-dependence in their extractions. The CREX result will help constrain various nuclear structure models and provide important constraints to the isovector sector of the nuclear equation of state of nuclear matter.

Appendix A

Run-ranged Segmentation Definitions

The CREX dataset spans several months of data collection and includes several kinds of segmentation corresponding to changing run conditions. The list of runs with their condition information is available on the online parity-violating run-control database (RCDB) [70] maintained by the experiment collaboration. The only conditions not stored in the RCDB relevant for the CREX data analysis are covered in chapter 3 and are given and described in that chapter or in this appendix. Conditions relevant for selecting the run list for the asymmetry analysis that are included in the RCDB include the following parameters: run number, slug number, target position, IHWP setting, Wien setting, average beam current, good run quality determination, production or calibration status, and HRS magnet status. The segmentation definitions that are not described in the RCDB and are given in this appendix are the dithering beam tune “segments,” the eigenvector monitor “part” definitions, and the “Pitt” segmentation slow control definitions.

A.1 Dithering Segmentation

The dithering calibration data is measured at 10 minute intervals during most production runs, and the slopes and sensitivities for the dithering and Lagrange analyses, respectively, are calculated by averaging the calibration data collected within each run. To fill in gaps for runs without successful sets of all seven beam modulation coil calibration data the resultant slopes and sensitivities are averaged, with equal weight, across the runs over stable segments. These segment definitions across the CREX run range are given in table A.1, the list of runs whose calibration data is unusable and cut from the calibration data-set is given in table A.2 for runwise and cyclewise outliers.

Table A.1: Runranges for the CREX dithering segmentation. Segments 25-32 are the transverse polarization running period. There is no segment 1, due to a lack of beam modulation measurements for the first run-range.

Segment	Start	Stop	Segment	Start	Stop	Segment	Start	Stop
No data	5408	5438	30	6405	6408	64	7734	7758
2	5130	5454	33	6424	6513	65	7759	7778
3	5455	5580	34	6514	6562	66	7779	7798
4	5581	5612	35	6563	6570	67	7799	7834
5	5613	5635	36	6571	6607	68	7835	7859
6	5636	5644	37	6608	6626	69	7860	7869
7	5645	5748	38	6627	6643	70	7870	7886
8	5749	5768	39	6644	6661	71	7887	7902
9	5770	5785	40	6662	6683	72	7903	7916
10	5786	5912	41	6684	6752	73	7917	7964
11	5913	5923	42	6753	6882	74	7965	7976
12	5924	5938	43	6883	6908	75	7977	8011
13	5939	6030	44	6909	6993	76	8012	8081
14	6031	6084	45	6994	7039	77	8082	8122
15	6085	6101	46	7040	7057	78	8123	8141
16	6102	6105	47	7058	7085	79	8142	8165
17	6106	6115	48	7086	7105	80	8166	8185
18	6116	6158	49	7106	7138	81	8186	8211
19	6159	6175	50	7139	7164	82	8212	8237
20	6176	6233	51	7165	7206	83	8238	8256
21	6234	6247	52	7207	7225	84	8257	8294
22	6248	6283	53	7226	7234	85	8295	8319
23	6284	6327	54	7235	7248	86	8320	8343
24	6328	6423	55	7249	7281	87	8344	8367
25	6344	6348	56	7282	7330	88	8368	8389
26	6349	6353	57	7331	7367	89	8390	8420
27	6354	6358	58	7368	7390	90	8421	8465
28	6359	6366	59	7391	7412	91	8466	8485
29	6367	6379	60	7413	7499	92	8486	8525
30	6380	6385	61	7500	7656	93	8526	8545
31	6386	6393	62	7657	7701	94	8546	8558
32	6394	6404	63	7702	7733			

Table A.2: List of run numbers and beam modulation cycle numbers that are removed from the calibration data-set for calculating slopes and sensitivities.

Run	Run	Cycle
5648	6792	4210
5649	6803	4633
5787	6927	5210
5791	6963	5270
5794	7075	5294
5971	7196	6276
6035	7232	6277
6108	7238	6278
6109	7267	6279
6408	7310	6280
6434	7635	6318
6463	8143	6850
6464	8147	8163
6515	8187	8754
6516	8194	8772
6517	8238	8836
6518	8359	8937
6519	8371	8957
6520	8426	
6585		

Table A.3: Table of eigenvector monitor “part” segmentations for CREX.

Parts	Part 1	Part 2	Part 3
Runs	5000-6327	6328-7500	7501-8558

A.2 Eigenvector Monitor Parts

The basis set of beam monitors is diagonalized with respect to correlated measurement of the beam, producing eigenvectors of the beam monitors that reduce the correlation of the correction slopes. The CREX data-set is split into three run-ranges of beam delivery optics tune, where the correlations between the monitors are stable. The eigenvector compositions are averaged over the three parts so that the systematic uncertainty estimate in terms of confidence in the slope calculations apply equally to all slopes calculated within each part. The underlying minirun-wise eigenvector monitor definitions are sorted and ranked in terms of the monitors’ RMS width. This is done by looping over the runs of each part, locking the eigenvector to point in the same direction as the average of previous runs, and ranking the resulting locked eigenvector by comparing the RMS for each minirun to the average RMS from the prior miniruns.

The choice of starting point to begin the RMS ranking comparisons is non-trivial for determining the most similar eigenvector definitions between the three parts, and to simplify the process the ranking averaging algorithm is set to use a starting minirun from midway through the part’s data-set to compare each minirun against. Due to instability in the beam tune optics at the beginning of the experiments, part 1 uses the result of averaging starting midway through the part as a starting point for locking and sorting each minirun’s eigenvector monitor definition, part 2 uses the run 6516 values as a single baseline starting point, and part 3 uses run 8003 as the baseline starting point.

The run-ranges of the three eigenvector monitor “parts” of CREX are given in table A.3 and the 12 BPM eigenvector monitor compositions for the three parts of CREX in terms of their constituent BPMs are given in tables A.4, A.5, and A.6.

A.3 Slugs, Slow Controls, and Pitts

The Pitt definitions combine neighboring slugs with equal amounts of opposite IHWP states. Each Pitt has approximately two slugs of each IHWP in and out states, and for slugs that are smaller than the typical slug may contain more. The relative weights of the Pitts compared with each other are shown in Fig A.1 and relative weights of the slugs that comprise the Pitts are shown in Fig A.2. The list of slugs comprising the Pitt definitions are given in table A.7 and the average A_{det} result for CREX using the Pitt averaging timescale is shown in Fig A.3.

Table A.4: CREX part averaged 12 BPM eigenvector monitor combinations, for the first part, averaged across runs 5000-6327.

	12X	11X	4eX	4aX	1X	16X	4eY	4aY	1Y	16Y	11Y	12Y
0	0.64	0.23	-0.35	-0.40	-0.40	0.31	-0.05	-0.05	-0.03	0.03	0.02	0.04
1	0.03	0.01	0.07	0.09	0.09	-0.07	-0.41	-0.48	-0.47	0.14	0.46	0.33
2	-0.65	-0.32	-0.34	-0.37	-0.35	0.28	-0.05	-0.06	-0.07	0.02	0.07	0.03
3	0.04	-0.02	0.01	-0.01	-0.05	-0.01	0.50	0.36	-0.13	-0.40	0.60	0.28
4	0.03	-0.03	0.02	-0.01	-0.04	-0.03	-0.12	-0.19	-0.42	-0.75	-0.20	-0.41
5	0.16	-0.44	0.53	0.03	-0.66	-0.23	-0.04	-0.01	0.06	0.06	-0.01	0.00
6	0.05	-0.10	-0.31	0.08	-0.04	-0.36	-0.50	0.07	0.56	-0.31	0.30	-0.04
7	0.06	-0.11	-0.35	-0.26	0.05	-0.72	0.27	-0.05	-0.25	0.27	0.00	-0.23
8	-0.08	0.18	0.21	-0.30	0.05	-0.05	0.34	-0.68	0.43	-0.12	0.17	-0.09
9	0.27	-0.60	0.14	-0.45	0.52	0.16	-0.12	0.09	0.06	0.01	0.10	-0.11
10	0.21	-0.46	-0.42	0.55	0.01	0.19	0.30	-0.35	0.09	0.00	-0.03	0.01
11	0.03	-0.12	-0.06	-0.17	0.06	-0.24	0.03	-0.09	0.03	-0.26	-0.50	0.75

Table A.5: CREX part averaged 12 BPM eigenvector monitor combinations, for the second part, averaged across runs 6328-7500.

	12X	11X	4eX	4aX	1X	16X	4eY	4aY	1Y	16Y	11Y	12Y
0	0.93	0.35	-0.02	-0.02	-0.01	0.01	-0.06	-0.06	-0.01	0.05	0.00	0.03
1	0.00	-0.07	-0.53	-0.57	-0.52	0.35	0.00	0.00	-0.01	0.00	0.01	0.01
2	-0.07	-0.04	0.00	0.01	0.01	0.00	-0.40	-0.47	-0.45	0.23	0.48	0.36
3	0.07	0.00	0.02	0.00	-0.02	-0.01	0.51	0.33	-0.25	-0.43	0.56	0.24
4	-0.02	0.02	-0.02	0.01	0.02	0.01	0.20	0.25	0.49	0.66	0.24	0.40
5	0.19	-0.50	0.58	0.01	-0.60	-0.11	-0.05	0.02	0.07	0.02	0.02	0.00
6	-0.07	0.18	0.37	-0.11	0.00	0.43	0.46	-0.11	-0.44	0.32	-0.32	0.03
7	0.15	-0.38	-0.29	-0.10	0.05	-0.59	0.38	-0.13	-0.27	0.32	-0.08	-0.21
8	-0.07	0.19	0.18	-0.26	0.01	-0.10	0.35	-0.68	0.42	-0.15	0.23	-0.15
9	0.21	-0.55	0.14	-0.39	0.58	0.34	-0.10	0.03	0.10	-0.07	0.07	-0.01
10	0.12	-0.32	-0.33	0.64	-0.02	0.45	0.21	-0.30	0.13	-0.06	-0.02	0.05
11	-0.01	0.07	0.04	0.13	-0.05	0.21	-0.06	0.15	-0.05	0.27	0.49	-0.77

Table A.6: CREX part averaged 12 BPM eigenvector monitor combinations, for the third part, averaged across runs 7501-8558.

	12X	11X	4eX	4aX	1X	16X	4eY	4aY	1Y	16Y	11Y	12Y
0	0.68	0.39	0.29	0.32	0.30	-0.25	-0.11	-0.10	-0.04	0.05	-0.11	-0.04
1	0.58	0.20	-0.41	-0.43	-0.38	0.37	-0.01	0.00	0.01	0.00	-0.03	-0.01
2	-0.07	-0.05	-0.05	-0.06	-0.06	0.03	-0.52	-0.58	-0.50	0.24	0.19	0.19
3	0.12	0.02	0.05	0.02	-0.02	-0.06	0.27	0.18	-0.13	-0.06	0.78	0.49
4	-0.04	0.05	0.10	0.03	-0.09	0.04	0.02	0.10	0.38	0.84	-0.11	0.31
5	0.16	-0.31	0.51	-0.06	-0.68	-0.33	0.07	-0.09	-0.03	-0.11	-0.03	-0.12
6	-0.05	0.11	0.51	-0.07	-0.09	0.40	0.53	-0.15	-0.42	0.09	-0.25	0.05
7	0.09	-0.20	-0.12	-0.31	0.08	-0.43	0.48	-0.11	-0.25	0.49	0.04	-0.33
8	-0.10	0.21	0.12	-0.23	0.10	0.01	0.18	-0.65	0.56	-0.12	0.27	-0.14
9	0.29	-0.60	0.15	0.10	0.22	0.39	-0.14	0.05	0.14	0.16	0.31	-0.39
10	0.03	-0.05	-0.42	0.73	-0.31	0.06	0.31	-0.29	0.01	0.04	0.02	-0.08
11	-0.23	0.52	0.09	0.07	-0.24	0.04	-0.16	0.26	-0.12	0.20	0.36	-0.57

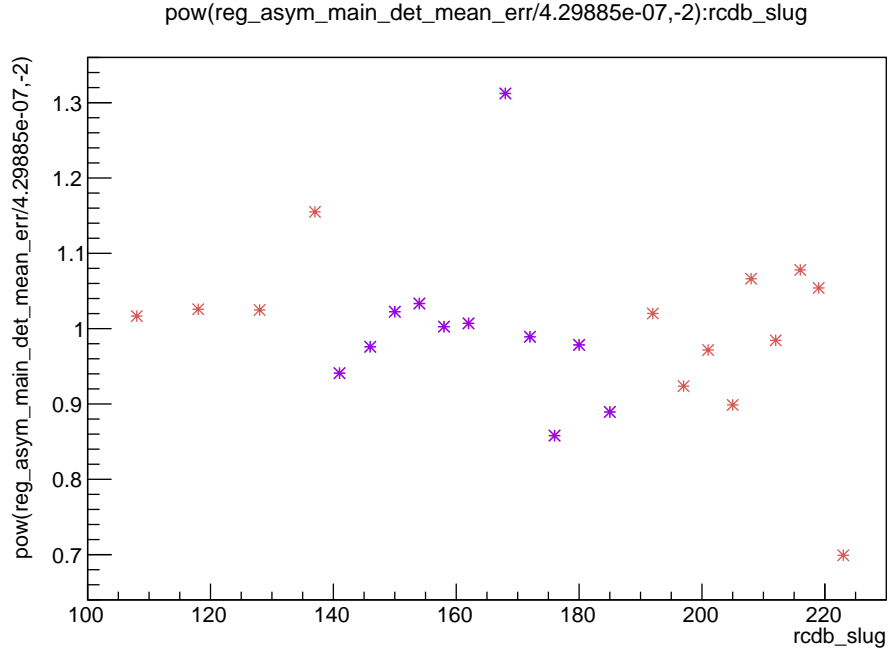


Figure A.1: Relative statistical weights of the Pitts (in arbitrary units, approximately normalized to the average weight for all Pitts) versus Pitt number. Orange is Wien right and purple is Wien left.

Table A.7: Table of Pitt slug range definitions, indicating the Wien and IHWP states included.

Pitt	Wien	IHWP Out Slugs	IHWP In Slugs
0	Right	100, 102, 104, 106, 107	101, 103, 105, 108
1	Right	109, 111, 113, 116, 117	110, 112, 114, 115, 118
2	Right	119, 121, 124, 125, 127	120, 122, 123, 126, 128
3	Right	129, 131, 133, 135, 137	130, 132, 134, 136
4	Left	138, 140	139, 141
5	Left	142, 143, 145	144, 146
6	Left	147, 149	148, 150
7	Left	151, 153	152, 154
8	Left	155, 157	156, 158
9	Left	159, 161	160, 162
10	Left	163, 165, 167	164, 166, 168
11	Left	169, 171	170, 172
12	Left	173, 175	174, 176
13	Left	177, 179	178, 180
14	Left	181, 183, 185	182, 184
15	Right	186, 188, 190, 191	187, 189, 192
16	Right	193, 194	195, 197
17	Right	196, 198	199, 201
18	Right	200, 202	203, 205
19	Right	204, 206	207, 208
20	Right	209, 210	211, 212
21	Right	213, 216	214, 215
22	Right	217, 219	218, 220
23	Right	222, 223	221

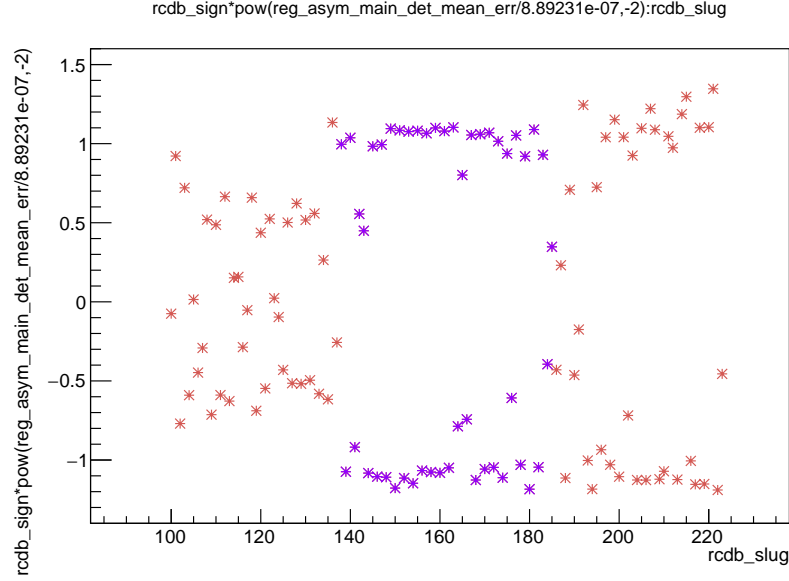


Figure A.2: Relative statistical weights of the slugs used to assign Pitt definitions (in arbitrary units, approximately normalized to the average weight for all slugs) versus slug number. The sign corresponds to the IHWP state, indicating the similar amounts of data taken in each slow control setting. See table A.7 for the slug to Pitt correspondence. Orange is Wien right and purple is Wien left.

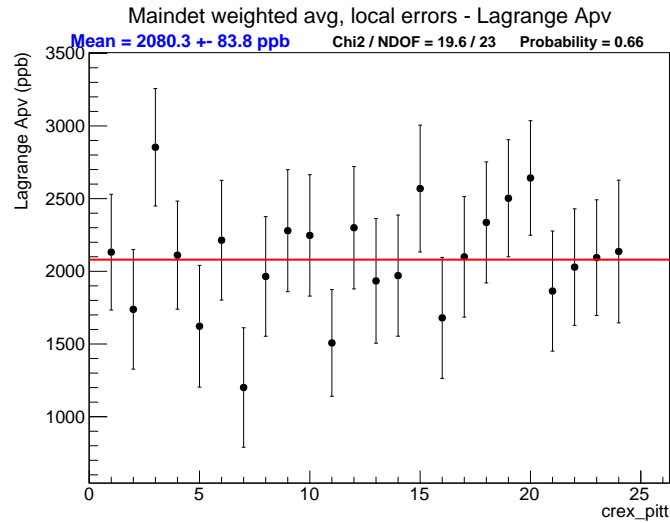


Figure A.3: 12 eigenvector monitor Lagrange multipliers analysis corrected A_{det} vs. Pitt.

Appendix B

Non-Technical Overview

This appendix, intended for a junior scientist audience, is a non-technical introduction to the ideas of quantum mechanics underlying the Calcium Radius EXperiment (CREX) described in the body of this dissertation.

B.1 Quantum Mechanics

Humanity has been trying to understand the universe since the beginning of society when celestial objects and natural cycles were attributed personality and godhood. Over the centuries alternate ideas have emerged, and gradually more sophisticated explanatory models and philosophical ideas have been proposed and tested to sate our need for understanding. Even as early as the 5th century BCE, Democritus put forth the philosophical idea of an uncuttable “atom,” the basic building block from which all matter, including ourselves, is built [73].

It wasn’t until 1905 that Einstein was able to provide an adequate scientific grounding for Democritus’ idea and prove the existence of such fundamental building blocks, by means of his theory implementing atoms to unequivocally explain Brownian motion, the random motion of small particles in liquids, even though the atoms were still invisible at the time [74, 75]. At the same time, Einstein and others were encountering and attempting to explain progressively harder to explain phenomena in the theory of electromagnetism, such as the existence of various kinds of radiation and the microscopic details of the relationship between light and electricity. The theoretical explanation of the quantum photo-electric effect is what eventually won Einstein his Nobel prize and gave birth to quantum mechanics [76].

Quantum mechanics (QM) can be intimidating, but the core idea is in the name: the mechanics, which are the laws of motion, of physical quanta, which are fundamental countable objects. The revolutionary idea of QM is that everything is quantized, including light, which had previously been understood as propagating waves of electromagnetic field. This immediately meant that the wave-mechanics ideas that had been the primary topic of re-

search of the 19th century must give way to a quantum-mechanical description, but also that the quantized particles - the atoms and other newly discovered forms of radiation from radioactive decays - must obey some kind of wave-mechanics. The combination of these two ideas, particle mechanics and wave mechanics, gave rise to wave-particle duality and the quantum mechanical equations of motion.

The wave and particle nature of QM appear in the probabilities of interactions and propagation. The mathematical element governed by the quantum mechanical equations of motion is called the “wave function”, which is a distribution as a function of time and position. The square of the wave function is a probability amplitude which tells the probability of finding one quanta in that place and time based only on the knowledge of the interacting particles’ starting conditions and possible available interaction channels.

The fundamental prediction made by the laws of quantum mechanics which is observable is the probability amplitude. The physically meaningful interactions of matter and energy take place at the wave function level, where the interesting wave-like phenomena of quantum physics reside and are revealed by measurements of the probability distributions involving those interactions. Quantum mechanical calculations and experimental measurements all boil down to defining some set of initial conditions, interaction mechanisms, and finite sized modes of detection. The initial conditions and available kinds of quantum particles define the things that exist, the interaction mechanism determine what kinds of events are able to take place and the kinds of more complicated structure can form, and the definitions of detection determine the limits of measurement and their correspondence to human experience.

B.2 Quantum Field Theory

The development of QM was driven by the observation of quantized behaviors, primarily those having to do with electrons and photons. Many years later, the effort to describe electrons interacting with photons has given rise to Quantum Electrodynamics (QED), a form of Quantum Field Theory (QFT), which involves adding together the contributions to probability amplitudes from every possible particle path, spanning the entire universe, all time, all energies, and interactions. Quantum particles are excitations of the underlying quantum field which exists at all points in space-time, and so calculations must consider that all possible paths are all occurring, producing a resultant wave function of the possible paths combined, calculating the probability amplitudes for each possible outcome from a specified process.

As a simple example, due to spatial symmetry, where a symmetry is the invariance of physical laws with respect to some change, the probability amplitude for a particle going in a direction with some amount of momentum is a small localized point traveling in a straight path with constant momentum, as you would expect from classical physics. This straight-path behavior is due to the contributions from all of the infinitely many alternate paths’ symmetrically cancelling each other out, except in the simple straight line case [77]. In a

similar way, the double slit experiment corresponds to the wave function passing through both slits simultaneously and then re-radiating from each slit, with the two wavefronts leaving the two slits as the collection of possible paths now overlapping and interfering, producing a wave-like interference pattern on a downstream detector. QED is the most successful scientific theory ever discovered, describing the interaction of electrically charged particles, most notably the electron, via the exchange of photons as the force mediating particle. Gradually, all of the phenomena of radiation, atoms, and even nuclear and nucleon physics have come to be expressed in the QFT formalism, in the Standard Model of particle physics.

B.3 Nuclear Physics

Nuclear physics is also a form of quantum mechanics, which is governed by the weak and strong nuclear forces, the other two components of the Standard Model, alongside QED's electromagnetism. The strong force behaves similarly to QED, except that its force mediating particle, the gluon, also is able to interact with itself, due to there being three types of charges and the complication of the possible interactions that this brings. The strong nuclear force charges, analogous to the electric charge, are given the creative but not meaningful name of "color charge," with "red," "green," and "blue" as the names of the three different charges.

The self-interaction of the strong force makes it impossible to isolate a free strong-charged particle - the amount of energy required to pull a strong-charged particle away from others is so high that, in the process of pulling, enough energy is expended that new particles are excited into existence, thwarting the attempted isolation-extraction. This self-interaction barrier causes an increase in the interaction strength of the strong force as the distance scale increases and interaction energy scale decreases. This limits the scale at which strong interactions are easily calculable, and is called "color-confinement." Going the other direction, as the energy scale increases, the interaction distance scale correspondingly decreases. This is because the incoming probe is able to get closer to the source charge without its trajectory being significantly bent by their interaction. The interaction strength gets weaker as the probe gets closer because the closer a probe gets to the source of color charge the less other charged force mediating gluons within the nuclear matter exist between the probe and the source charge. This fall-off of the probed effective charge is called "asymptotic freedom" and allows measuring the strong interactions at high energies and small distances.

As a result of the low energy and long distance color-confinement barrier, the fundamental formulation of the strong force in terms of gluons interacting between the strong-charged matter particles, called quarks, is not useful for describing the interactions at the higher level between the stable states of strong-charged particles, the proton and neutron. The proton and neutron are called "nucleons" as they comprise the atomic nucleus, and the quarks and gluons that make up the nucleons are called "partons" and are the most fundamental building blocks.

B.4 Effective Field Theory

To describe the interactions of nucleons within nuclear matter or of the bulk nuclear matter in atomic nuclei in even more general ways, effective field theories (EFTs) must be implemented. A useful model for describing and understanding bulk nuclear physics is the semi-empirical mass formula, which captures the relationships of mass and binding energy of nuclei to the quantities of protons and neutrons [78]. Here “semi-empirical” means that the terms in the formula are partly provided by theoretical considerations, derived from treating the nucleus as a liquid droplet of nucleons, while the relative strengths are determined by measured observations.

The binding energies described by the semi-empirical mass formula can be roughly used to explain the masses and reactions of nuclei of a wide range of proton and neutron number, typically represented by atomic number which is the number of protons and the sum of protons and neutrons. The alchemist’s dream of transmutation of elements, first consciously observed in the natural decay of Thorium into Argon by Rutherford and Soddy in 1902, as well as nuclear fusion and fission are captured by this formula [79]. The terms in the formula depend on the energy cost of increased surface area, increased internal volume, the electric charge repulsion of the protons, the quantum mechanical overlap of identical particles, and the mismatch between the quantity of neutrons versus protons. This last term is called the nuclear symmetry energy, which parametrizes the energy cost of having different numbers of neutrons and protons, and therefore plays an important role in the physics of neutron-rich systems such as heavy nuclei and even neutron stars. Explanatory nuclear physics models do not necessarily have to produce terms that can be mapped onto those of the semi-empirical mass formula, but it serves as an useful starting point, drawing from the liquid drop model of the nucleus.

B.5 Electroweak Theory

The nuclear symmetry energy is an interesting part of nuclear physics to explore as it determines how neutrons are distributed in nuclei. However, it is difficult to measure the distribution of neutrons when they are not electrically charged and therefore don’t primarily interact with charged particle probes such as electrons. This is where the weak nuclear force is useful. In the standard model the weak force is combined with the electromagnetic QED theory, describing the electroweak interactions where the familiar massless photons and the weak force’s massive Z and W^\pm particles are all related to each other.

A key difference between the weak and electromagnetic forces, other than the interaction strengths, is that the photon interacts with particles that have different quantum spin angular momentum quantities identically, while the Z particle does not. This is due to the intrinsic violation of the spatial “parity” symmetry in the weak force, which interacts differently based on the particle’s spin. As a result, particles respond differently to interactions with the weak

Z particle, allowing the measurement of parity violation in spin-polarized electron scattering to probe the target’s weak charge. Experimentalists can exploit this feature by changing the polarization state of the incoming electron beam while leaving the experiment set up unchanged. The symmetry conserving electromagnetic interaction between the target and the polarized electrons will be the same, and any asymmetry between the two polarization states is proportional to the weak charge of the target. Polarized nuclear scattering yields a parity-violating scattering rate asymmetry, A_{PV} , that is sensitive to the neutron distribution.

It is possible to use the measured A_{PV} and the measured kinematic distribution of scattered angles and energies to extract the weak charge form factor. The form factor is the scattering probability distribution Fourier transform in terms of the momentum exchanged between the electron and the target. This momentum-space form factor is directly related to the three dimensional spatial distribution of the struck target nucleus. This relationship is essentially the quantum mechanical interference of the incident electron wave-function scattering around the circular cross-section of the target nucleus. The interference of a wave-front around a hard circle is a well characterized distribution, and taking into account a parametrization of the soft shape of the nucleus gives a tool to extract the spatial charge distribution information from the observed momentum-space form factor. As a result, a measurement of the electron scattering form factor in a small region of the momentum-space gives constraints for what the rest of the form factor distribution nearby must look like, and paired with sufficient theoretical input it is possible to extract information about the radius of the weak charge distribution.

B.6 Calcium Radius EXperiment

CREX is a measurement that does just that, utilizing polarized electron scattering to make a precise and accurate measurement of A_{PV} corresponding to the weak charge form factor in ^{48}Ca . With some nuclear structure physics model input this yields the neutron distribution radius and excess neutron skin thickness of ^{48}Ca . In addition to being an accurate measurement of an otherwise difficult to measure physical quantity, CREX is also valuable as a test of predictive theories, especially when taken in conjunction with their predictions of other phenomena at different scales, such as the related lead radius experiment (PREX) and neutron star observations. CREX, as well as other A_{PV} measurements, is a beautiful experiment because it requires a tremendous number of complex systems precisely set up such that everything works together and the final data set is straightforward to analyze and interpret.

When encountering an A_{PV} measurement such as CREX for the first time, many of its components may appear strange or counter intuitive. For example, the detectors are used differently from standard nuclear or particle physics measurements, where traditional detectors will count every passing particle and store its signal strength, timing and position data. Meanwhile CREX instead opts for setting up the experiment in such a way that only

occasional absolute measurements of the individual passing particles are required, as long as we can stably measure the relative rates of particles quickly to produce millions of individual asymmetry measurements. As such, the detector set up, data acquisition, beam delivery and polarization, and signal backgrounds are all the subject of great scrutiny and care.

B.7 Outline

To help illuminate these differences and ambiguities, the body of thesis describes how to prepare and analyze CREX, including plain English descriptions of the various choices that were made. This thesis is intended to be a resource for future A_{PV} experiment students, covering components in as much detail as is necessary to be able to replicate the measurement.

- Chapter 1 introduces the theoretical background of CREX, covering nuclear structure physics and the parity-violating electron scattering technique in much more technical detail than this overview.
- Chapter 2 gives an experimental overview, discussing the function and use of the experimental apparatus.
- Chapter 3 covers the asymmetry analysis methods and results.
- And Chapter 4 wraps up the parity-violating asymmetry results and looks prospects for its theoretical interpretation.

Bibliography

- [1] S Riordan. CREX, Proposal to Jefferson Lab PAC 40, 2013. URL http://halloweb.jlab.org/parity/prex/c-rex2013_v7.pdf.
- [2] D Adhikari, H Albataineh, D Androic, K Aniol, DS Armstrong, T Averett, CA Gayoso, S Barcus, V Bellini, RS Beminiwattha, et al. Accurate Determination of the Neutron Skin Thickness of Pb 208 through Parity-Violation in Electron Scattering. *Physical Review Letters*, 126(17):172502, 2021.
- [3] MH Mahzoon, MC Atkinson, RJ Charity, and WH Dickhoff. Neutron skin thickness of Ca 48 from a nonlocal dispersive optical-model analysis. *Physical review letters*, 119(22):222503, 2017.
- [4] G Hagen, A Ekström, C Forssén, GR Jansen, W Nazarewicz, T Papenbrock, KA Wendt, S Bacca, N Barnea, B Carlsson, et al. Neutron and weak-charge distributions of the 48Ca nucleus. *Nature Physics*, 12(2):186–190, 2016.
- [5] FJ Fattoyev and J Piekarewicz. Neutron skins and neutron stars. *Physical Review C*, 86(1):015802, 2012.
- [6] W Nazarewicz, P-G Reinhard, W Satuła, and D Vretenar. Symmetry energy in nuclear density functional theory. *The European Physical Journal A*, 50(2):1–13, 2014.
- [7] CJ Horowitz, KS Kumar, and R Michaels. Electroweak measurements of neutron densities in CREX and PREX at JLab, USA. *The European Physical Journal A*, 50(2):1–13, 2014.
- [8] X Roca-Maza and N Paar. Nuclear equation of state from ground and collective excited state properties of nuclei. *Progress in Particle and Nuclear Physics*, 101:96–176, 2018.
- [9] JM Lattimer and Y Lim. Constraining the symmetry parameters of the nuclear interaction. *The Astrophysical Journal*, 771(1):51, 2013.
- [10] C Drischler, RJ Furnstahl, JA Melendez, and DR Phillips. How well do we know the neutron-matter equation of state at the densities inside neutron stars? A Bayesian approach with correlated uncertainties. *Physical Review Letters*, 125(20):202702, 2020.

- [11] BT Reed, FJ Fattoyev, CJ Horowitz, and J Piekarewicz. Implications of PREX-2 on the Equation of State of Neutron-Rich Matter. *Physical Review Letters*, 126(17):172503, 2021.
- [12] S Ban, CJ Horowitz, and R Michaels. Parity violating electron scattering measurements of neutron densities. *Journal of Physics G: Nuclear and Particle Physics*, 39(1):015104, 2011.
- [13] J Piekarewicz, BK Agrawal, G Colo, W Nazarewicz, N Paar, P-G Reinhard, X Roca-Maza, and D Vretenar. Electric dipole polarizability and the neutron skin. *Physical Review C*, 85(4):041302, 2012.
- [14] J Birkhan, M Miorelli, S Bacca, S Bassauer, CA Bertulani, G Hagen, H Matsubara, P von Neumann-Cosel, T Papenbrock, N Pietralla, et al. Electric Dipole Polarizability of Ca 48 and Implications for the Neutron Skin. *Physical review letters*, 118(25):252501, 2017.
- [15] J Zenihiro, H Sakaguchi, S Terashima, T Uesaka, G Hagen, M Itoh, T Murakami, Y Nakatsugawa, T Ohnishi, H Sagawa, et al. Direct determination of the neutron skin thicknesses in $^{40,48}\text{Ca}$ from proton elastic scattering at $E_p=295$ MeV. *arXiv preprint arXiv:1810.11796*, 2018.
- [16] M Thiel, C Sfienti, J Piekarewicz, CJ Horowitz, and M Vanderhaeghen. Neutron skins of atomic nuclei: per aspera ad astra. *Journal of Physics G: Nuclear and Particle Physics*, 46(9):093003, 2019.
- [17] Y Chao, SA Bogacz, and VA Lebedev. Simultaneous multiple pass steering at Jefferson Lab. In *Proceedings of the 1999 Particle Accelerator Conference (Cat. No.99CH36366)*, volume 2, pages 738–740 vol.2, 1999. doi: 10.1109/PAC.1999.795339.
- [18] KD Paschke. Controlling helicity-correlated beam asymmetries in a polarized electron source. *The European Physical Journal A*, 32(4):549–553, 2007. doi: 10.1140/epja/i2006-10442-8.
- [19] R Silwal. *Probing the Strangeness Content of the Proton and the Neutron Radius of ^{208}Pb using Parity Violating Electron Scattering*. PhD thesis, University of Virginia, 2012. URL https://libraetd.lib.virginia.edu/public_view/3j3332545.
- [20] JW Wexler. *Measurement of the Parity Violating Asymmetry in Elastic Electron Scattering off ^{208}Pb* . PhD thesis, University of Massachusetts, Amherst, 2014. URL https://scholarworks.umass.edu/dissertations_2/246.
- [21] KA Aniol et al. Parity-violating electroweak asymmetry in e-p scattering. *Physical Review C*, 69(6):065501, 2004. URL <https://journals.aps.org/prc/abstract/10.1103/PhysRevC.69.065501>.

- [22] KD Paschke. Sources of Helicity-correlated Electron Beam Asymmetries. In *AIP Conference Proceedings*, volume 1149, pages 853–858. American Institute of Physics, 2009. doi: 10.1063/1.3215778.
- [23] T Satogata, Y Roblin, MG Tiefenback, and DL Turner. 12 GeV CEBAF Transverse Emittance Evolution. In *Proc. 6th International Particle Accelerator Conference (IPAC'15), Richmond, VA, USA, May 3-8, 2015*, number 6 in International Particle Accelerator Conference, pages 640–642, Geneva, Switzerland, June 2015. JACoW. ISBN 978-3-95450-168-7. doi: <https://doi.org/10.18429/JACoW-IPAC2015-WEBD1>.
- [24] K Saenboonruang. *Measurement of the Neutron Radius of ^{208}Pb Through Parity Violation in Electron Scattering*. PhD thesis, University of Virginia, 5 2013.
- [25] JM Grames. *Measurement of a weak polarization sensitivity to the beam orbit of the CEBAF accelerator*. PhD thesis, University of Illinois at Urbana-Champaign, 2000. URL <ftp://ftp.jlab.org/pub/grames/thesis.pdf>.
- [26] S Covrig Dusa. The PREX2/CREX Target, 2 2020. URL <https://prex.jlab.org/cgi-bin/DocDB/private/ShowDocument?docid=494>.
- [27] J Brock, C Carlin, S Covrig Dusa, C Keith, J Maxwell, D Meekins, and R Michaels. The target for the PREX2 and CREX experiments, 9 2020. URL <https://prex.jlab.org/cgi-bin/DocDB/private/ShowDocument?docid=446>.
- [28] D Adhikari. *Neutron Skin Measurement of ^{208}Pb Using Parity-Violating Electron Scattering*. PhD thesis, Idaho State University, 2021. URL <https://etd.iri.isu.edu/ViewSpecimen.aspx?ID=1984>.
- [29] C Gal. New precision measurements of the neutral weak form factor of ^{208}Pb . In *APS Division of Nuclear Physics Meeting Abstracts*, volume 2020, pages AA–002, 2020.
- [30] J Alcorn, BD Anderson, KA Aniol, JRM Annand, L Auerbach, J Arrington, T Averett, FT Baker, M Baylac, EJ Beise, et al. Basic Instrumentation for Hall A at Jefferson Lab. *Nuclear Instruments and Methods in Physics Research Section A: Accelerators, Spectrometers, Detectors and Associated Equipment*, 522(3):294–346, 2004.
- [31] T Allison, M Anderson, D Androić, DS Armstrong, A Asaturyan, T Averett, R Averill, J Balewski, J Beaufait, RS Beminiwattha, et al. The Qweak experimental apparatus. *Nuclear Instruments and Methods in Physics Research Section A: Accelerators, Spectrometers, Detectors and Associated Equipment*, 781:105–133, 2015.
- [32] RS Beminiwattha. *A measurement of the weak charge of the proton through parity violating electron scattering using the Qweak apparatus: a 21% result*. PhD thesis, Ohio University, 2013. URL <https://www.osti.gov/biblio/1108591-measurement-weak-charge-proton-through-parity-violating-electron-scattering>

- [33] A Rakhman. *The design and construction of a green laser and Fabry-Perot cavity system for Jefferson Lab's Hall A Compton polarimeter*. PhD thesis, Syracuse University, 2011.
- [34] BT Reed and CJ Horowitz. Private communication, 11 2021.
- [35] C Clarke. Lagrange US Avg outliers, 9 2021. URL <http://ace.phys.virginia.edu/HAPPEX/4606>.
- [36] BT Reed, Z Jaffe, CJ Horowitz, and C Sfienti. Measuring the surface thickness of the weak charge density of nuclei. *Physical Review C*, 102(6):064308, 2020.
- [37] BA Brown. Neutron radii in nuclei and the neutron equation of state. *Physical review letters*, 85(25):5296, 2000.
- [38] CF v Weizsäcker. Zur theorie der kernmassen. *Zeitschrift für Physik*, 96(7-8):431–458, 1935.
- [39] P Langacker. *The Standard Model and Beyond*. Taylor & Francis, 2017.
- [40] CJ Horowitz, SJ Pollock, PA Souder, and R Michaels. Parity violating measurements of neutron densities. *Physical Review C*, 63(2):025501, 2001.
- [41] CJ Horowitz and J Piekarewicz. Impact of spin-orbit currents on the electroweak skin of neutron-rich nuclei. *Physical Review C*, 86(4):045503, 2012.
- [42] P-G Reinhard, J Piekarewicz, W Nazarewicz, BK Agrawal, N Paar, and X Roca-Maza. Information content of the weak-charge form factor. *Physical Review C*, 88(3):034325, 2013.
- [43] BG Todd-Rutel and J Piekarewicz. Neutron-rich nuclei and neutron stars: A new accurately calibrated interaction for the study of neutron-rich matter. *Physical review letters*, 95(12):122501, 2005.
- [44] WH Dickhoff and RJ Charity. Recent developments for the optical model of nuclei. *Progress in Particle and Nuclear Physics*, 105:252–299, 2019.
- [45] WH Dickhoff. Linking nuclear reactions and nuclear structure to study exotic nuclei using the dispersive optical model. In *Compound-Nuclear Reactions: Proceedings of the 6th International Workshop on Compound-Nuclear Reactions and Related Topics CNR* 18*, pages 83–90. Springer International Publishing, 2021.
- [46] F Sammarruca. Proton skins, neutron skins, and proton radii of mirror nuclei. *Frontiers in Physics*, 6:90, 2018.

- [47] A Le Fevre, Y Leifels, W Reisdorf, J Aichelin, and Ch Hartnack. Constraining the nuclear matter equation of state around twice saturation density. *Nuclear Physics A*, 945:112–133, 2016.
- [48] CW Leemann, DR Douglas, and GA Krafft. The continuous electron beam accelerator facility: CEBAF at the Jefferson Laboratory. *Annual Review of Nuclear and Particle Science*, 51(1):413–450, 2001. doi: 10.1146/annurev.nucl.51.101701.132327.
- [49] C Palatchi. *Laser and Electron Beam Technology for Parity Violating Electron Scattering Measurements*. PhD thesis, University of Virginia, 5 2019. URL https://libraetd.lib.virginia.edu/public_view/2j62s542k.
- [50] R Flood, J Hansknecht, S Higgins, and R Suleiman. Helicity control board user’s guide. *Jefferson Lab*, 2010.
- [51] L Harwood. The JLab 12GeV Energy Upgrade of CEBAF. In *Proc. 5th International Particle Accelerator Conference (IPAC’13), Pasadena, CA, USA, Sept 29 - Oct 4, 2013*, number 5 in International Particle Accelerator Conference, pages 1–5, Geneva, Switzerland, October 2013. JACoW. ISBN 978-3-95450-138-0. URL <https://accelconf.web.cern.ch/pac2013/papers/mozaa1.pdf>.
- [52] A Freyberger. Commissioning and Operation of 12 GeV CEBAF. In *Proc. 6th International Particle Accelerator Conference (IPAC’15), Richmond, VA, USA, May 3-8, 2015*, number 6 in International Particle Accelerator Conference, pages 1–5, Geneva, Switzerland, June 2015. JACoW. ISBN 978-3-95450-168-7. doi: <https://doi.org/10.18429/JACoW-IPAC2015-MOXGB2>.
- [53] C Yan, N Sinkine, and R Wojcik. Linear beam raster for cryogenic targets. *Nuclear Instruments and Methods in Physics Research Section A: Accelerators, Spectrometers, Detectors and Associated Equipment*, 539(1-2):1–15, 2005.
- [54] PA Souder. PREX-II, Proposal to Jefferson Lab PAC 38, 2011. URL <http://hallaweb.jlab.org/parity/prex/prexII.pdf>.
- [55] S Riordan. Simple Figure of Merit, 3 2018. URL <http://ace.phys.virginia.edu/HAPPEX/3481>.
- [56] S Riordan. PREX and CREX Collimator Figure of Merit, 12 2018. URL <https://prex.jlab.org/cgi-bin/DocDB/private/ShowDocument?docid=293>.
- [57] CJ Horowitz. Parity violating elastic electron scattering and Coulomb distortions. *Physical Review C*, 57(6):3430, 1998.

- [58] R Richards. *Measurements of the Beam Normal Asymmetry using Polarized Elastic Electron Scattering off Various Spin-0 Nuclei at 1 GeV*. PhD thesis, Stony Brook University, 8 2021.
- [59] WA Watson, J Chen, G Heyes, E Jastrzembski, and D Quarrie. CODA: a scalable, distributed data acquisition system. *IEEE transactions on nuclear science*, 41(1):61–68, 1994.
- [60] LR Mercado. *Probing novel properties of nucleons and nuclei via parity violating electron scattering*. PhD thesis, University of Massachusetts Amherst, 5 2012. URL https://scholarworks.umass.edu/open_access_dissertations/587/.
- [61] BJ Moffit. *Elastic scattering of longitudinally polarized electrons from helium-4: A measurement of $G(E)(S)$ at $Q^2=0.1(\text{GeV}/c)^2$* . PhD thesis, The College of William and Mary, 5 2007. URL <https://scholarworks.wm.edu/etd/1539623515/>.
- [62] GA Krafft, J-C Denard, RW Dickson, R Kazimi, VA Lebedev, and MG Tiefenback. Measuring and controlling the energy spread in CEBAF. *arXiv preprint physics/0009087*, 2000. URL <https://arxiv.org/abs/physics/0009087>.
- [63] D Higinbotham and C Keppel. Jefferson Lab Hall A Standard Equipment Manual, 6 2017. URL <https://hallaweb.jlab.org/github/halla-osp/version/Standard-Equipment-Manual.pdf>.
- [64] KB Unser. Design and preliminary tests of a beam intensity monitor for LEP. In *Proceedings of the 1989 IEEE Particle Accelerator Conference, Accelerator Science and Technology*, pages 71–73. IEEE, 1989.
- [65] D Higginbotham. CREX Beam Energy Measurement, 3 2020. URL <https://logbooks.jlab.org/entry/3805058>.
- [66] M Friend, D Parno, F Benmokhtar, A Camsonne, MM Dalton, GB Franklin, V Mamyan, R Michaels, S Nanda, V Nelyubin, et al. Upgraded photon calorimeter with integrating readout for the Hall A Compton polarimeter at Jefferson Lab. *Nuclear Instruments and Methods in Physics Research Section A: Accelerators, Spectrometers, Detectors and Associated Equipment*, 676:96–105, 2012.
- [67] T Ye. *Precision Measurement of the Parity Violating Asymmetry in Elastic Electron Scattering of ^{208}Pb* . PhD thesis, Stony Brook University, 8 2021. URL <https://prex.jlab.org/cgi-bin/DocDB/private/ShowDocument?docid=503>.
- [68] P King et al. Just Another Parity ANalyzer (JAPAN), 2021. URL <https://github.com/JeffersonLab/JAPAN>.

- [69] T Ye. Pedestals have non-trivial effect on BPM yields, 8 2019. URL <https://logbooks.jlab.org/entry/3722096>.
- [70] M Ito. Run Control Database, 12 2018. URL <https://github.com/JeffersonLab/rcdb>.
- [71] H Liu. *Measurement of the Ratio of the Neutron to Proton Structure Functions, and the Three-Nucleon EMC Effect in Deep Inelastic Electron Scattering Off Tritium and Helium-3 Mirror Nuclei*. PhD thesis, Columbia University, 12 2020.
- [72] J Yang, JA Hernandez, and J Piekarewicz. Electroweak probes of ground state densities. *Physical Review C*, 100(5):054301, 2019.
- [73] S Berryman. Democritus, 2004. URL <https://plato.stanford.edu/entries/democritus/>.
- [74] A Einstein. Über die von der molekularkinetischen Theorie der Wärme geforderte Bewegung von in ruhenden Flüssigkeiten suspendierten Teilchen. *Annalen der physik*, 4, 1905.
- [75] J Bernstein. Einstein and the existence of atoms. *American journal of physics*, 74(10): 863–872, 2006.
- [76] A Einstein. Über einem die Erzeugung und Verwandlung des Lichtes betreffenden heuristischen Gesichtspunkt. *Annalen der physik*, 4, 1905.
- [77] RP Feynman. QED: The Strange Theory of Light and Matter Princeton University Press. *Princeton, New Jersey*, page p15, 1985.
- [78] KS Krane, D Halliday, et al. *Introductory Nuclear Physics*, volume 465. Wiley New York, 1988.
- [79] E Rutherford and F Soddy. XXXIII.—The radioactivity of thorium compounds. I. An investigation of the radioactive emanation. *Journal of the Chemical Society, Transactions*, 81:321–350, 1902.